DOTTORATO DI RICERCA IN CHIMICA

Convenzione tra

UNIVERSITÀ DEGLI STUDI DI TRIESTE

e

UNIVERSITÀ CA' FOSCARI DI VENEZIA

CICLO XXX

PHOTOLUMINESCENT MATERIALS: FROM ORGANIC MOLECULES TO NANOMATERIALS

Settore scientifico-disciplinare: **__CHIM/06_CHIMICA ORGANICA_____**

DOTTORANDO
FRANCESCO RIGODANZA

COORDINATORE
PROF. MAURO STENER

SUPERVISORE DI TESI
PROF. MAURIZIO PRATO

ANNO ACCADEMICO 2016/2017

Table of contents

1. Photoluminescent materials

1.1 Luminescence

Figure 1.1 Aurora Borealis in Canada

Human beings are fascinated by luminescence. They have always been spectators of natural phenomena such as aurora borealis, lightening or luminous animals of various sorts.[1,2] In absence of knowledge, all these experiences were connected with magic or religion, with the mystery of these phenomena being ignored for long time. However, men tried reproducing luminescence for ages (indeed, there are many fascinating and slightly believable stories about “luminescent” human beings). A landmark in this field was the discovery of the Bolognan-stone in 1603 by Vincenzo Casciarolo. Casciarolo was a poor shoemaker with the passion of alchemy, who, while looking for

Figure 1.2 Bolognan-stone

the famous philosopher's stone, calcined a stone containing barium sulfate with coal and obtained luminescent barium sulfide.[3] This "magic stone", he called "lapis solaris", was a real phosphor which glowed after exposure to light. The discovery created a huge debate between the scientists of the period with G. Galileo dedicating his last essay to this topic.[4] The interest on these new materials grew exponentially in the following centuries. In 1852, Sir George G. Stokes discovered photoluminescence studying the mineral fluorspar and coined, for the first time, the term fluorescence. Then, in 1888, When Wiedemann classified luminescence into six kinds according to the method of excitation, classification that hasn't changed through the years: photoluminescence, thermoluminescence, electroluminescence, crystalloluminescence, triboluminescence and chemiluminescence.[5]

As the title of this doctoral thesis may suggest, our main interest is photoluminescence, which is any form of light emission that happens after photons are absorbed. This release of energy can take place in two different ways, via fluorescence or phosphorescence.[6] Fluorescence is fast, it has an emission rate of 10^{-8} s^{-1} and a typical lifetime of 10 ns. Phosphorescence is slower because it involves the emission of light from triplet-excited states, in which the electron has the same spin orientation both at the excited-state and at the ground

state. These transitions are forbidden therefore the emission rate are slow (10^{-3} to 1 s^{-1}) and the lifetimes longer (10^{-3} to 10^{3} s). What distinguishes the two phenomena is the electronic configuration of the excited state and the emission pathway, processes that are usually illustrated by the Jablonski diagrams as in Figure 1.3.[7–9]

In both phenomena, excitation is the first key process as it happens very fast (10^{-15} s) and a cascade of events follows light absorption. Aa fluorophore is excited to a higher vibrational level, either S_1 or S_2. The second step is the vibrational relaxation of excited state electrons to lower energy, which is called internal relaxation and it occurs in 10^{-10} - 10^{-12} s. The emission of a photon at longer wavelength while the molecule returns at the ground state is a competitive process but, since fluorescence lifetime are typically near 10^{-8} s, the emission usually

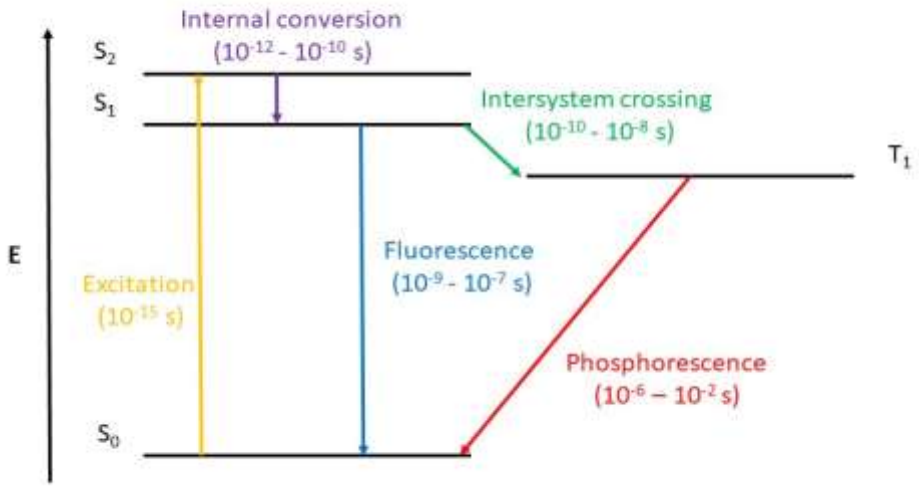

Figure 1.3 Jablonski diagram illustrating the transitions between electronic states of a molecule for the quantum mechanical processes of fluorescence and phosphorescence

results from the lowest energy vibrational state of S_1. The sequence of

events happens very rapidly, with many electrons involved, some absorbing, some giving off energy, so that the visible light we see looks continuous and not interrupted.[10–12] Un-like fluorescence, phosphorescence does not re-emit the photons it absorbs immediately. The electron in the excited state undergoes an intersystem crossing relaxation into an energy state of higher multiplicity, usually a triplet state. This electron is now trapped in this state T_1 and the return to the ground state is accessible only through forbidden transitions. Since T_1 has a lower energy than S_1, emission from this state is generally shifted to longer wavelengths relative to fluorescence. Emission from T_1 is slow, some phosphors have triplet lifetimes on the order of milliseconds but there are interesting compounds which can store this energy for longer time, up to hours or days.[9,13]

Fluorescence is characterized by a number of general features in common with most of the fluorophores: the stokes shift, the Kasha's rule, the mirror-image rule.

The Stokes shift, named after the physicist G. G. Stokes, is the difference between the maxima positions of absorption and emission spectra due to energy loss between the two phenomena. As we introduced previously, after light absorption the electron undergoes a rapid decay to the lowest level vibrational level of S_1. Moreover, fluorescence brings back the molecule to higher vibrational levels of S_0, therefore the emission peak is shifted to longer wavelength. In addition to these effects, energy loss can involve other process which expand the Stokes shift like: solvent effects, excited-state reactions, complex formation, energy transfer.

1. Photoluminescent materials

Kasha's rule, named after the spectroscopist M. Kasha, states that fluorescence emission spectrum is independent of the excitation wavelength since the photon emission occurs in appreciable yield only from the lowest excited state. However, exceptions exist such as molecules that display different absorption and emission or fluorophores that emit from S_2 level. In particular, one of the most interesting feature of carbon-based dots (CDs), materials, which will be introduced in the following sections and will be examined in the last two chapters of this thesis, is their emission excitation-dependency.

Most of the fluorophores display an emission spectrum that is the mirror image of the S_0-S_1 absorption spectrum. This behavior is called mirror image rule and it is related to the Franck-Condon principle that states all electronic transitions are vertical without change in the position of the nuclei, therefore absorption and emission involve the same transitions and similar vibrational energy levels of S_0 and S_1. Whereas in most of the cases the mirror image rule is related only to S_0-S_1 transitions, when they are not aggregated perylene bisimides show emission spectra, which are the specular image of the total absorption. Indeed the photoluminescence of these dyes can provide many information about their packing in solution, information that will be exploited in the next three chapters of the thesis.

The luminescence efficiency is expressed in terms of quantum yield (QY) and it is the most important characteristic of a fluorophore.[14] It is defined as the number of emitted photons divided by the number of adsorbed photons. The higher the quantum yield, the brighter the emission. It can be close to unity if the non-radiative decay rate is much smaller than the radiative decay. Many processes compete with the

radiative transition. Usually these processes are undesired, like vibrational energy loss, but there are also interesting alternatives of simple emission such as Förster Resonance Energy Transfer (FRET), which is the energy migration between two light-sensitive molecules: a donor and an acceptor. For this process to occur, the emission spectrum of the donor must overlap the absorption spectrum of the acceptor, however energy transfer does not involve light emission, there is no emission reabsorbed by the acceptor. This energy transfer happens through non-radiative dipole-dipole coupling in the excited states and it is very sensitive to the distance between the two species, indeed, it is inversely proportional to the sixth power of the distance between the fluorophores.

FRET can give significant structural information regarding the donor-acceptor pair. Since it is not sensitive to the surrounding solvent shell of a fluorophore, the energy transfer produces unique molecular information to that revealed by solvent-dependent events, such as fluorescence quenching, excited-state reactions, solvent relaxation, or anisotropic measurements. The major solvent impact on fluorophores, involved in resonance energy transfer, is the effect on spectral properties of the donor and acceptor. Notably, Nature has always exploited FRET in enzymatic processes taking place in light harvesting complexes, whose the most famous is the photosynthesis.[15–18] To reach the highest photocatalytic performances, proteins subunits and photosynthetic pigments focus the incoming light on the reaction center using energy transfer. The detailed mechanism will be discussed in Chapter 4 where we design an artificial catalytic system able to mimic Nature processes.

1. Photoluminescent materials

In his attempts to produce philosopher's stone, Casciarolo could have not imagined that his discovery would have been much more valuable than gold. Nowadays, photoluminescent materials are heavily present in everyday life, starting from fluorescent lamps[19] to glow sticks[20], and still capture a big part in the scientific research as in analytical chemistry,[21] fluorescence spectroscopy,[22] biochemistry,[23,24] fluorescence microscopy,[25] biosensors,[26] DNA sequencing[26], DNA detection,[27] criminology,[28] catalysis.[29]

In the following paragraphs, we will introduce two different photoluminescent materials that have been investigated during this doctoral thesis: perylene bisimides and carbon dots.

1.2 Perylene bisimides

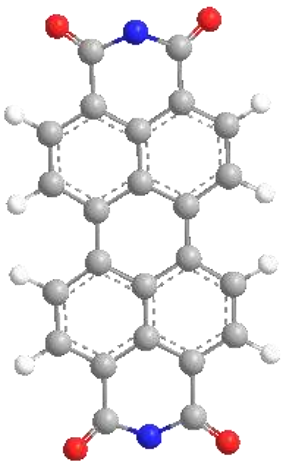

Figure 1.4 PBIs structure

Perylene-3,4,9,10-tetracarboxylic acid bisimides (PBIs) and their derivatives represent one of the most promising class of electron accepting materials, due to their outstanding optical and electronical properties, including high electron mobility and high molar absorption coefficients.[30–32] Their rigid, fused aromatic core favors π-π intermolecular interactions imparting n-type semiconducting properties useful for optoelectronic applications. Perylene-3,4,9,10-perylene tetracarboxylic acid bisimides were discovered in 1913 by Kardos[33] and were firstly applied as dyes for textiles and later on as high performance pigments mainly in the red, violet and black shades.[34] The chemical modification of the PBI structure can be readily accomplished by introducing alkyl or aryl

substituents at the N-positions or at the aromatic core,[35,36] generating soluble PBIs with optimized electronic and optical properties. PBI molecules, in addition to exceptional chemical-, thermal- and photo-stability, exhibit large optical absorption in the visible to near-infrared spectral region, they irradiate fluorescence with quantum yields near unity and show significant charge transport properties.[37,38]

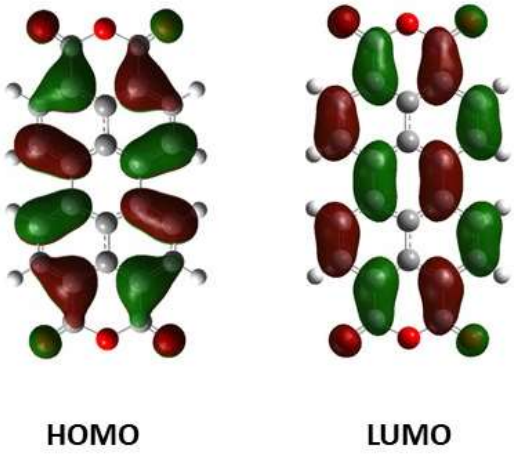

Figure 1.5 Molecular orbitals of perylene bisimides

Many PBIs have been synthesized for their application as fluorescent standards. For this purpose, it has been demonstrated that the imide substituent has negligible influence on the optical properties of the dyes since the nodes of the HOMO and LUMO orbitals pass along the imide positions.[39] Therefore, PBIs can be considered as a closed chromophoric system with an S_0-S_1 transition, whose position and intensity remain unchanged by the functionalization on the imide substituents. Moreover, absorption and emission properties are poorly affected upon the environment. Indeed, they show little solvatochromism. Bigger changes in these properties are observed if the perylene bisimides are substituted at the aromatic core in the bay area, that are positions 1, 6, 7 and 12.[38,40–42] If two phenoxy groups are attached, the absorption maximum shifts by about 20 nm and with four phenoxy groups by almost 50 nm.[43] Consequently, the

fluorescence color changes from yellow, to orange and red respectively. The tuning of the absorption/emission maxima does not affect the rest of the optical properties: high fluorescence QY, small solvatochromism and high photo-stability are retained. Greater spectral changes occur upon substitution at the aromatic core with two pyrrolidino groups, electron-donors through conjugation.[41] The dye is green with a maximum absorption at 686 nm and emits in the infrared region. The shift is a consequence of charge transfer, thus a pronounced solvatochromism and a lower QY are observed. On the other side, little changes happen if the perylene core is functionalized by electron withdrawing groups, while new electronic properties arise by expansion of the π-coniugated system orthogonal to the imide-imide axis.[42]

The high stability of perylene bisimide dyes originate from their electron-deficiency, thus they are easy to reduce and rather difficult to oxidize.[44] Most of PBIs show two reversible reduction and one

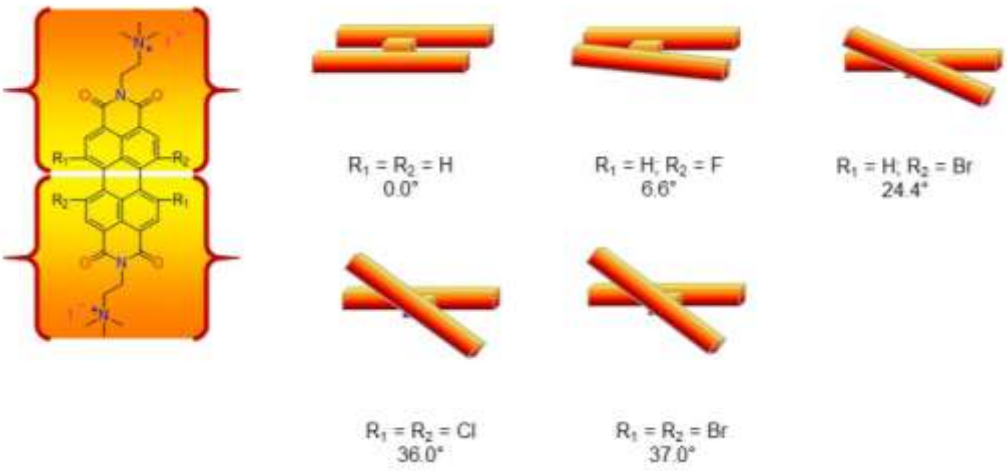

Figure 1.6 Distortion of the aromatic core depending on the sterical hindrance of the substituents.

oxidation wave in cyclic voltammetry. As for optical properties, substituents in the bay-area have a pronounced effect on the respective redox potentials. Electron-withdrawing groups, like cyanide and chloride, lead to strong oxidants. By contrast, phenoxy substituents disfavor reduction of about 0.1 V, whereas reversible oxidation waves are observed at lower potential. Also in the case of functionalization with pyrrolidines, reduction waves are observed at low potentials. Accordingly, the latter dyes are the only ones in the series that cannot be considered as electron-poor.[41] Most of the PBIs are strong reductants in the photoexcited state leading to long-lived charge-separated states employed in photoinduced electron transfer.

The structures of simple unsubstituted perylene bisimides have been analysed by several X-ray diffraction studies, all exhibiting flat π-systems.[45] According to these analyses, perylene bisimides can be considered as two naphthalene units, each of which is attached to an imide unit and connected to the other naphthalene unit by two C sp^2-sp^2 single bonds. The planarity of the system can be affected by the insertion of substituents in the bay-positions. For instance, tethrachloro-substituted perylene bisimide shows a twist angle of 37° and a tetraphenoxy a smaller angle of 25°. This distortion has consequences on the solubility and the packing of these dyes.[46]

In the last years, the applications of PBIs have grown exponentially: in biochemical applications for living cell staining,[47] in finger-mark detection[48] and in electronic devices such as sensors[49,50] and light emitting diodes.[51] PBIs became also an interesting building block for organic photovoltaic; perylene-based compounds are used in solar cells mainly as electron acceptor materials because of their electronic

affinity and their good harvesting of solar light, being a feasible alternative to fullerenes conventionally used as n-semiconductors.[42,52,53] The most recent breakthrough in the energy field has been the employment of PBI derivatives as photosensitizers in the delicate catalytic process of artificial photosynthesis. Remarkable results have been achieved either in the hydrogen evolution either in water oxidation. Indeed Chapter 3 will be dedicated to the latter process, aiming to better stability and performances.

1.3 Carbon dots

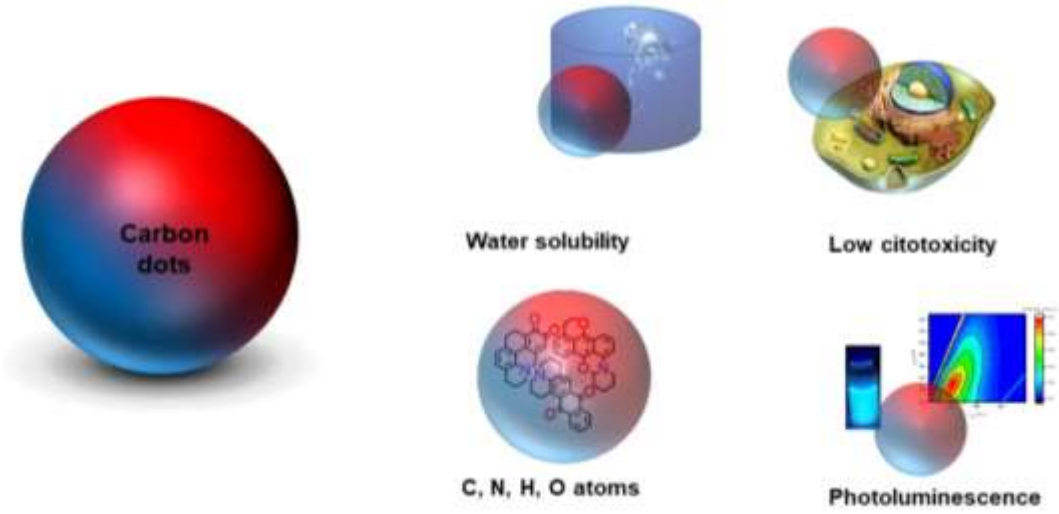

Figure 1.7 Carbon dots and their peculiar properties.

Carbon-based dots (CDs) are nanoparticles composed of carbon, oxygen and hydrogen which have been accidentally discovered during the purification of carbon nanotubes in 2004.[54] Since then, they have merged as one of the most prominent members of carbon nanomaterials due to their fascinating photoluminescence. [55] Moreover, CDs are considered as a non-toxic alternative to heavy metal-based quantum-dots (QDs), due to their benign composition and low cytotoxicity.[56]. However, the scientific community is still exploring the properties of carbon-based dots, leaving room for improving luminescence and electronic performances and completing the color palette emission, as a brush to fulfill their full potential and applications which currently comprehend bioimaging and biosensing,[54,57,58] photoacoustic and thermal theranostics,[59] inexpensive and environmentally friendly sensitizers in mesoscopic solar cells,[60] heavy metal-free light emitting diodes (LED),[61] photocatalysis. [62–65]

1. Photoluminescent materials

Over the past years, there has been a number of names to describe different categories of carbon-based dots, names that have been often used loosely and interchangeably generating confusion and misunderstanding in the use of the term “quantum”. Recently Valcarel comprised carbon dots in three classes: (i) graphene quantum dots (GQDs), (ii) carbon quantum dots (CQDs) and carbon nanodots (CNDs).[62] While all the CDs are composed by carbon, oxygen and hydrogen atoms, the three class of dots present substantial differences in terms of structure and shape. GQDs can be considered as small fragments of single or few-layers graphene sheets and hence are two dimensional disc-shaped nanoparticle with size typically under 20 nm.[57,58] On the contrary, CQDs and CNDs are quasi-spherical nanoparticles with a mixture of sp^3 and sp^2 carbon atoms (mainly sp^2 in the case of CQDs) with size below 10 nm, and while the former usually show a crystalline graphitic core structure, the latter are composed by an amorphous core. The word “quantum” is exclusive of particles that have predominantly delocalized band structure and display any quantum confinement effects. Indeed, CNDs have only molecular-like excited states.

The most intriguing and debated property of these materials is their photoluminescence. Indeed, it was the unexpected PL that revealed their presence during first experiments, namely, the emission wavelength that can be tuned simply varying the excitation wavelength, without modification of size or chemical composition. Same properties have been observed for various CDs in different solvents, so that the multi-color PL has become a key indicator of their presence. Despite the diversity of the syntheses and chemical structures, CDs possess similar optical properties. Typically, they show strong absorption in the

range 230-320 nm with a tail extending into in the visible region. The maximum peak at around 230 nm is related to π-π* transitions of aromatic C=C bonds, while the shoulder at around 300 nm is ascribed to the n-π* transition of C=O bonds or other similar groups. Other connected groups or heteroatom doping may contribute to the optical features. When deviations in absorptions spectra are observed, these indicate differences in chemical composition or hybridization.

Emission spectra are usually wide with larger Stoke shifts than organic dyes. Most of CNDs have PL emission from blue to green and very few dots possess emission at wavelength longer that 500 nm.[54,66,67] The dependency on the excitation wavelength has been ascribed to wide distribution of differently sized dots, different emissive traps and surface chemistry.[66] However, the mechanism of this phenomenon is still a matter of debate in scientific community and many various mechanisms have been invoked in the literature to explain the photoluminescence of carbon dots. The PL of CNDs shows similarities with semiconductor quantum dots but also many differences: it is inefficient to tune the emission wavelength by controlling the size of the nanodots, the PL color is mostly relative to surface groups rather than dimensions. The inhomogeneous chemical structure and the disparate PL centers lead to an other difference with QDs, which is wider bandwidth. When they were first discovered QY possessed rather low QYs, without even reaching 0.01 values.[55] However, the quantum efficiency can be increased after surface modification or passivation.[68] Year by year, the race to better optical properties has led to increase performances with CNDs reaching QYs close to unit.[69] Besides the intensity of emission, another important property of CNDs is their photostability: neither blinking nor meaningful reductions in PL are observed upon continuous

exposure to excitation.[70] However, CNDs exhibiting molecules-state emission, are damaged upon high power UV exposure.

Whereas carbon-base dots are a relatively new class of low-cost nanomaterial, their applications have widely spread ranging from biological to optoelectronic and energy related applications. In particular, their use as new type of biocompatible carbon-based nanomaterials in biomedical applications have been the most studied so far. However, there is still a lack of comprehension about the origin of the photoluminescence, the formation mechanism and the tuning of the energy levels. A better understanding of these fundamental features would be pivotal to catch up with the performances of inorganic quantum dots (CdSe, CdS and PbTe)[71–76] and extend their applications in other fields.

1.4 Abstract

Organic dyes, metal complexes, inorganic nanoparticles, semiconductors quantum dots. So many materials have been exploited and tuned to reach the highest performances and the most disparate applications in terms of photoluminescence, ranging from small molecules to nanomaterials. Indeed, the present doctoral thesis focuses on both organic molecules and nanomaterials, namely perylene bisimides and carbon dots. Perylene bisimides are organic dyes that have been known for long time as industrial pigments and only recently, due to a breakthrough in the aromatic core functionalization, have spread, their applications, ranging from living cell staining to photovoltaics. Carbon dots are the latest allotrope to join the nanocarbon family and are currently under the spotlight due to their superior properties: water solubility, low cytotoxicity and, especially, fascinating photoluminescence.

During this doctoral owrk, the tools of synthetic organic chemistry and materials chemistry have been exploited to investigate new synthetic routes, comprehension of optical and structural properties and the final application of perylene bisimides and carbon nanodots as light-harvesters in photocatalytic processes.

The work is divided in six chapters, which, besides the current introductive one, are:

- Chapter 2: **perylene bisimides: synthesis and aggregation behavior.** Due to the importance of perylene bisimides, many standard protocols have been devised to functionalize the imide position, which is a key reaction to control the solubility and the supramolecular aggregation of the dyes. Despite their wide range of applicability, these syntheses present still some

limitations such as long operation time, excess of reagents and harsh conditions. Therefore, the first task of this chapter has been to develop a new fast synthetic protocol for the production of PBIs. Herein we report a fast and versatile microwave-assisted method for the synthesis of a broad library of perylene bisimide derivatives. Imidation reactions of the perylene bisanhydride (PBA) were performed using a large variety of amines, such as alkyl amines, aminoalcohols, heteroaryl amines and aminoacids. This strategy turned out to be compatible also with bay-halogenated PBAs, functionalizing selectively the imide position without affecting the aromatic core. Different efficient work-up procedures gave highly pure products in short times. Despite of mild conditions, weak nucleophiles like aromatic amines and aminoacids efficiently provided functionalized perylene bisimides, with some novel entries not previously reported in the literature. One of the PBIs synthesized by this protocol has been made water soluble by methylation of the secondary amines on the imide substituents. We address the structural nature of low-concentrated biscationic PBI in aqueous media. Static absorption and emission spectroscopy measurements shine light onto low concentration regime <50μM, already suggesting the existence of π-π stacked PBI dimers. A series of X-ray and neutron scattering techniques provide evidence of dimer-growth into organic nanocrystals, which are thought to be building-blocks for liquid-crystalline materials. Yet, the dried structure of the PBI reveals a strikingly different morphology compared to the solvent state, underlining

the necessity of a thorough understanding of the compound behavior in aqueous media.

- Chapter 3: **a perylene bisimide hydrogel.** Whereas a number of PBI gels have been reported in literature, there is still a lack of knowledge about the precise structure of these materials and, in particular what happens to the aggregates present in solution while the gel is forming. In this chapter, we present a comprehensive picture of the physical and chemical origin of long-range conductivity in perylene bisimide-based hydrogels. We employed a suite of spectroscopic, scattering, single-crystal diffraction, imaging and electrochemical techniques to obtain the detailed structure of the hydrogel, spanning from the single-molecule to the macroscopic scale. Knowing the structure, we can explain the sites, where charge-transfer between the structure defining backbones occurs. Charge transfer at these sites requires hydrogen bonds, which are mediated by polar solvents. We verify the importance of these conduction bridges by massive and fast responses of the macroscopic conductivity upon exposure to millisecond pulses of polar vapors. Our contribution goes far beyond previously published work[77] and can be summarized as follows: i) We report the crystalline and supramolecular structure of the electronic backbone in the undried hydrogel. Knowing the precise arrangement of molecular core and functional groups at the backbone allows us to rationalize the conductivity within and between backbones. ii) We identify the local sites of the π-stacked backbones at which charge-transfer between neighboring stacks can occur. By means of millisecond pulsed polar vapour deposition, we control

these bridging sites and therefore mediate long-range conductivity throughout the material.

- Chapter 4**: perylene bisimides as photosensitizers**. A synthetic analogue of the photosystem II (PSII) has been designed under totally artificial environment by the spontaneous assembly of a synthetic chromophore and a molecular catalyst. Our approach builds on the aqueous chemistry of a positively charged perylene bisimide photosensitizer, evolving to nano-dimensional 1-D aggregates in water, where the peripheral cationic charges shield an internal hydrophobic core. Upon the addition of the water oxidation polyoxometalate catalyst, we were yielded into 2-D structures that have hydrophilic channels where the catalytic procedure take place. This phenomenon generates a cascade of exceptionally favorable events: (i) the self-structuring of photoactive nano-scaffolds armed with terminal cationic receptors (ii) photo-excitation to one of the most potent photo-oxidant generated in aqueous phase (iii) dynamic binding of a polyanionic ruthenium polyoxometalate as water oxidation catalyst and persulfate anion as sacrificial electron acceptor turning the photosynthetic aggregate in its active state. Oxygen evolution is observed in neutral pH, upon visible light irradiation; the photosynthetic particles maintain activity when arranged on a glass surface.

- Chapter 5: **a gaze into carbon nanodots synthesis**. A huge number of synthetic methods is available, all giving carbon dots different in size, shape, composition and optical properties. In principle, it is possible to adjust these properties in the desired

manner by controlling one of the different parameters (such as temperature, reaction time, precursors and so on) which essentially requires the understanding of the formation process. However, while many efforts have been directed towards the synthesis of new carbon dots and application in the most disparate fields, there is not a model that is able to predict the formation of the particles along time comprehensively. Researchers have made few attempts in these directions. These works are valid but are still not sufficient to gain a full comprehension of the CDs growth from molecular precursors. The main issues researchers have to deal with are the difficulty in monitoring their complicated reaction path, leading to unclear formation mechanism, and the high number of variables of the different methods. In this chapter, we investigate the mechanism of carbon nanodots formation discussing the growth of the nanoparticles and the origin of photoluminescence. Moreover, we present new structural insights by demonstrating that carbon nanodots consist of a dense amorphous core and a less dense shell, and we master these structural features by increasing the thickness of the shell through surface modification.

- Chapter 6: **mastering the electrochemical properties of CNDs.** Carbon dots hold a great promise in photocatalytic applications since, in addition to low-cost and low-toxicity, they possess both excellent photostability and high solubility in aqueous solution. However, the main drawback that impedes the advancement of this field is a lack of rational control of their photophysical and electrochemical properties. Herein, we show how CNDs redox potentials can be customized by employing

quinones, common electron acceptors, as dopants in a bottom-up microwave-assisted synthesis. Hence, we have designed, prepared and characterized a redox library of carbon nanodots. Benzoquinone-, naphthoquinone- and anthraquinone-based carbon nanodots exhibiting oxidation potentials between 1.48 V and 0.98 V vs SCE and reducing one in the range -1.52 V and -2.05 V vs SCE. Consequently, we tested these materials as light-harvesters for the photoreduction of methyl viologen upon solar light. All the showed CDs good activity overtaking the performances reported by Reisner for graphitized carbon dots. Therefore, these new class of carbon dots, is a promising candidate as primary photocatalyst for proton or CO_2 reduction.

1.5 References

[1] M. G. Lagorio, G. B. Cordon, A. Iriel, *Photochem. Photobiol. Sci.* **2015**, *14*, 1538–1559.

[2] J. L. Adcock, N. W. Barnett, P. S. Francis, in *Ref. Modul. Chem. Mol. Sci. Chem. Eng.*, Elsevier, **2014**.

[3] B. Valeur, M. N. Berberan-Santos, *J. Chem. Educ.* **2011**, *88*, 731–738.

[4] S. K. Deo, *Anal. Bioanal. Chem.* **2011**, *401*, 1457–1458.

[5] E. Wiedemann, *Ann. Phys.* **1888**, *270*, 446–463.

[6] P. Contents, *Techniques* **2009**, 1–11.

[7] W. M. Yen, *J. Lumin.* **2007**, *122–123*.

[8] N. T. Kalyani, H. Swart, S. J. Dhoble, in *Princ. Appl. Org. Light Emit. Diodes*, Elsevier, **2017**, pp. 1–37.

[9] M. Cesaria, B. Di Bartolo, in *NATO Sci. Peace Secur. Ser. B Phys. Biophys.*, Springer, Dordrecht, **2017**, pp. 15–42.

[10] L. Marcu, P. French, D. Elson, Eds. , *Fluorescence Lifetime Spectroscopy and Imaging*, CRC Press, **2014**.

[11] F. A. Villamena, in *React. Species Detect. Biol.*, Elsevier, **2017**, pp. 87–162.

[12] D. Weiß, H. Brandl, *Chemie unserer Zeit* **2013**, *47*, 122–131.

[13] G. Baryshnikov, B. Minaev, H. Ågren, *Chem. Rev.* **2017**, *117*, 6500–6537.

[14] C. Würth, M. Grabolle, J. Pauli, M. Spieles, U. Resch-Genger, *Nat. Protoc.* **2013**, *8*, 1535–1550.

[15] M. R. Wasielewski, *Chem. Rev.* **1992**, *92*, 435–461.

[16] J. Barber, *Chem. Soc. Rev.* **2009**, *38*, 185–196.

[17] D. G. Nocera, *Acc. Chem. Res.* **2012**, *45*, 767–776.

[18] A. Sartorel, M. Carraro, F. M. Toma, M. Prato, M. Bonchio, *Energy Environ. Sci.* **2012**, *5*, 5592.

[19] R. Kane, H. Sell, *Revolution in Lamps: A Chronicle of 50 Years of Progress*, Fairmont Press, **2001**.

[20] J. Birriel, I. Birriel, *Phys. Teach.* **2014**, *52*, 400–402.

[21] J. R. Albani, Albani, J. R., in *Encycl. Anal. Chem.*, John Wiley & Sons, Ltd, Chichester, UK, **2016**, pp. 1–25.

[22] K. G. Fleming, in *Encycl. Spectrosc. Spectrom.*, Elsevier, **2010**, pp. 628–634.

[23] W. Härtig, J.-M. Fritschy, in *Encycl. Life Sci.*, John Wiley & Sons, Ltd, Chichester, UK, **2009**, pp. 1–7.

[24] J. Yao, M. Yang, Y. Duan, *Chem. Rev.* **2014**, *114*, 6130–6178.

[25] T. M. Jovin, D. J. Arndt-Jovin, *Annu. Rev. Biophys. Biophys. Chern* **1989**, *18*, 271–308.

[26] C. L. Stevenson, R. W. Johnson, T. Vo-Dinh, *Biotechniques* **1994**, *16*, 1104–1111.

[27] J. L. Woodhead, H. Figueiredo, A. D. B. Malcolm, in *New Nucleic Acid Tech.*, Humana Press, New Jersey, **1988**, pp. 421–424.

[28] R. B. Taylor, *Research Methods in Criminal Justice*, Rowman & Littlefield Publishers, **1993**.

[29] G. C. Geoffrey, C. Bond, G. Webb, *Catalysis. Volume 6 : A Review of the Recent Literature Published up to Mid-1982*, Royal Society Of Chemistry, **1983**.

[30] F. Würthner, *Chem. Commun.* **2004**, *0*, 1564–1579.

[31] F. Würthner, C. R. Saha-Möller, B. Fimmel, S. Ogi, P. Leowanawat, D. Schmidt, *Chem. Rev.* **2016**, *116*, 962–1052.

[32] C. D. Schmidt, A. Hirsch, in *Ideas Chem. Mol. Sci. Adv. Synth. Chem.*, Wiley-VCH Verlag GmbH & Co. KGaA, Weinheim, Germany, **2010**, pp. 283–304.

[33] M. Kardos, *Deustches Reichspatent* **1913**, 276357.

[34] K. Hunger, W. Herbst, in *Ullmann's Encycl. Ind. Chem.*, Wiley-VCH Verlag GmbH & Co. KGaA, Weinheim, Germany, **2000**, pp. 35–154.

[35] C. Huang, S. Barlow, S. R. Marder, *J. Org. Chem.* **2011**, *76*, 2386–2407.

[36] H. Langhals, *Heterocycles* **1995**, *40*, 477–500.

[37] T. Heek, C. Fasting, C. Rest, X. Zhang, F. Würthner, R. Haag, *Chem. Commun.* **2010**, *46*, 1884.

[38] M.-J. Lin, Á. J. Jiménez, C. Burschka, F. Würthner, *Chem. Commun.* **2012**, *48*, 12050.

[39] J. Hou, M.-H. Park, S. Zhang, Y. Yao, L.-M. Chen, J.-H. Li, Y. Yang, *Macromolecules* **2008**, *41*, 6012–6018.

[40] J. M. Lim, P. Kim, M.-C. Yoon, J. Sung, V. Dehm, Z. Chen, F. Würthner, D. Kim, *Chem. Sci.* **2013**, *4*, 388–397.

[41] R. K. Dubey, M. Niemi, K. Kaunisto, K. Stranius, A. Efimov, N. V. Tkachenko, H. Lemmetyinen, *Inorg. Chem.* **2013**, 52 (17), 9761–9773.

[42] C. Li, H. Wonneberger, *Adv. Mater.* **2012**, *24*, 613–636.

[43] V. M. Blas-Ferrando, J. Ortiz, L. Bouissane, K. Ohkubo, S. Fukuzumi, F. Fernández-Lázaro, Á. Sastre-Santos, *Chem. Commun.* **2012**, *48*, 6241.

[44] S. Shoaee, T. M. Clarke, C. Huang, S. Barlow, S. R. Marder, M. Heeney, I. McCulloch, J. R. Durrant, *J. Am. Chem. Soc.* **2010**, *132*, 12919–12926.

[45] M. J. Ahrens, L. E. Sinks, B. Rybtchinski, W. Liu, B. A. Jones, J. M. Giaimo, A. V. Gusev, A. J. Goshe, D. M. Tiede, M. R. Wasielewski, *J. Am. Chem. Soc.* **2004**, *126*, 8284–8294.

[46] W. Qiu, S. Chen, X. Sun, Y. Liu, D. Zhu, *Org. Lett.* **2006**, *8*, 867–870.

[47] Y. Zhao, X. Zhang, D. Li, D. Liu, W. Jiang, C. Han, Z. Shi, *Luminescence* **2009**, *24*, 140–143.

[48] M. J. Choi, T. Smoother, A. A. Martin, A. M. McDonagh, P. J. Maynard, C. Lennard, C. Roux, *Forensic Sci. Int.* **2007**, *173*, 154–160.

[49] H. Langhals, W. Jona, F. Einsiedl, S. Wohnlich, *Adv. Mater.* **1998**, *10*, 1022–1024.

[50] W. Wang, W. Wan, H. H. Zhou, S. Niu, A. D. Q. Li, *J. Am. Chem. Soc.* **2003**, *125*, 5248–5249.

[51] T. L. Chiu, K. H. Chuang, C. F. Lin, Y. H. Ho, J. H. Lee, C. C. Chao, M. K. Leung, D. H. Wan, C. Y. Li, H. L. Chen, *Thin Solid Films* **2009**, *517*, 3712–3716.

[52] J. J. Walsh, J. R. Lee, E. R. Draper, S. M. King, F. Jäckel, M. A. Zwijnenburg, D. J. Adams, A. J. Cowan, *J. Phys. Chem. C* **2016**, *120*, 18479–18486.

[53] D. Görl, X. Zhang, F. Würthner, *Angew. Chem.* **2012**, *51*, 6328–48.

[54] L. Cao, X. Wang, M. J. Meziani, F. Lu, H. Wang, P. G. Luo, Y. Lin, B. A. Harruff, L. M. Veca, D. Murray, et al., *J. Am. Chem. Soc.* **2007**, *129*, 11318–11319.

[55] * Ya-Ping Sun, Bing Zhou, Yi Lin, Wei Wang, K. A. Shiral Fernando, Pankaj Pathak, Mohammed Jaouad Meziani, Barbara A. Harruff, Xin Wang, Haifang Wang, et al., *J. Am.*

Chem. Soc **2006**, *128*, 7756–7757.

[56] F. Yuan, S. Li, Z. Fan, X. Meng, L. Fan, S. Yang, *Nano Today* **2016**, *11*, 565–586.

[57] S. Y. Lim, W. Shen, Z. Gao, L. Cao, X. Wang, M. J. Meziani, F. S. Lu, H. F. Wang, P. G. Luo, Y. Lin, et al., *Chem. Soc. Rev.* **2015**, *44*, 362–381.

[58] X. Li, M. Rui, J. Song, Z. Shen, H. Zeng, *Adv. Funct. Mater.* **2015**, *25*, 4929–4947.

[59] J. Ge, M. Lan, W. Liu, Q. Jia, L. Guo, B. Zhou, X. Meng, G. Niu, P. Wang, *Sci. China Mater.* **2016**, *59*, 12–19.

[60] J. T. Margraf, F. Lodermeyer, V. Strauss, P. Haines, J. Walter, W. Peukert, R. D. Costa, T. Clark, D. M. Guldi, B. O'Regan, *Nanoscale Horiz.* **2016**, *1*, 220–226.

[61] X. Chen, X. Bai, C. Sun, L. Su, Y. Wang, Y. Zhang, W. W. Yu, *RSC Adv.* **2016**, *6*, 96798–96802.

[62] A. Cayuela, M. L. Soriano, C. Carrillo-Carrión, M. Valcárcel, A. I. Ekimov, A. A. Onushchenko, S. Zhu, Y. Song, X. Zhao, J. Shao, *Chem. Commun.* **2016**, *52*, 1311–1326.

[63] B. C. M. Martindale, G. A. M. Hutton, C. A. Caputo, E. Reisner, *J. Am. Chem. Soc.* **2015**, *137*, 6018–6025.

[64] B. C. M. Martindale, E. Joliat, C. Bachmann, R. Alberto, E. Reisner, *Angew. Chem.* **2016**, *55*, 9402–9406.

[65] S. Sahu, Y. Liu, P. Wang, C. E. Bunker, K. A. S. Fernando, W. K. Lewis, E. A. Guliants, F. Yang, J. Wang, Y.-P. Sun, *Langmuir,* **2014**, *30*, 8631–8636.

[66] L. Wang, S. J. Zhu, H. Y. Wang, S. N. Qu, Y. L. Zhang, J. H. Zhang, Q. D. Chen, H. L. Xu, W. Han, B. Yang, et al., *ACS Nano* **2014**, *8*, 2541–2547.

[67] S. N. Baker, G. A. Baker, *Angew. Chem.* **2010**, *49*, 6726–6744.

[68] G. E. LeCroy, S. T. Yang, F. Yang, Y. Liu, K. A. S. Fernando, C. E. Bunker, Y. Hu, P. G. Luo, Y. P. Sun, *Coord. Chem. Rev.* **2016**, *320–321*, 66–81.

[69] D. Qu, M. Zheng, L. Zhang, H. Zhao, Z. Xie, X. Jing, R. E. Haddad, H. Fan, Z. Sun, *Sci. Rep.* **2014**, *4*, 5294.

[70] G. A. M. Hutton, B. Reuillard, B. C. M. Martindale, C. A. Caputo, C. W. J. Lockwood, J. N. Butt, E. Reisner, *J. Am. Chem. Soc.* **2016**, *138*, 16722–16730.

[71] A. P. Alivisatos, *Science* **1996**, *271*, 933–937.

[72] A. J. Shields, *Nat. Photonics* **2007**, *1*, 215–223.

[73] Y. Yang, Y. Zheng, W. Cao, A. Titov, J. Hyvonen, J. R. Manders, J. Xue, P. H. Holloway, L. Qian, *Nat. Photonics* **2015**, *9*, 259–265.

[74] C. R. Kagan, E. Lifshitz, E. H. Sargent, D. V. Talapin, *Science* **2016**, *353*, aac5521-5523.

[75] P. Senellart, G. Solomon, A. White, *Nat. Nanotechnol.* **2017**, *12*, 1026–1039.

[76] S. Silvi, A. Credi, *Chem. Soc. Rev.* **2015**, *44*, 4275–4289.

[77] A. S. Weingarten, R. V. Kazantsev, L. C. Palmer, M. McClendon, A. R. Koltonow, A. P. S. Samuel, D. J. Kiebala, M. R. Wasielewski, S. I. Stupp, *Nat. Chem.* **2014**, *6*, 964–970.

2. Perylene bisimides: synthesis and aggregation

2.1 Introduction

Perylene bisimides (PBIs) are robust and photostable dyes, with outstanding optical and electronic properties.[1] As a consequence, these compounds have been widely studied as pigments, fluorescence sensors, n-semiconductors in organic electronics, photovoltaics and bases for copolymers or oligomers, with important role in single junction devices.

In spite of the importance of these dyes in industrial applications, the development of efficient synthetic protocols, directed to faster, cheaper and more sustainable reactions, is still a matter of study. Moreover, new uses of PBIs, such as photocatalysis and photoactive hydrogels, require mastering the complicated supramolecular structures these dyes form in water. This chapter is focused on the chemical, optical, supramolecular properties of PBIs. More specifically, we deal with the reactivity of these dyes by developing a new efficient synthetic protocol and we investigate the aggregation phenomena and the supramolecular structure of one of these dyes in water. Part of the results herein reported have been published in the following papers:

- F. Rigodanza, E. Tenori, A. Bonasera, Z. Syrgiannis, M. Prato, Fast and efficient microwave-assisted synthesis of perylenebisimide, Eur. J. Org. Chem., 2015, 23, 5060-5063.
- M. Burian, F. Rigodanza, H. Amenitsch, L. Almasy, I. Khalakhan, Z. Syrgiannis, M. Prato, Structural and optical properties of a perylene bisimide in aqueous media, 2017, 683, 454-458.

2.1.1 Synthetic strategies

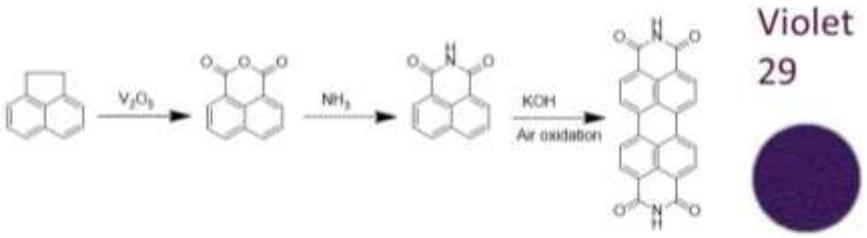

Figure 2.1 Synthesis of pigment Violet 29

Perylene bisimides have been an object of research for more than 100 years and their derivatives are still under the spotlight, with properties and applications much different compared to the ones Kardos was looking for back in 1913.[2] At the time, industry was asking for dyes with excellent stability towards weather, temperature, light and chemicals, and the violet pigment he synthesized and patented while working at BASF matched all these requirements. The PBI was synthesized by the heating of 1,8-naphtalenedicarboximide with KOH (Figure 2.1) and it is still employed for the coloration of automotive paint, mass coloration of synthetic fiber and engineering resins under the name of pigment Violet 29.[3,4] However, the chemical structure of PBIs has different sites that have been lately exploited to tune the desired properties from the nano- to the macro-scale and widen the applications to sensors, polymers, n-semiconductors and photovoltaics. Indeed, the perylene core has twelve functionalizable positions: the peri (3, 4, 9, 10), the bay (1, 6, 7, 12) and the ortho (2, 5, 8, 11) as shown in Figure 2.2. The three different generations of perylene bismides

known as first, second and third generation or yesterday, today, tomorrow generation, are based on these functionalizing positions. The 1st generation is distinguished by peri substitutions. In the 2nd one, additional or exclusive bay-functionalization was intensively developed. Finally, the last generation is grounded on the discovery of the synthetic route towards ortho-functionalization.[5]

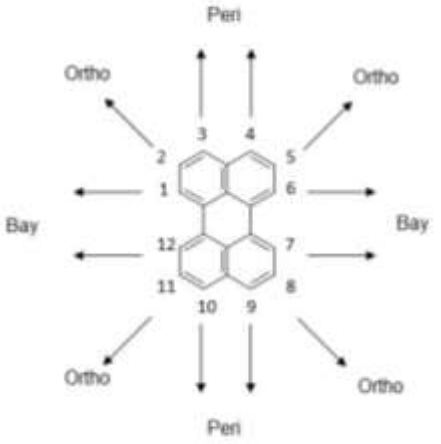

Figure 2.2 Perylene functionalizable positions

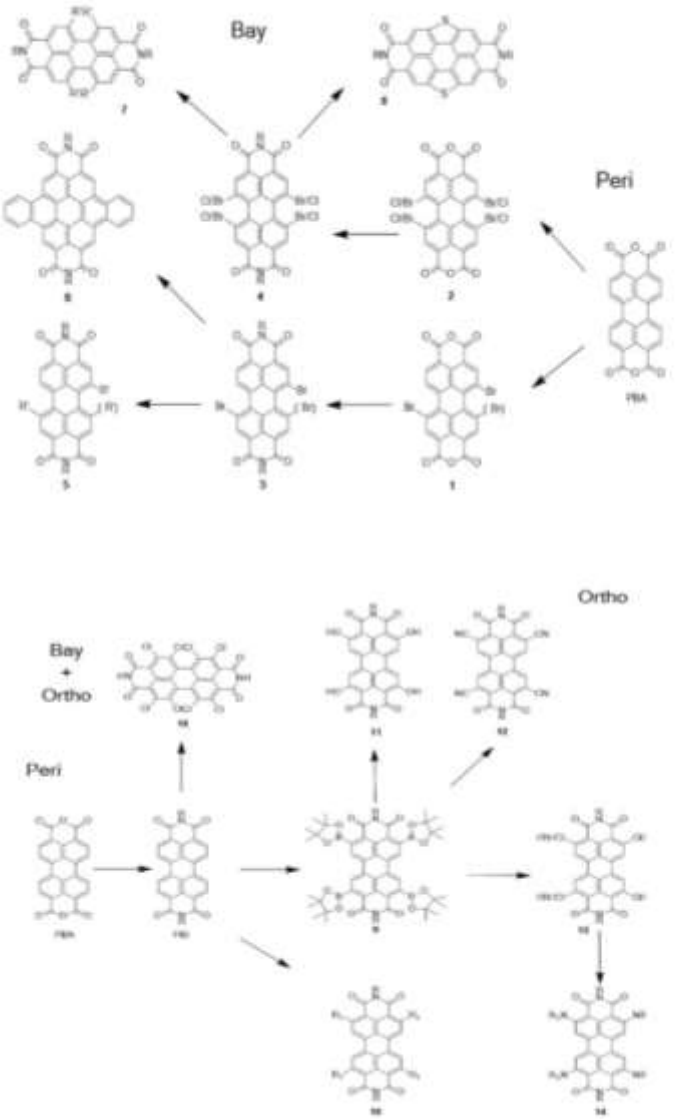

Figure 2.3 Synthesis of perylene bisimides

2. Perylene bisimides: synthesis and aggregation

The easiest way to synthesize a PBI is to use the cheap commercially available perylene bisanhydride as the starting material and, by imidation reactions with aliphatic or aromatic amines, produce the bisimide with easy purification methods. The final solubility of the dye depends strongly on the substituents on the imide positions. A small alkyl chain will lead to insoluble PBIs in most of the organic solvents. For instance, the Pigment Red 179, used in coatings industry, is synthesized by reaction of PBA with N,N'-dimethylamine.[3] On the other side, bulky aryl or alkyl substituents are introduced to achieve solubility in most of the organic solvents such as DCM, THF, acetone, toluene, acetonitrile etc. without losing thermal stability.[6,7] Nevertheless, all these compounds show very similar absorption spectra since the optical properties are not affected by the imide substituents. While in the early time of perylene bisimides research, industry was focused primarily on using PBA as starting materials, new high-tech applications require the tuning of optical and electronical as well as morphological properties.[8] A first breakthrough was the discovery of a way to halogenate PBA to synthesize 1,7(6)-dibromoperylene bisanhydride **1** and 1,6,7,12-tetrachloroperylene bisanhydride **2-Cl**, compounds that are the fundamental building blocks for advanced PBI chemistry.[9] The common approach is to make them react with amines in acidic environment to form bay-halogenated PBIs. Subsequently, nucleophilic substitutions and metal catalyzed reactions are performed.[10] For example, after reaction of **2-Cl** with phenol in basic solvent, it is obtained a PBI bearing four phenoxy groups in the bay-positions. This dye exhibits bathochromic shift

absorption (around 50 nm) compared to unsubstituted one and, due to the bulky substituents that prevent aggregation, it retains high fluorescence with quantum yield (QY) close to the unit.[11,12] Moreover, due to the particular nature of the substituents, this PBI keeps a perfectly planar structure, differently from most of the other bay-substituted perylene bisimides. A stronger bathcromatic shift is achieved when **1** reacts with pyrrolidine, with green absorption at 680 nm.[13] The one-step palladium-catalyzed Stille reaction yields **8**, a bay-extendend PBI with two sulfur bridges which exhibits a clear hypsocromic shift, a phenomenon that is observed also in other bay-expansions of PBIs, including coronene diimides, dibenzocoronene dimides and dinaphtacoronene dimides, all synthesized from dibromo-PBIs.[14,15] Other possible functionalization are cyanations via cyano copper and fluorinations via potassium fluoride.[16,17]

Besides the peri and the bay functionalization, the recent discovery of a regioselective reaction by ruthenium catalyst for the functionalization of the ortho positions represents the last big step forward in PBI chemistry.[18,19] Thereby, it is now possible to introduce alkyl or aryl substituents into the 2,5,8,11 positions of PBIs employing alkenes or arylboronates (**9**). These new dyes combine the best of the previous generations. They have better solubility and higher solid-state fluorescence. Furthermore, once the PBI is tetraboronated, it does offer a variety of functionalizing choices.[20,21] The boron substituents can be converted into hydroxyl (**11**), cyano (**12**) and chloro, bromo, iodo groups (**13**) under copper(II) catalyzed reactions. Subsequently, the ortho-

halogenated PBIs can be further used to introduce a secondary or tertiary amines to form perylene bisimide **14**. A complete functionalization of the perylene core has been obtained with 1, 2, 5, 6, 7, 8, 11, 12-ortachloro-PBI **15**, however the latter is poorly soluble and difficult to functionalize. For this reason no further information on this compound is available.[22]

In conclusion, the PBI chemistry has been characterized by three different stages beginning with the modification of the imide groups and ending with the reactions on the ortho-positions. In the first generation, it is possible to play only on the solubility and the solid-state color of the dyes. However, the strong π-π interactions and electron acceptor abilities made these PBIs relevant as n-type organic semiconductor. The second stage paved the way to optical and electronical tuning by modification of the bay-positions. Unfortunately, these dyes have a twisted perylene core that weakens the molecular interactions, which is unfavorable for some application. This issue was solved in the last generation of ortho-substituted PBIs since it is now possible to improve the electrochemical properties without affecting the planarity of the system, making this last group the most promising for tomorrow's applications.

2.1.2 Water soluble dyes

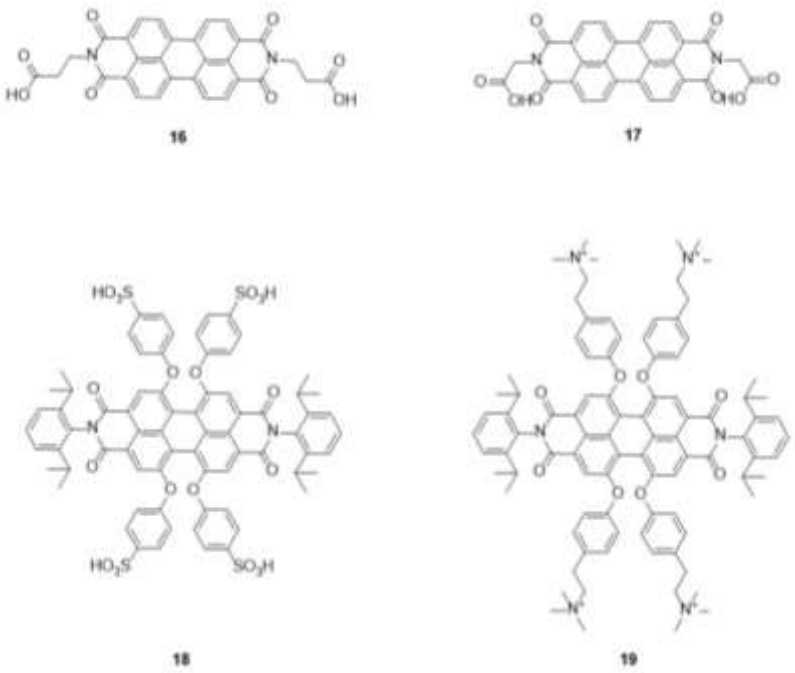

Figure 2.4 Water soluble PBIs

As already introduced in Chapter 2.1.1, perylene bisimides possess high fluorescence quantum yields, high extinction coefficients, and high chemical and photophysical stability.[23] The strong π-π interactions between the perylene cores are what makes these molecules so special since they lead to a number of supramolecular architectures with different optoelectronic properties. Unfortunately, in polar environments, for example, water, PBI dyes tend to strongly aggregate driven by hydrophobic interactions, with consequent loss of their desirable optical features. For this reason, the development of successful strategies

to confer water-solubility and preserve their high fluorescence quantum yields is of fundamental importance.[24] The first PBIs designed to be soluble in aqueous media date back to 1980s and 1990s.[9,25] Dyes **16** and **17**, bearing ionic substituents at the imide positions were known to be strongly fluorescent. Furthermore, it was demonstrated that the fluorescence of **16**, synthesized by imidation reaction between PBA and glycine in basic solutions, is

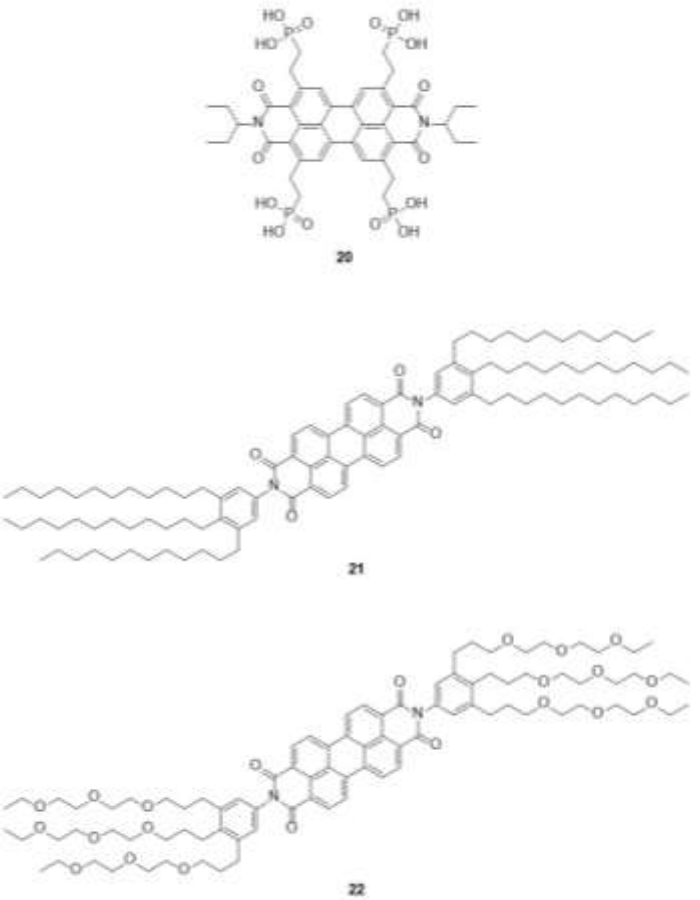

Figure 2.5 Water soluble PBIs

almost completely quenched, whereas as monomer it has QY close to the unit. The potential of water soluble PBIs was expanded by Mullen, introducing ionic groups at the bay positions (**18, 19**), which block π-π interactions through electrostatic shielding and steric hindrance.[26–28] Clearly, inserting bulky substituents like dendrons enhance the emission. As mentioned in the previous chapter, the ortho-functionalization is the most recent and fascinating way to tune optoelectronic properties and it has been already exploited by Mullen to prepare **20** by Muray-type alkylation with phosphonate derivatives.[20]. As previously introduced, the amount of functionalizations that can be performed on a PBI to make it water-soluble are infinite. It is possible to employ all the kinds of anionic, cationic, non-ionic substituents. However, the design of these dyes is not the focus of this thesis and at this point we refer the interested reader to a recent review on this topic by Yin.[29] What will be instrumental for the discussion in this and the following chapters is how water affects the interactions between the PBI molecules and, consequently, the structure and the stability of the aggregates. Wurthner showed by quantum calculations that π-π interactions of the dyes are influenced by multiple factors, with electrostatic and dispersion forces being the most relevant. SEM and TEM analyses revealed that **21** and **22** aggregate in one-dimensional columns, both in organic and aqueous solvents. Moreover, the aggregation process of these dyes was followed by spectral changes happening to **21** and **22** upon increasing concentration.[30,31] Whenever the PBIs do not aggregate, it is possible to observe a clear vibronic fine structure of the electronic

transitions S_0-S_1 but this information disappears once the molecules start aggregating due to strong excitonic interactions.[32,33]. Consequently, the ratio of the most intense absorptions bands inverts. The spectrum loses its fine structure and become broad and unstructured with lower extinction coefficient. The increase of the band at longer wavelength determines a hypsocromic shift of the aggregates that can be referred as H-aggregates. Remarkably, water soluble PBIs have, in aqueous media, a structure similar to the PBIs, owing hydrophilic residues, in organic solvents. Wurthner proposed a structural model, based on aggregation formation and quantum chemical calculations, in which the individual monomers are π-π stacked with about 30° of rotation between each other.[32,34]. This structure is characterized by a long-lived red-shifted emission, which is attributed to a modification of the excited state.

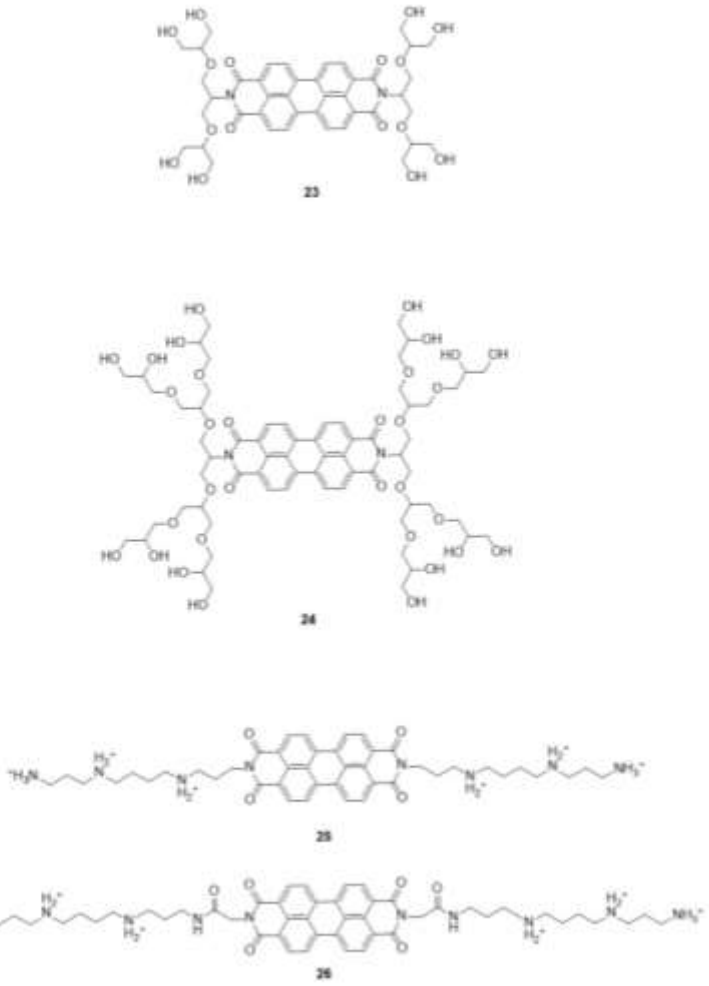

Figure 2.6 Water soluble PBIs

The functionalization of PBIs with dendrons of different generations was instrumental to achieve new information about the transition from dissolved molecules to aggregates, in particular how this process affects the optical properties. UV-Vis studies revealed that **23** exists in aggregates in the whole accessible concentration

range since the residues at the imide positions seem to be too short to give an efficient steric hindrance and, then, prevent aggregation. On the other side, the transitions from monomers to aggregates is observed in **24**. Going to larger dendrons, the substituents will shield effectively the π-π interactions and it will be

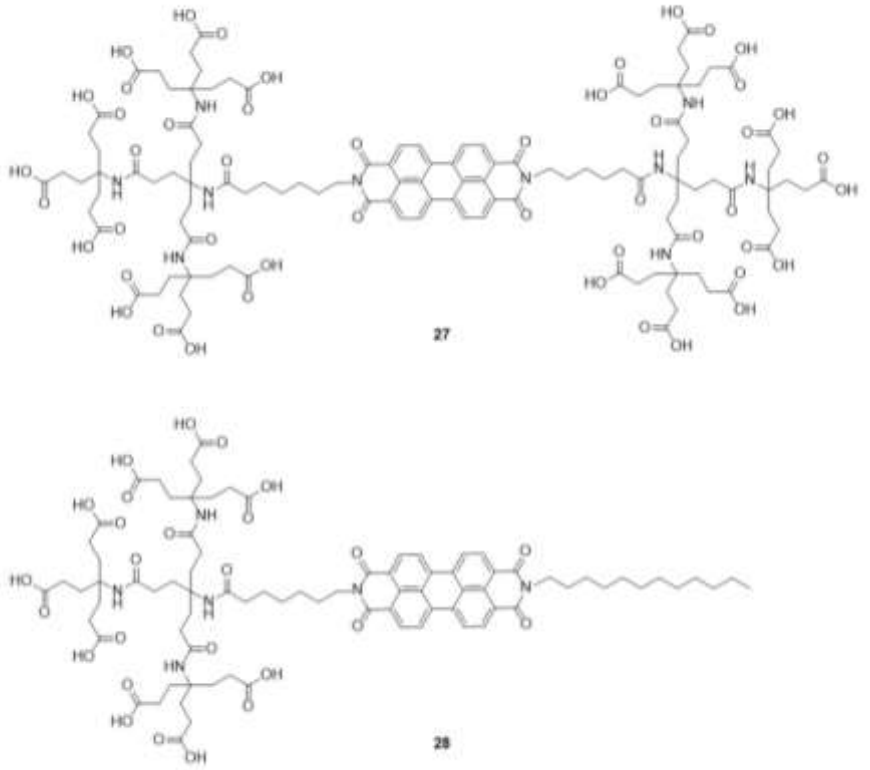

Figure 2.7 Water soluble PBIs

possible to observe the monomeric features in the whole concentration range. The size of the dendrons do not affect only absorption spectra, but also the fluorescence quantum yields. Indeed, while the QY of **23** is 0.33, it becomes 1 for the fourth

generation one. If substituents are correctly designed and the aggregation is efficiently suppressed, PBIs can own similar QYs in water as in organic solvents.

Besides long PEG-chains and large dendrons, the aggregation of PBIs can be hindered in more simple ways, such as the introduction of ionic chains as for spermine functionalized PBIs **25** and **26**.[35] These dyes are well dissolved when in low concentrations and neutral pH. Intuitively, when the amino-groups are protonated the aggregation is prevented through electrostatic repulsion. In these conditions **26** reaches a remarkable QY of 0.9. Increasing the concentration, aggregation takes place, and, simultaneously, the protons on the side chains are transferred to the surrounding water to minimize electrostatic repulsion, causing a decrease of the pH value. As this process takes place, the neutral amines can interact with the positive residues trough hydrogen bonds, fostering the π-π stacking. If **26** is slightly modified with increased distance between the cationic groups and the perylene core, QY will be lower. Hydrophobic interactions will stabilize the π-π stack and hence favorite the aggregation. When analyzed by TEM and AFM, these PBIs showed a large rod-type rearrangement, whose diameter and length increase with the spacer dimension. Similar rod-type nanostructures have been reported for B-cyclodestrin-substituted and crown ether functionalized.[36]

The latter form big aggregates that appear to form a dispersion rather than a limpid solution. An inhibition of the aggregates in water has been observed also for PBIs functionalized with

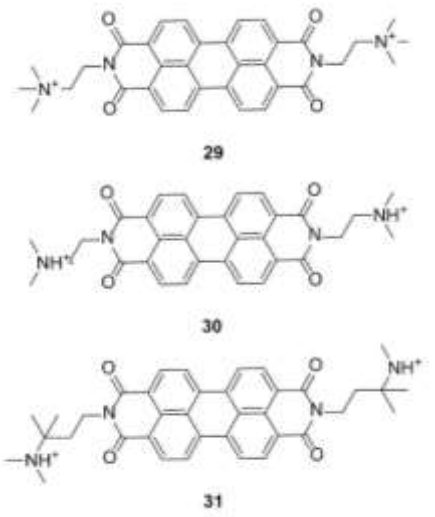

Figure 2.8 Water soluble PBIs

Newkome dendrons, **27** and **28**. Also in this case, the dyes are kept far apart by electrostatic interactions and steric hindrance. As discussed for **23** and **24**, first generation dendrons PBIs remain aggregated in the whole concentration range, with hypsocromically shifted absorption maximum and poor QY. However, second generation dendrons are charged (the eighteen carboxy groups are deprotonated at neutral pH) and bulky enough to prevent interactions between the aromatic cores resulting in enhanced fluorescence at low concentrations. TEM verified that the bolaamphiphile containing first generation Newkome dendrons forms larger aggregates with more irregular shapes. Defined aggregates are observed if a long alkyl chain replaces one of the dendrons, as in **28**, which self-assembles in spherical micelles where the Newkome dendrons are exposed to the aqueous media

and the dodecyl chains form the hydrophobic core. The water soluble PBIs herein mentioned all show aggregation sensitive to the pH and the steric hindrance. Although, it is possible to achieve solubility with smaller and more simple substituents like tryalkylammonium groups as in the case of **29-31**.[37,38] These dyes were employed as sensors through electric conductivity measurement since they are sensitive particularly towards reducing agents. A study of the aggregation process and the determination of their size and shape is not clear and it will be a matter of the discussion for the following chapters of the thesis.

2.1.3 Aim of the project

In this chapter we present an innovative and efficient microwave assisted synthesis of perylene bisimides. A large variety of amines, bearing different moieties, has reacted with PBA in high yield and short reaction times, using dimethylformamide (DMF) as the solvent. One of the PBI synthesized by this protocol has been made water soluble by methylation of the secondary amines on the imide substituents. We address the structural nature of low-concentrated biscationic PBI in aqueous media. Static absorption and emission spectroscopy measurements shine light onto low concentration regime < 50 μM, already suggesting the existence of π-π stacked PBI dimers. A series of X-ray and neutron scattering techniques provide evidence of dimer-growth into organic nanocrystals, which are thought to be building-blocks for liquid-crystalline materials. Yet, the dried structure of PBI reveals a strikingly different morphology compared to the solvent state,

underlining the necessity of a thorough understanding of the compound behavior in aqueous media.

2.2 Results and discussion

2.2.1 A fast and versatile synthesis

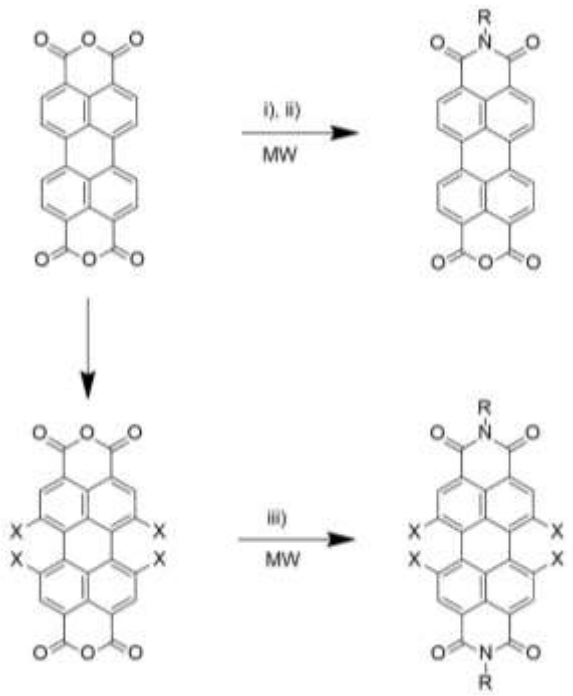

Figure 2.9 General scheme of imidation reaction. i) Reagents and conditions for alkylamines and aminoacids: DMF, R-NH_2 2 equiv., 50 min. irradiation, T_{max} 200°C, 50 W. ii) Reagents and conditions for aromatic amines: DMF, R-NH_2 4 equiv., Et_3N, 50 min, T_{max} 200°C, 80 W. iii) Reagents and conditions for bay-halogenated PDA with amines: DMF, R-NH_2 2 equiv., acetic acid, 10 min, T_{max} 200°C, 50 W.

Due to the importance of perylene bisimides, many standard protocols have been devised to functionalize the imide position. As discussed in the previous sections, this kind of functionalization has been known for more than 100 years and it is instrumental to control the solubility and the supramolecular aggregation of the

dyes.[2] Despite their wide range of applicability, these syntheses present still some limitations. Firstly, the condensation of PBA with aromatic amines and aminoacids requires long reaction times, up to 48 hours at reflux in non-common solvents, such as quinoline and imidazole.[39–41] Besides the harsh conditions, work up procedures represent another problem. Indeed, aromatic amines and aminoacids require long work-ups under strong conditions to get rid either of the unreacted anhydride and the side product, monoimide derivative. This does not occur for aliphatic amines, which give quantitative yields and need a simpler work-up to remove the excess of amines.

Consequently, a new and fast method for the synthesis of perylene bisimides with highly effective reactions appears to be instrumental, in order to produce a wider variety of these molecules in a more efficient way. Microwave-assisted synthesis has attracted the organic chemists, since it guarantees acceleration of the reactions, higher yields under milder reaction conditions and higher product purity.[42] Reactions were run in a dedicated microwave reactor in pressure-resistant, tightly sealed quartz tubes. Procedure was adjusted depending on the amines selected with reaction time and power of irradiation reported in Table 2.1. The final products were characterized by ^{1}H-NMR, ^{13}C-NMR, MALDI-MS, FT-IR, UV-Vis absorption and fluorescence spectroscopies. ^{13}C-NMR analysis was not possible for all compounds, due to their poor solubility in standard deuterated solvents.

Several standards methods for the synthesis of PBIs have been previously described.[7,41,43] A first procedure involves heating PBA

with the appropriate amine in the presence of dicylohexylcarbodiimide (DCC), using water as separating reagent at 220-240 °C and a small amount of quinoline as solvent, providing nearly quantitative yield after 18 hours. The work up consists of treating the suspension several times with methanol in order to remove quinoline, then with an aqueous solution of K_2CO_3 to dissolve unreacted PBA and finally crystallizing the imide derivative from toluene.[7] In order to prepare the carboxylated PBIs, an alternative strategy was exploited. PBA was heated in imidazole at 140 °C in the presence of the appropriate aminoacid for 10 hours, under argon. The crude was washed with ethanol and then precipitated with an aqueous solution of HCl.[6] Both methods require a large excess of amines.

By contrary, we synthesized several perylene derivatives (**A-Q**), as reported in Table 2.1, in short times and high yield. Several amines were used for our synthesis in order to set up a valid method for a wide variety of the PBIs, including alkyl amines (**A**-**F**), amino alcohols (**D, E, H**), heteroaryl amines (**G**), aminoacids (**I, J, K**). In addition, we managed to functionalize bay-halogenated PBIs with some of the latter amines (**L-Q**).

With this method, the reactions time goes from 6-10 min. for halogenated PBIs (**L-Q**), up to 2 hours for some other amines (**G-H**). The appropriate amine is used in stoichiometric amount (**A-F**, **I-Q**) or in a slight excess (**G-H**). DMF is the elected solvent for all the reactions. The selection of the solvent is based on several experiments dispersing PBA in sulfolane, water, THF. DMF is the only media that give sufficient yields and reproducible results for

the chosen amines. Table 2.1 reports the average yields after repeating the reactions three times each. The procedure is perfectly duplicable scaling-up the quantities of the reagents (2g of PBA instead of 100 mg). We developed two different work-up procedures depending on the nature of the amine. The products of uncharged amines (**A-H**, **L-Q**) were suspended in 50 mL of 10% KOH aqueous solution and stirred for 2 hours. The precipitate was filtered and washed thoroughly with water until neutralization of the filtrate. On the other hand, products of aminoacids (**I-K**) were dissolved in basic solution at pH 10 and filtered. The solution was then acidified with concentrated HCl to pH 1, filtered and washed until neutralization.

The starting PBA is insoluble in common deuterated solvents and is not detected in the NMR spectra. Consequently, reactions were monitored by IR spectroscopy to check the absence of unreacted anhydride. All the final compounds exhibited strong peaks at 1690 and 1650 cm^{-1} related to the C=O stretching of imide groups, while typical peaks related to C=O stretching of anhydride at 1765 cm^{-1} and 1730 cm^{-1} were not detected. Moreover, we observed that the presence of unreacted PBA in the crude affects the solubility of the final compounds. In fact, the addition of a small amount of PBA to a PBI solution causes precipitation of the latter, especially for those bearing amino acid groups (**I-K**). This experimental evidence confirms the hypothesis that traces of the perylene anhydride in solution facilitate the aggregation of the PBIs. Thus, appropriate work-up procedures appear instrumental to obtain the final compounds in high purity and to collect characterization data of

derivatives such as PBIs **D, E, G,** not reported in the literature to date.[44,45]

This study highlights that the main factors influencing the reactions are the steric hindrance and the polarity of amines.[46] In the experiments, the steric bulkiness at the *α*-carbon influences the outcome of the reaction. Amines with a small linear structure (**A-F**, **L-Q**) give higher yields in shorter time. To compensate the lower reactivity of some reagents (**G-H**), the number of cycles of irradiation was increased and both conditions and work-up procedures were slightly modified as reported in the Experimental Section. In addition, aminoacids react faster than nonpolar amines. On similar steric hindrance, derivative **I** is obtained in shorter time and higher yields than compound **G**. Indeed, the presence of carboxylic groups on the isophthalic amine promote the reaction, enhancing the polarity. On the other hand, the basicity of the amine does not particularly influence the outcome of reactions. Indeed, weak nucleophiles, such as isophtalic amine and 4-aminopyridine, show reaction times comparable to the ones of stronger nucleophiles, such as dopamine and β-alanine.

Table 2.1 Summary of the synthesized PBI derivatives

PBI	Starting anhydride	Amine	Yield%	MW irradiation
A	PBA	N,N-dimethylethylenediamine	99	50W 5x10’
B	PBA	2-methoxyethyl)amine	99	50W 5x10’
C	PBA	1-(3-aminopropyl)imidazole	99	50W 5x10’
D	PBA	2-(2-aminoethoxy)ethanol	99	50W 5x10’

E	PBA	4-amino-1-butanol	92	50W 5x10’
F	PBA	octylamine	87	50W 5x10’
G	PBA	4-aminopyridine	45	80W 10x10’
H	PBA	dopamine	43	80W 10x10’
I	PBA	5-amino-isophtalic acid	87	50W 5x10’
J	PBA	glycine	42	50W 5x10’
K	PBA	B-alanine	64	50W 5x10’
L	PBA-4Br	N,N-dimethylethylenediamine	80	60W 10’
M	PBA-4Br	(2-methoxyethyl)amine	87	60W 10’
N	PBA-4Br	1-(3-aminopropyl)imidazole	95	60W 10’
O	PBA-4Cl	N,N-dimethylethyelenediamine	95	60W 10’
P	PBA-4Cl	(2-methoxyethyl)amine	85	60W 10’
Q	PBA-4Cl	1-(3-aminopropyl)imidazole	95	60W 10’

Bay-halogenated PBIs are very reactive species due to the higher solubility of the related anhydride in DMF. Reactions take place in only 6-10 min. with all the tested amines, without detectable substitution at bay-positions. The yields are comparable to non-bay-halogenated PBIs, almost quantitative.

In conclusions, a fast and versatile microwave-assisted method for the synthesis of a broad library of perylene bisimide derivatives has been developed. Imidation reactions of the perylene bisanhydride (PBA) were performed using a large variety of amines, such as alkyl amines (**A-F**), amino alcohols (**D, E, H**), heteroaryl amines (**G**) and aminoacids (**I-K**). This strategy turned out to be compatible

also with bay-halogenated PBAs, functionalizing selectively the imide position without affecting the aromatic core. Different efficient work-up procedures gave highly pure products in short times. Despite of mild conditions, weak nucleophiles like aromatic amines and aminoacids efficiently provided functionalized perylene bisimides, with some novel entries not previously reported in the literature.

2.2.2 Structural and optical properties of PBI2+ in water

Figure 2.10 Structure of **PBI2+.**

As anticipated in Section 2.1.2, PBIs with alkyl-ammonium groups on the imide positions are water soluble with π-π stacking hindered the larger and the more charged the alkyl chains are. In particular bis-(N,N-trimethylammoniumcation)ethylene)-perylene-3,4,9,10-tetra-carbioxylic bisimides salts has the most simple and short residues which cannot prevent the aggregation efficiently nevertheless the strong cationic repulsion, leading to nanotubolar structures.[47] In solution, these nanotubes can present an orientation, making PBIs part of the family of chromic liquid crystal compounds.[15] Such chromic liquid crystals are structurally characterized by a transition from isotropic to nematic phase and finally, at higher concentrations, to a hexagonal phase.[38,48] In this context, a selection of investigations has focused especially on the

latter two phase transitions, whereas the structural analysis of the phenomena so far only took place in the solid state (deposition, crystallization) or at very high concentrations (crystalline conditions).[45,49,50] On similar grounds, PBIs, together with anionic phosphate surfactants, cause self-alignment of the constituents, further resulting in supramolecular liquid-crystals in bulk.[49] While these investigations supply a comprehensive description of the final compounds at both the meso- and nanoscale, no attention has so far been directed towards the formation of the liquid-crystalline building blocks at low-concentrations.

In this section, we address the structural nature of low-concentrated **PBI2+** in aqueous media. We synthesized PBIs and derivatives via the synthetic protocol discussed in the previous section. For this work we methylated the secondary amines of PBI **A** and Cl^- was chosen as a charge-balancing counter-ion. Static absorption and emission spectroscopy measurements shine light onto low concentration regime < 50µM, already suggesting the existence of π-π stacked **PBI2+** dimers. A series of X-ray and neutron scattering techniques provide evidence of dimer-growth into organic nanocrystals, which are thought to be building-blocks for liquid-crystalline materials. Yet, the dried structure of **PBI2+** reveals a strikingly different morphology compared to the solvent state, underlining the necessity of a thorough understanding of the compound behavior in aqueous media.

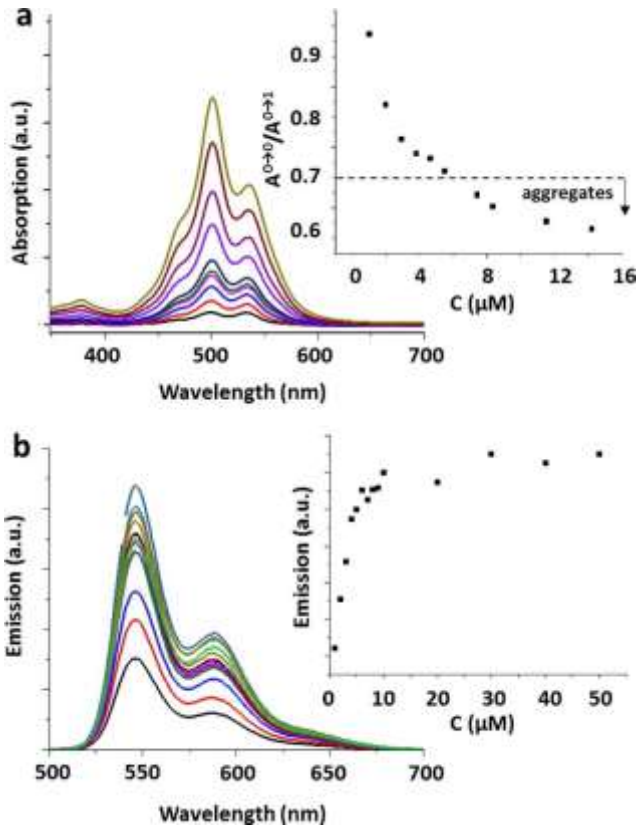

Figure 2.11 (a) Absorption spectra measured for **PBI2+** in deionized water, R.T., from 1 μM to 14 μM. The 537 nm/501 nm ratio dependence on **PBI2+** concentration is shown in the inset. (b) Corresponding fluorescence spectra measured for ranging from 1 to 50 μM. Similar to above, a clear correspondence between the **PBI2+** concentration and the emission intensity at 545 nm is seen in the inset.

Amphiphilic **PBI2+** carries two positive peripheral tetra-alkyl ammonium pendants at the central imide position with Cl^- as the counter anion. We introduced in section 2.1.2 that PBIs tend to self-assemble into supramolecular architectures in protic media such as water.[51] A first indication of this phenomenon is found in the absorption spectra of very low concentrate **PBI2+** in aqueous media. As depicted in Fig 2.11a, the steady state absorption was performed in the concentration range between 1μM to 14 μM. All

recorded spectra exhibit two absorption peaks at 537 nm and 501 nm. The ratio of the intensity of peak absorbance of the lowest two energy transitions can be used to interpret the level of aggregation of the perylene chromophores in solution. In the case of individual molecules with normal Franck-Condon progression, this ratio should be around 1.6[52] whereas for aggregated species typical values are <0.7.[53,54] The experimentally determined dependency of the rate on the **PBI2+** concentration is shown in the inset Figure 2.11a, whereas the relative intensities between the two peaks significantly change with increasing concentration. Even at the lowest concentration of 1 μM the peak ratio is 0.95, already indicating evidence of aggregation. This ratio further decreases with increasing **PBI2+** concentration, reaching a minimum at around 0.60. This general intensity reversal is attributed to the strong electron-photon coupling in the aggregated structures and is characteristic for an H-type conformation (plane to plane stacking).[55] These results are in accordance with previous work and give us clues on the formation of aggregates in a parallel stacked H-type geometry.[50]

Similarly, the emission spectrum of the **PBI2+** is a mirror image of the absorption spectrum.[23,25] In the case of DMF as a solvent, the fluorescence quantum yield is near unity. However, the QY is immediately quenched in the presence of water (0.75 for a solution of 10μM) This effect is second piece of evidence of the formation of supramolecular aggregates at concentrations as low as 10 μM.[56] The emission quenching is further amplified at higher concentrations: as seen in Figure 2.11b the emission remains

apparently constant when increasing the concentration from 10 to 50 µM, whereas a further increase to 0.1 and 1 mM causes a lowering of the emission intensity.

To gain a more direct insight in the structural aspects, we performed small angle X-ray scattering (SAXS) measurements at the lowest possible concentration. As seen in Figure 2.12a the scattering pattern of **PBI2+** at 0.6 mM shows a distinct increase in the low-q regime ($q < 0.5$ nm^{-1}), characteristic of large-scale aggregate scattering.[57] However, the mid- and the higher-q regime (q>1 nm-1) are dominated by the form-factor scattering of a modeled **PBI2+** dimer. The full scattering-curve was hence fitted using a custom model, which includes both of the above scattering contributions.

Upon increase of **PBI2+** concentration to 20 mM, the scattering pattern changes drastically. Especially in the mid-q regime a strong deviation of the previous curve is observed, such that the dimeric **PBI2+** form-factor scattering is not witnessed any more. We hence changed the previous model function to now include the contribution of a core-shell cylinder. Also in this case, the full pattern is fitted, whereas as the best agreement is found for a cylinder of 4 nm height and 2 nm diameter, Comparison of these results with the characteristic dimensions of a single PBI molecule strongly suggest the formation of a stacked conformation, as sketched in the inset Figure 2.12b

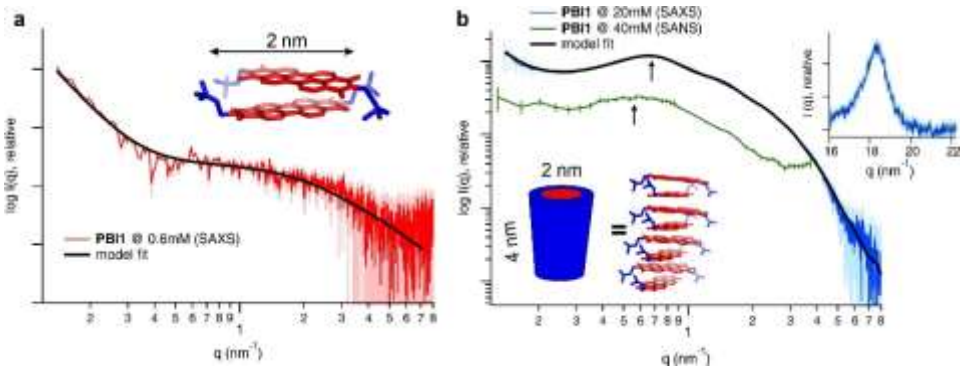

Figure 2.12 (a) SAXS pattern of PBI1 at 0.6 mM (red) as well as a corresponding model fit (black) utilizing the form-factor scattering of the **PBI2+** dimer shown in the inset. (b) SAXS (blue) and SANS (green) of **PBI2+** at 20 mM and 40 mM, respectively. The fitted model curve yields best agreement for a core-shell cylinder of p-p-stacked molecules as confirmed by the WAXS data (see p-p-stacking peak in the inset). The black arrows indicate the position of the first structure-factor peak relating to the mean distance between the cylindrical aggregates

To elucidate the intermolecular arrangement inside the cylinder, the simultaneously obtained WAXS measurements were further analyzed. As shown in the inset of Figure 2.12b, a strong diffraction peak at 18.35 nm-1 (d-spacing of d = 2π/q = 0.34 nm) is visible. This peak hence corresponds to the π-π stacking distance of **PBI2+**. Additionally, a coherent-domain size can be estimated from the peak width (FWHM = 1.35 nm^{-1}), such that the π-π stacking extends over approx. 3.9 nm. This value is in agreement with the length of the cylinder axis previously determined from the SAXS data fit, hence confirming the proposed model. Further, these results also imply that the cylindrical aggregates are crystalline such that they can be seen as nano-meter sized single-crystals.

However, the concentration increase of **PBI2+** from 0.6 mM to 20 mM affects SAXS data from more than one perspective: besides the discussed change in the form factor scattering, a significant structure-factor contribution is observed. In the context of this

investigation, the structure factor describes the interactive forces between the cylindrical aggregates. As an example, the first broad peak at approx. 0.65 nm^{-1} relates to the mean next-neighbor distance between the cylinders, whereas the fitting-results determined this distance to be about 4.0 nm. Comparison of this value with the cylindrical dimensions above suggest that the length of the π-π stacked nano-crystals dominates the mean interparticle distance. Additional neutron scattering experiments (SANS) of **PBI2+** at an increased concentration of 40 mM are consistent with this hypothesis: as the concentration increases, the nano-crystals are most likely growing along the π-π stacking direction, resulting in an increased cylinder length. This further increases the mean interparticle distance such that the first structure-factor peak shifts to lower q-values. Therefore, further concentration increase will

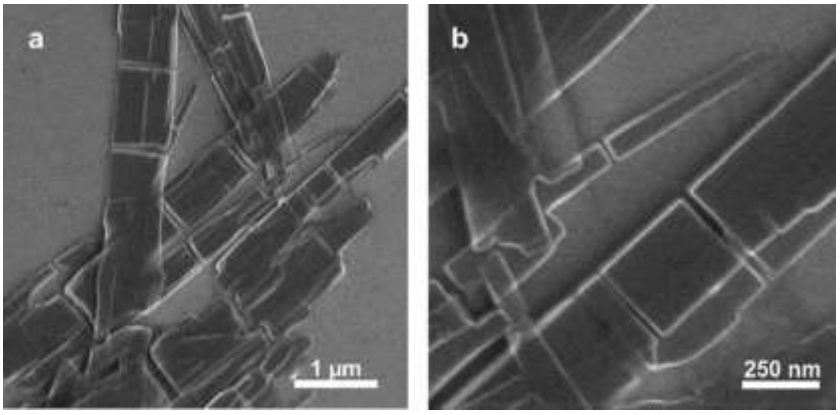

Figure 2.13 SEM images of **PBI2+** nano-scaffolds after spin-coating a 0.6 mM aqueous solution. (a) Contrary to the assumption that **PBI2+** forms columnar 1D assemblies, the microscopic morphology appears to be of a more planar nature with sheet-like character. (b) At such high-magnification, the **PBI2+** aggregates present sharp edges, suggesting a higher-ordered, maybe even crystalline, molecular structure

most-likely result in highly elongated rod-like structures, similar to what found in liquid crystalline phases for the same compound.[15]

The tendency of **PBI2+** to form highly ordered structures in aqueous solution is further confirmed by means of SEM. We selected a sample of 0.6 mM **PBI2+**, as under these conditions no nano-crystals formed in solution. Yet, after spin coating the sample on a Si wafer, the SEM images present micrometer-sized structures with sharp, well-defined edges as usually found for crystalline materials. Surprisingly, the overall morphology of the structures does not appear to be columnar, as often reported for perylene-based materials,[40,58] but more of planar, sheet-like nature. Hence, there exists a striking difference between the structure motive in solution and the morphology in the dry state.

In conclusion, we address the structural nature of **PBI2+** in aqueous solution, spanning over a concentration range from 1 μM to 40 mM. Under all the studied conditions, the hydrophobic π-π interactions appear to be dominant cause of molecular self-organization. Spectroscopic measurements suggest H-type aggregation, even at concentrations as low as 1 μM. SAXS data taken at 0.6 mM provides direct evidence of the presence of **PBI2+** dimers, hence confirming the spectroscopic results. Upon further increasing the concentration, the **PBI2+** dimers assemble along the π-π stacking direction, forming highly ordered cylindrical nanocrystals. Complete drying of the solution causes the loss of the cylinder-like conformation, whereas a planar sheet-like morphology is observed. Hence, there exists a significant difference between the solution and the solid-state nature of the aggregated compounds. The presented findings are of special interest in the design and production of solution-processed

materials, utilizing perylene bisimide compounds in aqueous light-harvesting systems, which will be the main topic of chapter 4.

2.3 Experimental section

2.3.1 Instruments and materials

Chemicals

All solvents used were of reagent quality and purchased commercially. All purchased starting materials were used without further purification. Perylene-3,4,9,10-tetracarboxylic dianhydride (Sigma-Aldrich 97%), N,N-dimethylethylenediamine (Sigma-Aldrich 99%), (2-methoxyethyl)amine (Sigma-Aldrich 98%), 1-(3-aminopropyl)imidazole (Sigma-Aldrich 97%), 2-(2-aminoethoxy)ethanol (Sigma-Aldrich 98%), 4-amino-1-butanol (Alfa Aesar 98%), octylamine (Sigma-Aldrich 99%), 4-aminopyridine (Sigma-Aldrich >99%), dopamine (Sigma-Aldrich 98%), 5-amino-isophtalic acid (Sigma-Aldrich 94%), glycine (Sigma-Aldrich >99%), B-alanine (Sigma-Aldrich 99%).

Microwave-assisted synthesis

Microwave-assisted synthesis of perylene derivatives was developed using a *CEM Discover® S.* The pressure-resistant, tightly sealed quartz tubes were 3 mm thick with a volume of 10 ml and designed for microwave reactor.

Nuclear Magnetic Resonance (NMR)

1H spectra were recorded at 500 MHz on a *Varian VNMRS - 500 MHz*. All spectra were registered at 298 K.

UV/VIS absorption and emission

Steady-state absorption spectroscopy studies have been performed at room temperature on a *Varian Cary 5000* UV-Vis-NIR double beam spectrophotometer; 10 mm path length Hellma Analytics 100 QS quartz cuvettes have been used.

Steady-state fluorescence spectra have been recorded on a *Varian Cary Eclipse Fluorescence* spectrophotometer; 10 mm path length *Hellma Analytics 117.100F QS* quartz cuvettes have been used.

IR Spectra

IR Spectra were measured on Bruker ALPHA spectrometer in FT-TR mode by simple KBr pellets.

Small Angle Neutron Scattering (SANS)

Small-angle neutron scattering experiments were performed on the Yellow Submarine instrument in Budapest Neutron Center. The scattering vector q ranged from 0.1 to 3.7 nm^{-1}, by using two sample - detector distances of 1.2 and 5.2 m, and one wavelength of 0.5 nm. The samples were placed in Hellma quartz cuvettes of the latest design, with flight path of 1 mm, and thermostated at 25 °C. The measured scattering curves were corrected for background scattering from the D_2O solvent, and put on absolute scale using water as secondary calibration standard. The data were processed by the BerSANS-PC software.[59]

Small and Wide Angle X-Ray Scattering (SAXS & WAXS)

Small angle X-ray scattering (SAXS) experiments were performed at the Austrian SAXS beamline of Elettra synchrotron (Trieste, Italy) using 8 keV photon energy. The liquid samples were filled in

standard 1.5 mm quartz capillaries whereas 6-8 consecutive images were taken over time, to rule out possible radiation damage by comparison of the scattering pattern. The two-dimensional Pilatus1M image detector (Dectris, Switzerland) was placed at a distance of approximately 90 cm to obtain an accessible q-range from 0.15 - 9.25 nm^{-1}. A reference measurement was made using silver-behenate as a standard for the calibration of the angular regime. Azimuthal integration of the 2D images was done using the Fit2D program. The resulting integrated scattering curves were corrected for dark-current, normalized by sample transmission and subsequently the background was subtracted using the pure solvent-scattering. Theoretical formfactors were calculated using the CRYSOL software.[60]

Wide angle x-ray scattering (WAXS) data was recorded simultaneously with the corresponding SAXS measurement. In addition, a second Pilatus100K image detector (Dectris, Switzerland) was placed vertically to cover scattering angles from 22° - 34°, resulting in an approximate q-range from 16-22 nm-1. Further data treatment was done in analogue to the SAXS data.

Scanning Electron Microscopy (SEM)

Scanning electron microscopy images were obtained using the MIRA3 microscope (Tescan, Czech Republic) operating at an accelerating voltage of 30kV. The liquid samples were dropped onto a Si wafer and spin-coated at 600 rpm for 120 sec.

2.3.2 Methods

Small Angle X-Ray Scattering – Model Fits

The scattering intensity $I_{calc}(q)$ for both theoretical models presented in this work was calculated according to

$$I_{calc}(q) = a * F(q) * S_{SHS}(q) + I_{Porod}(q) + BG \qquad \text{(eq. 2.1)}$$

where

- a denotes an intensity scalar,
- $F(q)$ denotes the form-factor scattering,
- $S_{SHS}(q)$ denotes the structure-factor contribution,
- $I_{Porod}(q)$ denotes the Porod-contribution resulting from large scale aggregates,
- and BG denotes a constant background offset.

Form-Factor scattering – PBI2+ dimer

In case of the dimeric scattering as presented in Figure 2.12a, the theoretical form-factor $F(q)$ was calculated numerically from the molecular dimer model shown in Figure 2.12a using CRYSOL.[60]

Form-Factor scattering – core-shell cylinder

In case of the π-π-stacked **PBI2+** cylinder, we used a core-shell model as depicted in Figure 2.13. If such a geometry is chosen, the form-factor scattering-intensity $F(q)$ can be calculated according to the literature whereas the corresponding fitting parameters are explained graphically in scheme 2.4.

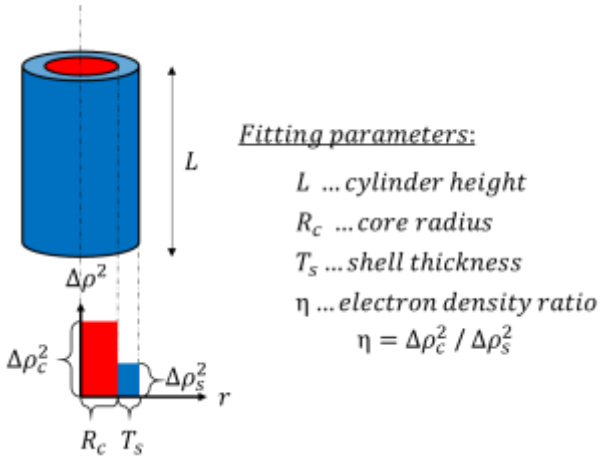

Figure 2.14. Graphical illustration explaining the fitting parameters used for the calculation of the form-factor scattering of the π-π-stacked **PBI2+** cylinder.

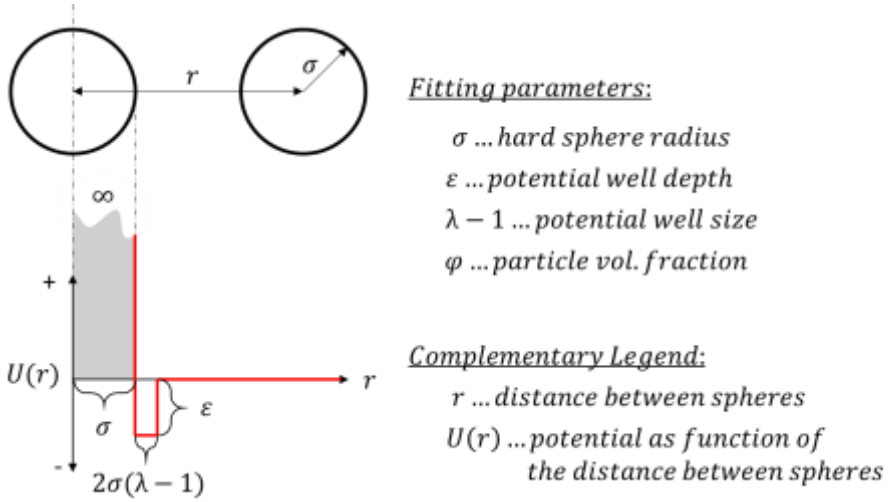

Figure 2.15. Graphical illustration explaining the fitting parameters used for the calculation of the sticky-hard-sphere structure factor. The red line describes the potential U(r) as a function between two particles separated by a given distance r.

Structure-Factor contribution

In the case of the 20 mM **PBI2+** sample, we use a sticky-hard-sphere potential to describe the interaction term between the π-π-

stacked aggregates. A graphical overview of the underlying potential $U(r)$ between particles separated by a given distance r is depicted in Figure 2.12.

Porod contribution of large-scale aggregates

The experimental scattering curves of both, the 0.6 and 20 mM, **PBI2+** samples present a low-q ($q < 0.5\ nm^{-1}$) increase, characteristic of large-scale aggregate formation beyond the resolution limit of SAXS.[5] We hence added a Porod contribution [5] according to

$$I_{Porod}(q) = c_p * q^{-4} \qquad \text{(eq. 2.2)}$$

to describe this intensity increase. In this formalism, only the absolute scalar c_p is optimized throughout the fitting process.

Small Angle X-Ray Scattering – Results

All parameters were optimized by least-square fitting the corresponding models to the experimental scattering intensity. The final results as well as the weighted least-square value χ^2 as a measure for goodness-of-fit are shown in Tables S1 and S2.

Table 2.2. Fitting results corresponding to the model shown in Figure 2.11, describing the SAXS pattern recorded from **PBI2+** at 0.6 mM.

Parameter	$\mathbf{a}$ [−]	$\mathbf{c_p}$ [−]	**BG** [−]	$\boldsymbol{\chi^2}$ [−]
Value	1.240 ± 0.013	0.035 ± 0.001	0.031 ± 0.001	1.302

Table 2.3 Fitting results corresponding to the model shown in Figure 2.11 b, describing the SAXS pattern recorded from **PBI2+** at 20 mM. As there exists a correlation between the potential well size λ and its depth ε, we kept λ fixed at 1.1.

Parameter	$\mathbf{a}$ [−]	$\mathbf{L}$ [nm]	$\mathbf{R_C}$ [nm]	$\mathbf{T_S}$[nm]	$\boldsymbol{\eta}$ [−]
Value	11.52 $\pm$ 0.02	3.88 $\pm$ 0.02	0.42 $\pm$ 0.01	0.58 $\pm$ 0.02	5.42 $\pm$0.56

Parameter	$\boldsymbol{\sigma}$ [−]	$\boldsymbol{\varphi}$[−]	$\boldsymbol{\varepsilon}[\mathbf{k_BT}]$	$\mathbf{c_p}$ [−]	**BG** [−]	$\boldsymbol{\chi^2}$ [−]
Value	4.04 $\pm$ 0.01	0.007 $\pm$ 0.0003	25.57 $\pm$ 0.18	0.05 $\pm$ 0.002	0.011 ± 0.002	1.021

2.3.3. Synthesis and characterization

Synthesis of perylene bisimides with alkylamine. General Procedure. (A-F)

100 mg of perylene-3,4,9,10-tetracarboxylic bisanhydride were suspended in dry DMF (5 mL) with 2 equiv. of the corresponding amine in a pressure tight microwave tube.

The suspension was sonicated for few minutes before heating under microwave irradiation at 50W for 10 min. 5 cycles. Max T was set at 200 °C.
After cooling, the color turned to dark red and the mixture appeared more homogenous.
50 mL of NaOH 1 M were added to the starting material and stirred for 20 min. The precipitate was filtered and washed abundantly with water until pH neutralization and dried using a vacuum pump.

Synthesis of perylene bisimides with aromatic amines. General Procedure. (G-H)

100 mg of perylene-3,4,9,10-tetracarboxylic bisanhydride were suspended in dry DMF (5 mL) with 4 equiv. of the corresponding amine and 50 uL of Et_3N in a pressure tight microwave tube.
The suspension was sonicated for few minutes before heating under microwave irradiation at 80 W for 10 min. 10 cycles. Max T was set at 200 °C. After cooling, the color turned to dark red and the mixture appeared more homogenous. To the mixture 50 mL of KOH 10% aq. solution was added and solution was stirred for 2h. The precipitate was filtered and washed abundantly with water until pH neutralization and dried using a vacuum pump.

Synthesis of perylene bisimides with aminoacids. General Procedure. (I-M)

100 mg of perylene-3,4,9,10-tetracarboxylic bisanhydride were suspended in dry DMF (5 mL) with 4 equiv. of the corresponding amine and 50 uL of Et_3N in a pressure tight microwave tube. The

suspension was sonicated for few minutes before heating under microwave irradiation at 50 W for 10 min, 5 cycles. Max T was set at 200 °C. After cooling, the color turned to dark red and the mixture appeared more homogenous. To the mixture 50 mL of pH 8 aq. solution was added and stirred for 2 hours. The precipitated unreacted anhydride was filtered off. The filtrate was then acidified with HCl 5 %. The precipitate was filtered and washed abundantly with water until pH neutralization and dried using a vacuum pump.

Synthesis of halogenated perylene bisimides with alkylamine. General procedure. (N-Q)

100 mg of tetrachlorinated or tetrabrominated perylene-3,4,9,10-tetracarboxylic bisanhydride were suspended in dry DMF (5 mL) with 2 equiv. of the corresponding amine and 1 mL of acetic acid in a pressure tight microwave tube. The suspension was sonicated for few minutes before heating under microwave irradiation at 60W for 10 min. Max T was set at 200 °C. After cooling, the color turned to dark red-black and the mixture appeared more homogenous. 50 mL of NaOH 1 M were added to the starting material and stirred for 20 min. The precipitate was filtered and washed abundantly with water until pH neutralization and dried using a vacuum pump.

A. 2,9-bis(2-(dimethylamino)ethyl)anthra[2,1,9-def:6,5,10-d'e'f']diisoquinoline-1,3,8,10(2H,5a1H,5b1H,9H)-tetraone[1]

^{1}H-NMR (CF_3COOD, 500 MHz), δ: 8.89 (d, J=8 Hz, 4H), 8.81 (d, J=8, 4H), 4.78 (s, 4H), 3.75 (s, 4H), 3.19 (s, 12H). ^{13}C-NMR (CF_3COOD, 125 MHz): 168.8, 138.7, 135.5, 131.6, 128.8, 126.8, 123.7, 60.6, 46.2, 38.5. $\lambda_{abs(CF3COOH)}$ 537 nm. FT-

IR (cm^{-1}): 1695, 1652, 1592, 1509, 1444, 1404, 1341. m/z calculated for $C_{32}H_{28}N_4O_4$: 532, found MALDI (+): 533 m/z (MH^+). Yield%: 99

B. 2,9-bis(2-methoxyethyl)anthra[2,1,9-def:6,5,10-d'e'f']-diisoquinoline-1,3,8,10(2H,5a1H,5b1H,9H)-tetraone[2]

^{1}H-NMR (CF_3COOD, 500 MHz), δ: 8.76 (d, J=8 Hz, 4H), 8.74 (d, J=8 Hz, 4H), 4.69 (t, J=5 Hz, 4H), 4.13 (t, J=5 Hz, 4H), 3.65 (s, 6H).. $\lambda_{abs(CF3COOH)}$ 537 nm. FT-IR (cm_{-1}): 1682, 1656, 1596, 1507, 1436, 1404, 1348, m/z calculated for $C_{30}H_{22}N_2O_6$: 506, found MALDI (+): 506 ($M^{\circ+}$). Yield%: 99

C. 2,9-bis(3-(1H-imidazol-1-yl)propyl)anthra[2,1,9-def:6-,5,10-d'e'f']diisoquinoline-3,8,10(2H,5a1H,5b1H,9H)tetraone[3]

^{1}H-NMR (CF_3COOD, 500 MHz), δ: 8.75 (m, 10H), 7.47 (d, J=8 Hz, 2H), 7.37 (d, J=8 Hz, 2H), 4.43 (s, 4H), 4.37 (s, 4H), 2.47 (s, 4H). $\lambda_{abs(CF3COOH)}$ 537 nm. FT-IR (cm-1): 1686, 1644, 1593, 1439, 1343, 1252. m/z calculated for $C_{32}H_{28}N_4O_4$: 606, found MALDI (+): 538 (M^+-[imidazole]). Yield%: 99

D. 2,9-bis(2-(2-hydroxyethoxy)ethyl)anthra[2,1,9-def:6,5,10-d'e'f']diisoquinoline-1,3,8,10(2H,5a1H,5b1H,9H)-tetraone

^{1}H-NMR (CF_3COOD, 500 MHz), δ: 8.82 (s, 8H), 4.96 (t, J=10 Hz, 4H), 4.76 (q, J=6 Hz, 4H), 4.02 (m, 4H), 3.87 (m, 4H). ^{13}C-NMR: (CF_3COOD, 125 MHz) 168.2, 138.2, 135.2, 131.8,

128.9, 126.5, 124.1, 78.0, 70.4, 68.9, 41.7, 21.8. $\lambda_{abs(CF3COOH)}$ 535 nm. FT-IR (cm^{-1}): 1687, 1651, 1591, 1438, 1402, 1369, 1336. $C_{32}H_{26}N_2O_8$: 566, found MALDI (+): 567 m/z ($M\text{-}H^+$). Yield%: 99

E. 2,9-bis(4-hydroxybutyl)anthra[2,1,9-def:6,5,10-d'e'f']diisoquinoline-1,3,8,10(2H,5a1H,5b1H,9H)-tetraone[4]

^{1}H-NMR (C_5D_5N, 400 MHz), δ: 8.68 (d, J=7.2 Hz, 4H), 8.49 (d, J=7.2 Hz, 4H), 4.89 (t, J=8 Hz, 4H), 4.41 (q, J=8 Hz, 4H), 2.54 (m, J=8 Hz, 4H), 2.17 (m, J=8 Hz, 4H). $\lambda_{abs(CF3COOH)}$ 537 nm. FT-IR (cm^{-1}): 1693, 1649, 1594, 1577, 1436, 1404, 1341. $C_{32}H_{26}N_2O_6$: 535, found MALDI (+):536 m/z (MH^+). Yield%: 92

F. 2,9-dioctylanthra[2,1,9-def:6,5,10-d'e'f']diisoquinoline-1,3,8,10(2H,5a1H,5b1H,9H)-tetraone[5]

^{1}H-NMR: (CF_3COOD, 500 MHz) , δ:= 8.74 (s, 4H), 4.21 (m, 4H), 1.73 (m, 4H), 1.22 (m, 20H), 0.76 (m, 6H) $\lambda_{abs(CF3COOH)}$ 537 nm. FT-IR (cm^{-1}): 1696, 1650, 1598, 1432, 1400. $C_{40}H_{44}N_2O_4$: 617, found MALDI (+):618 (MH^+). Yield%: 87

G 2,9-di(pyridin-4-yl)anthra[2,1,9-def:6,5,10-d'e'f']diisoquinoline-1,3,8,10(2H,9H)-tetraone

^{1}H-NMR (C_5D_5N, 500 MHz), δ: 8.23 (d, J=3Hz, 4H), 8.21 (d, J=3Hz, 4H), 7.85 (d, J=4 Hz), 7.83 (d, J= 4Hz). $\lambda_{abs(C5H5N)}$ 529 nm. FT-IR (cm^{-1}): 1705, 1665, 1590, 1360. $C_{44}H_{16}N_4O4_4$: 544, found MALDI (+):544 ($M^{\circ+}$). Yield%: 45

H. 2,9-bis(3,4-dihydroxyphenethyl)anthra[2,1,9-def:6,5,10-d'e'f']diisoquinoline-1,3,8,10(2H,9H)-tetraone

^{1}H-NMR (C_5D_5N, 500 MHz), δ: 8.38 (s, 8H), 7.80 (d, J=1 Hz, 2H), 7.56 (d, J=8 Hz), 7.33 (dd, J1=8 Hz, J2=1 Hz, 2H), 5.01 (t, J=8 Hz, 4H), 3.58 (t, J=8 Hz, 4H). $\lambda_{abs(CF3COOH)}$ 537 nm. FT-IR (cm^{-1}): 1691, 1648, 1631, 1401 $C_{40}H_{26}N_2O4_8$: 662, found MALDI (+):645 (M^+-[OH]). Yield%: 43

I. 5,5'-(1,3,8,10-tetraoxoanthra[2,1,9-def:6,5,10-d'e'f']diisoquinoline-2,9(1H,3H,8H,10H)-diyl)diisophthalic acid[6]

^{1}H-NMR (D_2O, 500 MHz), δ: 8.52 (s, 4H), 8.35 (d, J=7.2 Hz, 4H), 8.25 (s, 2H), 8.05 (brs, 4H), 7.76 (d, J=7.2 Hz, 4H). $\lambda_{abs(H2O)}$ 537 nm. FT-IR (cm^{-1}): 1690, 1650, 1593, 1506, 1405, 1300 $C_{40}H_{12}N_2O_{12}$: 720, found MALDI (+):720 ($M^{\circ+}$). Yield%: 87

J. 2,2'-(1,3,8,10-tetraoxoanthra[2,1,9-def:6,5,10-d'e'f']diisoquinoline-2,9(1H,3H,8H,10H)-diyl)diacetic acid[7]

^{1}H-NMR (D_2O, 500 MHz), δ: 7.75 (8H), 4.15 (4H), 2.50 (4H). $\lambda_{abs(CF3COOH)}$ 466 nm. FT-IR (cm^{-1}): 1697, 1661, 1593, 1506, 1403, 1347, 1300. $C_{28}H_{14}N_2O_8$: 506, found MALDI (-):503 (M^{2-}/2): 252. Yield%: 42

K. 3,3'-(1,3,8,10-tetraoxoanthra[2,1,9-def:6,5,10-d'e'f']diisoquinoline-2,9(1H,3H,8H,10H)-diyl)dipropanoic acid[8]

^{1}H-NMR (D_2O, 500 MHz), δ: 8.39 (d, J=7.2 Hz, 4H), 7.79 (d, J=7.2 Hz, 4H), (4.76 (s, 4H). $\lambda_{abs(CF3COOH)}$ 538 nm FT-IR (cm^{-1}): 1687, 1642, 1591, 1576, 1507, 1441, 1401. $C_{30}H_{18}N_2O_8$: 534, found MALDI (-): 533 (M-$[H^+]^-$). Yield%: 64

L. 5,6,12,13-tetrabromo-2,9-bis(2-(dimethylamino)ethyl)anthra[2,1,9-def:6,5,10-d'e'f']diisoquinoline-1,3,8,10(2H,9H)-tetraone

^{1}H-NMR (CF_3COOD, 500 MHz), δ: 8.90 (s, 4H), 4.77 (s, 4H), 3.75 (s, 4H), 3.20 (s, 12H). ^{13}C-NMR (CF_3COOD, 125 MHz), δ: 166.3, 140.3, 139.8, 136.3, 131.0, 130.6, 59.5, 46.1, 38.4, 21.8. FT-IR(cm^{-1}): 1689, 1645, 1591, 1426. $\lambda_{abs(CF3COOH)}$ 558 nm. $C_{32}H_{26}Br_4N_4O_4$: 850, found MALDI (-): 424 (M-$[2H^+]^{2-}$). Yield%: 80

M. 5,6,12,13-tetrabromo-2,9-bis(2-methoxyethyl)anthra[2,1,9-def:6,5,10-d'e'f']diisoquinoline-1,3,8,10(2H,9H)-tetraone

^{1}H-NMR (CF_3COOD, 500 MHz), δ: 8.90 (4H), 4.84 (4H), 4.26 (4H), 3.78 (6H), $\lambda_{abs(CF3COOH)}$ 558 nm FT-IR(cm^{-1}): 1690, 1655, 1591, 1507, 1436, 1402, 1370, 1340. $C_{30}H_{20}Br_4N_2O_6$: 824, found MALDI (+): 825 (MH^+). Yield%: 87

N. 2,9-bis(3-(1H-imidazol-1-yl)propyl)-5,6,12,13-tetrabromoanthra[2,1,9-def:6,5,10-d'e'f']diisoquinoline-1,3,8,10(2H,9H)-tetraone

^{1}H-NMR ($CDCl_3$, 400 MHz), δ: 8.83 (m, 4H), 7.70 (s, 2H), 7.10 (d, J=4 Hz, 2H), 7.05 (d, J=4 Hz, 2H), 4.27 (t, J=5 Hz, 4H), 4.13 (t, J=5 Hz), 2.30 (m, J=5 Hz, 4H). $\lambda_{abs(CF3COOH)}$ 540nm FT-IR(cm^{-1}): 1701, 1659, 1584, 1507, 1507, 1435, 1413, 1386, 1371, 1308, 1282. $C_{36}H_{24}Br_4N_6O_4$: 922, found MALDI (+): 922 (M^+), 1844 ($2M^+$). Yield%: 99

O. 5,6,12,13-tetrachloro-2,9-bis(2-(dimethylamino)ethyl)anthra[2,1,9-def:6,5,10-d'e'f']diisoquinoline-1,3,8,10(2H,9H)-tetraone[9]

^{1}H-NMR (CF_3COOD, 400MHz), δ: 8.82 (s, 4H), 4.85 (s, 4H), 3.85 (s, 4H), 3.27 (s, 12H). ^{13}C-NMR (CF_3COOD, 125 MHz): 162.2, 135.7, 132.2, 129.3, 128.8, 128.3, 125.3, 123.3, 123.0, 46.0, 38.1, 29.2, 23.1. $\lambda_{abs(CF3COOH)}$ 537 nm. FT-IR(cm^{-1}): 1702, 1661, 1589, 1506, 1437, 1392, 1314, 1287. $C_{32}H_{26}Cl_4N_4O_4$: 672, found MALDI (+): 673 (MH^+). Yield%: 95

P. 5,6,12,13-tetrachloro-2,9-bis(2-methoxyethyl)anthra[2,1,9-def:6,5,10-d'e'f']diisoquinoline-1,3,8,10(2H,9H)-tetraone

^{1}H-NMR (CF_3COOD, 400 MHz), δ: 8.74 (s, 4H), 4.65 (4H), 4.09 (4H), 3.61 (6H), $\lambda_{abs(CF3COOH)}$ 537 nm FT-IR (cm^{-1}): 1702, 1662, 1588, 1562, 1451, 1430, 1388, 1339, 1307. $C_{30}H_{20}Cl_4N_2O_6$: 646, found MALDI (+): 647 m/z (MH^+). Yield%:85

Q. 2,9-bis(3-(1H-imidazol-1-yl)propyl)-5,6,12,13-tetrachloroanthra[2,1,9-def:6,5,10-d'e'f']diisoquinoline-1,3,8,10(2H,9H)-tetraone

^{1}H-NMR ($CDCl_3$, 400 MHz), δ: 8.68 (m, 4H), 7.63 (s, 2H), 7.07 (s, 2H), 7.03 (s, 2H), 2H 4.27 (s, 4H), 4.13 (s, 4H), 2.31 (s, 4H). $\lambda_{abs(CF3COOH)}$ 537 nm. FT-IR(cm-1): 1699, 1659, 1594, 1437, 1394, 1340. $C_{36}H_{24}Cl_4N_6O_4$: 746, found MALDI (+): 746 m/z (M^+). Yield%: 95

Synthetis of N,N′-Bis(2-(trimethylammonium)-ethylene)perylene-3,4,9,10-tetracarboxylic acid bisimide bischloride salt (PBI^{2+} 2Cl$^-$)

PBI (0.25 gr, 0.46 mmol) and MeI (40 mmol) were solubilized in toluene (20 mL) and the mixture was refluxed for 5 h. The solution was cooled to r.t. and the precipitate was filtered and washed with Et2O (2 x 30 mL). The resulting solid was dried under vacuum to afford compound iodine salt of 1 (0.32 gr, 98 %) as a dark red powder For the exchange of the counterion, the precursor (**PBI^{2+}** 2I$^-$ is solubilized in a mixture 2-propanol/$HCl_{conc.}$ and the solution is stirred for 2 h at room temperature. The precipitate is filtered and washed with 2 × 30 ml toluene and 2 × 30 ml Et_2O. The operation is repeated 3 times. The resulting solid is dried under vacuum to afford **PBI^{2+}** 2Cl$^-$ (2.19 gr, 80 %) as a dark red powder; ^{1}H (TFA_d, 270 MHz), δ: 8.88 (d, J=8.10 Hz, 4H), 8.80 (d, J=7.83 Hz, 4H), 4.83 (bt, 4H), 3.84 (bt, 4H), 3.36 (s, 12H); ^{13}C (TFA_d, 270 MHz), δ: 36.4, 55.6, 64.6, 123.5, 126.7, 128.7, 131.6, 135.5, 138.6, 167.8; IR

(powder, ν cm^{-1}): 1694, 1657 (>CO), 1593 (–C=C-), 1439, 1403, 1343 (>C-N-R); ESI-MS, m/z: 597.4 [**PBI**·Cl]$^{+}$, 281.5 [**PBI**]$^{2+}$.

2.4 References

[1] F. Würthner, *Chem. Commun.* **2004**, *0*, 1564–1579.

[2] M. Kardos, *Deustches Reichspatent* **1913**, 276357.

[3] E. B. Faulkner, R. J. Schwartz, *High Performance Pigments.*, Wiley-VCH, **2009**.

[4] K. Hunger, W. Herbst, *Ullmann's Encycl. Ind. Chem.* **2000**, pp. 35–154.

[5] C. Li, H. Wonneberger, *Adv. Mater.* **2012**, *24*, 613–636.

[6] F.-C. Chen, C.-H. Liao, *Appl. Phys. Lett.* **2008**, *93*, 103310.

[7] H. Langhals, *Heterocycles* **1995**, *40*, 477–500.

[8] S. Shoaee, T. M. Clarke, C. Huang, S. Barlow, S. R. Marder, M. Heeney, I. McCulloch, J. R. Durrant, *J. Am. Chem. Soc.* **2010**, *132*, 12919–12926.

[9] G. Seybold, G. Wagenblast, *Dye. Pigment.* **1989**, *11*, 303–317.

[10] M.-J. Lin, Á. J. Jiménez, C. Burschka, F. Würthner, *Chem. Commun.* **2012**, *48*, 12050.

[11] M. Schneider, K. Müllen, *Chem. Mater.* **2000**, *12*, 352–362.

[12] X. Lu, Z. Guo, C. Sun, H. Tian, W. Zhu, *J. Phys. Chem. B* **2011**, *115*, 10871–10876.

[13] Y. Zhao, M. R. Wasielewski, *Tetrahedron Lett.* **1999**, *40*, 7047–7050.

[14] H. Qian, C. Liu, Z. Wang, D. Zhu, *Chem. Commun.* **2006**, *0*, 4587–4589.

[15] S. Roy, D. K. Maiti, S. Panigrahi, D. Basak, A. Banerjee, H. C. Fry, J. M. Garcia, M. J. Medina, U. M. Ricoy, D. J. Gosztola, *Phys. Chem. Chem. Phys.* **2014**, *16*, 6041.

[16] P. Gu, Y. M. Zhao, Y. Q. Tu, Y. Ma, F. Zhang, *Org. Lett.* **2006**, *8*, 5271–5273.

[17] M. J. Ahrens, M. J. Fuller, M. R. Wasielewski, *Chem. Mater.* **2003**, *15*, 2684–2686.

[18] S. Nakazono, S. Easwaramoorthi, D. Kim, H. Shinokubo, A. Osuka, *Org. Lett.* **2009**, *11*, 5426–5429.

[19] D. Dasgupta, A. M. Kendhale, M. G. Debije, J. Ter Schiphorst, I. K. Shishmanova, G. Portale, A. P. H. J. Schenning, *ChemistryOpen* **2014**, *3*, 138–141.

[20] G. Battagliarin, C. Li, V. Enkelmann, K. Mullen, *Org. Lett.* **2011**, *13*, 3012–3015.

[21] T. Teraoka, S. Hiroto, H. Shinokubo, *Org. Lett.* **2011**, *13*, 2532–2535.

[22] M. Gsänger, D. Bialas, L. Huang, M. Stolte, F. Würthner, *Adv. Mater.* **2016**, *28*, 3615–3645.

[23] F. Würthner, C. R. Saha-Möller, B. Fimmel, S. Ogi, P. Leowanawat, D. Schmidt, *Chem. Rev.* **2016** *116*, 962–1052.

[24] D. Görl, X. Zhang, F. Würthner, *Angew. Chem.* **2012**, *51*, 6328–6348.

[25] W. E. Ford, P. V. Kamat, *J. Phys. Chem.* **1987**, *91*, 6373–6380.

[26] T. Tang, A. Herrmann, K. Peneva, K. Müllen, S. E. Webber, *Langmuir* **2007**, *23*, 4623–4628.

[27] C. Kohl, T. Weil, J. Qu, K. Müllen, *Chem. - Eur. J.* **2004**, *10*, 5297–5310.

[28] J. Qu, C. Kohl, M. Pottek, K. Müllen, *Angew. Chem.* **2004**, *43*, 1528–1531.

[29] M. Sun, K. Müllen, M. Yin, *Chem. Soc. Rev.* **2016**, *45*, 1513–1528.

[30] Z. Chen, B. Fimmel, F. Würthner, *Org. Biomol. Chem.* **2012**, *10*, 5845.

[31] X. Zhang, Z. Chen, F. Würthner, *J. Am. Chem. Soc.* **2007**, *129*, 4886–4887.

[32] Z. Chen, V. Stepanenko, V. Dehm, P. Prins, L. D. A. Siebbeles, J. Seibt, P. Marquetand, V. Engel, F. Würthner, *Chem. - Eur. J.* **2007**, *13*, 436–449.

[33] J. Seibt, T. Winkler, K. Renziehausen, V. Dehm, F. Würthner, H. D. Meyer, V. Engel, *J. Phys. Chem. A* **2009**, *113*, 13475–13482.

[34] T. Heek, C. Fasting, C. Rest, X. Zhang, F. Würthner, R. Haag, *Chem. Commun.* **2010**, *46*, 1884.

[35] S. Rehm, V. Stepanenko, X. Zhang, T. H. Rehm, F. Würthner, *Chem. - A Eur. J.* **2010**, *16*, 3372–3382.

[36] H. Langhals, W. Jona, F. Einsiedl, S. Wohnlich, *Adv. Mater.* **1998**, *10*, 1022–1024.

[37] S. W. Tam-Chang, J. Helbley, I. K. Iverson, *Langmuir* **2008**, *24*, 2133–2139.

[38] J. Lydon, *J. Mater. Chem.* **2010**, *20*, 10071.

[39] C. D. Schmidt, C. Böttcher, A. Hirsch, *Eur. J. Org. Chem.* **2007**, *2007*, 5497–5505.

[40] C. Huang, S. Barlow, S. R. Marder, *J. Org. Chem.* **2011**, *76*, 2386–2407.

[41] Y. Nagao, *Prog. Org. Coatings* **1997**, *31*, 43–49.

[42] C. O. Kappe, *Angew. Chemie-International Ed.* **2004**, *43*, 6250–6284.

[43] S. Sciencedirect, J. Yuan, W. Xing, G. Gu, L. Wu, **2014**, 4–7.

[44] J. T. Kern, P. W. Thomas, S. M. Kerwin, *Biochemistry* **2002**, *41*, 11379–11389.

[45] A. Datar, K. Balakrishnan, L. Zang, L. Zang, Y. Che, J. S. Moore, F. Wurthner, A. C. Grimsdale, K. Müllen, A. P. H. J. Schenning, et al., *Chem. Commun.* **2013**, *49*, 6894.

[46] Z. Yao, M. Zhang, R. Li, L. Yang, Y. Qiao, P. Wang, *Angew. Chem.* **2015**, *54*, 5994–5998.

[47] A. S. Weingarten, R. V. Kazantsev, L. C. Palmer, M. McClendon, A. R. Koltonow, A. P. S. Samuel, D. J. Kiebala, M. R. Wasielewski, S. I. Stupp, *Nat. Chem.* **2014**, *6*, 964–970.

[48] S.-W. Tam-Chang, L. Huang, *Chem. Commun.* **2008**, *0*, 1957.

[49] A. Laiho, B. M. Smarsly, C. F. J. Faul, O. Ikkala, *Adv. Funct. Mater.* **2008**, *18*, 1890–1897.

[50] H. Yongwei, Q. Baogang, W. Zhixiang, L. Guangtong, S. Lianfeng, *J. Phys. Chem. C* **2009**, *113*, 3929–3933.

[51] H. Sirringhaus, *Adv. Mater.* **2014**, *26*, 1319–1335.

[52] W. Wang, J. J. Han, L. Q. Wang, L. S. Li, W. J. Shaw, A. D. Q. Li, *Nano Lett.* **2003**, *3*, 455–458.

[53] W. Wang, W. Wan, H. H. Zhou, S. Niu, A. D. Q. Li, *J. Am. Chem. Soc.* **2003**, *125*, 5248–5249.

[54] R. F. Fink, J. Seibt, V. Engel, M. Renz, M. Kaupp, S. Lochbrunner, H.-M. Zhao, J. Pfister, F. Würthner, B. Engels, *J. Am. Chem. Soc.* **2008**, *130*, 12858–12859.

[55] S. Yagai, T. Seki, T. Karatsu, A. Kitamura, F. Würthner, *Angew. Chem.* **2008**, *47*, 3367–3371.

[56] D. Görl, X. Zhang, F. Würthner, *Angew. Chem.* **2012**, *51*, 6328–48.

[57] O. Glatter, *J. Appl. Crystallogr.* **1977**, *10*, 415–421.

[58] K. Bag, P. K. Sukul, D. Chandra Santra, A. Roy, S. Malik, *RSC Adv.* **2016**, *6*, 34027–34037.

[59] U. Keiderling, A. Wiedenmann, A. Rupp, J. Klenke, W. Heil, in *Meas. Sci. Technol.* **2008**, p. 34009.

[60] D. Svergun, C. Barberato, M. H. Koch, *J. Appl. Crystallogr.* **1995**, *28*, 768–773.

3. Perylene bisimide hydrogels

Hydrogelation, the self-assembly of molecules into soft, water-loaded networks, bridges the structural gap between single molecules and functional materials. The potential of hydrogels, based on perylene bisimides, lies in their chemical, physical, optical, and electronic properties, which are all governed by the inter- and supramolecular structure of the gel. However, these structural motifs and their precise role for long-range conductivity are unknown. In this chapter, we present a comprehensive structural framework of a perylene bisimide hydrogel, suggesting that its long-range conductivity is limited by charge-transfer between electronic backbones. We reveal nano-crystalline ribbon-like structures as the electronic and structural backbone between which charge transfer is mediated by polar solvent bridges. We exemplify this effect with gas sensing, where exposure to polar vapor enhances conductivity by five orders of magnitude in milliseconds, emphasizing the crucial role of the interplay between structural motif and surrounding medium for the rational design of devices based on nano-crystalline hydrogels.

The results here presented have been done in a collaborative work with Mr. Max Burian (Technisce Universität of Graz, Austria) who carried out the SAXS analysis and the gas sensing experiments.

3. Perylene bisimide hydrogels

3.1 Introduction

3.1.1 π-π gelators

Supramolecular structures through molecular self-assembly are omnipresent procedures in nature.[1–4] In particular self-assembly of π-π conjugated systems into well-defined manner is an interesting way to prepare useful conductive materials through the formation of aggregates with different size and shape distribution. Some molecules employ these interactions to self-assembly in organogels and, thus, they are called π-π gelators.[5,6] π-π gels are soft, non-flowing materials derived from gelators with more than one aromatic π-unit which can be conjugated (π-π-henylenevinyles, π-π-henyleneethylenes, thienylenevinylenes, etc) or fused (naphthalene, perylene, pyrene, anthracene etc.). π-π interactions, besides driving the gelation process, are the best point of this kind of gels since they result in delocalization of the electrons, charge carrier mobility and electronic conductivity.[5] Consequently, these materials find application mainly in electronics such as PVDs, FETs and LEDs.[7–9] Whenever they are used in such devices, the size and shape of the aggregates influence deeply the final properties, therefore the optimization passes through control of their aggregation and dimension.[10] Mastering size and shape can be achieved with gel chemistry, utilizing hydrogen bonding and π-π stacking as the main forces to create supramolecular architectures from nano to microscale dimensions.[11]

3. Perylene bisimide hydrogels

In a gel, the gelator is just the minor component, the majority of the volume is filled by gelled solvent. Therefore, the nature of the solvent is fundamental for the final properties. Small changes in polarity, behavior of functional groups, hydrophobic-hydrophilic interactions, viscosity etc. will result in big differences at the macro scale in the final product.[12,13] Since the solvent needs to disrupt the hydrogen bonds between the gelators, also temperature is a variable that must be monitored. Indeed, the solvent has to favor the inter-gelators interactions and assist the nucleation and growth of the self-assembly.

As it appears now clear the importance of the chemical structure of the gelator and the kind of solvent, most of the π-π gels are formed in non polar or lowpolar hydrocarbon solvents. In less cases polar or aqueous media are good candidates for the gelation process. However, the latter are the most interesting for today's application and have been be applied to hygienic products , agriculture, drug delivery systems, sealing, coal dewatering, artificial snow, food additives , pharmaceuticals, biomedical applications, tissue engineering and regenerative medicines, diagnostics, wound dressing, separation of biomolecules or cells and barrier materials to regulate biological adhesions, and biosensor.[14–18]

3.1.2. How to design a gelator

It happens frequently that most of the gelators are found by serendipity rather than by design. However there are some particular requirements that molecules and their self-assembly need to fulfill in

order to be good candidates as new gelators since they have to promote formation of 1D aggregates via anisotropic growth process, intertwining of 1D fibers to form 3D networks and prevention of crystallization or precipitation of the aggregate.[6,19] Consequently, new gelators are designed with features that are known to induce aggregation, however the variables that must be taken in account are numerous and the research of π-π gelling agents is still a challenging task. The information collected from a variety of different types of gelators made possible a rationalization of the requirements molecular gelators have to match: i) multiple hydrogen bonds with specific directions and rigidity, ii) presence of aromatic core that helps π-π stacking iii) dipole-dipole and donor-acceptor interactions iv) a long alkyl chain with optimum length to maintain the equilibrium between precipitation and solubility. In most of the cases, more than one structural requirement is fulfilled, even though there can be exceptions. Once selected the right gelator, different processes can lead to gelation. A warm supersaturated solution of the gelators can be cooled down at room temperature to promote nucleation and growth. Otherwise, basification or acidification of the media can strengthen the H-bonds and foster aggregation. In other cases, the addition of a second solvent or a salt is necessary to start gelation.

PBIs have strong π-π interactions and can be easily functionalized at the imide positions to add the appropriate functional groups to promote gelation or to tune the solubility.[20] Consequently, it is no surprise that, in literature, various PBI gels are reported mainly as organogels.

3.1.3 PBI Gels

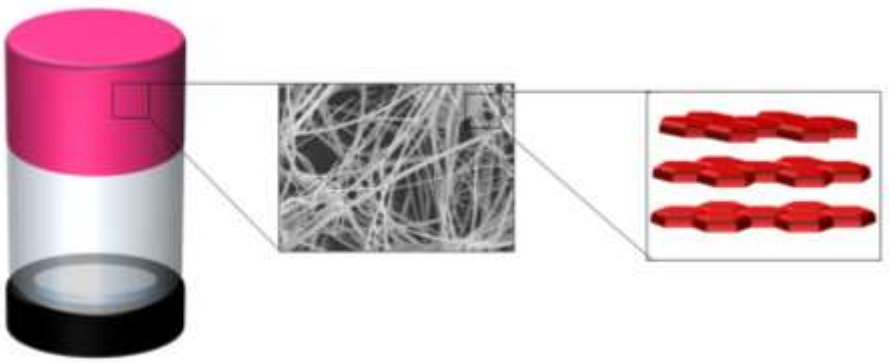

Figure 3.1 Scheme of PBI hydrogel structure

A first interesting case are the cholesterol functionalized PBI derivatives **23-26** whose gels showed cascade energy transfer when mixed together. As reported by Shinkai,[21] in a mixture of p-xylene/1-propanol, the gel formed was very stable above 0.5 wt/vol%. AFM and SEM images revealed a network structure composed of fibers, with the smallest having a diameter of 3 nm, which is comparable with the length of the molecular axis of the PBI. The emission of **23** in the green region is quenched to a 67% when mixed with **24**, 53% with **25** and 34% with PBI **26**. The data are in accordance with the decreasing of the D-A spectra overlap. When the corresponding thiophene derivative is added to **23** they form a self-sorting organogel of two different π-π coniugated molecules with π-n heterojunctions.[22] Wurthner synthesized a PBI (**27)** with long aliphatic chains through urea moieties.[23] The urea units are instrumental to direct the H-bonds and to form stacks separated from

perylene cores. Indeed the gelator works the best in CCl_4 (1.0 wt/vol%) and does not form gels in polar solvents like DMSO and methanol. AFM showed fibers-like structures with little branching with a diameter ranging from 30 to 100 nm. These big aggregates

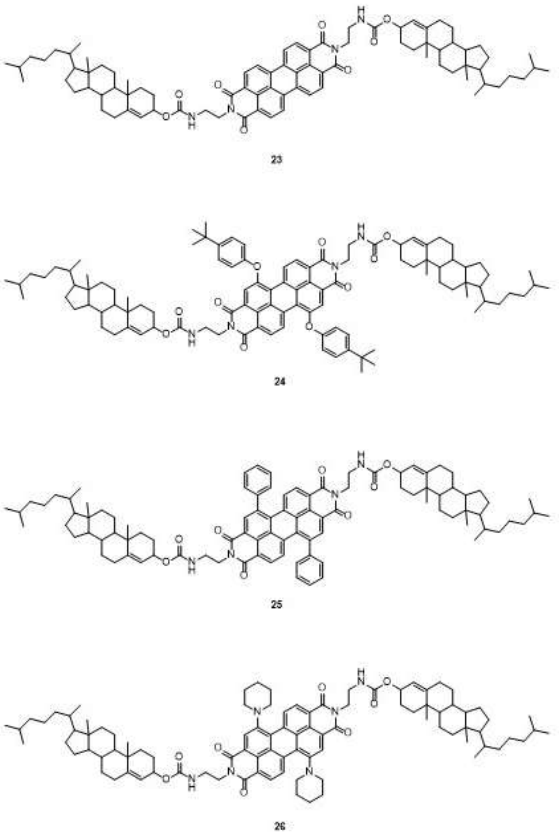

Figure 3.2 Structures of PBI gelators

are probably formed by small filaments aligned. In a similar case, the

replacement of the urea units with imides, as in **28**, shows gelation in different organic solvents.[24] The spectral features of the aggregated dyes exhibit a close face to face stacking of the rotationally displaced perylene core along the π-π stacking. Studying the gelation process of perylene bisimides of **28-31**, that present progressively shorter more branched peripheral alkyl side chains, was instrumental to understand the aggregation mode from H- to J-aggregates. Investigation of the gelation, as well as of the optical spectra, revealed that PBIs with linear alkyl chains **28-29** form H-type supramolecular architectures and red gels, while branched residues lead to J-type ones and green gels. Remarkably, the fibrous structures observed at the AFM are quite similar, insignificantly influenced by the kind of gelator. The fibers are helical, with a mean height of 3.1 nm, 8.0 width and a pitch of 15.0 nm. The functionalization of the bay-positions distorts the planarity of the core and affects drastically the π-π stacking. If **28** shows H-aggregation, introducing tert-butylphenoxy substituents (**32**) ends up in a change from H- to J-type.[25] Moreover, weaker π-π interactions decrease the aggregation tendency in polar solvents and impose gelation at higher concentrations and, instead of fibers, less regular structures are observed. In some cases, the gelation process is induced by the interaction between different molecules.

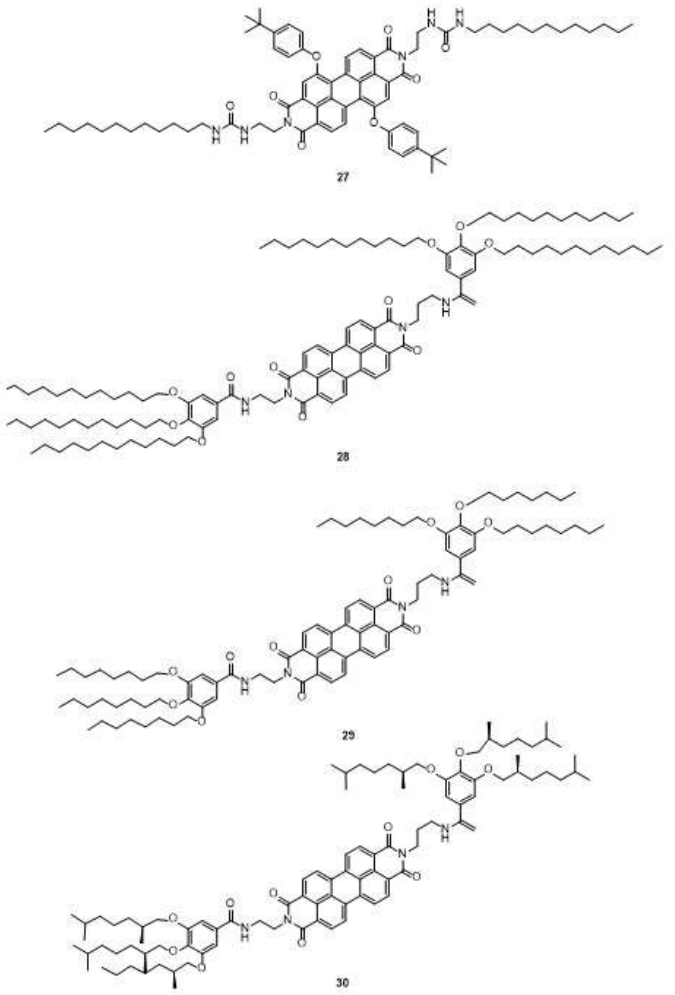

Figure 3.3 Structures of PBI gelators

For example, Yagai took advantage of the hydrogen bonds between cyanurates and melamines to fabricate gels with **33** and **34** .[26,27] **33** gelates once complexed 1:1 with N-dodecylcianurate, and forms a flexible gel. Similarly, **34**, in a mixture 1:1 with cyanurates, gelates in many non polar solvents. In analogous way, a PBI bearing melamines units with chiral chains mized 3:1 with

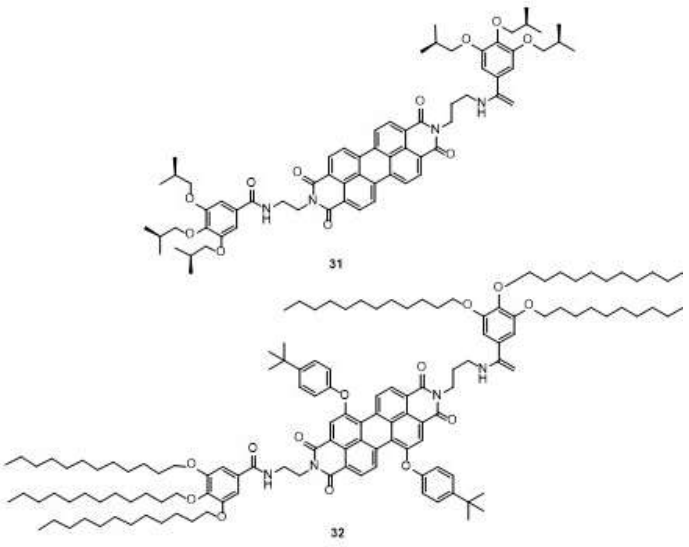

Figure 3.4 Structures of PBI gelators

cyanuric acid form helical columnar assemblies with extended chiral stacks that lead to gelation as confirmed by circular dichroism and time-resolved microwave conductivity.

Ulijn looked for new gelators between PBIs functionalized with dipeptides at the imide positions.[28] The π-π stacking and the hydrogen bonding are tailored depending on the nature of the aminoacids employed. In aqueous buffer they form achiral spherical aggregates but it forms chiral nanofibers both in DMF and DMSO that lead to gel formation.

3. Perylene bisimide hydrogels

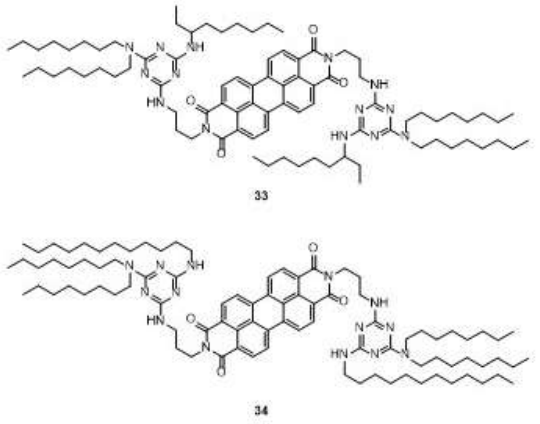

Figure 3.5 Structures of PBI gelators

As we mentioned in Chapter 2, the applications of PBIs have been limited for long time by their insolubility in polar solvents, mainly water. Side chains, at the bay or imide positions, have to shield sterically or electrostatically the π-π stacking and prevent the aggregation. On the other side, gelation requires self-assembly. The design of hydrogels, by far the most interesting group of gels for everyday applications, has to take in account both the requirements. Fortunately, the aqueous media offers some parameters that can guide aggregation in addition to temperature: pH and ionic strength. The majority of soluble PBI hydrogelators rely on polyethylene glycol (PEG) units as a water solubility-providing element. If PBIs are functionalized with PEG, the chains self-assembles to form extended supramolecular fibers and a hydrogel stable up to 70°C.[29] Further heating leads to reversible solvent expulsion and shrinkage of the gel without damages on the morphology. Leaving the shrunken hot

gel at room temperature, cooling it slowly down for a period of 24h, resulted in swelling of the material. This behavior is caused by a complex interplay between the hydrophobic interactions and the solvation of PEG chains at high temperature. Optical and electron spin resonance analyses indicated stimuli responsiveness towards reduction and oxidation to the reversible charging of the bipyridine bridge. Indeed the swelling process can be accelerated by addition of the reductant $Na_2S_2O_4$, which causes gel to sol transition, followed by gelation due to air oxidation. The PBI derivatives reported by Wurthner, differ only in a methylene unit at the end of the alkyl chain exhibiting same optical and aggregation properties, yet their lower critical solution temperature (LCST) is different.[30] Researchers exploited distinctive traits, to develop tunable temperature responsive hydrogels with PBI co-aggregates, that show a remarkable color change during LCST phase transition from dark red to bright orange-red that can be adjusted to any temperature in the range 26 °C - 51 °C depending on the ratio of the two dyes.

Another way to synthesize water soluble PBIs is the introduction of charged residues on the imide positions. For this purpose aminoacids suit perfectly, because, besides the mentioned properties, they provide specific molecular recognition, availability, functional flexibility and biodegradability.[31,32]

A PBI bearing a tetrapeptide on the imide position, which was designed to be molecularly dispersed at basic pH (above aspartic acid pKa) due the electrostatic repulsion among the carboxylic acids.

3. Perylene bisimide hydrogels

Gelation process is driven by lowering pH and protonation of the carboxylates. The final material is made by flat 1-D nanostructures ca. 2 nm in height without larger hierarchically ordered objects. The peptide unit can be separated by inserting a long alkyl chain, which forms a soft hydrogel with nanofibrillar network structure at neutral pH retaining high fluorescence.[33] Moreover, the material has shown semiconducting and photo-switching behaviour when exposed to white light.[33] A long and bulky peptide sequence is not necessary, several PBI-gelators functionalized by a single aminoacid are known. A PBI bearing an L-tyrosine unit at the imide position was reported as a remarkable semiconducting, photo switching material. The hydrogel, in the range 5.0 - 9.0 pH, shows photocurrent increase upon light irradiation making it a promising ON-OFF semiconductor for applications such as photodetector and photovoltaic cells.[34] Addition of potassium perylene-3,4,9,10-tetracarboxylate to PBI(tyrosine) strengthen the hydrogen bonds lowering the minimum gelation concentration.[35] Remarkably, also PBIs terminated with phenylalanine, leucine, isoleucine, cysteine and methionine were tested but none of them forms gel in the same conditions.

Other aminoacids have given satisfying results, as in the case of B-alanine. The PBI so functionalized at the imide position, formed nanofibers via pH triggered hydrogelation route.[36] The authors hypothesized an ordered nanofibers structure interconnected by perpendicular hydrogen-bonds. The so produced nanofibers exhibit strong fluorescence polarization and one-dimensional charge transport because of the π-π stacking. Cowan presented a

mechanistic study for a similar dye exploring the factors that control charge separation both in solution and as dried film in order to prove the viability of these materials in OPV heterojunction.[37] Since the gel showed photoconductivity in water but not in the dried state, it was proposed that it is the alanine functionality that acts as an electron donor.[38]

3.1.4. Aim of the project

Whereas we previously listed a number of PBI gels, there is still a lack of knowledge about the precise structure of these materials and, in particular what happens to the aggregates present in solution while the gel is forming. Herein, we presents new insights into the physical and chemical nature of long-range conductivity in perylene-based hydrogels and show that control of this charge-transfer mechanism can be used for sensing applications. We report a comprehensive structural framework of the pH-triggered hydrogel using single-crystal diffraction, mechanical, spectroscopic, scattering, imaging and computational techniques and we provide evidence for solvent-mediated inter-backbone charge transfer in PBI hydrogels. We reconstruct the underlying structural motif over a wide length-scale ranging from crystalline ribbon-like nanostructures, which act as the electronic and structural backbone, to their macroscopic arrangement. We find macroscopic conductivity of the dried gel only in the presence of a polar vapor, revealing the importance of inter-backbone hydrogen-bonding as charge-transfer bridges. We use this effect in gas-sensing devices that enhance electronic conductivity by five orders of magnitude within milliseconds response to polar vapor concentration. The awareness of this inter-backbone charge-transfer mechanism is not only crucial to understand and design PBI-based hydrogels, but also to exploit the full potential of chemically related nano-crystalline hydrogel-based devices.

3.2 Results and discussion

3.2.1 The precursor

We synthesized *N*,*N*'-bis(propanoic acid)-perylene-3,4,9,10-tetracarboxylic bisimide (**PBIK**) using a microwave-assisted protocol introduced in chapter 2.2 and prepared a 8.8 mM **PBIK** precursor in basic (pH 10) aqueous triethylamine (TEA) solution.[39] To

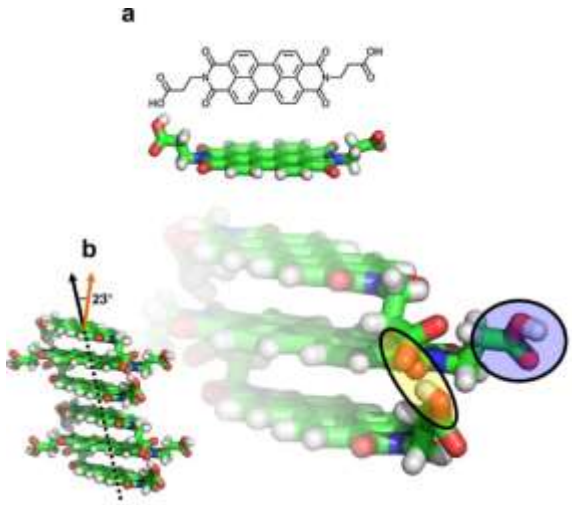

Figure 3.6 Structural characterization of **PBIK** at the nanoscale**. a**, Representation and graphical model of the **PBIK** molecule. **b**, Molecular model of the π-π-stacked columns found in the crystal structure, illustrating the 23° difference between column axis (black arrow) and the direction perpendicular to the **PBIK** core (orange arrow). The magnified view highlights the intra-columnar hydrogen bonding between carboxylic groups within the characteristic **PBIK** triplet (yellow circle), leaving one sandwiched carboxylic group unbound (blue circle).

understand the molecular interactions of **PBIK** under these conditions, we obtained crystallographic data of single crystals grown from the precursor (for details see single-crystal analysis in the experimental section). In its single-crystalline form, **PBIK** forms typical π-π-stacked columns as shown in Figure 3.6b and Figure 3.7.

Within these columns, the molecules are both longitudinally and transversally shifted so that the stacking direction is tilted by 23° away from the direction perpendicular to the perylene plane (Figure 3.6). The tilted axis is most likely caused by intra-columnar hydrogen-bonding between the carboxylic groups, resulting in sandwiched **PBIK**-trimers (yellow circle Figure 3.6b and Figure 3.7). This motif leaves two unused carboxylic acids per triplet, which offer binding moieties capable of cross-linking between longitudinal neighboring columns (blue circle in Figure 3.6b). In addition, the hydrophobic interaction between units of the perylene core causes transversal attraction between the stacks to minimize the core's exposure to the polar medium. This single-crystalline motif, in particular the columnar arrangement of **PBIK**, is the structural cornerstone for the following sections.

3. Perylene bisimide hydrogels

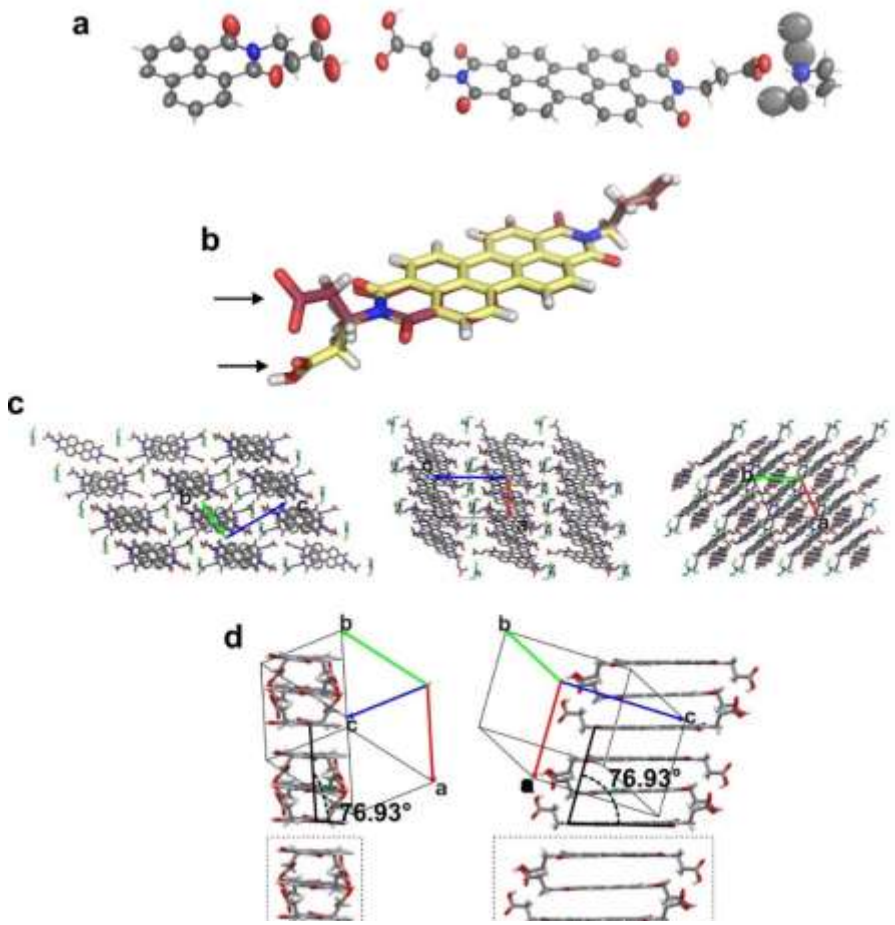

Figure 3.7 **Single-crystal structure for PBIK as retrieved from x-ray diffraction. a,** Ellipsoid representation of 1.5 **PBIK** molecules according a single unit-cell content (50% probability). Disordered conformations of the TEA cation and one carboxylate group omitted for clarity. **b**, Overlap of the two crystallographically independent **PBIK** molecules found, showing different protonation states and different carboxylate arrangement (see black arrows). These conformational differences reflect different hydrogen bond interactions of the two moieties. **c,** Crystal packing views along a, b and c unit cell axes, of triclinic **PBIK** crystal form. TEA cations are represented with green sticks. Disordered conformations and hydrogens are omitted for clarity. **d,** Perpendicular views of the π-π columns in respect to the unit cell. The measured angle of less than 90° reveals that **PBIK** is not perpendicular to the stacking direction and therefore to the column axis. In this representation, the columnar building-block, the **PBIK** trimer, is clearly visible (black rectangle).

4.2.2 Gel formation and characterization.

Acidifying the basic precursor solution of **PBIK** with 4 M aq. HCl to pH 4 commences the gelation process. After an aging period of approx. 4 min, the liquid precursor transforms into a gel-like substance that it is capable of holding its own weight in a glass vial (Figure 3.8). Oscillatory rheometry analysis of the gelation process (Figure 3.8) shows a rapid increase in storage modulus G' up to 3-4 kPa within the first 10 minutes, and then a further slow increase up to 20 kPa within the first hour. Frequency sweep analysis confirms viscous and elastic moduli independence from applied frequency, as expected for a hydrogel, while stress sweep analysis confirms an extended linear viscoelastic regime up to values above 100 Pa of applied stress. Differential scanning calorimetry (DSC) of the final gel reveals a remarkably high gel-to-sol transition temperature with an onset at 83.7 ± 1.0 °C, and an endothermal peak, corresponding to the melting temperature T_m, at 91.9 ± 1.1 °C (Figure 3.8).

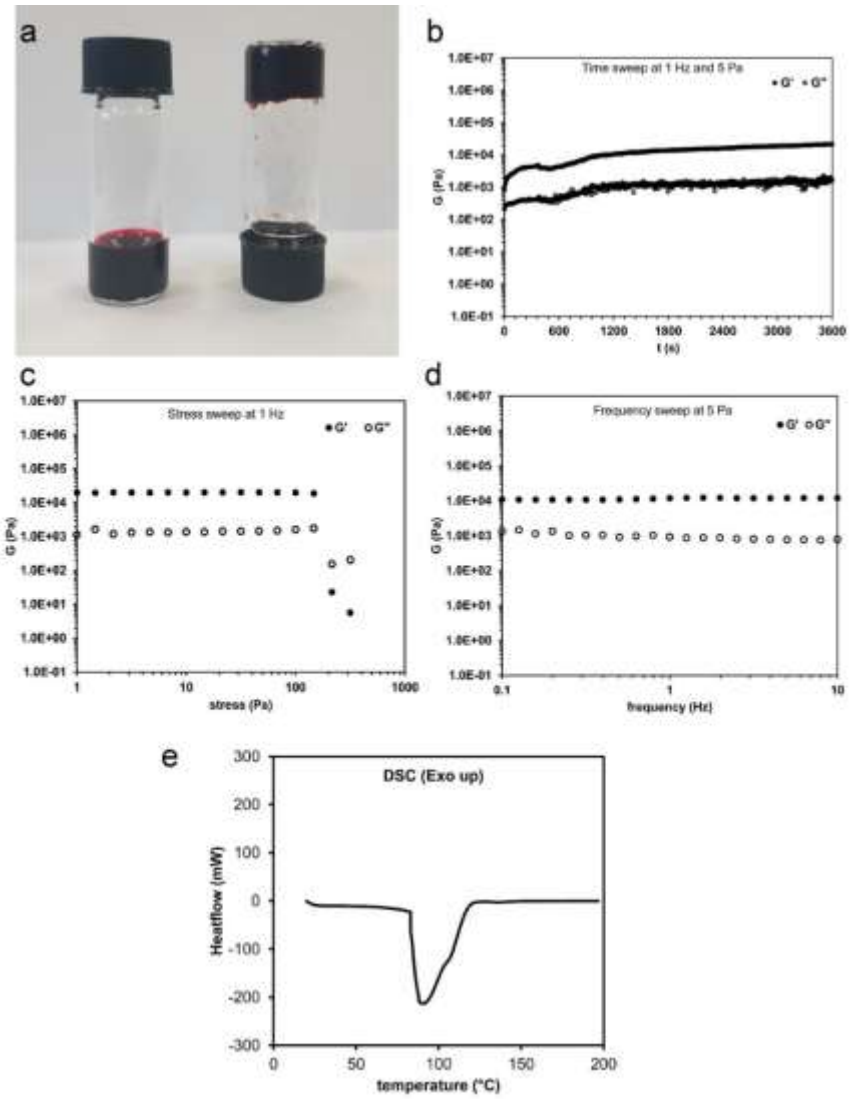

Figure 3.8 Mechanical analysis of the PBIK hydrogel. a, Photograph of **PBIK** in the precursor state (left) and after the gelation process (right), showing that the hydrogel is capable of holding its own weight. **b,** Oscillatory rheometry measurements performed during the gelation process. **c,** Stress-sweep, identifying the linear- viscoelastic region of the hydrogel well above 100 Pa. **d,** Frequency-sweep, confirming independence of elastic and viscous moduli from the applied frequency. **e,** DSC measurement, revealing a gel-sol transition with an endothermic minimum at T_m = 91.9 ± 1.1 °C.

Gelation changes the sample color from dark red to black/dark brown (Figure 3.8). This color change suggests a structural reorientation and electronic states alteration, in accordance with the general structure-function relation in molecular photodyes, such as **PBIK**.[40] To understand this transition, we investigated the optical and structural nature of precursor and hydrogel by means of UV/Vis absorption, small angle-x-ray scattering (SAXS) and cryogenic transmission electron microscopy (Cryo-TEM) (Figure 3.6 and Figure 3.9-3.11).

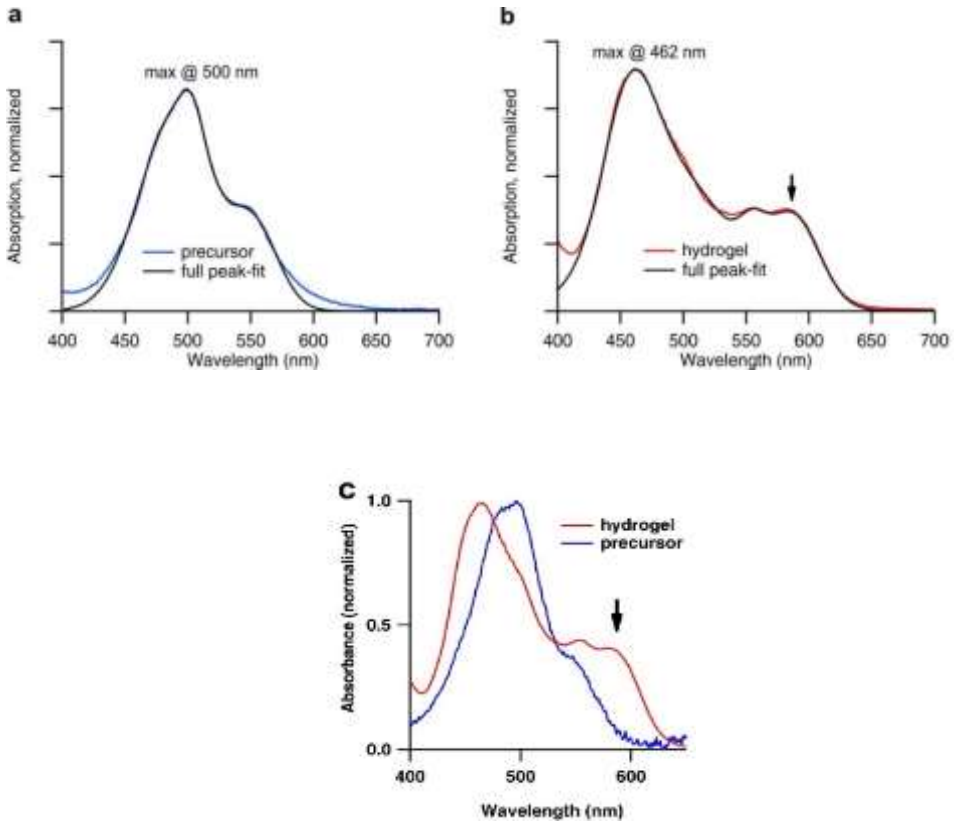

Figure 3.9 Peak-fit analysis of the UV/VIS absorption spectra. **a**, UV/VIS absorption spectrum of the **PBIK** precursor. The absorption maximum is found at 500 nm whereas the blue-shifted absorption shoulder is in agreement with literature.[6] **b**, UV/VIS absorption spectrum of the **PBIK** hydrogel, fitted using four Gaussian peaks. Upon gelation, the absorption maximum blue-shifts to 462 nm. An additional peak at 588 nm arises (black peak). UV/Vis absorption spectra of the **PBIK** precursor solution before addition of HCl (blue) and in the hydrogel (red) state. The black arrow indicates the absorption peak characteristic of the J-band for aggregation in the hydrogel.

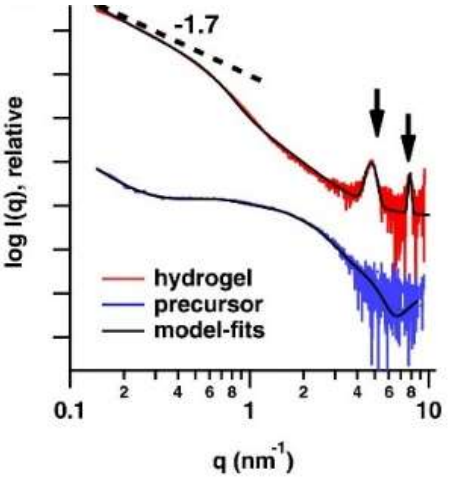

Figure 3.10 SAXS patterns corresponding to the UV/Vis absorption measurements in Figure 3.9, together with the full-pattern refined model-fits (black). The two black arrows indicate the positions of Bragg-peaks, characteristic for the nano-crystalline nature of the hydrogel

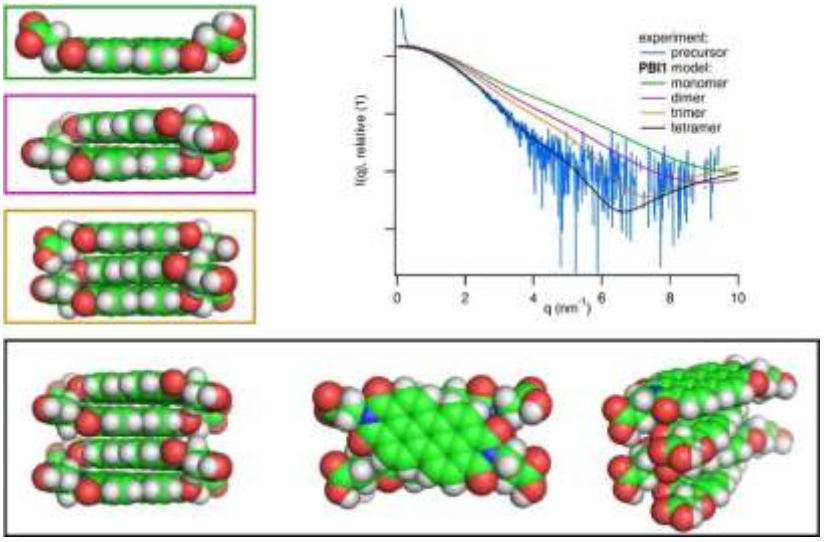

Figure 3.11 Structural analysis of **PBIK** in the precursor state from SAXS data. We built consecutive models of *H*-type stacked **PBIK** aggregates, i.e. monomer (green), dimer (violet), trimer (gold), tetramer (black) from which we calculated the theoretical scattering patterns using CRYSOL[41]. The best agreement between experimental and model data is found for the case of tetramers.

3. Perylene bisimide hydrogels

Generally, perylene bisimides exhibit a fine vibronic structure of the main electronic transitions. Yet, molecular aggregation induces strong exciton interactions between neighboring chromophores, which not only suppresses the monomeric fine structure but also leads to new absorption bands.[42–44] In case of the precursor solution, we observe the absorption maximum at 496 nm together with a weaker, red-shifted *J*-band at 554 nm (Figure 3.6, blue trace and Figure 3.9 for peak-fit). Such a spectrum results from H-type exciton coupling – a typical observation for perylene bisimides in solution, liquid-crystalline mesophases and spin-coated films of columnar π-π-stacks.[42–44] Gelation of the precursor causes a blue shift of the absorption maximum from 496 to 466 nm (Figure 3.6, red trace and Figure 3.9b for peak-fit).[45–47] We further observe the appearance of a new peak at 585 nm (see black arrow in Figure 3.9) – a behavior that has previously been linked to re-orientation or translation of π-π-interacting perylene bisimide cores.[48,49] Thus, UV/Vis suggests the gelation process to cause a change in the transition type, possibly related to a shift of the stacking direction away from the axis perpendicular to the **PBIK** molecular core or a change in the angle between the transition dipole moments of **PBIK**.[48,49]

To obtain more direct information on the structural motif of the **PBIK** in the precursor, the transition during gelation, and the final gel, we performed SAXS measurements. The scattering data of the protonated precursor state (basic aqueous solution) shows a low–q transition to the Guinier regime (q^{-0}), which is characteristic for form-

factor scattering of non-aggregated particles (Figure 3.6). To model the pattern, we used a single **PBIK** molecule from the single-crystal structure to build a series of progressively stacked *H*-type arrays (more details about the modelling are given in the section “SAXS model fitting” in the experimental section). Best agreement between model and data was found for π-π-stacked tetramers (Figure 3.11), and full pattern refinement suggests 4 nm mean distance between the tetramers (Figure 3.6, black trace). It should, however, be noted that the tetrameric conformation only represents a *mean* observation, where in fact a series of other conformations, such as *e.g.* trimers, tetramers, decamers, etc., are present in solution.[50] Thus, the hydrophobic attraction of the perylene cores causes short column-like assemblies, in agreement with literature and the UV/Vis measurements.

We recorded the structural transition from precursor to hydrogel using *in-situ* SAXS measurements during the gelation process (Figure 3.11) and found two distinct phenomena. First, the strongly increasing scattering intensity in the low–*q* regime ($1 < q < 2$ nm^{-1}) signals a growing structural motif. Second, the two diffraction peaks that form in the mid–*q* regime ($4 < q < 5$ nm^{-1}) result from crystalline ordering. The comparison of the integral intensities of the two reciprocal space regions connects these named mechanisms (Figure 3.11). Analyzing the SAXS pattern of the hydrogel (Figure 3.10, red trace) in more detail shows as the most striking difference to the precursor the transition in the low–*q* region: the power-law slope has increased from q^{-0} to $q^{-1.8}$. Such a behavior characterizes

the presence of a two-dimensional motif, such as, sheet- or ribbon-like structures with internal disorder and porosity (q^{-2} slope in the case of a solid sheet-like structure). The Guinier fit reveals an approximate sheet thickness of 5 nm (see SAXS model fitting in the experimental section for more details). Transmission electron microscopy (TEM) images taken under cryogenic conditions (Cryo-TEM) show a similar motif (Figure 3.6 and 3.12), whereas the ribbon-like nanostructures act as the structural backbone through cross-linking between them. Atomic force microscopy (AFM) images of a drop-casted sample confirm a ribbon thickness of approx. 5 nm (Figure 3.13).

The SAXS pattern of the final hydrogel shows two distinct peaks as indicated by the black arrows in Figure 3.6. These peaks are caused by a recurrent structural motif in the hydrogel and can hence be used to reverse-engineer the molecular architecture. The wide-angle X-ray diffraction (XRD) pattern (Figure 3.8) presents five strong reflections in addition to three weaker. This scattering pattern compared with single-crystal pattern from the precursor (Figure 3.14) immediately identifies only one consistent structural feature: the strong peak at 18.28 nm^{-1} linked to the π-π-stacking between perylene cores within a single **PBIK** column (Figure 3.8). Other reflections seen in the single-crystal scattering are not found in the hydrogel scattering, suggesting a different arrangement of the prevailing π-π-stacked columns in the hydrogel compared to the single-crystal. Indeed, all but the latter two reflections can be indexed using a two-dimensional oblique ($p1$) lattice[5] with a = 2.188 nm, b =

1.367 nm, and γ = 36.14°. The peak at 18.86 nm^{-1} following the characteristic π-π-stacking peak is most likely caused by a vertical misalignment between the π-π diffraction planes of neighboring columns.

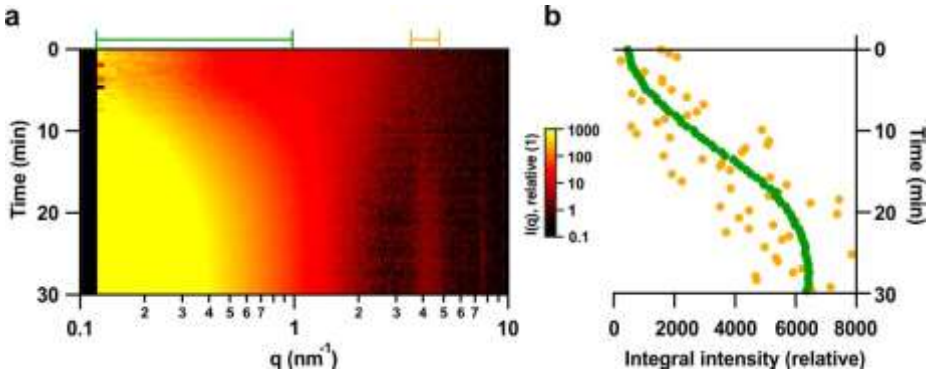

Figure 3.11 In-situ SAXS during the gelation process. Scattering intensity map as a function of time. Two separate phenomena are witnessed: 1) **a** strong increase in intensity in the low-q regime (green bar) and 2) the formation of a diffraction peak in the mid-q region **b,** Integral intensity calculated over these regions shows that the two phenomena are linked.

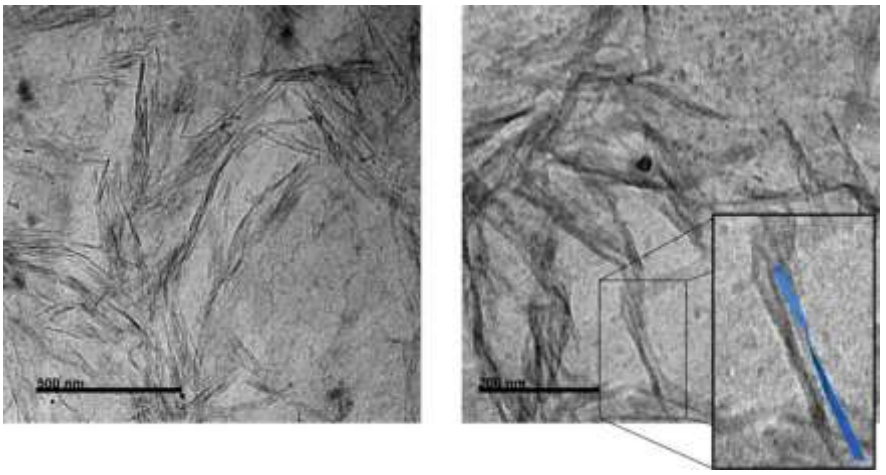

Figure 3.12 CryoTEM images of the hydrogel**.** Both images are magnifications of the representative images shown in Figure 3.6. Comparison of a single strand with a characteristic twisted ribbon confirms the ribbon-like nature of the hydrogel.

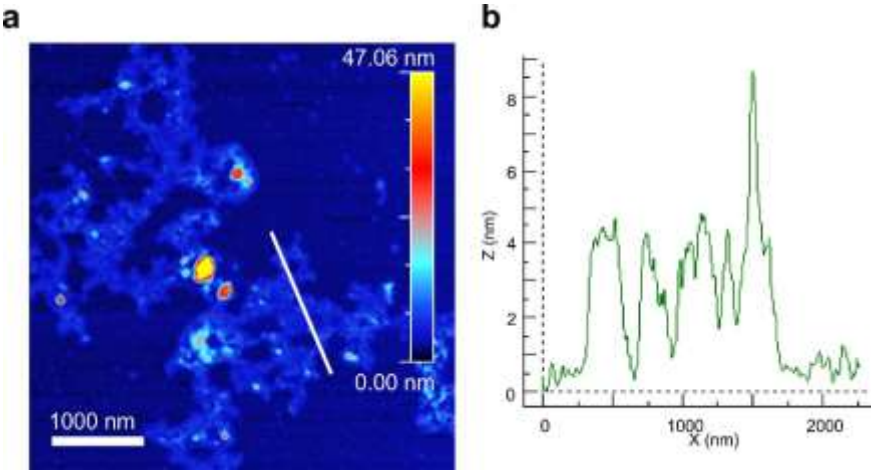

Figure 3.13 AFM analysis of the **PBIK** hydrogel, spin-coated on a Si wafe**r. a,** AFM image showing a 2D, ribbon-like coverage-area. **b,** Vertical profile along the white line shown in **a**, revealing a sheet/ribbon thickness of approx. 5nm.

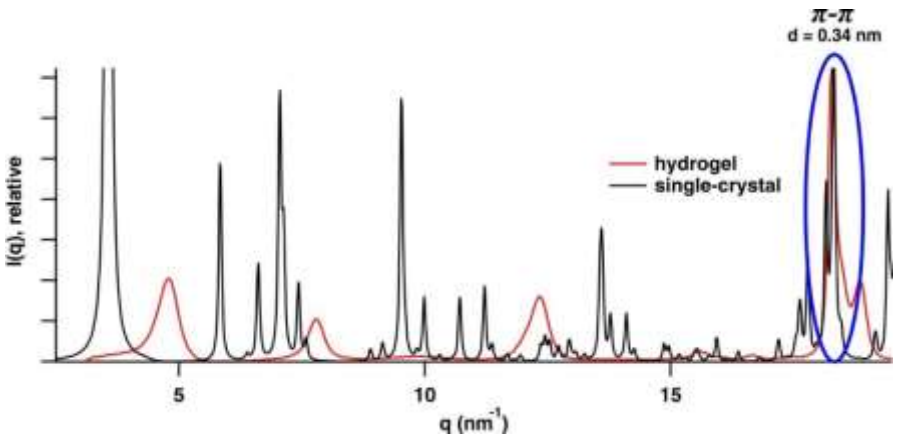

Figure 3.14 XRD comparison of hydrogel and single-crystal. A detailed overlay of the wide angle scattering pattern of the hydrogel (red) and the scattering pattern of single-crystal immediately identifies only one consistent structural feature: the strong peak at 18.28 nm^{-1} (blue circle) is indicative of the π-π-stacking distance between perylene cores within a single **PBIK** column. In the angular regime between $2 < q < 19$ nm^{-1} no other similarities between the two scattering patterns are apparent. This clearly indicates different structural motifs for both phases, the single-crystal and the hydrogel.

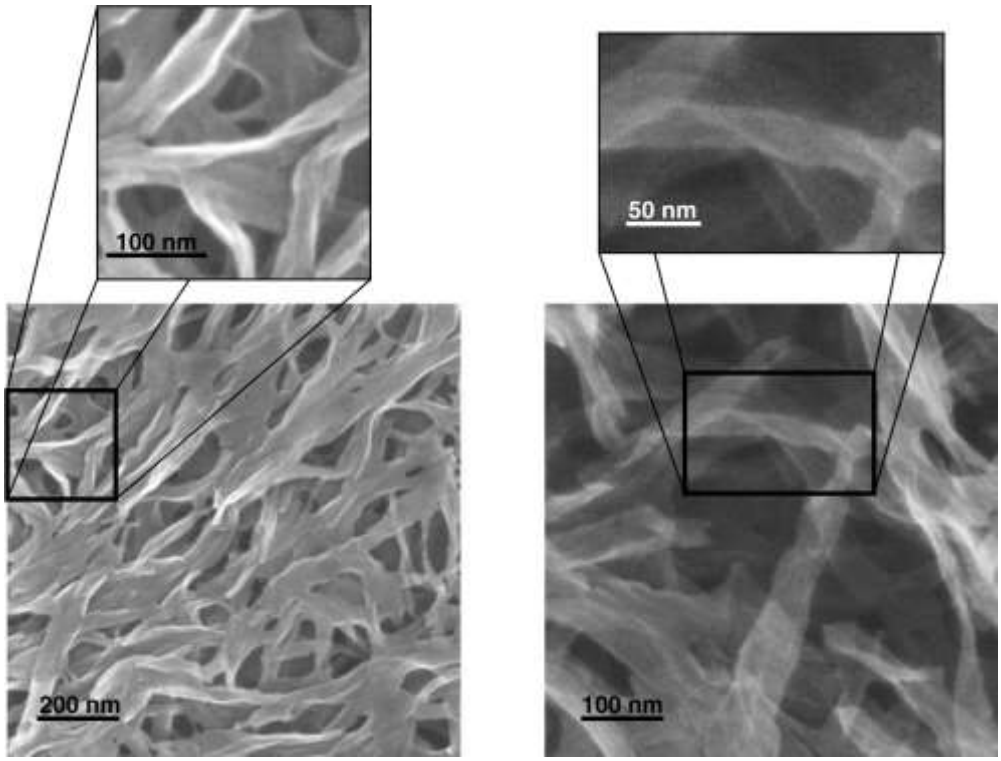

Figure 3.15 Detailed SEM analysis of the dried hydrogel. Magnified SEM images of the drop-casted and dried hydrogel. The images show, for one, the branched nature of the hydrogel network and, for the other, confirm that the **PBIK** nano-ribbons are conserved even after drying.

3.2.3. Structural model

Single crystal- compared to hydrogel-scattering implies that only the intra-columnar *π*-*π*-stacked motif previously found in the single-crystal (Figure 3.8) is preserved in the gel state. Consequently, the oblique unit cell dimensions determined by XRD measurements relate to mean distances between these *π*-*π*-stacked columns. We take advantage of this circumstance and use a single molecular column from the crystallographic structure to build a structural

model. By doing so, the columnar cross-section only fits inside the hydrogel unit cell if both long axis are aligned parallel (Figure 3.8). The full structural arrangement then becomes apparent by multiplying the unit cell using its oblique dimensions. The resulting model compared to the single-crystalline structure is shown in

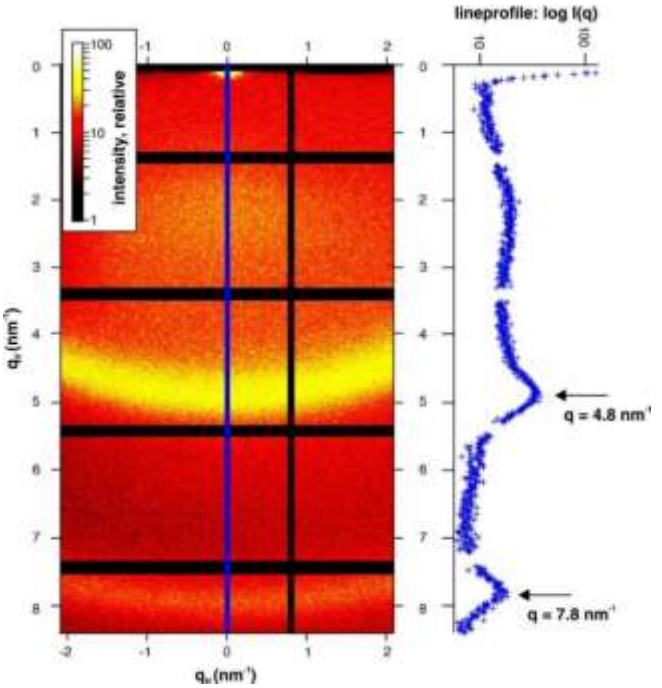

Figure 3.16 GISAXS analysis of the dried hydrogel. GISAXS scattering image of the dried hydrogel to investigate the structural stability of the hydrogel after drying. Two scattering rings are found in the GISAXS image. From a vertical line-profile (blue line - width of Δq = 0.2 nm^{-1}) we determine the exact peak positions of 4.8 and 7.8 nm^{-1}. As the same two peaks are found in the scattering pattern of the undried gel (see Fig. 2d and peaks 1 and 2 in supporting table 4) the structural motifs are similar in both, the undried and dried, cases is consistent.

Figure 3.8, revealing a similar structural motif in both cases: the columns appear to cross-link preferentially between the now protonated carboxylic groups. Yet, the distance along this direction is identical, leaving polar channels for water to penetrate. In lateral

direction, the oblique unit cell angle decreases from 54.78° to 36.14°, resulting in a linear alignment of neighboring imide groups. Infrared spectra confirm this arrangement: the peaks related to both the carboxylic and amidic C=O distances red-shift due to increasing peripheral interaction, such as hydrogen bonding (Figure 3.17). This suggests hydrogen bonding between these moieties instead of electrostatic repulsion between the carbonyl oxygen atoms. Hence, the hydrogel consists of **PBIK** nano-ribbons with high crystalline order (Figure 3.8). A crucial side effect of this crystallinity is that the nano-ribbons are encapsulated by the carboxylic chains. These chains cross-link *via* hydrogen bonds and are therefore responsible for the structural cohesion between nano-ribbons

Figure 3.17 AR-FTIR measurements of PBIK before (blue) and after (red) the gelation process. a, FTIR spectrum over the accessible wavelength range. The

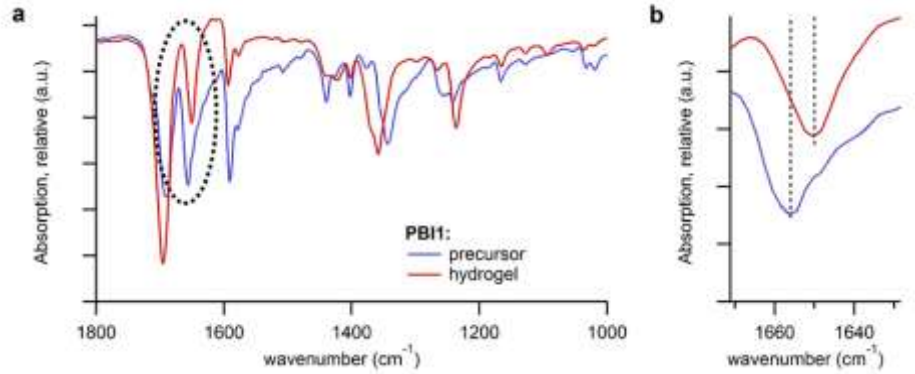

black dotted circle marks the C=O double bond of the **PBIK** imide group, whereas the detailed view is shown in **b**. **b**, Zoom-in of the peak corresponding to the C=O double bond of the **PBIK** imide group. As indexed by the black dotted lines, there occurs a red-shift and therefore weakening of the C=O bond upon gelation. This suggests increase in the peripheral interaction due to the close-packed nature of **PBIK** within the crystalline nano-ribbons.

3.2.4 Electrochemistry

To probe the accessibility of the imide groups and to derive additional information of the nano-ribbons inner structure, we performed CO_2 absorption measurements. A variety of organic pigments, including imides, has been shown to absorb CO_2 at carbonyl positions to form semicarbonates.[51–54] This phenomenon is directly seen in the redox properties of the pigments and can therefore be probed by cyclic voltammetry (CV). A CV of the precursor **PBIK** in by N_2 flux deaerated aqueous solution shows two reduction processes centered around –0.3 and –0.7 V vs. Ag/AgCl, which correlate to the reduction of the carbonyl moieties (Figure 3.20). This redox activity disappears after purging the solution for 10 min with CO_2, which indicates the formation of the related semicarbonate. The latter is not electrochemically active in the potential window between 0.2 and –0.8 V. The same measurements obtained of the hydrogel yield a strikingly different result (Figure 3.20). The voltammograms are unaffected by the presence of CO_2 and show, both under N_2 and CO_2 atmosphere, a reversible redox couple centred around –0.3 V. This indicates that the imide groups are blocked by the close, intermolecular arrangement within the crystalline nano-ribbons, such that CO_2 cannot access the absorbing atomic sites. This effect emphasizes the importance of the structure-function interplay and further corroborates the molecular model of the hydrogel in Figure 3.8.

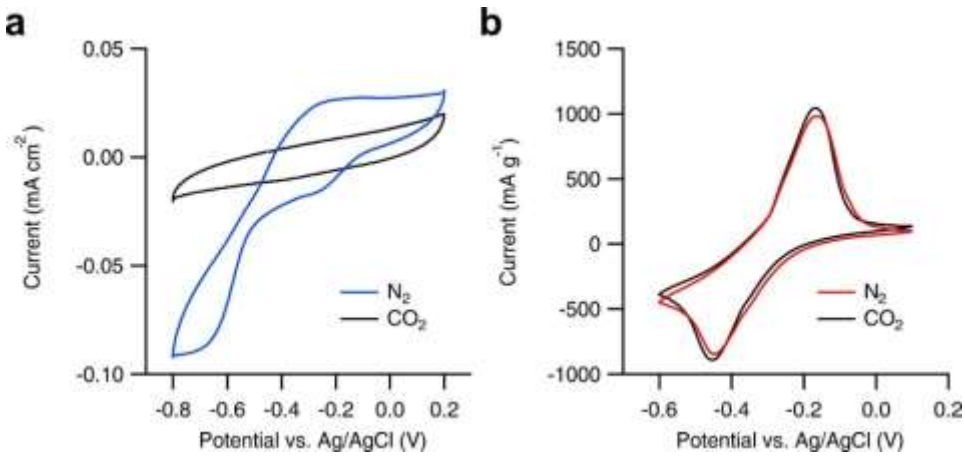

Figure 3.18 CO_2 absorption by the PBIK and the hydrogel. a, Cyclic voltammograms of the **PBIK** precursor solution when N_2 purged (blue) and after 10 min purging with CO_2 (black) at a glassy carbon working electrode. **b**, Cyclic voltammograms of the immobilized hydrogel under N_2 (red) and CO_2 atmosphere (black). All measurements were recorded at 50 mV s^{-1}.

3.2.5 Inter-ribbon charge transfer.

The crystalline nature of the nano-ribbons is of particular importance for long-range charge-transfer as it enables charge-mobility along the π-π stacked columns.[55,56] However, this mechanism is only one-dimensional. Bulk-conductivity over all three dimensions therefore requires lateral charge transfer, that is between the π-π stacked columns and further between the crystalline nano-ribbons. Since both, the π-π stacked columns as well as the crystalline nano-ribbons, are inter-connected *via* hydrogen-bonding, charge-transfer between two entities must occur via bridging sites. If this hypothesis is correct, absorbing protic media should be able to activate the hydrogen-bridging sites and therefore allow long-range charge-transfer.

To investigate these lateral inter-columnar charge transfer mechanisms, we fabricated simple gas-sensing devices by drop-casting a **PBIK** hydrogel film between two Au electrodes on a glass substrate as detailed in the Methods. The electrode spacing of 300 µm is unlikely to be bridged by a single hydrogel ribbon and thus this setup measures overall bulk-conduction including inter-backbone conduction. SEM images and grazing incidence SAXS (GISAXS) measurements confirm that the hydrogel-characteristic nano-ribbons as well as the intermolecular motif remain intact after drying (Figure 3.20-3.21). In a dry state, the current through the hydrogel is as low as 2 pA at a bias of 2 V. When the sample was repeatedly exposed to 300 ms pulses of H_2O saturated air using a custom gas-flow setup (see illustration in Figure 3.21), the current increased by nearly five orders of magnitude to 93.3 ± 3.3 nA (Figure 3.21). We probed the response time to humidity changes using 100 ms pulses, which led to a sharp rise in current within 10s of ms and re-equilibration to the dry conditions within two seconds (Figure 3.21).

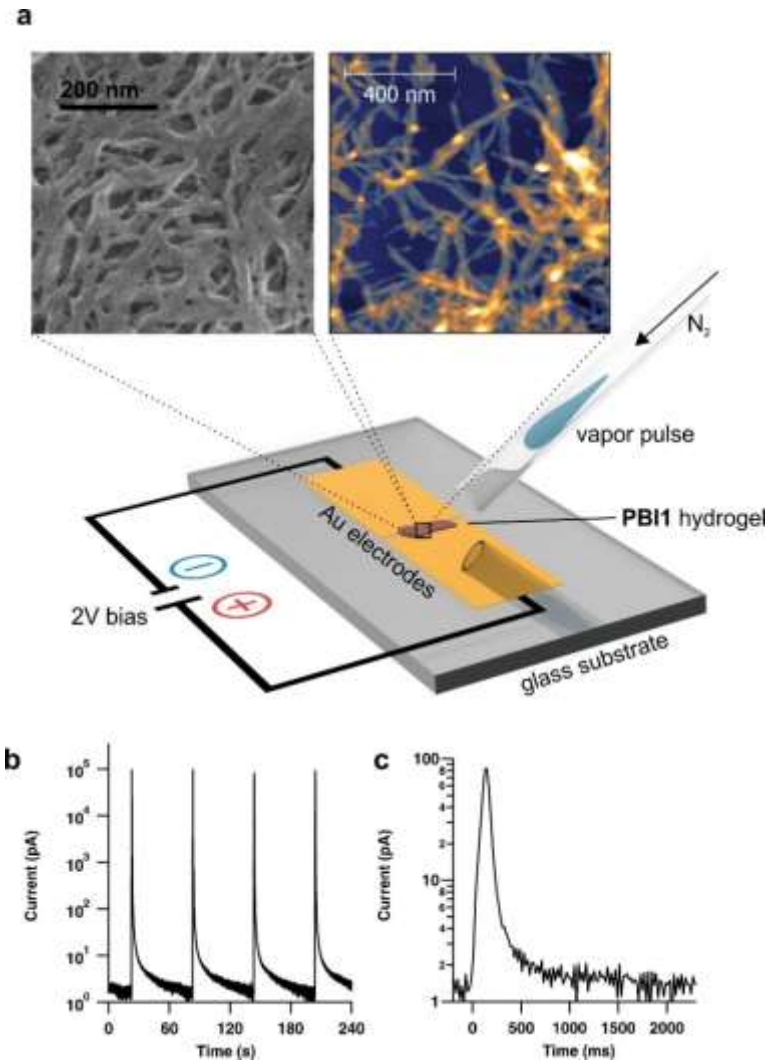

Figure 3.19 Electric response of the dried hydrogel to polar vapor. a, Schematic representation of the experimental setup together with AFM and SEM image of the dried hydrogel, confirming the ribbon-like nature of the hydrogel also in the dried state. **b**, Electrical response after deposition of 300 ms pulses of saturated H_2O vapor, showing an increase of conductivity over 5 orders of magnitude. **c**, Time-resolved electrical response of a single 100 ms pulse of saturated H_2O.

We attribute this behaviour to the solvent-induced activation of the *lateral* inter-columnar charge transfer. We stipulate that the previously determined carboxylic groups are not only responsible for

the structural cohesion, but also act as conduction bridges between nano-ribbons. Water forms temporary hydrogen bridges between the nano-ribbons, allowing for charge transfer between them. Upon flushing the sample with N_2, the intercalated water is removed such that conduction between the nano-ribbons is suppressed.

3.2.6 Conclusions

Synthetic routes and theoretical calculations of amphiphilic perylene imide hydrogels are known in literature.[34,36] Despite the large number of works that appeared in the field of perylene bisimides gels,[28,33,57] only few examples presented hydrogels[58,59] and fewer provide experimental insights into the hydrogels structure.[60] However, it is so far unsubstantiated how precisely molecular interactions relate to the structural intermediate, the nano-ribbons, and how these nano-ribbons interact on a higher structural level. Consequently, it is unknown at which specific sites charge-transfer between nano-ribbons can occur and hence how long-range charge transfer within the gel is plausible. With the aim of closing this gap between the hydrogel structure and its properties, we present an experimental and theoretical consistent structural model for perylene imide based hydrogels, in particular the basic derivative *β*-alanine functionalized perylene bisimide **PBIK**.

Datar *et al.* suggested hydrogen bonding between adjacent carboxylic groups to be responsible for the gel-like nature of the hydrogel, however without concrete structural model.[36] By combining scattering, microscopic, electrochemical, and electrical

methods, we could construct a comprehensive structural model based on a hierarchy of structure-directing motifs. First, π-π-stacking is without doubt the characteristic structural motif to form **PBIK** columns. Second, the protonated carboxylic groups of **PBIK** are responsible for longitudinal cross-linking between the π-π-stacked columns. Third, from the X-ray scattering data we find the symmetric imide groups to be responsible for the lateral *in-plane* attachment between the π-π-stacked columns (Figure 3.8). We find confirmation for this structure in the CO_2 absorption measurements. While accessible in the precursor, the imide positions are structurally blocked in the hydrogel, such that CO_2 cannot access the carbonyl groups and cannot be absorbed. The X-ray scattering data provides further support for this arrangement of the π-π-stacked columns within the nano-ribbons, since other arrangements would result in different diffraction peaks for the unit-cell family.

This detailed structural framework allows understanding charge-transfer phenomena as a prominent feature of the hydrogel. We have shown that the nano-ribbon surface is mostly defined by dangling carboxylic groups looking to cross-link with neighboring sites. This cross-linking is responsible for the structural cohesion of the gel in aqueous media and provides mechanical deformability. The bonding sites are the only sites to give the structural vicinity for charge-hopping and they are very likely decisive for inter-ribbon charge-transfer. Hence, carboxylic groups of adjacent nano-ribbons form conduction bridges, responsible for the structural and electronic properties of the overall hydrogel.

We probed the cross-linking by measuring how the dried hydrogel's conductivity responds to polar vapor. Short water vapor pulses directed onto the dry hydrogel activate conduction bridges between the nano-ribbons as seen by a fast conductivity increase of almost five orders of magnitude. Upon re-drying of the gel with N_2 these bridges are broken up and long-range charge-transfer is impeded.

In conclusion, we reconstructed the structural motif of a pH triggered perylenebisimide hydrogel from scattering data and complementary methods and could derive an understanding of the charge-transfer mechanisms within the gel. We draw a precise structure-function correlation dominated by the electronegative carbonyl sites of the PBI. These groups are not only responsible for the mechanical properties of the gel, but also enable long-range charge-transfer within the gel's inner skeleton. The underlying conduction bridges can be passivated and reactivated by consecutive drying and exposure to polar solvent vapor – a working principle for gas-sensing applications.

3.3 Experimental section

3.3.1 Instruments and materials

All solvents used were of reagent quality and purchased commercially. All purchased starting materials were used without further purification.

Microwave-assisted synthesis

Microwave-assisted synthesis of perylene derivatives was developed using a *CEM Discover® S.* The pressure-resistant, tightly sealed quartz tubes were 3 mm thick with a volume of 10 ml and designed for microwave reactor.

Nuclear Magnetic Resonance (NMR)

1H spectra were recorded at 500 MHz on a *Varian VNMRS - 500 MHz*. All spectra were registered at 298 K.

UV/VIS Absorption

Uv/Vis measurements were carried out on an Agilent Cary60 spectrometer. Samples were placed between two mica-foils with 100 µm Kapton-foil spacer in between.

IR Spectra

IR Spectra were measured on Bruker ALPHA spectrometer in ATR mode by simple drop-casting of the solutions.

Atomic Force Microscopy

Atomic Force Microscopy (AFM) measurements of the drop-casted samples were performed using a Nanoscope V microscope (Digital Instruments Metrology Group, model MMAFMLN) in tapping mode in air at room temperature, using standard μmash® SPM probe (NSC15/AIBS) with tip height 12-18μm, cone angle <40° (Resonant frequency 325kHz, force constant of ~40N/m). Image analysis has been performed with WsXM software (Nanotec Electronica S. L.)[1]. The accuracy of the AFM diameter determination was improved by tip deconvolution. Considering the diameter of AFM tip and the larger dimensions of particles, we calculated real particle diameter from formula:

$$r_c = r\,(\cos\theta_0 + (\cos^2\theta_0 + (1+\sin\theta_0)(-1+(\tan\theta_0/\cos\theta_0) + \tan^2\theta_0))^{1/2})$$

where r is the particle radius, θ_0 is the mean half angle of the tip and r_c is the AFM radius of a particle, as seen in the image.

Atomic Force Microscopy (AFM) measurements of the drop-casted hydrogel were taken on a MultiMode V AFM (Veeco) in tapping mode under ambient conditions. The hydrogel was drop-casted on a polished and acetone cleaned Si wafer. Subsequently, the samples were dried for 30 minutes under pure N_2 conditions to remove all water. TESPA-HAR silicon probes (Bruker) were used with a nominal tip radius of 10 nm. Image processing was carried out using the Gwyddion software.

CryoTEM images

CryoTem images were recorded with a Gatan system mounted on a Tecnai12 electron microscope from FEI Company equipped with a LaB6 filament operating at 120 kV. Electron micrographs were recorded on a Gatan Bioscan CCD 1kx1k camera. The samples were prepared using manual preparation method: After applying the sample to the EM support grid (holey carbon film on copper grid) the excess has been carefully blotted away with a small piece of filter paper. Afterwards the TEM grids were plunged into liquid ethane as fast as possible to prevent the formation of ice-crystals. Finally the grids were stored in liquid nitrogen until they were investigated within the microscope.

SEM images of the drop-casted hydrogel were taken on a Tescan MIRA 3 microscope operated with 30 kV electron beam energy. The hydrogel was drop-casted on a polished and acetone cleaned Si wafer. Subsequently, the samples were dried for 30 minutes under pure N_2 conditions to remove all water.

Grazing incidence SAXS (GISAXS) measurements of the dried hydrogel were performed at the Austrian SAXS beamline of the electron storage ring ELETTRA using a photon energy of 8 keV. The beamline setup was adjusted to a sample to detector distance of 790 mm to result in an accessible q-range 0.13–8.4 nm^{-1}. All images were recorded using the Pilatus 1M detector (Dectris, Switzerland) with at least 4 exposures of 10 seconds per sample to check for radiation damage. Reference patterns to calibrate the q-scale were collected of silver-behenate (d-spacings of 5.838 nm). All

measurements were performed using a polished Si wafer as substrate. The hydrogel was drop-casted onto the acetone cleaned Si wafer. Subsequently, the samples were dried for 30 minutes under pure N_2 conditions to remove all water. The dried sample was then placed up-side down in a hanging configuration in the x-ray beam such that the downward scattering was recorded. The image calibration was conducted using the Nika2D package[4].

3.3.2 Methods

Small angle x-ray scattering

Small angle x-ray scattering (SAXS) measurements were performed at the Austrian SAXS beamline of the electron storage ring ELETTRA using a photon energy of 8 keV.[61] The beamline setup was adjusted to a sample to detector distance of 760 mm to result in an accessible q-range 0.12–9 nm^{-1}. All images were recorded using the Pilatus 1M detector (Dectris, Switzerland) with at least 5 exposures of 20 seconds per sample to check for radiation damage. Reference patterns to calibrate the q-scale were collected of silver-behenate (*d*-spacings of 5.838 nm). All measurements were done using a 1.5 mm quartz flow cell capillary. The radial averaging and the image calibration were conducted using the FIT2D software.[62] All presented data was corrected for fluctuations of the primary intensity and the corresponding background has been subtracted from each solution scattering pattern.

Electrochemical measurements

The electrochemical measurements were performed by means of cyclic voltammetry, employing a standard three-electrode setup in an air-tight glass cells with separate gas inlet and outlet through an oil-filled bubbler. In all cases, Pt and Ag/AgCl were used as counter and reference electrode, respectively. The voltammograms were recorded using an SP-150 potentiostat (Biologic, France) with a scan rate of 50 mV s^{-1}. In case of the precursor measurements, 1 mL precursor solution was mixed with in 3 mL 0.1 M $NaSO_4$ and a 3 mm diameter glassy carbon was used as working electrode. In case of the hydrogel, the working electrode was made by immobilizing 250 µl of the final hydrogel between two pieces of carbon paper (Freudenberg, H2315). 0.1M $NaSO_4$ was equally used as electrolyte. The cell was purged either with N_2 or with CO_2.

Vapor response measurements

We carried out vapor-response measurements using a custom-built humidity setup. Substrates were prepared by depositing 40 nm Au on 15 nm Cr electrodes onto glass (previously cleaned in piranha solution) under clean-room conditions. The effective distance between the electrodes was 300µm. After cleaning the substrates with isopropanol, 100 µl of the final gel were drop-casted between the electrodes and dried for 2 hours under N_2 atmosphere. During the measurement, samples were kept under continuous N_2 flow (2 L/min). Vapour pulses were generated using a function generator (Highland P400) controlling gas-flow valves to briefly redirect the N_2 flow into a container with saturated solvent vapour such that only

small vapor pulses arrive directly at the sample. All measurements were conducted at both +2 and –2V to ensure repeatability and avoid possible mass-transport effects. The current was measured using a 4-probe setup directly placed on the Au electrodes (Agilent B1500 Semiconductor Device Analyser).

DFT calculations.

The geometries of the dimers were optimized by dispersion-corrected DFT according to Grimme's PBEh-3c[63] approach implemented in ORCA 4.0.1. The UV/Vis spectra were calculated using the long-range corrected ωB97X[64] functional in ORCA 4.0.1. For more details, see the Supplemental Information.

Synthesis

PBIK was synthesized according the method previously reported in chapter 2, using the following protocol: 100 mg of perylene-3,4,9,10-tetracarboxylic bisanhydride were suspended in dry DMF (5 mL) with 2 equiv. of *β*-alanine in a pressure tight microwave tube. The suspension was sonicated for few minutes before heating under microwave irradiation at 60 W for 10 min. 10 cycles. Max T was set at 200 °C. After cooling, the color turned to dark red and the mixture appeared more homogenous. To the mixture 50 mL of KOH 10% aq. solution was added and solution was stirred for 2h. The precipitate was filtered and washed abundantly with water until pH neutralization and dried using a vacuum pump.

^{1}H-NMR (D_2O, 500 MHz), δ: 8.39 (d, J=7.2 Hz, 4H), 7.79 (d, J=7.2 Hz, 4H), (4.76 (s, 4H). $\lambda_{abs(H2O)}$: 538nm FT-IR (cm^{-1}): 1687, 1642, 1591, 1576, 1507, 1441, 1401. MALDI-TOF-TOF MS m/z calcd. for $C_{30}H_{18}N_2O_8$ $[M - H]^-$ 534, found 533 m/z. Yield%: 64

The hydrogel was formed by adding 120 μl of 4M HCl to a 1 ml homogenous aqueous solution of **PBIK** 8.8 mM and TEA 44 mM. This addition was performed using a hand syringe: the HCl acid was hand injected onto the surface of the **PBIK** and TEA precursor within a 4 ml vial. The procedure was adapted by the one reported by Datar et al[6]. The gelation period was approx. 4 minutes, darkening the colour of the solution to dark red. Successful gelation was tested by vial inversion.

Microwave-assisted synthesis of perylene derivatives was developed using a *CEM Discover® S.* The pressure-resistant, tightly sealed quartz tubes were 3 mm thick with a volume of 10 ml and designed for microwave reactor. Nuclear Magnetic Resonance (NMR) 1H spectra were recorded at 500 MHz on a *Varian VNMRS - 500 MHz*. All spectra were registered at 298 K.

Single Crystal analysis

Data collections were performed at the X-ray diffraction beamline (XRD1) of the Elettra Synchrotron, Trieste (Italy). Thin dark red needles, prone to radiation damage, appeared upon diffusion of ethanol into the precursor solution (8.8 mM) after 2 months. Crystals were dipped in NHV oil (Jena Bioscience GmbH) and mounted on

the goniometer head with a nylon loop. Complete datasets were collected at 100 K (nitrogen stream supplied through an Oxford Cryostream 700 - Oxford Cryosystems Ltd., Oxford, United Kingdom) through the rotating crystal method. Complete datasets have been obtained merging two different data collections done on the same crystal, mounted with different orientations. Data were acquired using a monochromatic wavelength of 0.700 Å on a Pilatus 2M hybrid-pixel area detector (DECTRIS Ltd., Baden-Daettwil, Switzerland). The diffraction data were indexed and integrated using XDS[8]. Semi-empirical absorption corrections and scaling were performed on datasets, exploiting multiple measures of symmetry-related reflections, using SADABS program.

The structures were solved by the dual space algorithm implemented in the SHELXT code. Fourier analysis and refinement were performed by the full-matrix least-squares methods based on F^2 implemented in SHELXL-2014. Thermal motion and geometric restrains on bond lengths, angles (DFIX, DANG, FLAT and SIMU) have been used for disordered fragments (triethylammine molecule and a carboxylic lateral group). Hydrogen atoms were included at calculated positions with isotropic $U_{factors} = 1.2 \cdot U_{eq}$ or $U_{factors} = 1.5 \cdot U_{eq}$ for methyl and hydroxyl groups (U_{eq} being the equivalent isotropic thermal factor of the bonded non hydrogen atom). All the crystals, obtained from different crystallization batches, diffracted poorly, to a maximum resolution of 0.94 Å. Anisotropic thermal motion modeling has then been applied to all atoms with occupancy

not less than 70%. The Coot program was used for structure building.

PBIK crystallized in a triclinic unit cell containing one and half crystallographically independent **PBIK** molecules, showing different protonation states (Figure 3.7). Each **PBIK** molecule stacks (with two crystallographically not equivalent molecules) to form molecular pillars with characteristic π-π orientations and average distance of **PBIK** planes of 3.44 (10) (shortest ring centroids distance of 3.498(3) Å, with a slippage of 1.06 Å).

Intrinsic resolution limit of the data doesn't allow hydrogens to be directly located in electron density maps, however clear hydrogen bond contacts can be recognized between crystallographic, not equivalent, **PBIK** moieties. The **PBIK** molecules lying on crystallographic inversion center have two protonated carboxylate groups that links two lateral **PBIK** moieties, partially protonated. This hydrogen bond pattern keeps tightly linked neighbor columns and is terminated on lateral moieties by ionic couples formed with TEA counterions. Furthermore, each partially protonated **PBIK** molecule is involved in intra-pillar H-bond contacts forming sandwiches where a fully protonated **PBIK** is enclosed in a cage of molecules with only one uncharged carboxylate group. The two **PBIK** protonation variants have superimposable **PBIK** scaffolds but different carboxylate arrangements (Figure 3.7).

Crystal packing shows no voids, with layers of TEA parallel to *ab* unit cell face evenly spaced by 17.7 Å (corresponding to crystallographic

axis *c* cell length). In between TEA layers, **PBIK** pillars form a closed pack arrangement held together by hydrophobic interactions (Figure 3.7)

Pictures were prepared using Pymol software. Essential crystal and refinement data (Table1) are reported below.

Table 3.1. Crystallographic data and refinement details for compound **PBIK** crystal form.

	PBIK [1.5$C_{30}H_{18}N_2O_8$·$C_6H_{15}N$]
CCDC Number	1551775
Chemical Formula	$C_{51}H_{42}N_4O_{12}$
Formula weight	902.88 g/mol
Temperature	100(2) K
Wavelength	0.700 Å
Crystal system	Triclinic
Space Group	*P* -1
Unit cell dimensions	*a* = 10.856(2) Å
	b = 11.859(2) Å
	c = 17.712(4) Å
	α = 92.06(3)°
	β = 93.78(3)°
	γ = 114.52(3)°
Volume	2065.1(8) $Å^3$
Z	2
Density (calculated)	1.452 g·cm^{-3}
Absorption coefficient	0.100 mm^{-1}
F(000)	944
Crystal size	0.08 x 0.01 x 0.01 mm^3
Crystal habit	Dark red thin needles
Theta range for data collection	1.14° to 21.86°

Index ranges	-11 ≤ h ≤ 11, -12 ≤ k ≤ 12, -18 ≤ l ≤ 18
Reflections collected	15497
Independent reflections	5096, 2370 data with $I>2\sigma(I)$
Data multiplicity (max resltn)	2.98 (2.86)
$I/\sigma(I)$ (max resltn)	3.90 (1.59)
R_{merge} (max resltn)	0.134 (0.471)
Data completeness (max resltn)	98% (97%)
Refinement method	Full-matrix least-squares on F^2
Data / restraints / parameters	5096/43/552
Goodness-of-fit on F^2	1.020
Δ/σ_{max}	0.002
Final R indices [$I>2\sigma(I)$]	R_1 = 0.0977, wR_2 = 0.2587
R indices (all data)	R_1 = 0.1919, wR_2 = 0.3263
Largest diff. peak and hole	0.690 and -0.336 eÅ^{-3}
R.M.S. deviation from mean	0.073 eÅ^{-3}

$R_1 = \Sigma \, ||Fo|-|Fc|| \, / \, \Sigma \, |Fo|$, $wR_2 = \{\Sigma \, [w(Fo^2 - Fc^2)^2] \, / \, \Sigma \, [w(Fo^2)^2]\}^{½}$

Oscillatory rheometry analysis

Samples were analyzed in a Kinexus Ultra + (Malvern Scientific) with cone-plate (4° 40 mm conical plate) geometry and Peltier temperature controller at room temperature (25 °C). Hydrogelation kinetics were evaluated within the viscoelastic linear region of applied stress (5 Pa) and frequency (1 Hz) values by preparing the sample *in situ* with a gap of 1 mm (Figure 3.9). Briefly, 3.0 ml of a

8.8 mM PBIK and 44 mM TEA aqueous solution were placed on the bottom plate and 360 µl of 4 M HCl were added on top, just before lowering the top plate and starting data acquisition. However, it was not possible to observe the sol-gel transition due to immediate hydrogel formation, thus indicating a highly cooperative self-assembly mechanism. Stress sweeps were conducted at a frequency of 1 Hz to identify the linear viscoelastic region (Figure 3.9). Frequency sweep analysis was performed at 5 Pa and confirmed independence of both elastic and viscous moduli from the applied frequency, thus confirming a hydrogel nature of the system (Figure 3.9). Measurements were repeated at least twice with time-sweep measurements shown as average of two datasets, and viscoelastic characterization was confirmed by acquiring data also at 2 Pa of applied stress and 0.345 mm gap (and 1 Hz of frequency). In this case, 1.8 ml of a 8.8 mM and TEA 44 mM aqueous solution were placed on the bottom plate and 216 µl of 4 M HCl were added on top, just before lowering the top plate and starting data acquisition.

Differential scanning calorimetry

Differential scanning calorimetry (DSC) was used to assess the supramolecular system stability within a range of temperature values from RT up to 200 °C. DSC data were collected on a Q100 calorimeter (TA Instruments). The hydrogel samples were prepared directly in the DSC aluminum pans. Pans were closed with their lids. DSC scans started with an isotherm at 20 °C for 10 min, followed by

a 10 °C min^{-1} ramp up to 200 °C. Measurements were repeated in triplicates. The hydrogel revealed a remarkable thermal stability with the gel-sol transition displaying an onset temperature of 83.7 ± 1.0 °C, and the endotherm minimum corresponding to the T_m at 91.9 ± 1.1 °C.

SAXS hydrogel model fitting

The scattering intensities $I_{calc}(q)$ for the theoretical models presented in this work were calculated according to two formalisms. We will address them separately. For the in-situ experiments capturing the transition from precursor to hydrogel, we calculate the integral intensity in a given regime $q_{min} < q < q_{max}$ according to $I_{Int} = \int_{q_{min}}^{q_{max}} I(q)\, dq$.

In case of scattering from the precursor solution, according to literature, **PBIK** is suggested to form π-π-stacked aggregates in solution. We hence first determined the mean number of **PBIK** molecules involved in the aggregates. **PBIK** molecules, previously determined from the single-crystal data, were stacked on top of each other[14] with respective 45° degree twist. From these models, we calculated theoretical scattering patterns using CRYSOL. Best agreement is found for the case of **PBIK** stacked tetramers. However, we note that in fact a distribution of linear aggregates will be present in solution – the tetrameric model in fact only represents the mean conformation. The scattering pattern of this tetrameric

configuration is then used as the form-factor scattering $F(q)$ for the subsequent steps.

In order to describe the experimental scattering pattern over the full q-range, we constructed a parametric model. This model assumes sticky-hard-sphere interaction between the **PBIK** tetramer building-blocks, resulting in a structure-factor contribution $S_{SHS}(q)$ in the scattering patternì. Further, in order to describe the observed low-q ($q < 0.3\,nm^{-1}$) intensity increase characteristic of large-scale aggregate formation beyond the resolution limit of SAXS, a Porod contribution according to

$$I_{por}(q) = c_{por} * q^{-4} \qquad (eq.S1)$$

is added to the model. In the parametric formalism, only the absolute scalar c_{por} is optimized throughout the fitting process. In summary, the SAXS pattern of the precursor solution is fitted using the parametric model according to,

$$I_{calc}(q) = a * F(q) * S_{SHS}(q) + c_p * q^{-4} + BG \qquad (eq.S2)$$

where

- a denotes an intensity scalar,
- $F(q)$ denotes **PBIK**-stacked tetramer form-factor scattering,
- $S_{SHS}(q)$ denotes the sticky-hard-sphere structure-factor contribution[16],
- $c_{por}(q)$ denotes the absolute scalar of the Porod-contribution[17],

- and BG denotes a constant background offset.

The fitted scattering curve of the full-pattern refinement is found in Figure 3.6 of the main text, whereas the results are represented in Supplementary Table 2: the **PBIK** tetramers show attractive interaction with a hard-sphere diameter of 4.1 nm, in agreement with literature.

Table 3.2 Fitting results of the full-pattern refinement of the SAXS data from **PBIK** in the precursor state. The experimental scattering pattern as well as the parameter-model fit can be found in Figure 3.6.

Parameter	$\boldsymbol{a}$ $[-]$	$\boldsymbol{R_{HS}}$ $[\boldsymbol{nm}]$	$\boldsymbol{\varphi}[\%]$	$\boldsymbol{\varepsilon}[\boldsymbol{k_BT}]$	$\boldsymbol{c_p}$ $[-]$	$\boldsymbol{BG}$ $[-]$
Value	95.55 ± 0.61	4.08 ± 0.57	0.21 ± 0.03	3.14 ± 0.08	0.17 ± 0.04	0.02 ± 0.008

As there exists a correlation between the potential well size λ and its depth ε, we kept λ fixed at 1.5. Please refer to literature for detailed explanation of the model parameters[16]. In short, R_{HS} denotes the sticky-hard-sphere distance and φ denotes the particle volume fraction.

In case of scattering from the hydrogel, we built a second parametric model based on the chemically cross-linked hydrogel model by *M.Shibayama, et.al.*[19] This model includes two separate terms: the first term describes the electron-density fluctuations between the compound rich and poor regions whereas the second term describes

the domains in which correlated cross-linking occurs. In order to describe the two visible correlation peaks found in the experimental scattering curve we included two Gaussian peaks into the model. In summary, the SAXS pattern of the hydrogel is fitted using the parametric model according to,

$$I_{calc}(q) = a * I_{HG}(q) + I_{P1}(q) + I_{P2}(q) + BG \qquad (eq.S3)$$

and

$$I_{HG}(q) = e^{-\frac{R_G^2 q^2}{3}} + \frac{I_L}{I_G} \frac{1}{\{1 + [(D+1)/3]\xi^2 q^2\}^{D/2}} \qquad (eq.S4)$$

where

- a denotes an intensity scalar,
- $I_{HG}(q)$ denotes the scattering intensity according to the Shibayama model[19] (see eq.S4)
- $I_{P1}(q)$ denotes the first correlation peak,
- $I_{P2}(q)$ denotes the second correlation peak,
- and BG denotes a constant background offset.

The fitted scattering curve of the full-pattern refinement is found in Fig. 1c of the main text, whereas the results are represented in Supplementary Table 3. The obtained dimensionality parameter $D = 3.29$ suggests hydrogen bonding in the system $(D > 2)$[19]. While the retrieved dimensions $\boldsymbol{R_G}$ and $\boldsymbol{\xi}$ are in agreement with general literature on hydrogels, they do not allow further conclusions on discrete shape/size of the hydrogel's intermediate building blocks. We hence performed a power-law fit of the low-q region $(0.12 < q <$

$0.22\ nm^{-1}$), whereas the retrieved slope of 1.78 suggests slightly-porous ($s_1 < 2$) plate-like structures[20]. A corresponding Guinier fit of the $I(q) \cdot q^2$ weighted scattering curve[20] suggests an approximate plate-thickness of 5.3 nm. The two correlation peaks indicate crystalline order within the plate-like structures.

Supplementary Table 3| Fitting results of the full-pattern refinement of the SAXS data from the **PBIK** hydrogel. The experimental scattering pattern as well as the parameter-model fit can be found in Fig. 1c of the main text.

Parameter	$\boldsymbol{a}\ [-]$	$\boldsymbol{R_G}\ [\boldsymbol{nm}]$	$\boldsymbol{I_L/I_G}[-]$	$\boldsymbol{\xi}[\boldsymbol{nm}]$	$\boldsymbol{D}\ [-]$
Value	869.98 ± 13.6	4.12 ± 0.43	51.43 ± 0.87	9.06 ± 1.2	3.29 ± 0.14

$\boldsymbol{x_{0,P1}}\ [\boldsymbol{nn}$	$\boldsymbol{\sigma_{P1}}[\boldsymbol{nm}^{-}$	$\boldsymbol{i_{P1}}[-]$	$\boldsymbol{x_{0,P2}}\ [\boldsymbol{nn}$	$\boldsymbol{\sigma_{P2}}[\boldsymbol{nm}^{-}$	$\boldsymbol{i_{P2}}[-]$	$\boldsymbol{BG}\ [-]$
4.77 ± 0.09	0.27 ± 0.02	1.14 ± 0.05	7.81 ± 0.81	0.12 ± 0.02	0.32 ± 0.01	0.01 ± 0.003

Please refer to literature[19] for detailed explanation of the Shibayama model parameters In short, R_G denotes the characteristic length of the polymer rich regions, I_L/I_G denotes the scaling factor between the two model terms, ξ denotes the domain size of the correlated regions and D denotes the fractal dimensionality ($D > 2$ for hydrogen-bonded gels). Each Gaussian peak is defined by its position in reciprocal space x_0, its width σ and its intensity i.

X-ray diffraction analysis on the hydrogel

In order to determine the crystalline unit-cell within the hydrogel nanoribbons, we obtained additional x-ray scattering data that cover the angular range corresponding to $2 < q < 20\, nm^{-1}$. The XRD measurements were performed at the X-ray diffraction beamline (XRD1) of the Elettra Synchrotron, Trieste (Italy) (Lausi A, Polentarutti M, Onesti S, Plaisier JR, Busetto E, Bais G*,et al.* Status of the crystallography beamlines at Elettra. *The European Physical Journal Plus* 2015, **130**(3)**:** 43.

)using a photon energy of 12.4 keV. The beamline setup was adjusted to a sample to detector distance of 250 mm. All images were recorded using the Pilatus 2M detector (Dectris, Switzerland) with at least three exposures of 60 seconds per sample to check for radiation damage. Reference patterns to calibrate the q-scale were collected of Lanthanum-hexaborid LaB6 NIST standard. The wet hydrogel was mounted onto the goniometer head inside a nylon loop. During each exposure, the sample was rotated by 360°. The radial averaging and the image calibration were conducted using the FIT2D software (Hammersley AP, Svensson SO, Thompson A, Graafsma H, Kvick Å, J P Moy. Calibration and correction of distortions in 2D detector systems. *Rev Sci Instr* 1995, **66:** 4.)

For background correction, the scattering of the solvent (solution in nylon loop) was subtracted from the measurement.

Supplementary Table 4| Results of the x-ray diffraction analysis of the **PBIK** hydrogel. Peak positions were obtained using Gaussian fits whereas the fitting of the unit cell was done by a least-square optimization.

$peak$	$x_0[nm^{-1}]$	$\sigma[nm^{-1}]$	$i_0[-]$	$d_{exp}[nm]$	$d_{fit}[nm]$	$q_{fit}[nm^{-1}]$	h	k
1	4.778 ± 0.003	0.311 ± 0.005	3943.2 ± 48.3	**1.315**	**1.290**	4.870	1	0
1					**1.307**	4.809	1	1
2	7.793 ± 0.002	0.225 ± 0.004	1758.7 ± 24.5	**0.806**	**0.807**	7.790	0	1
3	9.811 ± 0.009	0.471 ± 0.025	125.57 ± 4.32	**0.640**	**0.645**	9.739	2	0
4	12.311 ± 0.004	0.298 ± 0.006	2882.1 ± 45.1	**0.510**	**0.521**	12.069	1	-1
5	15.608 ± 0.008	0.236 ± 0.007	364.56 ± 6.24	**0.403**	**0.403**	15.580	0	2
6	16.659 ± 0.002	0.207 ± 0.009	201.06 ± 7.88	**0.377**	**0.377**	16.676	2	-1
7	18.285 ± 0.003	0.124 ± 0.004	13428 ± 373	**0.344**	**π–π-stacking peak**			
8	18.838 ± 0.003	0.191 ± 0.010	3780.4 ± 143	**0.334**	**π–π*-stacking peak**			

Here, x_0, σ and i_0 denote the Gaussian peak-position, peak-width and peak-height determined from the experimental scattering curve, respectively. From the peak-position, the corresponding d-spacing $d_{exp}$was calculated. The unit-cell parameters were determined by minimizing the least-square sum of the difference between experimental and theoretical peak-positions x_0 and q_{fit},

respectively[21]. For better comparison, the resulting d-spacings d_{fit} are compared to the experimental ones (marked bold).

The measurements reveal a total of 8 peaks. Peak positions, widths and intensities were determined by Gaussian fits. From the obtained peak positions, we reconstruct the oblique 2D unit-cell parameters (*p*1 lattice with a = 2.188 nm, b = 1.367 nm, and γ = 36.14°) of the π-π-stacked columns within the nano-ribbons via a least-square fitting procedure[21]. The experimental peak values as well as the fitted theoretical peak positions are shown in Supplementary Table S4 whereas a graphical comparison of the experimental scattering pattern with the peak indices can be found in Fig. 2a of the main text.

3.4 References

[1] X. Du, J. Zhou, J. Shi, B. Xu, *Chem. Rev.* **2015**, *115*, 13165–13307.

[2] A. Vintiloiu, J. C. Leroux, *J. Control. Release* **2008**, *125*, 179–192.

[3] Y. Zhao, B. Liu, L. Pan, G. Yu, *Energy Environ. Sci.* **2013**, *6*, 2856.

[4] M. Motornov, Y. Roiter, I. Tokarev, S. Minko, *Prog. Polym. Sci.* **2010**, *35*, 174–211.

[5] S. S. Babu, S. Prasanthkumar, A. Ajayaghosh, *Angew. Chem.* **2012**, *51*, 1766–1776.

[6] F. Fages, K. Araki, *Low Molecular Mass Gelators : Design, Self-Assembly, Function*, Springer, **2005**.

[7] A. Ajayaghosh, V. K. Praveen, *Acc. Chem. Res.* **2007**, *40*, 644–656.

[8] L. Maggini, D. Bonifazi, *Chem. Soc. Rev.* **2012**, *41*, 211–241.

[9] M. Muccini, *Nat. Mater.* **2006**, *5*, 605–613.

[10] D. Venkataraman, S. Yurt, B. H. Venkatraman, N. Gavvalapalli, *J. Phys. Chem. Lett.* **2010**, *1*, 947–958.

[11] D. González-Rodríguez, A. P. H. J. Schenning, *Chem. Mater.* **2011**, *23*, 310–325.

[12] J.-L. Li, X.-Y. Liu, *Adv. Funct. Mater.* **2010**, *20*, 3196–3216.

[13] Y. Jeong, K. Hanabusa, H. Masunaga, I. Akiba, K. Miyoshi, S. Sakurai, K. Sakurai, *Langmuir* **2005**, *21*, 586–594.

[14] F. Wang, Z. Li, M. Khan, K. Tamama, P. Kuppusamy, W. R. Wagner, C. K. Sen, J. Guan, *Acta Biomater.* **2010**, *6*, 1978–1991.

[15] X. Chen, B. D. Martin, T. K. Neubauer, R. J. Linhardt, J. S. Dordick, D. G. Rethwisch, *Carbohydr. Polym.* **1995**, *28*, 15–21.

[16] K. N. Plunkett, J. S. Moore, *Langmuir* **2004**, *20*, 6535–6537.

[17] T. R. Hoare, D. S. Kohane, *Polymer.* **2008**, *49*, 1993–2007.

[18] A. Singh, P. K. Sharma, V. K. Garg, G. Garg, *Int. J. Pharm. Sci. Rev. Res.* **2010**, *4*, 97–105.

[19] S. S. Babu, V. K. Praveen, A. Ajayaghosh, *Chem. Rev.* **2014**, *114*, 1973–2129.

[20] F. Würthner, *Chem. Commun.* **2004**, *0*, 1564–1579.

[21] K. Sugiyasu, N. Fujita, S. Shinkai, *Angew. Chem.* **2004**, *43*, 1229–1233.

[22] K. Sugiyasu, S. I. Kawano, N. Fujita, S. Shinkai, *Chem. Mater.* **2008**, *20*, 2863–2865.

[23] X.-Q. Li, V. Stepanenko, Z. Chen, P. Prins, L. D. A. Siebbeles, F. Würthner, *Chem. Commun.* **2006**, *0*, 3871–

3873.

[24] X. Q. Li, X. Zhang, S. Ghosh, F. Würthner, *Chem. - A Eur. J.* **2008**, *14*, 8074–8078.

[25] S. Yagai, Y. Monma, N. Kawauchi, T. Karatsu, A. Kitamura, *Org. Lett.* **2007**, *9*, 1137–1140.

[26] T. Seki, S. Yagai, T. Karatsu, A. Kitamura, *Chem. Lett.* **2008**, *37*, 764–765.

[27] R. V. Ulijn, *J. Mater. Chem.* **2006**, *16*, 2217.

[28] E. Krieg, E. Shirman, H. Weissman, E. Shimoni, S. G. Wolf, I. Pinkas, B. Rybtchinski, *J. Am. Chem. Soc.* **2009**, *131*, 14365–14373.

[29] D. Görl, B. Soberats, S. Herbst, V. Stepanenko, F. Würthner, J.-M. Lehn, T. Aida, E. W. Meijer, S. I. Stupp, T. Kato, et al., *Chem. Sci.* **2016**, *7*, 6786–6790.

[30] R. V. Ulijn, *J. Mater. Chem.* **2006**, *16*, 2217.

[31] G. S. Vadehra, B. D. Wall, S. R. Diegelmann, J. D. Tovar, *Chem. Commun.* **2010**, *46*, 3947.

[32] R. V. Ulijn, *J. Mater. Chem.* **2006**, *16*, 2217.

[33] S. Roy, D. K. Maiti, S. Panigrahi, D. Basak, A. Banerjee, H. C. Fry, J. M. Garcia, M. J. Medina, U. M. Ricoy, D. J. Gosztola, et al., *Phys. Chem. Chem. Phys.* **2014**, *16*, 6041.

[34] S. Roy, D. Kumar Maiti, S. Panigrahi, D. Basak, A. Banerjee,

RSC Adv. **2012**, *2*, 11053.

[35] P. Bairi, B. Roy, A. K. Nandi, *RSC Adv.* **2012**, *2*, 264–272.

[36] A. Datar, K. Balakrishnan, L. Zang, L. Zang, Y. Che, J. S. Moore, F. Wurthner, A. C. Grimsdale, K. Müllen, A. P. H. J. Schenning, et al., *Chem. Commun.* **2013**, *49*, 6894.

[37] E. R. Draper, J. J. Walsh, T. O. McDonald, M. A. Zwijnenburg, P. J. Cameron, A. J. Cowan, D. J. Adams, *J. Mater. Chem. C* **2014**, *2*, 5570–5575.

[38] J. J. Walsh, J. R. Lee, E. R. Draper, S. M. King, F. Jäckel, M. A. Zwijnenburg, D. J. Adams, A. J. Cowan, *J. Phys. Chem. C* **2016**, *120*, 18479–18486.

[39] F. Rigodanza, E. Tenori, A. Bonasera, Z. Syrgiannis, M. Prato, *Eur. J. Org. Chem.* **2015**, *2015*, 5060–5063.

[40] E. R. Draper, B. J. Greeves, M. Barrow, R. Schweins, M. A. Zwijnenburg, D. J. Adams, *Chem* **2017**, *2*, 716–731.

[41] D. Svergun, C. Barberato, M. H. Koch, *J. Appl. Crystallogr.* **1995**, *28*, 768–773.

[42] F. Würthner, Z. Chen, V. Dehm, V. Stepanenko, *Chem. Commun.* **2006**, *0*, 1188.

[43] F. Würthner, C. Thalacker, S. Diele, C. Tschierske, *Chemistry* **2001**, *7*, 2245–2253.

[44] M. R. Hansen, T. Schnitzler, W. Pisula, R. Graf, K. Müllen, H.

W. G. Spies, *Angew. Chem.* **2009**, *48*, 4621–4624.

[45] S. Ghosh, X. Q. Li, V. Stepanenko, F. Würthner, *Chem. - A Eur. J.* **2008**, *14*, 11343–11357.

[46] Z. Chen, A. Lohr, C. R. Saha-Möller, F. Würthner, *Chem. Soc. Rev.* **2009**, *38*, 564–584.

[47] J. M. Lim, P. Kim, M.-C. Yoon, J. Sung, V. Dehm, Z. Chen, F. Würthner, D. Kim, *Chem. Sci.* **2013**, *4*, 388–397.

[48] S. Yagai, T. Seki, T. Karatsu, A. Kitamura, F. Würthner, *Angew. Chem.* **2008**, *47*, 3367–3371.

[49] F. Würthner, C. R. Saha-Möller, B. Fimmel, S. Ogi, P. Leowanawat, D. Schmidt, *Chem. Rev.* **2016,** *116*, 962–1052.

[50] Z. Chen, V. Stepanenko, V. Dehm, P. Prins, L. D. A. Siebbeles, J. Seibt, P. Marquetand, V. Engel, F. Würthner, *Chem. - A Eur. J.* **2007**, *13*, 436–449.

[51] N. L. Weinberg, A. Kentaro Hoffmann, T. B. Reddy, *Tetrahedron Lett.* **1971**, *12*, 2271–2274.

[52] N. Wu, C. Wang, P. M. Slattum, Y. Zhang, X. Yang, L. Zang, *ACS Energy Lett.* **2016**, *1*, 906–912.

[53] J. H. Rheinhardt, P. Singh, P. Tarakeshwar, D. A. Buttry, *ACS Energy Lett.* **2017**, *2*, 454–461.

[54] J. H. Rheinhardt, P. Singh, P. Tarakeshwar, D. A. Buttry, *ACS Energy Lett.* **2017**, *2*, 454–461.

[55] N. Wu, C. Wang, P. M. Slattum, Y. Zhang, X. Yang, L. Zang, *ACS Energy Lett.* **2016**, *1*, 906–912.

[56] R. F. Fink, J. Seibt, V. Engel, M. Renz, M. Kaupp, S. Lochbrunner, H.-M. Zhao, J. Pfister, F. Würthner, B. Engels, *J. Am. Chem. Soc.* **2008**, *130*, 12858–12859.

[57] A. Wang, L. Cui, S. Debnath, Q. Dong, X. Yan, X. Zhang, R. V. Ulijn, S. Bai, *ACS Appl. Mater. Interfaces* **2017**, *9*, 21390–21396.

[58] A. S. Weingarten, R. V. Kazantsev, L. C. Palmer, D. J. Fairfield, A. R. Koltonow, S. I. Stupp, *J. Am. Chem. Soc.* **2015**, *137*, 15241–15246.

[59] A. M. Castilla, E. R. Draper, M. C. Nolan, C. Brasnett, A. Seddon, L. L. E. Mears, N. Cowieson, D. J. Adams, *Sci. Rep.* **2017**, *7*, 8380.

[60] P. K. Sukul, P. K. Singh, S. K. Maji, S. Malik, *J. Mater. Chem. B* **2013**, *1*, 153–156.

[61] H. Amenitsch, M. Rappolt, M. Kriechbaum, H. Mio, P. Laggner, S. Bernstorff, *J. Synchrotron Radiat.* **1998**, *5*, 506–508.

[62] A. P. Hammersley, S. O. Svensson, M. Hanfland, A. N. Fitch, D. Hausermann, *High Press. Res.* **1996**, *14*, 235–248.

[63] S. Grimme, J. G. Brandenburg, C. Bannwarth, A. Hansen, *J. Chem. Phys.* **2015**, *143*, 54107.

[64] J. Da Chai, M. Head-Gordon, *J. Chem. Phys.* **2008**, *128*, 84106.

4. Perylene bisimides as photosensitizer

As it will be introduced in section 4.1, scientists are currently looking for a synthetic analogue of the PSII oxygen evolving center, a complex system Nature has designed to store clean energy from sunlight. In this chapter, we report an artificial system mimicking the natural enzyme by the assembly of positively charged perylene bisimides and a ruthenium polyoxometalate, the forunner in its series. Continuous oxygen evolution is observed in neutral pH, upon visible light irradiation. Morevoer, we built a novel dye-sensitized photoanode where the structural motif of the assembly is transferred onto the semicondutcor layer, showing high photocurrent compared to literature analogues.

The work presented in this chapter has been done in a collaborative work with Dr. Erica Pizzolato (Università degli Studi di Trieste) and Max Burian (Technische Universität Graz) that contributed with the experimental design and results. For this particular chapter, it was instrumental the collaboration with the group of Prof. Marcella Bonchio (Università degli Studi di Padova) where all the catalytic screening was conducted.

4. Perylene bisimides as photosensitizer

4.1 Introduction

4.1.1 Energy crisis

One of the biggest challenge mankind has to face is the increasing need for energy. We currently rely on fossil fuels for the 80% of our needs but we do know that these sources are not infinite.[1] The most optimistic previsions believe coal, oil and gas will last only three or four decades more. This situation will not become different without drastic policy changes, on the contrary, the energy demand is supposed to grow almost half over. There is the real fear that we will soon run out of energy resources and the later we start deal with this issue, the worse the consequences will be.[2–4] The issue does not affect only the global economy but also the climate change. The emission of carbon dioxide into atmosphere is primarily caused by combustion of fossil fuels and it has been proven several times how this phenomenon is related to rising global temperature (even if the popular opinion is still skeptical).[5–7] Additionally, the supplies of fossil fuels are unevenly spread over the world leading to political tension and security problems.[8]

The race to the development of an economically viable energy sources is becoming every day more relevant. If the rather optimistic assumptions of population's growth and energy consumption will come true, in 2050 the energy demand will be of 28 TW. More than twice the need of 2000. Only solar energy, in

addition to nuclear fusion, can provide this energy. It is estimated that the solar potential values, coming from the energy that strikes the Earth, would be about 600 TW.[2,9] Thus, just using 5% efficient solar farms we could supplied all the needed power. For these reasons, huge research has been done in the past years to develop new solar cells, cheaper and cheaper, more and more efficient and more and more stable.[10,11]. However, sun does not shine everywhere in the same way and for the same amount of time. There are nights and clouds, sun exposure in Greenland will be different to the one in Saudi Arabia. Moreover, the electricity produced by these devices is difficult to store and the best way to do so is to convert it in chemical fuel, which is exactly what nature has been doing for billions of years.[12,13]

4.1.2 Natural solar fuels

Nature (plants, algae and cyanobacteria) has developed such fascinating photosynthetic processes to store energy from sunlight in useful chemicals.[14] Indeed, the production of oxygen and the assimilation of CO_2 into organic matter has determined the composition of our atmosphere and has provided all living beings with food and fuel. Therefore, natural systems are an excellent source of inspiration for the design of synthetic systems that can store solar energy.

Plant photosynthesis is accomplished by a number of reactions that take place mainly in the chloroplast: light-dependent water oxidation, NADP reduction and formation for ATP. This kind of reactions is catalyzed by two different photosystems (PSI, and

PSII) and ATP synthase.[15,16] The formers contain chlorophylls and other pigments in order to harvest light and funnel the absorbed energy to the reaction center. When energy is captured by the reaction center, it induces the excitation of a special chlorophyll pair in PSI, starting the electron-transfer across the membrane through a chain of cofactors. The electron-donor for this process is water, which is oxidized by PSII into oxygen and protons. In this photosystem, when chlorophylls P680 are excited, an electron is transferred to the acceptor system which, subsequently, reduces CO_2.[17]

Once oxidized, P680 becomes a strong oxidant, with a potential of around 1.2 V vs. NHE and it is able to take one electron from MN4Ca-cluster in the oxygen evolving center (OEC). When the electron abstraction is repeated four times, the OEC oxidized two molecules of water into one of O_2 and four protons. Enzyme PSII generates oxygen with turnover frequency (TOF) exceeding 400-500 s^{-1} and overpotential as low as 300 mV. However, the life-span of the biological machinery is limited to ca. 30 min, being affected by the progressive demolition of the protein structure with leaching of the manganese co-factor.[18,19]

The core of the EOC has been a matter of study for both crystallographers and spectroscopists. Four manganese atoms and a calcium one are held together by surrounding μ-oxo and μ-hydroxo ligands in a cubane-like arrangement. The calcium atom covers three manganese atoms while the last manganese atom is linked to the cubane trough two μ-oxo bridges. Notably, this structure is preserved in all the photosynthetic organisms demonstrating its fundamental importance.[20,21]

As it happened for the structural motif, also the OEC mechanism has been intensively studied. The complex oxidized water through five steps called S_0-S_4, where S_0 is the most reduced state and S_4 is the most oxidized one, and the key transition S_4-S_0 is the one liberating O_2.[15,22,23]

4.1.3 Artificial photosynthesis

Whereas nature oxidize water to O_2 and transform atmospheric CO_2 into carbohydrates, for an artificial system is more practical to use solar energy to split H_2O into O_2 and H_2 coupling the two half reactions: [23,24]

$2\ H_2O \rightarrow O_2 + 4H^+ + 4e^-$

$4H^+ + 4e^- \rightarrow 2\ H_2$

$2\ H_2O \rightarrow O_2 + 2\ H_2$

These reactions involve multielectron transfers, therefore the correct design of synthetic photosystems is not elementary. To devise an efficient process it must absorb a photon by a chromophore, form a charge-separated state by transfer to a reduction catalyst, accept and accumulate two electrons at the reduction catalyst which will be used to reduce protons to hydrogen, allow regeneration of the photosensitizer by electron-transfer from the oxidation catalyst, accept and accumulate four positive holes which will be used to oxidize two molecules to one molecule of O_2 and four protons.[12,24,25]

4. Perylene bisimides as photosensitizer

To facilitate the correct flow of electrons the chromophore can be attached to a semiconductor. In this case, the charge-separated state is formed after electron transfer from the excited photosensitizer to the conduction band of the semiconductor. If this state lives long enough, the chromophore, to regenerate, takes an electron from the oxidation catalyst. After four consecutive electron abstractions, the catalyst is able to remove four electrons from water oxidizing it to oxygen and protons. This reserve of extracted electrons is delivered to a reduction catalyst which can mediate the reduction of protons or other chosen molecules like CO_2.[24,25]

All these processes seem straight-forward, however the combination of efficient light sensitizing, fast electron transfer and efficient catalysis, is a strenuous task. To date, most of the researches have been dedicated to the synthesis of efficient systems mimicking the half reactions of the whole photosynthetic process. In particular water oxidation into dioxygen and protons is recognized as the major bottle-neck of the cascade follow-up for solar hydrogen production, which is still awaiting for a conceptional breakthrough.[26]

As it may appear intuitive, the main interest of this thesis is to synthesize novel photoluminescent materials and use them for new applications. Therefore, our focus in artificial photosynthesis is directed towards the light absorption by a chromophore, which is the first key step that initiates the cascade of electron transfers to produce solar fuels. A photosensitizer has the task to harvest light and convert the incoming energy into an excited state that can give an electron to an acceptor to create a charge-separated state. This

role of light-harvester can be performed either by molecular dyes either by semiconductors.[27,28]

Ruthenium polypyridyl complexes have been the first to be studied since they have broad absorption, long-lived excited-state lifetimes and good electrochemical stability.[29,30] These properties can be easily tuned by modification of the ancillary ligands, typically bypridines or terpyridines.[31]

Upon light irradiation one electron in the t_{2g} orbital (metal-centered) is excited to the π-orbital (ligand-centered). Formally, the ruthenium centre is now photo-oxidized to Ru^{III}, while the ligand is reduced. This metal to ligand transfer state (MLCT) is a singlet state ($^1[Ru(bpy)_3]^{2+*}$) which is short-lived and, through intersystem crossing, rapidly yield a long lived triplet state $^3[Ru(bpy)_3]^{2+*}$. This triplet state has enough potential and long-lifetime to take part in bimolecular electro-transfer reactions.[32–34]

After the first discovery in the 70s, Graezel reported a series of ruthenium-polypyridyl complexes where two bypridyl ligands were substituted with Cl, Br, I, CN or SCN. The complex $[Ru(4\text{-}4'\text{-}(COOH)_2bpy_2(SCN)_2]^{2+}$, called “red dye”, exhibits the highest extinction coefficient (14000 M^{-1} at 534 nm) and, once couple with TiO_2, reaches an incident photon-to-current conversion efficiency (IPCE) above 80%.[35] Besides the increased absorption, the improvement is attributed to facilitation of charge transfer with the redox mediator iodide/triiodide.[36,37] These performances paved the way to other complexes bearing thiocyanates with absorbance extended in the IR region. “Black dye” is a ruthenium complex with

three SCN ligands and a terpyridine ligand with three carboxylate anchors, which absorbs in the near-IR region up to 920 nm.[38]

The appeal of ruthenium bypyridyl complexes brought to the synthesis of several other compounds with different substituents such as alkyl thiophene,[39,40] alkyl furan,[40] phenylene vinylene,[41,42] or 2-thiophene-2-yl-vinyl.[43] However all these chromophore base their light-harvesting properties on the ruthenium center, which has the weak point of being expensive and environmentally dangerous. Therefore, scientists focused on cheaper and more abundant alternatives: porphyrins. Porphyrin-based donor-acceptor dyads have been used to study the lifetime and charge recombination of photoinduced charge-separates states and photoinduced electron-transfer to catalytic electron mediators via non-covalent interactions.[44] High potential porphyrins have been reported to be good candidates for light-driven water oxidation. A zinc phorpryin, bearing electron-withdrawing pentafluorophenyl groups at the meso-carbon, once photoxidized has potential sufficient to thermodynamically drive water oxidation.[45,46] Compared to ruthenium complexes, porphyrins have higher extinction coefficient and absorption at longer wavelength. Indeed these materials have been used in DSSCs that achieve over 10% of power conversion efficiency (PCE).[47–49]

On the other side, these molecules tend to form aggregates where photoexcited species and ground-state species interact leading to worse efficiency. It is possible to prevent aggregation making stepwise modifications, however these synthetic routes can be challenging, in particular for non-symmetric porphyrins.

4. Perylene bisimides as photosensitizer

Besides porphyrins, hundreds of metal-free organic dyes have been synthesized as a viable alternative to expensive ruthenium-based sensitizer.[50] Between these photosensitizers, the electron accepting properties of **PBIs** emerged upon photoexcitation in combination with several electron donors, such as phthalocyanines,[51–53] porphyrins,[54] metal complexes[55] or endohedral metallofullerenes.[56]. Lately, few perylene derivatives have been used as primary photocalalysts in molecular photosystems. [57] In particular Wurthner compromised two PBIs with a ruthenium(II) complex to catalyze water oxidation.[58] The hybrids form nanofibers driven by strong π-π interactions between the perylene cores and shield the active ruthenium center in their interior. Compared to the free reference complex the dyad shows longer lifetime and 30% higher oxygen evolution. However, in nature catalyst and chromophore are not covalently bonded, instead reversible and dynamic supramolecular interactions are used to regulate the electron-transfer between the species.

4.1.4 The supramolecular approach

Seminal studies on the functional upgrade of the AP-architecture, indicate that the complexity of the covalent network should be highly increased to optimize both the light-harvesting components, their spatial organization and the rigidity of the photosystem, as a strategy to counteract back electron transfer (ET) and stabilize the photo-generated products at each step of the multi-photon/multi-electron mechanism.[59,60] While the art of mastering covalent chemistry has enabled key structures activity descriptors to tune

photo-induced ET in artificial environment, the effort to get into real-world applications is hampered by synthetic challenges, production costs and the irreversible fate of the covalent connectivity after exhaustion. This is why covalent bonds are rarely used in biological systems. Instead, non-covalent, but reversible and dynamic, supramolecular interactions are used by Nature to regulate the structure of photosynthetic systems and their modular assembly within the chloroplast membranes.[21,61] Besides the structural considerations, non-covalent interactions are known to play a crucial role to boost water oxidation catalysis. Kinetic and computational evidence confirm that both hydrophobic and electrostatic forces can be effective to (i) assemble competent intermediates,[62] (ii) leverage water transfer/confinement to the catalytic sites,[63–65] (iii) facilitate photo-induced electron transfer.[66–68] With a similar scope, a supramolecular photohydrogel made of perylene chromophores and synthetic hydrogenase catalysts has been recently reported for the hydrogen evolving reaction (HER) in aqueous phase.[69]

4.1.5 Aim of the project

Our approach is based on the unprecedented combination of metal-free perylene bisimides as photosensitizers[70,71] with totally inorganic polyoxometalates (POMs) as catalysts. Such component choice gathers a unique potential for photosynthetic applications: PBIs have been successfully applied in photovoltaic technologies as versatile organic semiconductors with tunable absorption cross-sections and electron accepting properties, while POMs are the emerging class of molecular water oxidation catalysts, that can

mimic the photosynthetic PSII oxygen evolving cluster, offering the robustness of totally inorganic metal oxide materials.[72–75]

In particular, N,N′-bis(2-(trimethylammonium)ethylene)perylene-3,4,9,10-tetracarboxylic acid bisimide, **PBI2+**, photosensitizer, is one of the strongest photo-generated oxidant in its excited state, E(**PBI2+**$^{*2+/1+}$) **=** 2.18 V vs NHE, which nicely complements, $[Ru_4(\mu\text{-}O)_4(\mu\text{-}OH)_2(H_2O)_4(\gamma\text{-}SiW_{10}O_{36})_2]^{10-}$ (**Ru$_4$POM**), the forerunner of its class as water oxidation catalyst (Figure 4.1).[73,75,76] This is a game-changing strategy with respect to all of the established methods based on the usual Ru(II)polypyridine photosensitizers[29] and/or conceived through the covalent design of photocatalytic electron donor-acceptor conjugates.[54] While the covalent approach guarantees a stringent molecular control on the electron donor-acceptor distances and geometries as governing factors for photo-induced electron transfer, the photocatalysis outcome is deceivingly inefficient and largely suppressed by fast recombination processes. Notably, the covalent strategy is not what Nature has used to tune the perfect mechanism of the photosynthetic complexity, which is ultimately based on non-covalent, supramolecular motifs.[26,61,77] The novel **PBI2+$^{2+}$•Ru$_4$POM** functional nanohybrid self-assembles in water via complementary and strong electrostatic interactions (Figure 4.1).

Our results address the water oxidation cycle emerging from the **PBI2+$^{2+}$•Ru$_4$POM** hybrid under visible light irradiation, by probing the key events of photo-induced charge separation, its time-resolved evolution (0-8 ns), and the resulting water oxidation kinetics under pseudo steady state conditions. Direct, reductive

quenching of photo-generated ***PBI2+**$^{2+}$ by **Ru$_4$POM** is taking place, showing exceptional robustness for long-time operation and recycling protocols. Continuous oxygen evolution is observed under photocatalytic conditions with quantitative conversion and quantum efficiency up to 6% (Figure 4.1). Noteworthy, the catalytic performance is maintained after immobilization onto functional surfaces, which paves the way to device applications.

4.2 Results and discussion

4.2.1 PBI2+: our photosensitizer

The amphiphilic, water soluble **PBI2+**, with two tetra-alkyl ammonium pendants, (Figure 4.1a) displays a peripheral biscationic charge and offers a valuable plug-and-play electrostatic

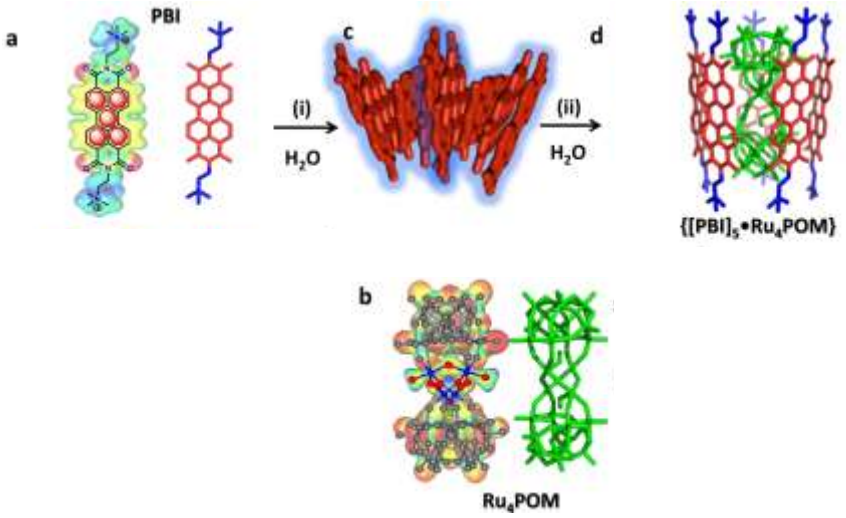

Figure 4.1. **Self-assembly of PBI2+ with Ru4POM in water**: ball-and stick structures, relative dimensions and molecular electrostatic potential (MEP) maps for **a**, the bis-cationic N,N'-bis(2-(trimethylammonium)ethylene)perylene-3,4,9,10-tetracarboxylic acid bisimide, **PBI2+** photosensitizer and of **b**, [Ru4(μ-O)$_4$(μ-OH)$_2$(H2O)$_4$(γ-SiW$_{10}$O$_{36}$)$_2$]$^{10-}$, **Ru4POM**, the deca-anionic, polyoxotungstate (grey framework) embedding the Ru_4O_6 oxygen evolving core (blue = Ru, red = O). MEPs profiles show the complementary charge interaction areas as positive blue and negative red zones; **c**, representation of supramolecular nano-stacks formed by self-assembly of **PBI2+** in water (path (i): 2.5 × 10-5 M, buffer PBS, pH 7, room temperature); **d**, POM induced exfoliation of the perylene π-π aggregates yielding the encapsulated {[**PBI2+**]$_5$•**Ru4POM**} complex (path (ii): 5 × 10^{-6} M**,** buffer PBS, pH 7.0, room temperature)**.**

connector as we already stated in Chapter 2.[78,79] This is instrumental for the co-assembly of the polyanionic **Ru4POM** in solution and for the shaping of functional interfaces on tailored electrodes. In particular, the supramolecular chemistry of **PBI2+** in

water is directed by both hydrophobic π-π interactions between aromatic cores, and by peripheral charge-repulsion/attraction forces, driving the self-assembly dynamics and the shaping of the **PBI2+** arrangement.[78,79] Formation of **PBI2+** aggregates is conveniently monitored by UV-Vis and fluorescence spectroscopy in aqueous solution ([**PBI2+**] = 1 – 50 μM), by comparison with the **PBI2+** monomer observed in DMF (Figure 4.2). In agreement with literature data, formation of nano-**PBI2+** in water is confirmed by a typical absorption fingerprint,[78,79] where the 501 nm band intensity grows stronger than the 539 nm band. As expected, the fluorescence quantum yield turns out to be as low as 7%, due to **PBI2+** self-quenching within the stacked arrays (Figure 4.2).[70]

The existence of **PBI2+** nano-stacks in solution has been further probed by X-Ray Scattering techniques. Wide Angle X-ray Scattering (WAXS) analysis shows a strong difraction peak corresponding to a π-π-stacking distance of 3.56 Å (q = 17.6 nm-1), which gives a direct proof for long range order in **PBI2+** aggregates (Fig. 2a). Dynamic Light Scattering (DLS) and Zeta Potential analysis of a **PBI2+** solution ([**PBI2+**] = 25 μM in 20 mM phosphate buffer pH 7.0) confirm the presence of aggregates with a size distribution centered at 500 nm and apparent surface charge close to zero (Figure 4.7). This is a result of the tight packing of the π–π nano-stacks, evolving into micron-sized large bundles, and likely incorporating small counter-ions to minimize charge repulsion.[80] With the aim to address the electron acceptor potential of the ground and excited states, the redox properties of **PBI2+** solutions have been probed by means of cyclic voltammetry (CV) and spectro-electrochemistry.[81] Under the conditions

explored, ([**PBI2+**] = 0.5 mM in 20 mM phosphate buffer pH 7, (Figure 4.5), the CV is characterized by a cathodic wave at E_{pc} = -0.20 vs NHE, and a anodic wave, in the reverse scan, at E_{pa} = +0.03 V vs NHE. Spectroelectrochemistry analysis performed from -0.26 V to +0.20 V vs NHE, (Figure 4.6) allows to ascribe this electrochemical process to the one electron-reduction of **PBI2+**,[81] by registering a steady increase of absorption in the 517-800 nm

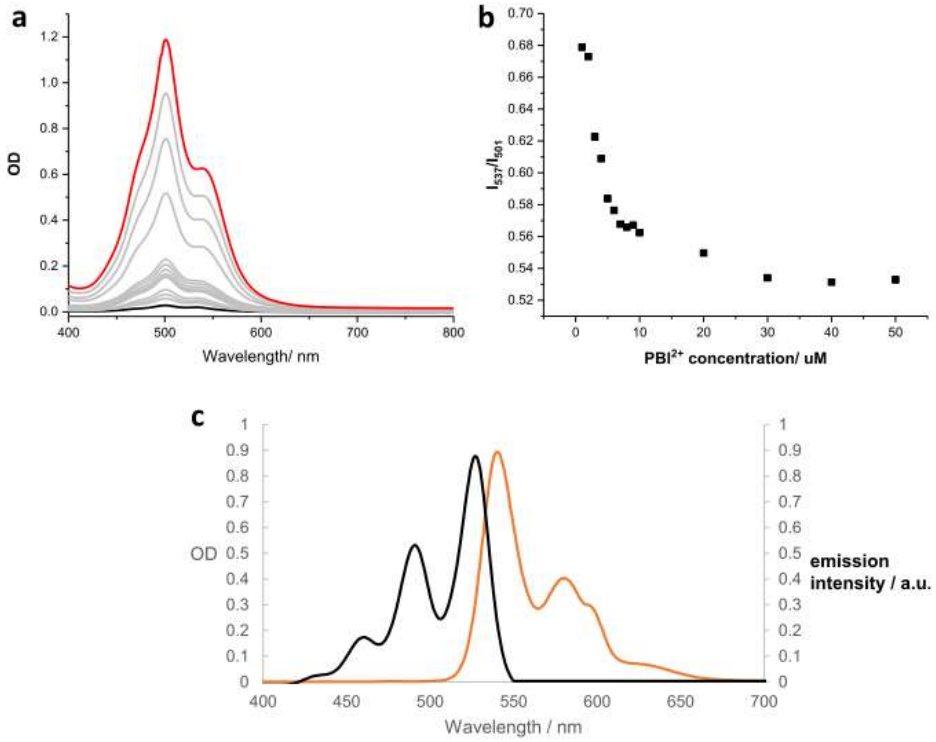

Figure 4.2 Absorption spectra measured for **PBI2+** in PBS buffer 20 mM, pH 7.0, R.T., from 1 μM (black line) to 50 μM (red line). **b**, 537 nm/501 nm ratio dependence on **PBI2+** **c**oncentration. PBS buffer 20 mM, pH 7.0, R.T. **c**, Normalized absorption (black) and fluorescence spectra (red) measured for **PBI2+** in DMF (10 μM). The excitation wavelength was 350 nm.

region and a parallel absorbance bleaching in the 435-517 nm region, with isosbestic points observed at 435 and 517 nm. The sigmoidal fitting of the differential absorbance features (ΔOD) versus the applied potential is used for determining the $E_{1/2}$

(**PBI2+/PBI2+$^{-\bullet}$**) = -0.10 V vs NHE (Figure 4.5). On this basis, and considering the singlet excited state (**PBI2+***) energy of 2.30 eV (available from the emission experiments in Figure 4.2, the redox potential turns out to be E(**PBI2+*/PBI2+$^{-\bullet}$**) = +2.20 V vs NHE. This is one of the most powerful one-electron oxidants that is generated in aqueous solutions, more positive than that of Cerium Ammonium Nitrate (CAN) (+1.75 vs NHE), and significantly more positive than that of $[Ru(bpy)_3]^{3+/2+}$ (+1.26 vs NHE).[82] When probed by CV under the same pH conditions, **Ru4POM** shows oxidations between 0.75 – 1.02 V vs NHE, followed by the catalytic onset of water oxidation at 1.2 V vs NHE (Figure 4.6).[83] Therefore, the thermodynamic driving force of **PBI2+*** is expected to promote a cascade of photoinduced electron transfer events from the **Ru4POM** catalyst and, in turn, to lead to its staircase oxidation, (**Ru4POM(h+)n,** up to the high valent intermediates responsible for the oxygen evolution (Figure 4.14).[73]

4.2.2 An insight into the photosynthetic assembly

The solution assembly of **PBI2+** (0.5 – 50 μM, in 20 mM phosphate buffer pH 7) with **Ru4POM** has been assessed by conductometric and spectrophotometric titrations, fluorescence quenching experiments, DLS and Zeta potential analysis, together with X-Ray Scattering structural studies and AFM imaging. The stoichiometry of the electrostatic interaction has been initially addressed by conductometric titrations, showing the equivalence point at a **Ru4POM/PBI2+** ratio of ca. 1 to 5 (Figure 4.1), as generally observed with organic counter-ions that net balance the POM

charge[66]. Spectrophotometric titration of **PBI2+** upon addition of **Ru4POM** ([**PBI2+**] = 25 μM and [**Ru4POM**] = 0.65 – 8.5 μM in 20 mM phosphate buffer), confirms a [**PBI2+**]$_5$•**Ru4POM** stoichiometry (titration curve registered at 501 nm) with isosbestic points at 465, 522 and 560 nm (Figure 4.3). Indeed, WAXS measurements of aqueous **PBI2+** before (Figure 4.8) and after the addition of **Ru4POM**, show a strong suppression and broadening of the prominent peak at q = 17.6 nm^{-1}, indicating that the π-π **PBI2+** nanostacks are exfoliated upon interaction with **Ru4POM** (Figure 4.1 path (ii)). This notion is further supported by mapping the

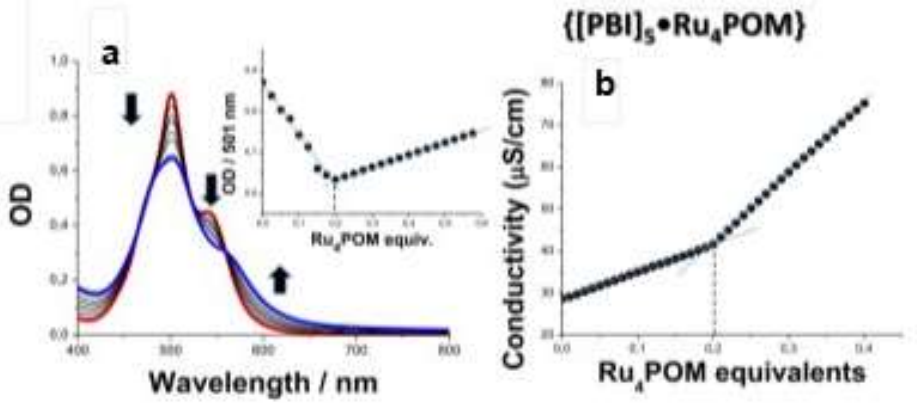

Figure 4.3 a spectrophotometric titration of **PBI2+** nano-stacks in buffer PBS at pH 7 (2.5 × 10-5 M, red line spectrum) with **Ru4POM** (up to 5 × 10^{-6} M, 0.2 eq.) with isosbestic points at 465, 522 and 562 nm, evolving to the {[**PBI2+**]$_5$•**Ru4POM**} quantasome (blue line spectrum), the photo-complex stoichiometry results from the titration curve monitored at 501 nm (inset) and from **f**, conductometric titration with equivalence point at 0.2 equivalents of **Ru4POM**.

electrostatic potential (MEP) of both the **PBI2+** and **Ru4POM** interacting surfaces: their complementary charge distribution is localized at the peripheries of the longest dimension on each of the two molecules, which suggests an almost parallel alignment of **PBI2+** and **Ru4POM** in their electrostatic assembly. The resulting

assembly is ascribed to a POM encapsulated complex, in which the inorganic polyanion templates the arrangement of five surrounding **PBI2+** (Figure 4.1). This supramolecular complex, still an amphiphile, is expected to evolve in solution into higher order aggregates.

How the POM induces exfoliation of the **PBI2+** nano-stacks has been monitored by Zeta Potential analysis (*ζ*-Potential), as a function of the surface charge modification of the supramolecular aggregates forming in solution (Figure 4.7). In the initial phase, addition of substechiometric **Ru4POM** (from 0.02 to 0.12 equivalents, right arrow in Figure 4.3) to the pristine **PBI2+** aggregates (25 μM in 20mM PBS, *ζ*-Potential ~ 0) leads to a steady increase of the zeta potential stage, further addition of **Ru4POM** (from 0.14 to 0.60 equivalents) produces a sharp reversion of the zeta potential values to negative potentials (up to -39.9 mV) which is ascribed to the formation of the **POM-PBI2+** aggregates, stabilized in solution by the negative POM charge. Moreover, DLS analysis shows a distinct shift of the particle size distribution, moving to ca. 1000 nm upon addition of **Ru4POM**.

Self-assembly of **PBI2+** and **Ru4POM** has been addressed by SAXS measurements of aqueous solutions after mixing the two components ([**PBI2+**] = $2x10^{-4}$ M [**Ru4POM**] = $5x10^{-5}$ M, Figure 4.8). A power law fit of the low-q regime reveals a slope of -1.90. This result is consistent with self-assembly of [**PBI2+]5·Ru4POM** into a nano-porous, 2D-superstructure with an approximate thickness of 8.2 nm (Guinier approximation for infinite plate-like particles, Figure 4.8). A closer look at the SAXS profile in the mid-q

scattering part, reveals two correlation peaks around 3 and 4 nm^{-1} (see inset in Figure 4.8) corresponding to molecular d-spacing of 2.25 and 1.62 nm, respectively (Table 4.1). The overall scattering intensity is dominated by the heavy atom POM clusters, making the **PBI2+** transparent to SAXS detection. As such, the scattering features arising from the supramolecular architecture are readily assigned to **Ru4POM-Ru4POM** distances. The analysis of the SAXS profile has been performed by considering the molecular dimensions of **Ru4POM**, showing a vertical length of 1.96 nm and two lateral diameters of 1.19 and 0.97 nm. Therefore, we attribute the d-spacing of 1.62 nm to a **Ru4POM-Ru4POM** motif with intercalated **PBI2+** pairs at a π-π-stacking distance of 0.36 nm, (Figure 4.13).[84] This structural motif is at the origin of the stronger correlation peak at ca. 4 nm^{-1} (Figure 4.8), and it is likely ascribed to an in-plane perpenpendicular alignment of **Ru4POM** within the 2D-nanoplates. On a slightly larger length scale, the mean distance between vertically diffracting planes within the nanoplates is responsible for the d-spacing of 2.25 nm, in agreement with the long-axis dimension of **Ru4POM** (Figure 4.13). Interestingly, the SAXS profile of the solution aggregates is not varied in the presence of ionic additives (e.g. saline buffers), including persulfate, [$Na_2S_2O_4$] = 20 mM, (Figure 4.8), used as sacrificial oxidant under photocatalytic screening. This result is indicative of the structural stability of the **{[PBI2+]$_5$·Ru4POM}n** supramolecular aggregates, which however precipitate over time from the reaction solution thus “switching off” the photocatalytic turnover as it will be discussed in the following sections. AFM imaging of spin coated **{[PBI2+]$_5$·Ru4POM}n** onto a silicon wafer, confirms the 2-D

morphology of the hybrid nano-flakes that collapse into micrometer porous networks, where the particle sub-structure is still apparent with a broad size distribution and an average height of ca 9 nm, in close agreement with the SAXS evidence (Figure 4.10).

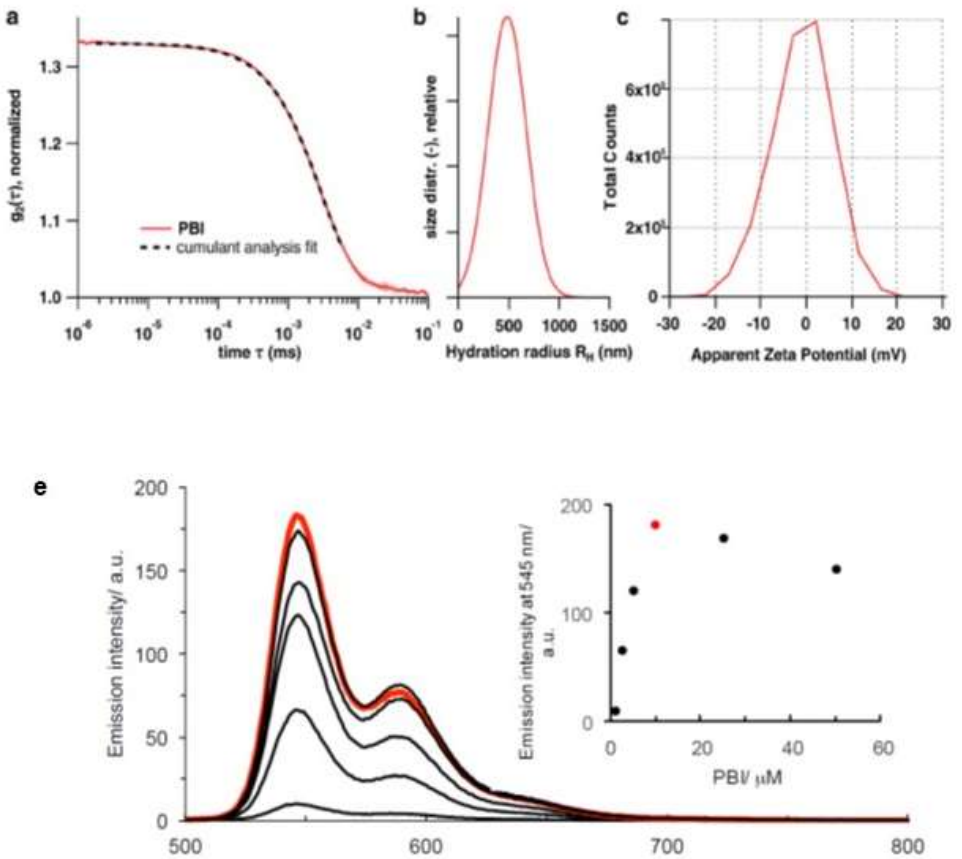

Figure 4.4. **a**, and **b**, Dynamic light scattering and **c**, Zeta potential analysis of **PBI2+** (0.6 mM in 20 mM phosphate buffer pH 7.0). **e** Fluorescence spectra measured for **PBI2+** in PBS 20 mM, pH 7.0, R.T. with concentrations ranging from 1-50 μM. The red line corresponds to [**PBI2+**] = 10 μM. Excitation wavelength 480 nm. Inset: Fluorescence at 545 nm at different [**PBI2+**]. The fluorescence quantum yield (vs Rhodamin 6G, QY = 95%) was found 7% in aqueous phase and 90% in DMF (monomers).

4. Perylene bisimides as photosensitizer

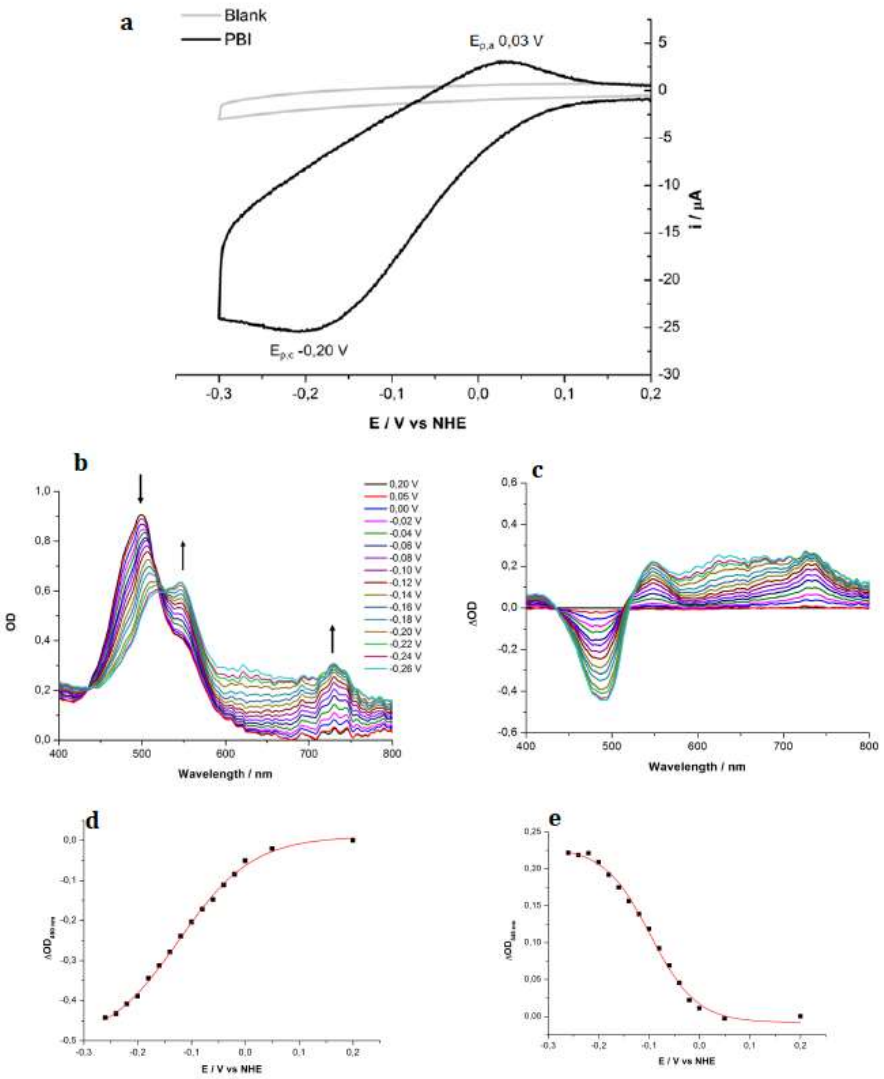

Figure 4.5. **a**, Cyclic voltammetry (CV) obtained under cathodic scan for a solution of **PBI2+** (0.1 mM in 0.2 M phosphate buffer pH 7.0). Working electrode: ITO; counter electrode: platinum wire; reference electrode: Ag/AgCl (3 M NaCl); scan rate = 50 mV/s. **b**, Spectroelectrochemical measurement obtained under cathodic scan (from 0.20 V to -0.26 V vs NHE) for a solution of **PBI2+** (0.5 mM in 0.2 M phosphate buffer pH 7.0, cuvette with 1 mm optical path). Working electrode: platinum grid; counter electrode: platinum wire; reference electrode: Ag/AgCl (3 M NaCl); potentials were then converted against NHE according to $E_{NHE} = E_{Ag/AgCl} + 0.197$ V; **c**, differential absorption spectra of **PBI2+** (0.5 mM) under cathodic scan. Sigmoidal fitting of the differential absorption spectra at **d**, 490 nm and **e**, 546 nm versus the applied potential.

4. Perylene bisimides as photosensitizer

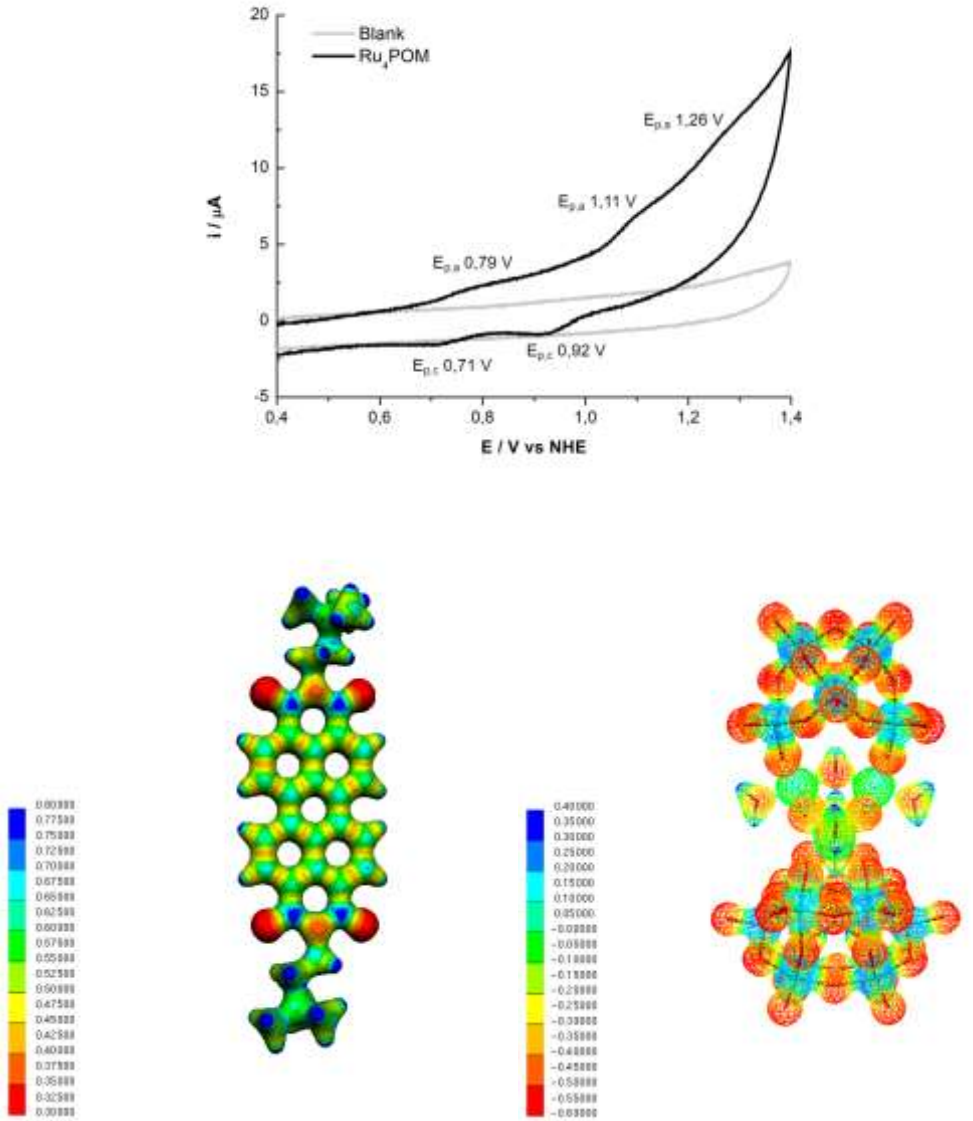

Figure 1.6 Cyclic voltammetry (CV) obtained under cathodic scan for a solution of **Ru4POM** (0.5 mM) in Britton-Robinson buffer pH 7 with 0.1 M KNO_3 as supporting electrolyte). Working electrode: platinum; counter electrode: platinum wire; reference electrode: Ag/AgCl (3 M NaCl). Potentials were then converted against NHE according to the equation $E_{NHE} = E_{Ag/AgCl} + 0.197$ V. Left: molecular electrostatic potential (MEP) of **PBI2+** (blue and red regions indicate positive and negative electrostatic potential, respectively). **PBI2+** geometry optimization was started from the crystallographic structure and was performed at the B3LYP/6-31g level. Right: MEP of **Ru4POM** (blue and red regions indicate positive and negative electrostatic potential, respectively). A single point energy of the **Ru4POM** was optimized, based on the crystallographic structure was performed at the B3LYP/6-31g level. MEP was represented with the Molekel program, 4.3 version.

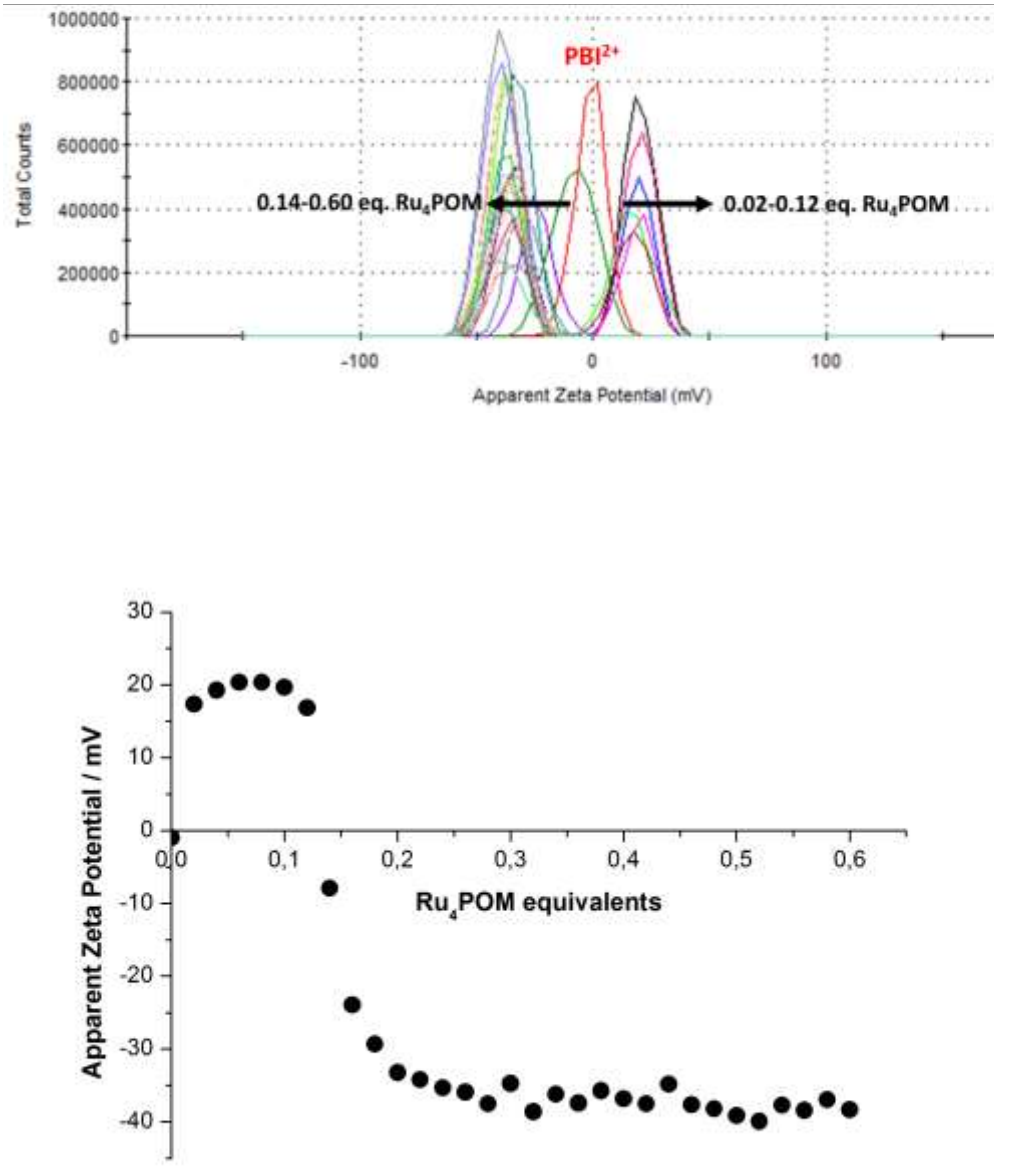

Figure 4.7 Top: ζ-Potential measurements of **PBI2+** (25 µM, red line) upon addition of **Ru4POM** (up to 0.6 eq., 15 µM) in 20 mM phosphate buffer pH 7.0. First additions (from 0.02 to 0.12 **Ru4POM** equivalents, right arrow) lead to positive potentials (up to +20.4 mV), while subsequent additions (from 0.14 to 0.60 **Ru4POM** equivalents, left arrow) lead to negative potentials (up to - 39.9 mV). Bottom: plot of the measured apparent zeta potential against **Ru4POM** equivalents. Experimental conditions: [**PBI2+**] = 25 µM, [**Ru4POM**] = 0 – 15 µM, in 20 mM phosphate buffer pH 7.0.

	Peak 1	**Peak 2**
Peak position (nm^{-1})	2.79 ± 0.03	3.87 ± 0.06
Corr. D-spacing (nm)	2.25 ± 0.04	1.62 ± 0.05
Peak width (nm^{-1})	0.78 ± 0.16	8.05 ± 3.45
Coherent domain size (nm)	2.70 ± 0.11	2.34 ± 0.19

Table 4.1. Parameters of the Gaussian peaks fitted to the SAXS data of **PBI2+•Ru4POM** with $Na_2S_2O_8$ shown in Figure 4.8. The grey entries are the translations of the fit-results in reciprocal space (q) into measures in real-space (d) according to $d = 2\pi/q$.

	PBI2+	**PBI2+°Ru4POM**
Temperature (°C)	22.14	22.23
Decay rate Γ (s^{-1})	159.64 ± 1.83	94.11 ± 1.03
Hydration radius RH (nm)	497.5 ± 5.08	843.74 ± 9.72
Size distribution σ (nm)	151.19 ± 30.21	425.67 ± 120.31

Table 4.2. Results of the cumulate analysis fits in Figure 4.8 from which the mean aggregate dimensions were retrieved. Measurements were made at an scattering angle of θ=90° whereas the refractive index of the buffer was n=1.33. The temperature was measured throughout the experiment.

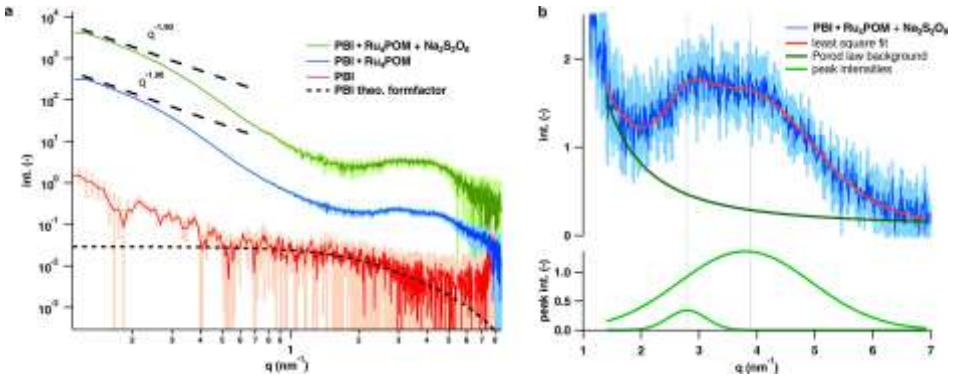

Figure 4.8 a, SAXS measurements of **PBI2+** (red) at [**PBI2+**] = 0.6 mM as well as **PBI2+•Ru4POM** before (green) and after (blue) the addition of Na2S2O8 at pH 7 (in PBS 20 mM pH 7) to result in [**Ru4POM**] = 50 µM, [**PBI2+**] = 0.2 mM and [$Na_2S_2O_8$]=20mM. A comparison of the experimental **PBI2+** scattering with a theoretically calculated formfactor (see black dotted line) highlights a distinct deviation in the low-q regime, characteristic for aggregate scattering. The addition of **Ru4POM** results in nanometer sized plates as confirmed by the low-q slope of -1.90. Already at this stage, two correlation peaks in the mid-q region can be seen. A subsequent addition of the SAE $Na_2S_2O_8$ yields no significant effect on the scattering behavior, confirming the structural stability of both the nano-morphology and the intermolecular motive of the hybrid. **b**, Detailed section of the correlation peaks seen in the SAXS measurement of **PBI2+•Ru4POM** with $Na_2S_2O_8$ as shown above. Two Gaussian peaks were fitted on top of a Porod background with slope q-2 using a least square method. The peaks are found at 2.79 ± 0.03 nm^{-1} and 3.87 ± 0.06 nm^{-1}, corresponding to d-spacings of 2.25 ± 0.04 nm and 1.62 ± 0.05 nm, respectively. The detailed results can be found in Table 4.1.

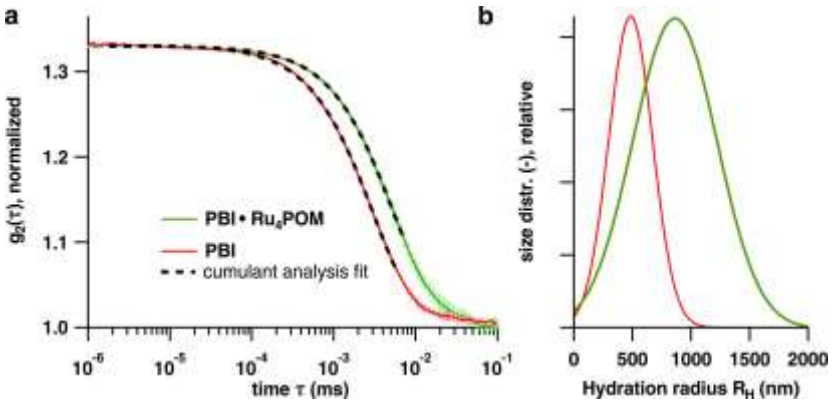

Figure 4.9 a, DLS measurements of **PBI2+** (0.6 mM, red) as well as **PBI2+•Ru4POM** at pH 7 (in PBS 20 mM pH 7) to result in [**Ru4POM**] = 50 µM, [**PBI2+**] = 0.2 mM . The autocorrelation functions were fitted (black lines) using the cumulant analysis, whereas the results are presented in Table 4.2. **b**, Relative size distributions calculated from the model fits shown in **A**. **PBI2+** in aqueous solution is in an aggregated state, whereas the mean hydration radius is approx. 500 nm. Upon addition of **Ru4POM,** this measure increases to approx. 850 nm.

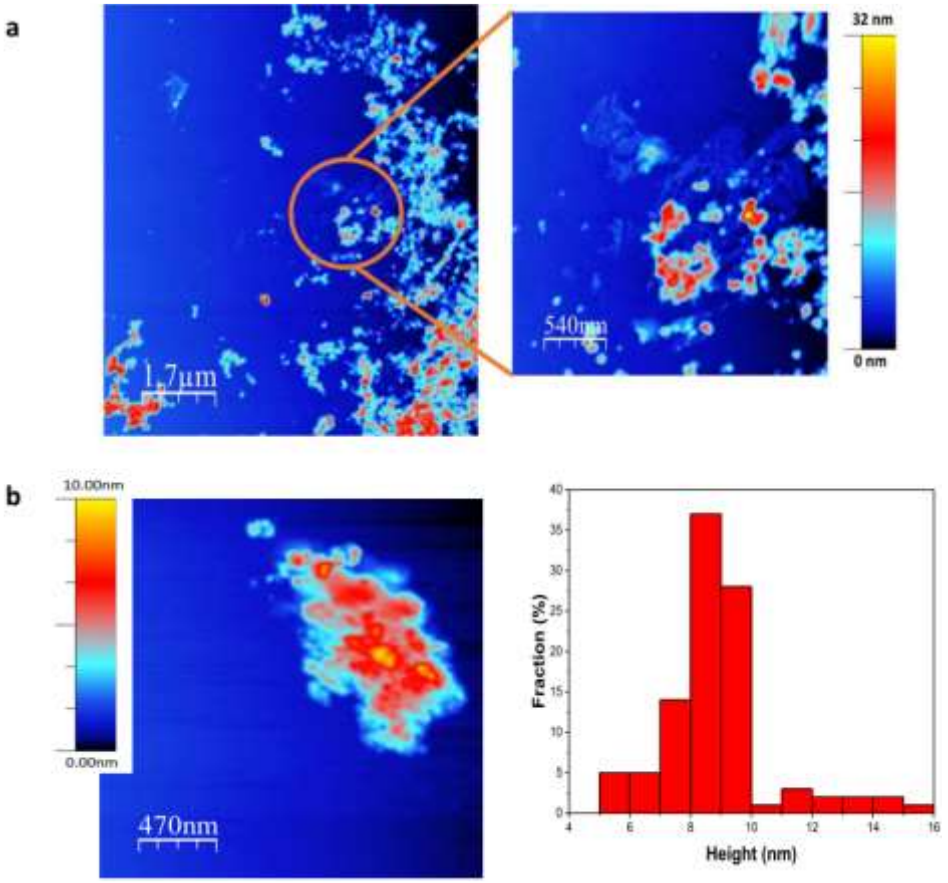

Figure 4.10. AFM images of **{[PBI2+]5·Ru4POM}*n*** aggregates formed in PBS 20mM, pH 7.0 and deposited onto a silicon wafer by spin coating. a, Representative overview images, confirming the presence micro-meter porous aggregates featuring a nano-flake substructure. b, Zoomed image of a composite fragment together with a corresponding height-distribution histogram.

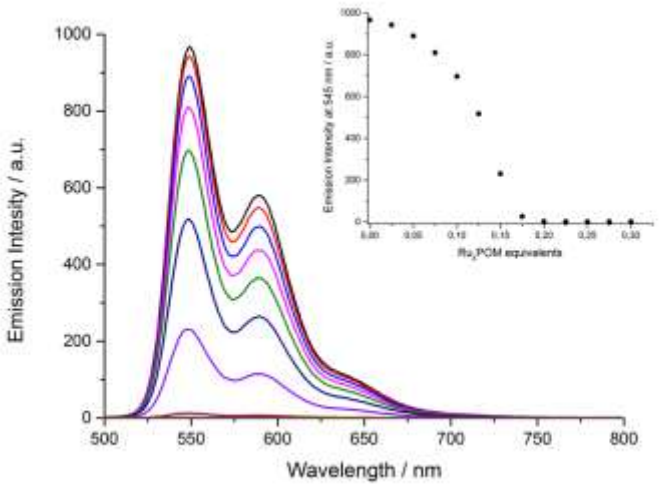

Figure 4.11. Fluorimetric titration of **PBI2+** (10 μM) in PBS 20 mM, pH 7.0, R.T., with **Ru4POM** (0 to 0.3 equivalents). Excitation wavelength 480 nm. Inset: Fluorescence at 545 nm upon addition of different **Ru4POM** equivalents.

,

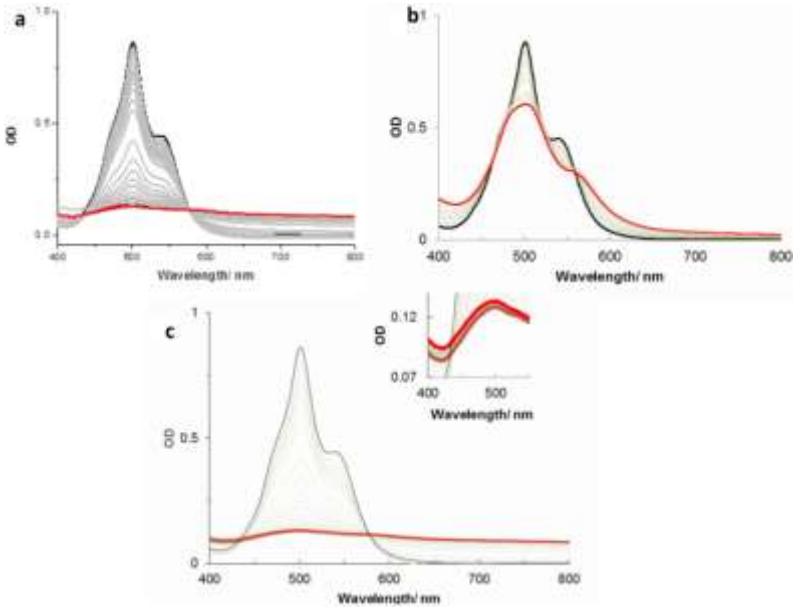

Figure 4.12 a, Spectrophotometric titration of **PBI2+** in PBS 20 mM, pH 7.0, R.T., **PBI2+** 25 μM (black line) with Na2S2O8 from 0 equiv. to 20 equiv. (red line). **b**, Spectrophotometric titration of **PBI2+** in PBS 20 mM, pH 7.0, R.T., **PBI2+** 25 μM (black line) first with **Ru4POM** from 0 equiv. to 0.2 equiv. (red line) and successively $Na_2S_2O_8$ from 0 equiv. to 20 equivalents (sequence of the addition: **PBI2+**, **Ru4POM**, $Na_2S_2O_8$). **c**, Spectrophotometric titration of **PBI2+** in PBS 20 mM, pH 7.0, R.T. 25 μM (black line) first with $Na_2S_2O_8$ from 0 equiv. to 20 equiv. (orange line) and successively **Ru4POM** from 0 equiv. to 0.3 equiv. (red line) (sequence of the addition: **PBI2+**, **$Na_2S_2O_8$**, **Ru4POM**).

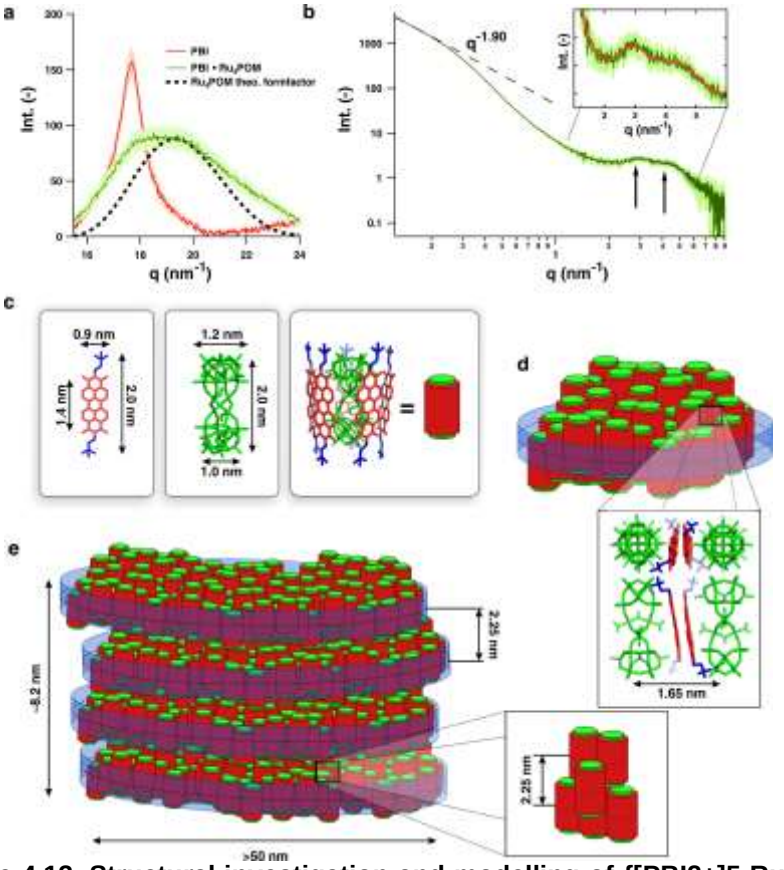

Figure 4.13. **Structural investigation and modelling of {[PBI2+]5·Ru4POM}n photosynthetic aggregates**. Wide angle x-ray scattering (WAXS) measurements of 40mM **PBI2+** before (red) and after (green) the addition of 10mM **Ru4POM** in aqueous solvent compared to the theoretical **Ru4POM** form factor scattering (black) calculated using CRYSOL**. b**, Small angle x-ray scattering (SAXS) data for {[**PBI2+]5•Ru4POM}n** (green) in aqueous solution (20mM [**PBI2+**] in 20mM PBS buffer, 0.075mM **Ru4POM** in 20mM PBS buffer, mixed in ratio 5:1). The low-q Porod slope of -1.9 indicates the formation of a porous 2D super-structure. Further, two disordered correlation peaks can be seen in the mid-q regime (black arrows): a peak-ftting (red line in inset) links these peaks to corresponding d-spacings of 1.62 and 2.25 nm; the coherent domain size of the 1.62 nm d spacing is significantly lower than the one corresponding to 2.25 nm, hence, the two peaks are caused by two different structural motifs, Table 4.1. **c**, Figurative representation of the encapsulated [**PBI2+]5•Ru4POM** building-block. **d**, Representation of single lamellar planes, built from the parallel alignment of {[**PBI2+]$_5$•Ru4POM}n** with a mean in-plane distance of 1.65 nm. The zoom-in highlights the **Ru4POM**–**PBI2+**//**PBI2+**–**Ru4POM** supramolecular motif of this arrangement, originating the second correlation peak in the data. **e**, Multi-scale model representation of stacked lamellae. Even though the building-blocks are not necessarily confined to the each lamellae, the mean molecular out-of-plane distance corresponds to 2.25 nm, causing the first correlation peak in the scattering data

4.2.3 Photo-assisted water oxidation

The electrostatic assembly of **PBI2+** with **Ru4POM** is expected to leverage an electron donor acceptor interaction, whereby photo-induced electron transfer takes place from **Ru4POM** to the photosensitizer excited state, **PBI2+***. Indeed fluorescence titration of aqueous **PBI2+** upon **Ru4POM** addition shows a progressive quenching of the **PBI2+** fluorescence that levels off at the expected stoichiometry of the assembly, ***{[PBI2+]5·Ru4POM}n*** (Figure 4.3).[81] Therefore, and according to the thermodynamics, a **PBI2+(e^-)•Ru4POM(h^+)** charge-separated state is generated as a primary event upon **PBI2+** excitation, followed by a photoinduced electron transfer mechanism that enables **Ru4POM** to climb several oxidation states (**Ru4POM(nh^+)**), in close analogy with the natural PSII cycle (4.14).[14,85] Photo-assisted water oxidation catalysis is generally probed in the presence of persulfate ($S_2O_8^{2-}$) used as terminal electron acceptor, to drive the multi-step oxidation cycle, while preventing unproductive back-electron transfer pathways.[82] In this specific case, the relevant steps include: (*i*) light absorption and generation of photoexcited **PBI2+*** (Eq. 4.1); (*ii*) photo-induced charge-separation (Eq. 4.2); (*iii*) electron scavenging by $S_2O_8^{2-}$, restoring **PBI2+** with simultaneous formation of SO_4^{2-} and $SO_4^{\bullet-}$ (Eq. 4.3); (*iv*) oxidation of **Ru4POM(h^+)** to **Ru4POM($2h^+$)** by $SO_4^{\bullet-}$ (Eq. 4.4); (*v*) a multi-hole accumulation loop via steps i-iv, (vi) oxygen evolution (Eq. 4.5).

PBI2+ + hv → **PBI2+*** (4.1)

PBI2+* + **Ru4POM** → **PBI2+$^{\bullet-}$** + **Ru4POM(h$^+$)** (4.2)

PBI2+$^{\bullet-}$ + $S_2O_8^{2-}$ → **PBI2+** + SO_4^{2-} + $SO_4^{\bullet-}$ (4.3)

Ru4POM(h$^+$) + $SO4^{\bullet-}$ → **Ru4POM(2h$^+$)** + SO_4^{2-} (4.4)

Ru4POM(nh$^+$) + $2H_2O$ → **Ru4POM((n-4)h$^+$)** + O_2 +$4H^+$ (4.5)

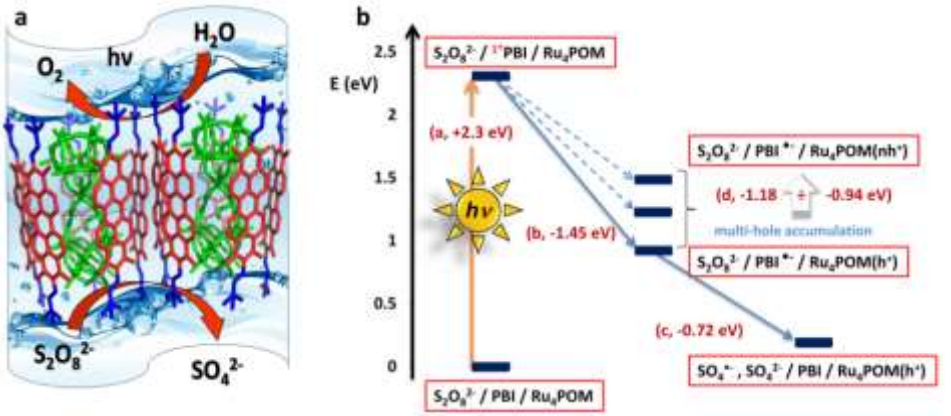

Figure 4.14. **Photoassisted water oxidation by {[PBI2+]5·Ru4POM}n** in the presence of persulfate as terminal electron acceptor (sacrificial cycle, equations 1.1-1.5). (a) schematic of the photosynthetic units and inter-lamellae hydrophilic channels for water access. (b) Energy levels for the first elementary steps involved in the photocatalytic cycle for oxygen production, in the S2O82- / **PBI2+** / **Ru4POM** system: (a) light absorption and generation of **1*PBI2+**; (b) electron transfer from **Ru4POM** to **1*PBI2+**, forming reduced **PBI2+•-** and oxidized **Ru4POM(h+)** (charge separation); (c) electron transfer from PBI2+•- to $S_2O_8^{2-}$, restoring **PBI2+** with simultaneous reduction of $S_2O_8^{2-}$ and formation of $SO_4^{\bullet-}$. The energy of the charge-separated states has been calculated without electrostatic correction applied; charge-recombination steps between **Ru4POM(h+)** and **PBI2+•-** are omitted for clarity. The dotted arrows represent the electron transfer steps between **Ru4POM** and **PBI2+*** leading to multi-hole accumulation on **Ru4POM** responsible for water oxidation (exergonic by 0.94 – 1.18 eV). For detailed description of the energy levels see Supplementary Information.

Equations 4.1-4.5 are represented in the energy diagram of Figure 4.14. Considering that E(**PBI2+*/PBI2+$^{\bullet-}$**) = +2.20 V vs NHE, the primary electron transfer forming **Ru4POM(h+)** is exergonic by 1.45 eV, and subsequent multi-hole accumulation occurs by

exergonic steps in the range from 1.18 to 0.94 eV. At the same time, the **PBI2+** ground-state is restored via irreversible electron scavenging by persulfate, $S_2O_8^{2-}$, that turns out to be also exergonic by 0.72 eV. This favorable thermodynamics data sets the basis for photo-assisted oxygen evolution in water by the ternary **PBI2+/Ru4POM/$S_2O_8^{2-}$** system. In this context, water oxidation experiments have been performed in buffer solution (PBS 20 mM, pH7), containing **PBI2+** (10^{-4} M), **Ru4POM** (3-60×10^{-6} M), and $S_2O_8^{2-}$ (10^{-3} M), upon irradiation with a LED white lamp (4.5 mW/cm^2) (Table 4.3, Figure 4.15). In all cases, the reaction solution shows the spectroscopic footprint of the **{[PBI2+]$_5$·Ru4POM}n** nano-hybrids, which is readily established upon mixing of the two components. No relevant spectral variation is observed upon addition of persulfate (Figure 4.16). This observation is consistent with the SAXS results and confirms a favored POM encapsulation by cationic **PBI2+** due to a strong electrostatic assembly. Control experiments confirm that oxygen evolution requires the simultaneous presence of all the three components, **PBI2+/Ru4POM/$S_2O_8^{2-}$** (Table 4.3). Inspection of data in Table 4.3 shows that the oxygen evolution kinetics depend on the **Ru4POM** concentration. In particular, the photocatalytic rate increases steadily for [**Ru4POM**] < 15 μM and saturates soon after (Figure 4.15). Both reaction rate and oxygen production reach the highest values at [**Ru4POM**] ~ 20 μM (Figure 4.15b), corresponding to a **PBI2+**/**Ru4POM** ratio of 5:1 (Figure 4.15b). This is the expected stoichiometry for the **PBI2+**-encapsulated **Ru4POM**, i.e the building block of the {[**PBI2+]$_5$·Ru4POM}*n*** lamellar-type structure, which turns out to be the minimal photosynthetic unit responsible for

oxygen evolution. In all cases, oxygen evolution ends after ca. 60 minutes (Figure 4.15) featuring a persulfate conversion up to 5% and turnover numbers <4 (Table 4.3). Sonication of the reaction mixture or further addition of persulfate fail to restore the pristine activity. Under these conditions, the sensitizer bleaching is negligible, as confirmed by Uv-Vis analysis of the recovered reaction mixture (Figure 4.16). While PBI sensitizers proved to be highly robust with respect to classical $Ru(bpy)_3^{2+}$, in the present case inhibition of the photocatalytic activity was found to depend on the sulfate (SO_4^{2-}) by-product, generated upon persulfate reduction. Indeed, addition of SO_4^{2-} (2×10^{-4} M) to a freshly prepared reaction mixture, leads to a remarkable abatement of the photosynthetic activity (entry 6 in Table 4.3), which is possibly ascribed to competitive equilibria involving persulfate in the assembly of the ternary photo-active material. This problem is limited to the persulfate sacrificial cycle in solution, and does not apply to regenerative photosynthetic cells (see next sections). The photo-induced water oxidation mechanism by the ternary **PBI2+**/**Ru4POM**/$S_2O_8^{2-}$ system has been probed by a detailed laser flash photolysis study.

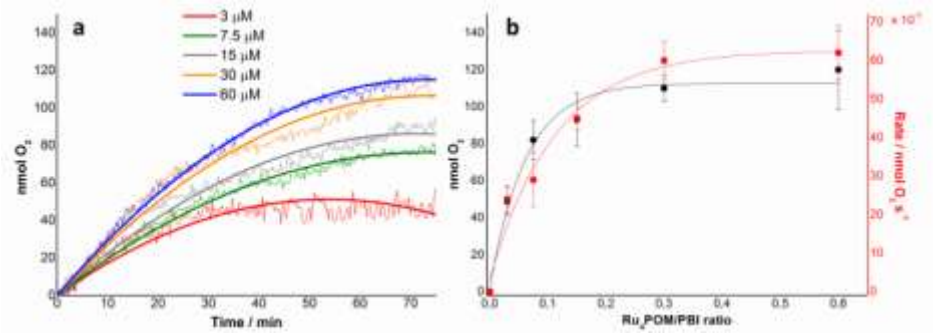

Figure 4.15 Photo-assisted water oxidation by {[**PBI2+**]5•**Ru4POM**}n with persulfate as sacrificial acceptor under visible light irradiation. **a**, Oxygen evolution kinetics (dashed lines) monitored in 20 mM phosphate buffer pH 7 upon irradiation with a LED white lamp (4.5 mW/cm^2) of **PBI2+** (10^{-4} M) in the presence of **Ru4POM** (3.0 - 60×10^{-6} M) and $S_2O_8^{2-}$ (10^{-3} M). **b**, Plot of O_2 production (left axis, black plot) and of the initial rate of O_2 production (right axis, red plot) against **Ru4POM**/**PBI2+** ratio. Kinetics conditions: [**PBI2+**] = 10-4 M, [$S_2O_8^{2-}$] = 10^{-3} M in 20 mM phosphate buffer pH 7.0, R.T. Fittings of the data are reported by solid lines.

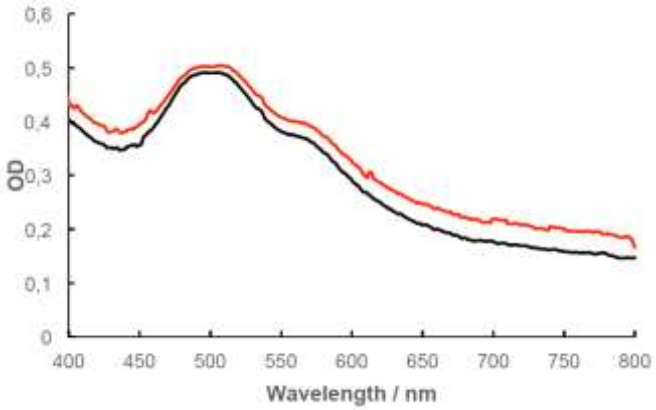

Figure 4.16 Absorption analysis (optical path 1 mm) of the reaction mixture before and after oxygen evolving catalysis. Conditions: $Na_2S_2O_8$ (1 mM), **PBI2+** (0.1 mM), **Ru4POM** (15 μM) in a 20 mM PBS buffer of pH 7.0 – see entry 2 in Table 4.3. The slight shift of the baseline is likely due to light scattering by aggregate

Table 4.3. Photo-assisted water oxidation by the ternary **PBI2+**/**Ru4POM**/$S_2O_8^{2-}$ system.[a]

#	[**Ru4POM**] μM	μmol O_2[b] (TON)[c]	Rate/10^{-6} [d], μmol O_2 s^{-1} (TOF/10^{-3}, s^{-1})[e]	Yield,[f] %	Φ,[g]
1	3.0	0.05±0.01 (3.6±0.5)	24±4 (1.78±0.27)	2.2	0.009
2	7.5	0.08±0.01 (2.4±0.3)	29±7 (0.86±0.21)	3.6	0.011
3	15	0.09±0.01 (1.4±0.2)	45±3 (0.67±0.04)	4.1	0.017
4	30	0.11±0.01 (0.8±0.1)	60±5 (0.44±0.04)	4.9	0.022
5	60	0.12±0.02 (0.4±0.1)	62±7 (0.23±0.03)	5.3	0.023
6	60	0.043 (0.16)	8.3 0.03	1.7	0.008

[a] Reaction conditions: 4.5 mL of 20 mM phosphate buffer, pH = 7.0, [**PBI2+**] = 0.1 mM, $[S_2O_8]^{2-}$ = 1 mM, irradiation with a spotlight (4.5 mW/cm^2). [b]μmol O_2 determined after 80 min. [c]Turnover number (TON) calculated as μmol O_2 per μmol **Ru4POM**. [d] Initial rate of O_2 production determined as the linear kinetic slope. [e] Turnover frequency (TOF) calculated as TON per second. [f] Determined on persulfate conversion after 80 min. [g] Quantum yield determined by the ratio of evolved oxygen and the absorbed photons, in the first 15 minutes of irradiation. [h]Reaction in the presence of 2×10^{-4} M Na_2SO_4.

4.2.4 Photo-induced Transient States

We have used femtosecond resolved pump probe spectroscopy to address the excited state dynamics of aqueous **PBI2+** in the absence and in the presence of **Ru4POM**. In the first case, upon 530 nm laser excitation, transient spectra develop and are characterized by a ground state bleaching centered at 500 nm accompanied by maxima at 590, 700, 860, and 950 nm. These transient features are assigned to the singlet excited state of **PBI2+** aggregates, evolving with a monoexponential decay with a fairly short lived nature of ca 200 ps. The impact of **Ru4POM** association on the excited state features has been investigated by time resolved experiments and the corresponding data were fitted by multiwavelength analysis as well as global analysis to address: (*i*) the evolution of the photoexcited hybrids into a charge-separated state, (*ii*) the mechanism and kinetics of photo-induced electron transfer, (*iii*) the nature of the photo-generated intermediates, and (*iv*) their lifetime and competitive recombination kinetics. The photosynthetic assembly ([**PBI2+**] = 10^{-4} M, [**Ru4POM**] = 6×10^{-5} M) that is responsible for the oxygen evolution plateau (entry 5 in Table 4.3) was probed in water (pH 7, 0.02 M phosphate buffer) upon 530 nm excitation (Figure 4.17). A differential absorption spectrum develops immediately after laser excitation, which includes a strong minimum ranging from 440 to 540 nm, originating from the ground state bleaching of the formed **{[PBI2+]$_5$•Ru4POM}*n*** hybrids, maxima at 430, 550, 865 and 990 nm and a broad transient, which spreads from 600 to 800 nm (Figure 4.17a). Notably, this latter feature transforms in less than 25 ps into a transient with a maximum at around 750 nm, whereas

the 865 nm feature shifts to 820 nm and the 990 nm maximum sharpens. These new signals, which are formed with the concomitant disappearance of the ground-state features, are ascribed to the one-electron reduced **PBI2+•** as confirmed by the spectroelectrochemistry data (Figure 4.18). We can conclude that photoexcitation of the **{[PBI2+]5•Ru4POM}*n*** hybrid is followed by a rapid intramolecular charge separation driven by the strong oxidation power of the **PBI2+** singlet excited state, to yield the **PBI2+(e-)•Ru4POM(h$^+$)** charge-separated state.

As a complement to multiwavelength analyses, we performed global analyses with the Glotaran software package (Figure 4.19). The sequential model analysis yields unimolecular rate constants for charge separation from the **{[PBI2+]5•Ru4POM}*n*** excited state (kcs = 4.0 ± 0.02 × 1010 s-1) and charge recombination from the **PBI2+(e$^-$)•Ru4POM(h$^+$)** charge-separated state (kcr= 9.5 ± 0.06 × 108 s^{-1}). In such conditions, recombination processes, which occur in hundreds of picoseconds regime are too fast to guarantee the sequential “hole-accumulation” at the water oxidation catalyst. Indeed, oxygen evolution has been confirmed only upon addition of persulfate as sacrificial acceptor (Table 4.3). The impact of $S_2O_8^{2-}$ addition on the photo-induced **PBI2+(e-)•Ru4POM(h+)** charge separated state has thus been probed under similar conditions. The shape of the differential absorption spectra in the presence of $S_2O_8^{2-}$ and the charge separation kinetics are identical to those seen in its absence, confirming the maintenance in solution of the hybrid photocomplex (Figure 4.17).

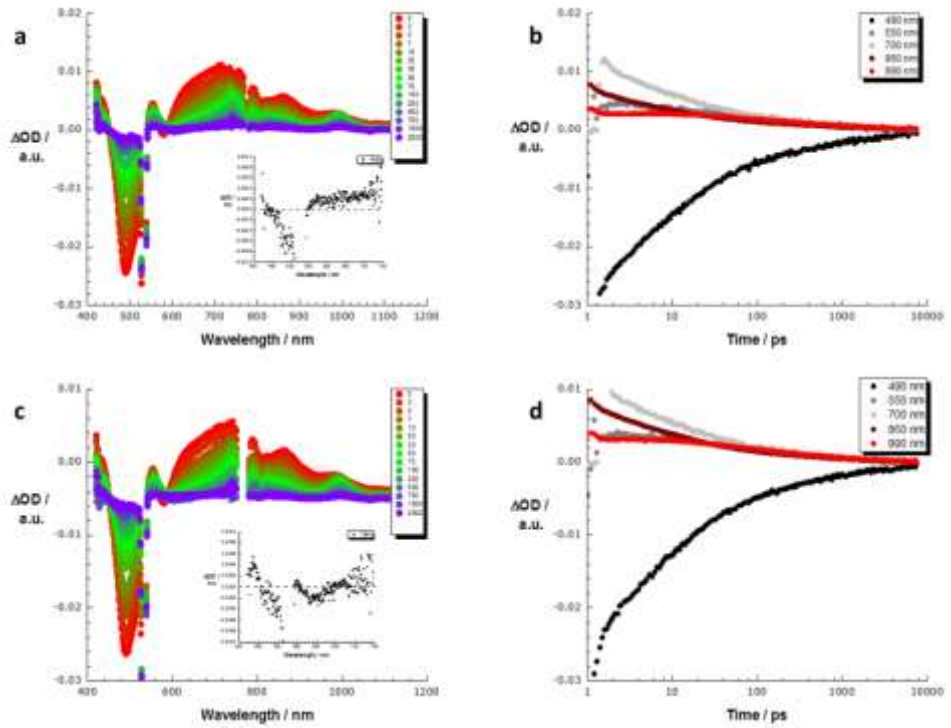

Figure 4.17. Temporal evolution and transient dynamics of the {[PBI2+]5•Ru4POM}n photosynthetic ensemble. **a**, Differential absorption spectra of {[**PBI2+**]5•**Ru4POM**}n with [**PBI2+**] = 1 × 10^{-4} M and [**Ru4POM**] = 6 × 10^{-5} M recorded in aqueous phosphate buffer (0.02 M / pH 7) with several time delays between 2 ps (red) and 2000 ps (purple) obtained upon femtosecond flash photolysis (530 nm). The inset displays the differential absorption spectra at a time delay of 7500 ps. **b**, Corresponding time absorption profiles taken at 490 nm (black), 550 nm (dark grey), 700 nm (light grey), 860 nm (brown), and 990 nm (red) monitoring the formation and decay of the PBI2+(e-)•Ru4POM(h+) charge-separated state in terms of charge separation and charge recombination. **c**, Differential absorption spectra of {[**PBI2+**]$_5$•**Ru4POM**}n with [**PBI2+**] = 1 × 10-4 M and [**Ru4POM**] = 6 × 10^{-5} M in presence of 1 x 10-3 M sodium persulfate recorded under the same conditions as in the case of (**a**). The inset displays the differential absorption spectra at a time delay of 7500 ps. **d**, Corresponding time absorption profiles taken at 490 nm (black), 550 nm (dark grey), 700 nm (light grey), 860 nm (brown) and 990 nm (red) monitoring the formation and decay of the **PBI2+(e-)•Ru4POM(h+)** charge-separated state in terms of charge separation and charge shift from sodium persulfate.

However, addition of variable $S_2O_8^{2-}$ concentrations (2 × 10^{-4}, 5 × 10^{-4}, and 1 × 10^{-}3 M) leads to a modification of the **PBI2+(e-**

)•Ru4POM(h+) dynamics. In particular, the decay of the one-electron reduced **PBI2+$^{\bullet-}$**, within the charge separated state, turns out to be accelerated in the presence of $S_2O_8^{2-}$ (Figure 4.17). This behavior is ascribed to the sacrificial oxidant, acting as one-electron acceptor and restoring the **PBI2+** ground state, while producing a long-lived **Ru4POM(h+)**. Global analyses of the transient decay including the electron scavenging step by $S_2O_8^{2-}$ (Figure 4.18), yields a rate constant for the **PBI2+** regeneration that outperforms the charge recombination event by ca. 6 folds (k4= 5.6 ± 0.1 × 109 s^{-1} versus k3= 9.5 ± 0.06 × 108 s^{-1}, 4.20). In summary, the $S_2O_8^{2-}$ attack on **PBI2+$^{\bullet-}$** opens an additional deactivation channel for the **PBI2+(e$^-$)•Ru4POM(h$^+$)** charge-separated state and guarantees a fast regeneration of the sensitizer ground state. This is instrumental for sequential hole scavenging by **Ru4POM** under photoirradiation. Control experiments performed by substituting persulfate with the spent sulfate by-product, showed no appreciable impact neither on the spectroscopy nor on the kinetics of the charge-separated state, which highlights the role played by the sacrificial electron acceptor.

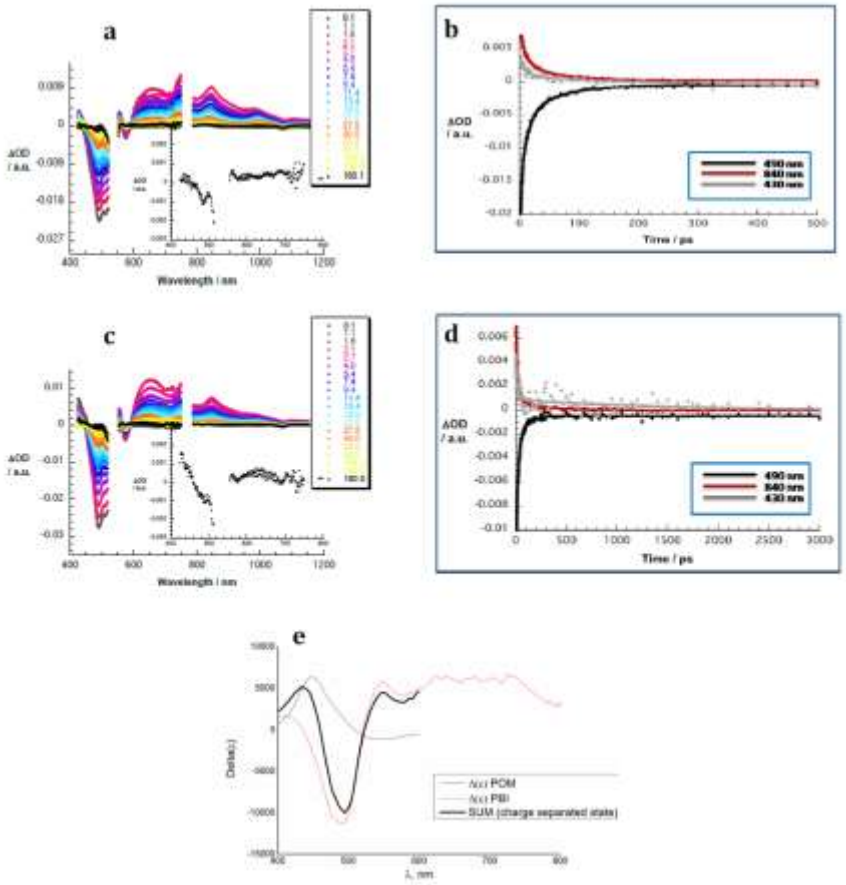

Figure 4.18 Temporal evolution and transient dynamics of the **PBI2+•Ru4POM** photosynthetic ensemble. **a**, Differential absorption spectra of **PBI2+•Ru4POM** (10-6 M) obtained upon femtosecond flash photolysis (530 nm) in hydrochloric aqueous solution (pH 2.5) with several time delays between 0.1 and 160.1 ps at room temperature, showing the spectral signature of the **PBI2+•-•Ru4POM(h+)** radical ion pair. Inset displays the differential absorption spectrum with a time delay of 160.1 ps. **b**, Time absorption profiles of the differential spectra shown in (a): grey line @430 nm – **Ru4POM(h+)**, black line at 490 nm – bleaching recovery of the ground state, and red line at 840 nm – (**PBI2+•-**), showing a lifetime of the **PBI2+•-•Ru4POM(h+)** of 136 ps. **c**, Differential absorption spectra obtained in the presence of persulfate (0.05 M) see description above. **d**, Time absorption profiles of the **Ru4POM(h+)/ PBI2+•-** radical ion pair transient in the presence of persulfate: **PBI2+•-**decay (red line at 840 nm) is accelerated to 69 ps, while **Ru4POM(h+)** (grey line @430 nm) survives the 8 ns time scale of the experiments. **e**, simulated differential absorption spectrum of the charge separated state **PBI2+•-•Ru4POM(h+)** obtained from the sum of the differential absorption spectra of **Ru4POM(h+)** and of **PBI2+•-**, obtained from spectroelectrochemistry.

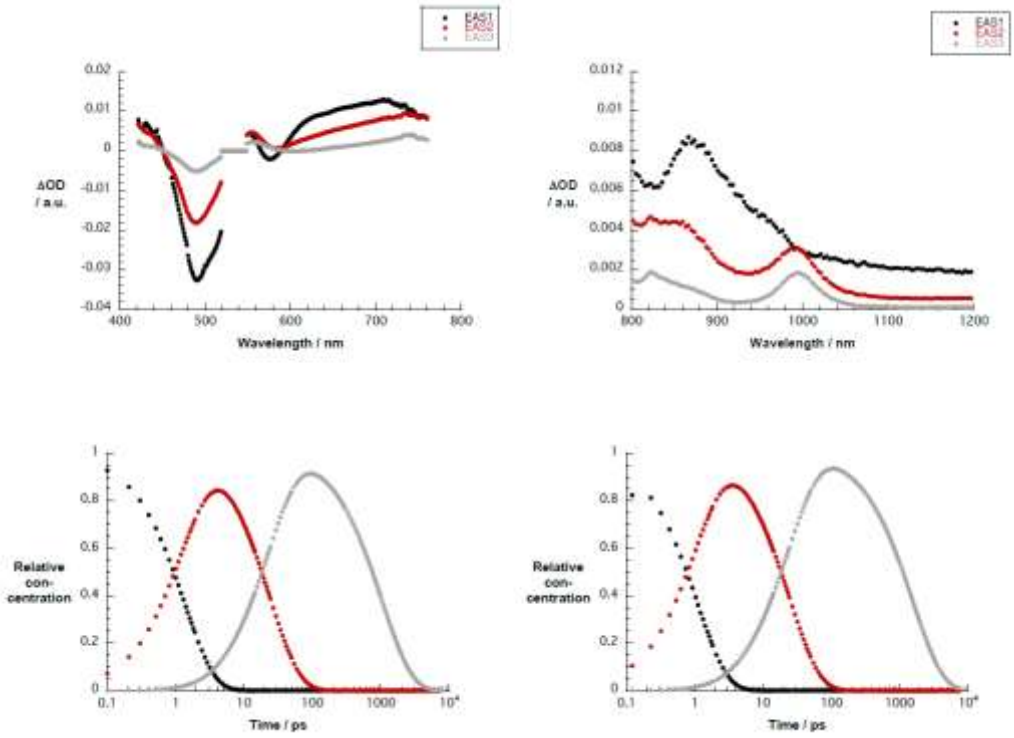

Figure 4.19. Top – Kinetic model used to fit / deconvolve the excited state surfaces of **PBI2+Ru4POM** at pH 7 via GloTarAn with states 1, 2, and 3 being a higher **{[PBI2+]5•Ru4POM}*n*** excited state, the **{[PBI2+]5•Ru4POM}*n*** excited state and the **PBI2+•-•Ru4POM(h+)** charge-separated state, respectively. Center left –Deconvoluted transient absorption spectra in the visible. Center right – (left) Deconvoluted transient absorption spectra in the near-infrared. Bottom – Evolution of the population of the involved states in the visible (left) and in the near-infrared (right).

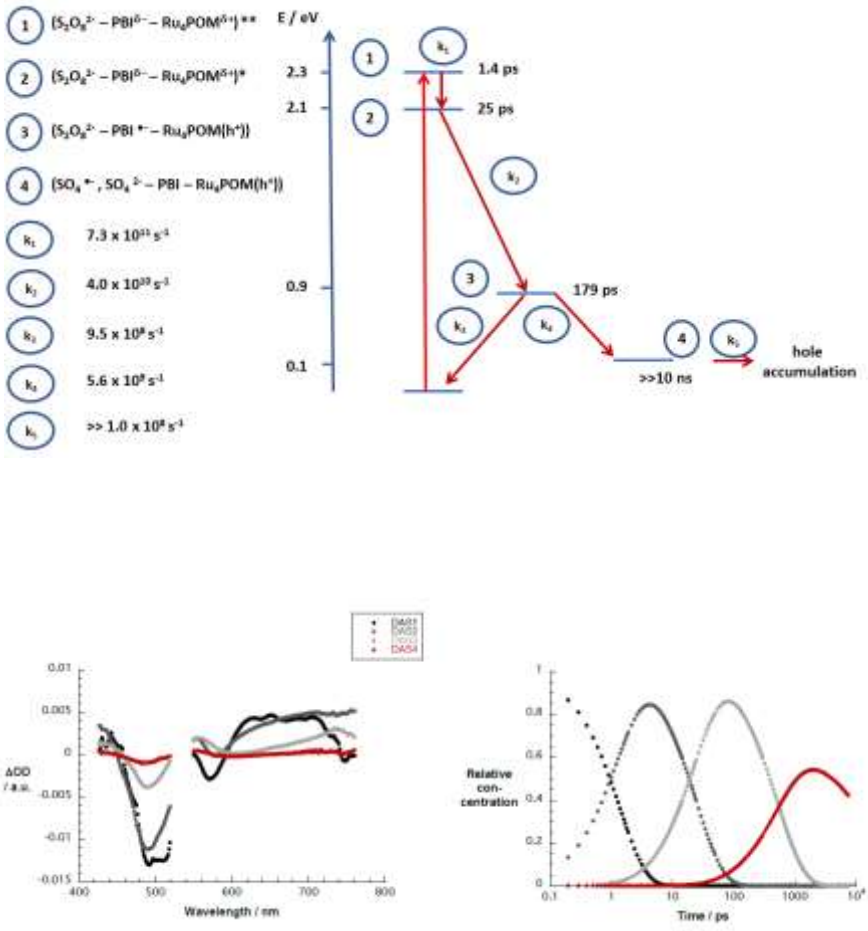

Figure 4.20 Top – Kinetic model used to fit / deconvolve the excited state surfaces of **PBI2+** / **Ru4POM** at pH 7 in the presence of 1.0 x 10-3 M S2O8 2- via GloTarAn. Bottom left – Deconvoluted transient absorption spectra in the visible. Bottom right– Evolution of the population of the involved states in the visible on the left. Global analysis pH 7.

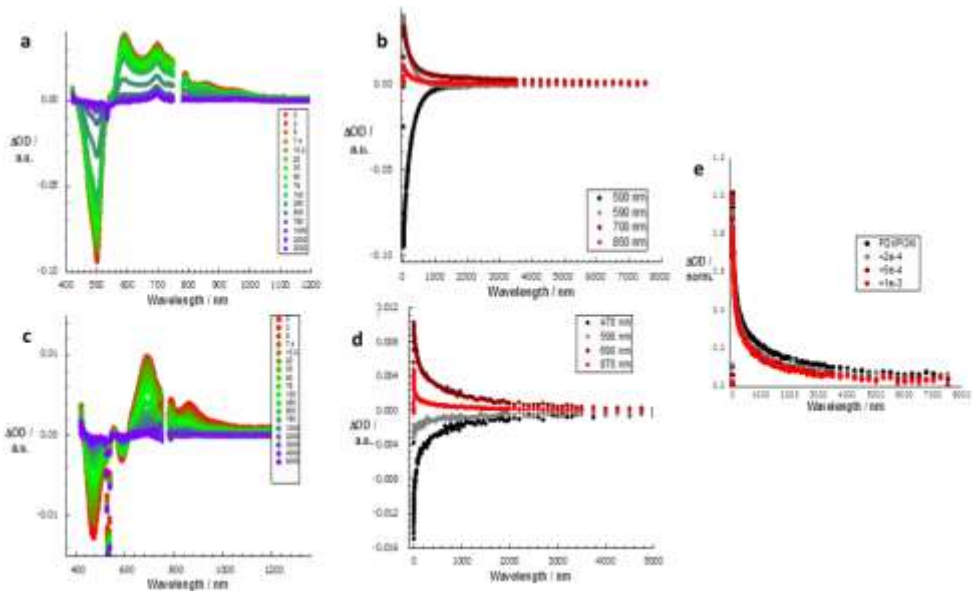

Figure 4.21 a, Differential absorption spectra of **PBI2+** (0.1 mM) obtained upon 530 nm laser flash photolysis in H_2O (pH 7, 20 mM $H_2PO_4^{2-}/HPO_4^-$) with different time delays from 2 (red) to 2000 ps (blue). **b**, Time absorption profiles at 500 (black), 590 (grey), 700 (brown) and 850 nm (red) obtained upon 530 nm laser flash photolysis of **PBI2+** (0.1 mM) in H_2O (pH 7, 0.02 M $H_2PO_4^{2-}/HPO_4^-$). **c**, Differential absorption spectra of **PBI2+** (0.1 mM) in presence of 1 mM $Na_2S_2O_8$ obtained upon 530 nm laser flash photolysis in H_2O (pH 7, 20 mM $H_2PO_4^{2-}/HPO_4^-$) with different time delays from 2 (red) to 5000 ps (blue). **d**, Time absorption profiles at 470 (black), 590 (grey), 690 (brown) and 870 nm (red) obtained upon 530 nm laser flash photolysis of **PBI2+** (0.1 mM) in H_2O (pH 7, 20 mM H_2PO_4 2-/ HPO_4^-) in presence of 1 mM $Na_2S_2O_8$. **e**, Normalized time bsorption profiles monitored at 990 nm of **PBI2+** (0.1 mM) following 530 nm laser flash photolysis in absence of $Na_2S_2O_8$ (black) and in presence of different concentrations of $Na_2S_2O_8$, namely 0.2 mM (grey), 5 mM (brown) and 1 mM $Na_2S_2O_8$ (red).

4.2.5 Building up a photoanode.

The wiring of oxygenic photosystems onto photoanodes is a key strategy for the design of regenerative photoelectrochemical cells (PEC), and for the continuous production of solar fuels from water splitting via PEC technology.[86] State-of-the-art dye-sensitized photoanodes are known, based on ruthenium polypyridine sensitizers in combination with **Ru4POM** on nano-TiO_2 semiconductor layers, providing photocurrent densities in the range JMAX=14-55 μA cm-2 at 0.54 V vs RHE applied potential (pH 5.8 in 80 mM Na_2SiF_6/$NaHCO_3$, 0.2 M $NaClO_4$, irradiation 455 nm at 33 mW cm-2, Table 4.4). In this asset, the Absorbed Photon to Current conversion Efficiency (APCE) levels up to 0.39 % (Table 4.4), because of competitive back-electron transfer pathways, arising from a poor control of the relative chromophore-catalyst loading and of their assembly geometry.[87] A promising alternative to the conventional dye-sensitized photoanode fabribrication, has been recently demonstrated by the direct wiring of the fully integrated PSII enzyme, with the aim to transfer the structural complexity of the native photosynthetic system onto the electrodic surface. The resulting PSII bio-electrodes exhibit photocurrent densities up to 930 μA cm-2 and Incident Photon to Current Efficiency > 17% (IPCE, at 680 nm on Inverse opal mesoporous ITO, Table 4.4). Following this approach, and building on the supramolecular properties of the **PBI2+**/**Ru4POM** building blocks, we have designed the fabrication of a novel photoanode, where the self-assembled **{[PBI2+]$_5$•Ru4POM}n** structural motif is transferred onto the semiconductor layer. To this aim, nano-structured

tungsten oxide (*nano*WO3) was used as the semiconductor layer, because of its high affinity towards **PBI**s and the suitable conduction band potential for photoinduced electron injection.[88] In particular, both the photoanode fabrication and PEC experiments were performed in aqueous medium at pH 3 (10^{-3} M $HClO_4$/0.1 M $NaClO_4$), which guarantees the optimal WO_3 film stability.[89] Photoelectrodes, were thus fabricated with mesoporous *nano*WO_3 (ca. 700 nm film thickness), deposited on a fluorine-doped tin oxide (FTO)-coated glass slide and loaded with the **{[PBI2+]5•Ru4POM}n** aggregates. Transferring of the photosynthetic assembly on the 20nanostructured electrode is confirmed by converging spectroscopic and microscopic evidence, including the Uv-Vis diagnostic footprint of the **{[PBI2+]5•Ru4POM}** unit (Figure 4.21).

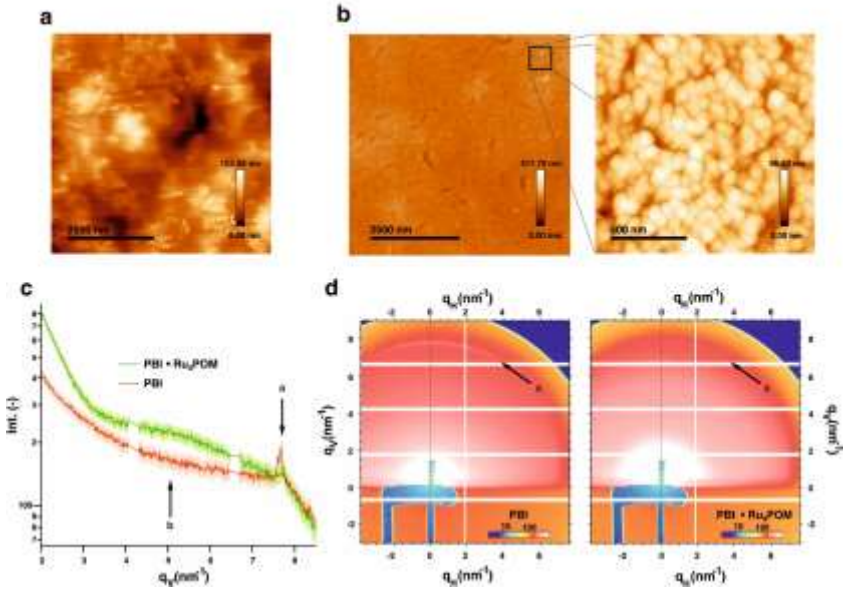

Figure 4.22: **Structural investigation of {[PBI2+]5•Ru4POM}n photosynthetic hybrids on nano-crystalline WO3. a**, AFM image of **PBI2+**-sensitized *nano*WO_3 and **b**, of **{[PBI2+]5•Ru4POM}n** on nanoWO_3 at different magnification, showing a smooth and uniform texture with a porous substructure in the nanometer scale. **c**, GISAXS scattering intensities along vertical cuts at qH=0 nm-1 (C), where a distinct **PBI2+** inherent scattering peak (peak a) is registered, that is strongly reduced for **{[PBI2+]5•Ru4POM}n**, while a broader correlation peak (peak b) arises corresponding to the **Ru4POM** – **Ru4POM** scattering centres with intercalated, π-π **PBI2+** doublets, thus confirming the deposition of the hybrid lamellar structure on the electrode surface. **d**, 2D scattering-images of the GISAXS analysis (D) provide an analogue evidence as the **PBI2+** inherent vertical scattering ring vanishes in case of the **{[PBI2+]5•Ru4POM}n** assembly deposited on *nano*WO_3.

Accordingly, the AFM images of the electrode surface show a clear modification of the **PBI2+** distribution with and without **Ru4POM**. Indeed the morphology of the **PBI2+** stacks evolves to a uniform texture when co-assembled with the inorganic POM on *nano*WO_3 (Figure 4.22). This latter templates the globular morphology of the photoeletrode surface. Moreover, grazing incidence SAXS (GISAXS) analysis confirms that the **PBI2+** stacks undergo exfoliation by the **Ru4POM** to form the supramolecular

photocomplex (Figure 4.22c). In particular, the scattering curves and GISAXS 2D-intensity maps exhibit a distinct out-of-plane peak corresponding to a d-spacing of 0.75 nm within the PBI2+-stack arrangement on the electrode (peak a in Figure 4.22). This feature is strongly suppressed in the **{[PBI2+]5•Ru4POM}n** supported films, while a distinct correlation peak is discernable at around 4 nm^{-1}. This latter is ascribed to **Ru4POM** – **Ru4POM** scattering centers with intercalated π-π **PBI2+** doublets, that is consistent with the expected structure of the photocomplex assembly (Figure 4.14). The PEC response of the ***nano*WO$_3$|{[PBI2+]$_5$•Ru4POM}n** photoanode (exposed area of 1.5 cm^2) was registered in the anodic range from 0.50 to 0.91 V, vs RHE at 20 mV/s scan rate, and under irradiation by a solar simulator with AM 1.5 G light. A 450 nm long-pass filter was used to avoid direct excitation of WO_3. By comparison with the dark scan (J < 5μA cm^{-2}), the photocurrent response under 100 $mWcm^{-2}$ (1 sun) is indicative of an efficient photocatalytic activity (Figure 7A). The onset potential of < 0.60 V vs. RHE shows a significant cathodic shift (ca 0.150 V) with respect to the bare *nano*WO_3 electrode (the onset potential of nanoWO_3 is 0.74 V vs. RHE, observed only when irradiated with λ < 420 nm). The photocurrent plateau of ca. 0.40 μA cm^{-2} is reached at <0.90 V vs. RHE (Figure 4.23), far below the thermodynamic limit ($E_0(O_2/H_2O)$ = 1.23 V vs. RHE). This result stems from the efficient hole scavenging and fast catalysis by **Ru4POM** integrated within the ***nano*WO3|{[PBI2+]5•Ru4POM}n** photoanode.

Further insight into the photoanode performance is obtained from analysis of the IPCE and APCE values. The IPCE results confirm that the action spectrum of the ***nano*WO$_3$|{[PBI2+]$_5$•Ru4POM}n**

photoanode overlaps with the absorption features of the integrated photocomplex (Figure 4.23). Indeed, the peak value of IPCE 0.5 % is obtained in the 470 - 490 nm range, corresponding to the **{[PBI2+]$_5$•Ru4POM}n** absorption maxima. Moreover, above 510 nm the photoanode IPCE remains in the 0.35-0.40 % range, where the photocomplex shows a broad absorption tail. Therefore, the experimental action spectrum confirms the **{[PBI2+]$_5$•Ru4POM}n** molecular motif on *nano*WO3 as the photosynthetic unit responsible for the observed photocurrent generation.

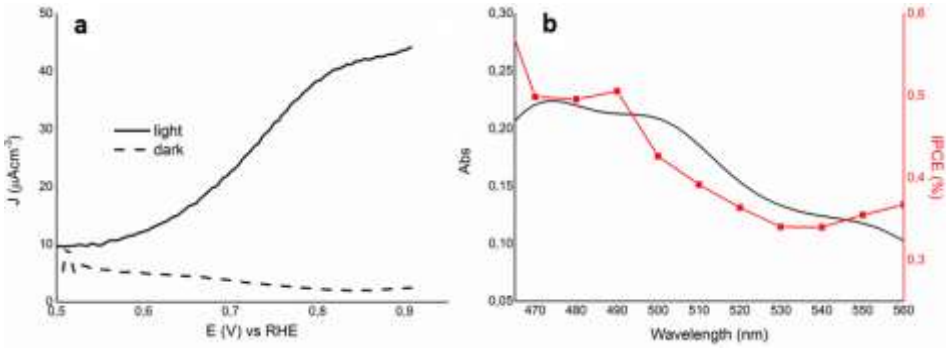

Figure 4.23. Characterization of the ***nano*WO3|{[PBI2+]5•Ru4POM}n** photoanode: **a**, Photocurrent density (solid line) versus dark current density (dashed line) as a function of the applied potential (oxidative scan up to 0.91V vs. RHE, scan rate 20 mV s^{-1},) under simulated solar irradiation (AMG 1.5, 1 Sun, with a cut-off filter at 450 nm), in aqueous $HClO_4$ pH 3, 0.1 M $NaClO_4$; counter electrode: Pt wire; reference electrode: Ag/AgCl. **b**, Action spectrum of the ***nano*WO3|{[PBI2+]5•Ru4POM}n** photoanode showing the incident photon to current conversion efficiency (IPCE, red squares) as a function of the irradiation wavelength and overlapped with the absorption spectra of the ***nano*WO3|{[PBI2+]5•Ru4POM}n** photoanode (black solid line)**.**

While the IPCE profile is indicative of the spectral window available for PEC applications, the APCE values, normalized as a function of the material absorbance, are generally used as a probe of the photoelectrode Internal Quantum Efficiency (IQE). In this specific

case, the maximum APCE value levels off at 1.3%, being fairly constant in the 470-540 nm wavelength range with an applied bias of 0.91 V vs RHE. The performance metrics for ***nano*WO$_3$|{[PBI2+]$_5$•Ru4POM}n** are collected in Table 2 together with a selection of benchmark dataset for relevant photoelectrode configurations (Table 4.4). The latter include the natural photosynthetic enzyme PSII onto ITO electrodes (*nano*ITO|PS II in Table 2), and photoanodes using of **PBI2+** in combination with IrO2-nanoparticles (*nano*WO3|PBI2+|IrOx in Table 4.4),[89] or using **Ru4POM** with ruthenium polypyridyl sensitizers (*nano*TiO2|[Ru(bpy)2(dpbpy)]2+|Ru4POM and *nano*TiO2|[Ru(Na-5-crown-phen)2(dpbpy)]4+|Ru4POM in Table 4.4).[87] Inspection of the APCE results, rank the ***nano*WO3|{[PBI2+]5•Ru4POM}n** photoanode at the top position in the series, with ca. a twofold IQE enhancement compared to *nano*ITO|PS II or to *nano*WO3|PBI2+|IrOx, and outperforming by ca. *one-order of magnitude* the classical TiO2- sensitized photoanodes based on **Ru4POM** (cfr 1.3 % vs 0.11-0.39%). Noteworthy, ***nano*WO3|{[PBI2+]5•Ru4POM}n** works with low energy photons, using a wavelength region (λ > 500 nm) where the IQE of photoactive semiconductors generally drops to zero. The kinetic advantage of the **{[PBI2+]5•Ru4POM}n** photo-electrocatalyst is further confirmed by the TOF obtained under Controlled Potential Electrolysis (CPE) at 0.91 V vs.

RHE and under solar irradiation (Table 4.4). The resulting TOF value is the highest in the series (up to 0.050 s-1 at 1.37 V vs RHE), and very close to what observed for the *nano*ITO|PS II photo-bioelectrode(Table 4.4).

Table 4.4. Photoanode performance metrics and literature benchmark values. All experiments were performed under simulated solar irradiation (AM 1.5G, 1 Sun, cut-off filter at 450 nm), in HClO4 (pH 3), 0.1 M NaClO4; counter electrode: Pt wire; reference electrode: Ag/AgCl; potentials are then converted to Reversible Hydrogen Electrode, RHE, using the equation: E (V) vs RHE = E (V) vs Ag/AgCl + 0.197 + (0.0592×pH).

#	E vs RHE (V)a	JMAXb (uA cm-2)	TOFc (s-1)	IPCEd (%)	APCEe (%)
***nano*WO3|{[PBI2+]5•Ru4POM}n**	0.91	44	0.026f	0.50	1.30g
*nano*ITO|PS IIh,(*53*)	0.93	0.3	0.030	0.125	0-70i
*nano*WO3|PBI2+|IrOxl,(*55*)	0.91	70	-	0.6m	0.80m
*nano*TiO2|[Ru(bpy)2(dpbpy)]2+ |Ru4POMn,(*75*)	0.54	14	0.004°	-	0.11p
*nano*TiO2|[Ru(Na-5-crownphen)2(dpbpy)]4+ |Ru4POMn, (*52*)	0.54	55	0.020°	-	0.39p

aPotential applied in controlled potential electrolysis under irradiation. bMaximum photocurrent density observed during the first scan under anodic potentials and irradiation. cTurnover frequency (TOF) referred to the Ru4POM determined from the equation TOF = JMAX/(4×F×lWOC), where JMAX is the maximum photocurrent density, F is the faraday constant = 96485 C mol-1, lWOC is the loading of the Ru4POM = 4.34 nmol cm-2, determined by ICP-OES analysis. dIncident Photon to Current conversion Efficiency (IPCE) determined in the 470-560 nm region (steps of 10 nm), under monochromatic illumination generated by an air cooled Luxtel 175 W Xe lamp coupled to an Applied Photophysics monochromator. Incident Irradiance was measure with a calibrated silicon photodiode. eAbsorbed Photon to Current conversion Efficiency (APCE) = lPCE(λ)/(1-10-A(λ)), where A(λ) is derived from the absorption spectra of the electrodes. fup to 0.050 s-1 at 1.37 V vs RHE. gRecorded at 490 nm. hnanostructured Indium tin oxide (ITO) loaded with photosystem II; general conditions: pH 6.5 in 40 mM 2-(N-morpholino)ethanesulfonic acid (MES) electrolyte. iRecorded at 680 nm. lDye sensitized WO3 with spin coated IrO2 nanoparticles; general conditions: HClO4 pH 3, 0.1 M NaClO4, illumination under AM 1.5 G with a cut-off filter at 435 nm. mRecorded at 470 nm. nDye sensitized TiO2 with **Ru4POM** deposited on it; general conditions: pH 5.8 in 80 mM Na2SiF6/NaHCO3 buffer electrolyte containing NaClO4 (200mM), irradiation 455 nm (33mW cm-2). oTurnover frequency (TOF) determined from the equation TOF = JMAX/(4×F×lWOC). pReported as internal quantum efficiency (IQE).

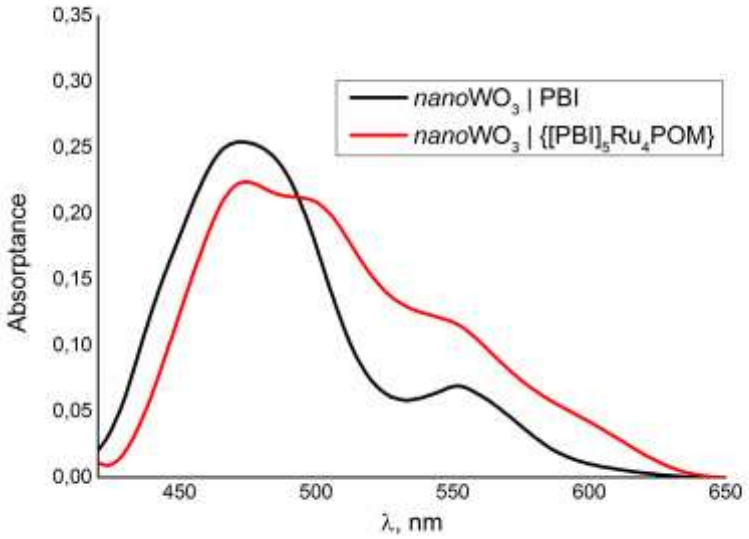

Figure 4.24 Comparison of UV-vis absorptance of *nano*WO3|**PBI2+** (black trace) and *nano*WO3|{[**PBI2+**]5·**Ru4POM**}n (red trace) photoelectrodes. Absorbed photon-to-current efficiency (APCE) of *nano*WO3|{[**PBI2+**]5·**Ru4POM**}n at different wavelengths; aqueous 10^{-3} M $HClO_4$ + 0.1 M $NaClO_4$, pH 3. Counter electrode: Pt wire; reference electrode: Ag/AgCl; applied potential: 0.55 V vs Ag/AgCl (0.91 V vs reversible hydrogen electrode, RHE); irradiation: AM 1.5 G + 450 nm long-pass filter.

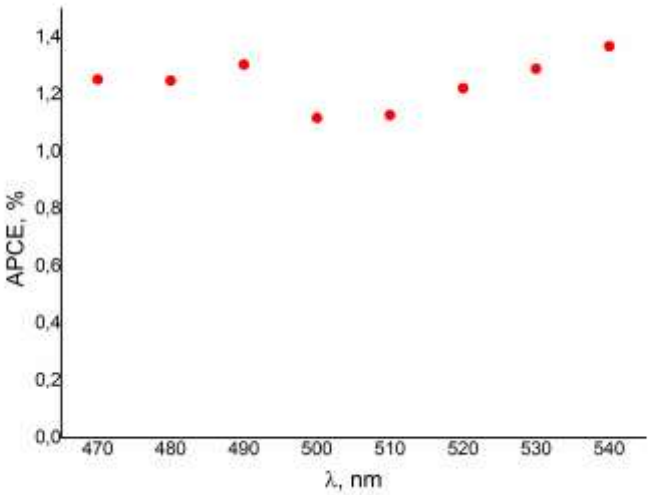

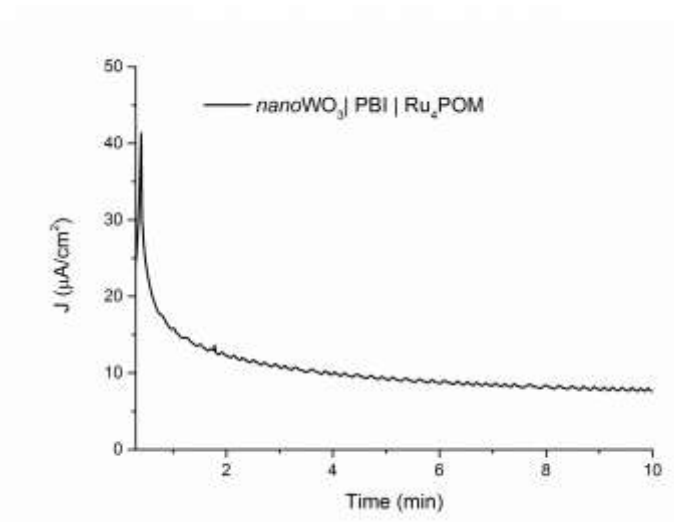

Figure 4.25. Controlled potential photoelectrolysis with a *nano*WO3|{[**PBI2+**]5·**Ru4POM**}n photoelectrode: photocurrent density vs time. Aqueous 10-3 M HClO4 + 0.1 M $NaClO_4$, pH 3. Counter electrode: Pt wire; reference electrode: Ag/AgCl; applied potential: 0.55 V vs Ag/AgCl (0.91 V vs reversible hydrogen electrode, RHE); irradiation: AM 1.5 G + 450 nm long-pass filter.

4.2.6. Conclusions

Taken as a whole, these results highlight the fascinating potential of organic PBIs for solar energy storage. We demonstrate the catalytic activity of a biscationic **PBI2+** is herein demonstrated in water, under visible light irradiation and within an exceptionally broad pH window featuring the unprecedented combination with a totally inorganic and very robust molecular catalyst, namely, $[Ru_4(\mu\text{-}O)_4(\mu\text{-}OH)_2(H_2O)_4(\gamma\text{-}SiW_{10}O_{36})_2]^{10-}$ (**Ru_4POM**). The catalytic triad reached 3.6 TON and 1.8 TOF, which yield above 5 % and operation time longer than one hour.

Morevoer, we built a novel dye-sensitized photoanode where the structural motif of the **{[PBI2+]$_5$•Ru4POM}n** assembly is transferred onto the semicondutcor layer of nanoWO_3. The Absorbed Photon to Current conversion Efficiency (APCE), which measures the performances of the photoanode, resulted to be 1.3 %, which is one order of magnitude higher than the classical TiO2 sensitized with TiO_2.

4.3 Experimental section

4.3.1. Instruments and materials

Chemicals and solvents for all synthetic and characterization procedures have been purchased from Sigma-Aldrich and Acros, and used as received if not differently specified. All solvents used for photochemical characterization of single molecules and hybrid materials are of spectroscopic grade (99.5%). Deuterated solvents have been purchased from Sigma-Aldrich and Cambridge Isotope Laboratories. N,N′-Bis(2-(trimethylammonium)ethylene)perylene-3,4,9,10- tetracarboxylic acid bisimide bischloride salt (**PBI2+**Cl_2) and $Na_{10}[Ru4(\mu\text{-}O)4(\mu\text{-}OH)_2(H_2O)_4(\gamma\text{-}SiW_{10}O_{36})_2]$ (**Ru4POM**) have been synthesized according to literature procedures.

Steady-state absorption spectroscopy studies have been performed at room temperature on a *Varian Cary 5000* UV-Vis-NIR double beam spectrophotometer or on a *Perkin Elmer Lambda 2* UV/Vis spectrophotometer; 10 mm path length Hellma Analytics 100 QS quartz cuvettes have been used.

Steady-state fluorescence spectra have been recorded on a *Varian Cary Eclipse Fluorescence* spectrophotometer or on a *Horiba FluoroMax3* spectrophotometer; 10 mm path length *Hellma Analytics 117.100F QS* quartz cuvettes have been used.

Femtosecond transient absorption studies have been performed using 530 nm laser pulses (1 kHz, 150 fs pulse width) from an amplified Ti:sapphire laser system (*Model CPA 2101, Clark-MXR Inc.*). In terms of sample preparation, **PBI2+** as well as **Ru4POM** were dissolved in 0.02 M aqueous phosphate buffer. To create the corresponding hybrids, Ru4POM solutions were added to solutions of **PBI2+**. For the experiments involving sacrificial Na2S2O8, the

chosen amount was added as solid to the solutions/dispersions after hybrid formation.

Cyclic Voltammetry (CV) studies have been carried out with a *BAS Epsilon EC 2000* electrochemistry system in a three-electrode cell under N2 anhydrous atmosphere in deoxygenated phosphate buffer solution (PBS) 0.2 M pH 7.0 and Britton-Robinson (BR) buffer pH 7.0, prepared according to literature procedures (*5*). For spectroelectrochemistry, a platinum minigrid has been used as working electrode, a Pt wire as counter electrode and Ag/AgCl (3M NaCl) as reference electrode, in a cuvette with 1 mm optical path.

Fourier-Transform Infrared (FT-IR) spectra have been recorded on a *Varian 660 FT-IR* with a *GladiATR™ Single Reflection* ATR accessory equipped with a Ge crystal. Raman spectra have been acquired with a *Renishaw inVia 15 reflex* spectrometer equipped with 532, 633, and 785 nm lasers. The Laser beam was focused on an area of about 2x2 μm with an output power lower than 1 mW. *ζ*-Potential measurements have been performed using a *Malvern Zetasizer Nano ZS90* instrument, in poly-(methyl methacrylate) (PMMA) cuvettes containing 1 ml of the solution under investigation.

Dynamic Light Scattering (DLS) measurements have been performed using a Helium-Neon-Laser (Spectra-Physics, P=25mW, λ=632.8nm). The data is acquired by a Perkin Elmer Photon Counting Module (Perkin Elmer, Voudreuil, Canada) and an ALV 7004 Digital Multiple-Tau Real-Time-Correlator (ALV, Langen, Germany), which allows a minimum time interval of 25 ns for the correlation function. The ALV software package is used to record

and store the correlation functions. Samples were placed in 120µl quartz cuvette inside a Stop-Flow apparatus (BioLogic, Seyssinet-Pariset, France).

Atomic Force Microscopy (AFM) measurements were performed using a *Nanoscope V* microscope (*Digital Instruments Metrology Group*, model *MMAFMLN*) in tapping mode in air at room temperature, using standard µmash® SPM probe (NSC15/AIBS) with tip height 12- 18µm, cone angle <40° (Resonant frequency 325kHz, force constant of ~40N/m). Image analysis has been performed with *WsXM* software (*Nanotec Electronica S. L.*)5. The accuracy of the AFM diameter determination was improved by tip deconvolution. Considering the diameter of AFM tip and the larger dimensions of particles, we calculated real particle diameter from formula: rc = r (cos θ0 +(cos2 θ0 +(1+ sin θ0)(−1+(tan θ0/cos θ0)+ tan2 θ0))1/2) where r is the particle radius, θ0 is the mean half angle of the tip and rc is the AFM radius of a particle, as seen in the image. For the preparation of sample surfaces the same concentration as in the SAXS experiments ([**PBI2+**]= 5×10-4M, [**Ru4POM**] =1.25×10$_{-4}$M in distilled H2O, pH=7) was used. Dispersions were spin coated and mica was used as substrate. Diameter and height distribution for the **PBI2+•Ru4POM** hybrids was evaluated considering 5 AFM images, size 25 × 25 µm. Light emission power density and irradiance spectrum were measured with an AvaSpec- ULS3648 StarLine high-resolution fiber-optic spectrometer (Avantes).

4.3.2 Methods

Oxygen evolution kinetics were performed in aqueous solution (4.5 mL) containing **PBI2+**, $Na_2S_2O^8$ and **Ru4POM**, kept under stirring. The mixture was fluxed 20 minutes with nitrogen to remove the dissolved oxygen. The glass reactor (8.0 mL volume,), was purged with nitrogen and allowed to equilibrate in the dark at 25 °C. Irradiation of the solution was conducted with one spotlight 10 cm far. (4.5mW/cm2). Oxygen evolution was monitored with a *FOSPOHOR-R-AF* probe, inserted in the reaction headspace and interfaced with a *Neofox Real-Time* software for data collection; dissolved oxygen was assumed to be negligible. The rate of oxygen production has been taken from the initial slope of the kinetic curves shown in Figure 4 (see also Table 1).

Reactions have been run in triplicates; it has been confirmed that the concomitant presence of **PBI2+**, $Na_2S_2O_8$, **Ru4POM** and light was necessary to achieve oxygen production. The number of absorbed photons has been assumed to be equivalent to the number of incident photons, given the high optical density of the solution and the negligible loss of photons by reflection events. The incident photons on the reactor have been obtained by measuring the power emitted from one LED by means of a *Newport 1835-C* Multi-FunctioFunction Optical Power Meter equipped with a model 818-UV calibrated silicon detector.

Quantum Yield for oxygen production

Since the light source used in photocatalytic experiments has a broad spectrum (nonmonochromatic spectrum), usual methods for determination of photon fluxes and quantum yields have to be

modified to take into account the different energies of the photons arriving at the

sample. The quantum yield of a reaction (Φ) can be calculated dividing the rate of the reaction, *vr* [mol s- 1], by the amount of excitation per second, *θ* [mol s-1] (Eq. SI.1); *θ* can be calculated from Eq. SI.2, where *φ0*(*λ*) is the photon flux per unit wavelength [mol s-1 nm-1]. In these calculation the validity of Kasha's rule is assumed, stating that the same excited state is reached for different energies of photons. The photon flux per wavelength, *φ0*(*λ*), can be determined from the emission spectrum of the LED white lamp according to Eq. SI.3. In this equation *P*(*λ*) [W nm-1] is given by Eq. SI.4, where *Ptot* is the total irradiation power of the lamp (4.5×10-3 W cm-2 multiplied by the irradiated surface of the reactor, 5.2×1.3 cm2). The term *θ* depends also on the probability of absorption of a photon of the incoming irradiation source by the photocatalytic mixture, *Pabs*(*λ*), and this probability depends on the wavelength of the incoming photon, according to Eq. SI.5. In this equation, *Atot*(*λ*) is the measured absorbance at wavelength λ for a UV-Vis cell. Since the absorption spectrum of the photocatalytic solution was measured on a cuvette with *b* = 0.1 cm optical path, whereas irradiation of the solution in the reactor was performed with an optical path length of *ℓ* = 1.3 cm (reactor depth), the total absorbance of the solution being irradiated by the lamp can be obtained, correcting *Atot*(*λ*) for *ℓ*/*b*.

Φ = v! (eq4.5)

$\theta = \varphi!(\lambda)P!"\#(\lambda)\ d\lambda$ (eq4.6)

$\varphi!(\lambda) = P(\lambda)\lambda hc\mathcal{N}!"$ (eq4.7)

$P!(\lambda)\ d\lambda = P!"!$ (eq4.8)

$P_{!"\#}(\lambda) = (1 - 10^{-!!"!\cdot\ell !})$ (eq4.9)

The calculated $\varphi_0(\lambda)$ and $P_{abs}(\lambda)$ are reported in the figure below (blue line and black line, respectively). The resulting product equals the θ value (red line), assuming that the quantum yield of the reaction is constant for the wavelength range studied, according to Kasha's rule. Plot of the incoming total photon flux $\varphi_0(\lambda)$ (blue curve, right axis) and of the probability of absorption $P_{abs}(\lambda)$ (black curve, left axis); the red curve (right axis) shows the resulting product of the two functions.

Finally, to determine the quantum yield of the reaction, the rate of product formation *vr* is divided by θ (2.70×10-9 mol s-1), according to Eq. 4.6.

SAXS measurements

Small angle x-ray scattering (SAXS) measurements were performed at the Austrian SAXS beamline of the electron storage ring ELETTRA (*7*) using a photon energy of 8 keV. The beamline setup was adjusted to a sample to detector distance of 734 mm to result in an accessible q-range 0.07 – 8.7 nm-1. All images were recorded using the Pilatus 1M detector (Dectris, Switzerland) with at least three exposures of 10 seconds each per sample to check for radiation damage. Reference patterns to calibrate the q-scale were collected of silver-behenate (dspacings of 5.838 nm). All measurements were done using a flow cell capillary. The radial averaging and the image calibration were conducted using the FIT2D software. All presented data was corrected for fluctuations of the primary intensity and the corresponding background has been subtracted from each solution scattering pattern. The presented formfactors were calculated

using the CRYSOL package, whereas corresponding PDB models were obtained from literature and preliminary MD simulations.

Dynamic Light scattering (DLS) results were derived from the recorded autocorrelation functions g2(τ). For each sample, a total of 5 measurements were made and subsequently merged. The data was fitted using the *cumulant analysis* method, whereas the detailed constants can be found in Table S2.

IPCE and APCE measurements: the photocurrents and photon flux were determined at different wavelengths by dark/light chronoamperometry steps, at 0.91 V vs RHE, in aqueous $HClO_4$ (pH 3, 0.1 M $NaClO_4$). Chronoamperometric experiments (100s light/dark intervals) were performed under monochromatic irradiation, in the range λ= 470 - 580 nm, with 10 nm steps, generated by a 175 W Xenon lamp coupled to an Applied Photophysics monochromator. The irradiance, i.e. the irradiated power per area, was calculated at each wavelength by a calibrated silicon photodiode.

4.4 References

[1] J. Chow, R. J. Kopp, P. R. Portney, *Science* **2003**, *302*, 1528–1531.

[2] N. S. Lewis, D. G. Nocera, *Proc. Natl. Acad. Sci. U. S. A.* **2006**, *103*, 15729–35.

[3] G. W. Huber, J. N. Chheda, C. J. Barrett, J. A. Dumesic, *Science* **2005**, *308*, 1446–1450.

[4] F. Ma, M. A. Hanna, *Bioresour. Technol.* **1999**, *70*, 1–15.

[5] I. Medhaug, M. B. Stolpe, E. M. Fischer, R. Knutti, *Nature* **2017**, *545*, 41–47.

[6] C. M. O'Reilly, S. Sharma, D. K. Gray, S. E. Hampton, J. S. Read, R. J. Rowley, P. Schneider, J. D. Lenters, P. B. McIntyre, B. M. Kraemer, *Geophys. Res. Lett.* **2015**, *42*, 10773–10781.

[7] S. Wolf, T. F. Keenan, J. B. Fisher, D. D. Baldocchi, A. R. Desai, A. D. Richardson, R. L. Scott, B. E. Law, M. E. Litvak, N. A. Brunsell, *Proc. Natl. Acad. Sci.* **2016**, *113*, 5880–5885.

[8] M. L. Ross, *J. Peace Res.* **2004**, *41*, 337–356.

[9] M. I. Hoffert, K. Caldeira, A. K. Jain, E. F. Haites, L. D. D. Harvey, S. D. Potter, M. E. Schlesinger, S. H. Schneider, R. G. Watts, T. M. L. Wigley, *Nature* **1998**, *395*, 881–884.

[10] Editorial, *Nat. Mater.* **2012**, *11*, 173.

[11] A. Polman, H. A. Atwater, *Nat. Mater.* **2012**, *11*, 174–177.

[12] N. D. McDaniel, S. Bernhard, *Dalt. Trans.* **2010**, *39*, 10021.

[13] O. Morton, *Nature* **2006**, *443*, 19–22.

[14] J. Barber, *Biochem. Soc. Trans.* **2006**, *34*, 619–31.

[15] G. Renger, T. Renger, *Photosynth. Res.* **2008**, *98*, 53–80.

[16] L. N. M. Duysens, J. Amesz, B. M. Kamp, *Nature* **1961**, *190*, 510–511.

[17] K. N. Ferreira, T. M. Iverson, K. Maghlaoui, J. Barber, S. Iwata, *Science* **2004**, *303*, 1831–1838.

[18] S. I. Allakhverdiev, J. J. Casal, T. Nagata, *Photochem. Photobiol. Sci.* **2009**, *8*, 137.

[19] N. Nelson, A. Ben-Shem, *Nat. Rev. Mol. Cell Biol.* **2004**, *5*, 971–982.

[20] J. P. McEvoy, G. W. Brudvig, *Chem. Rev.* **2006**, *106*, 4455–4483.

[21] J. Barber, *Chem. Soc. Rev.* **2009**, *38*, 185–196.

[22] B. KOok, B. Forbush, M. McGloin, *Photochem. Photobiol.* **1970**, *11*, 457–475.

[23] J. K. Hurst, *Science* **2010**, *328*, 315–316.

[24] J. J. Concepcion, R. L. House, J. M. Papanikolas, T. J. Meyer, *PNAS.* **2012**, *109*, 15560–4.

[25] D. Gust, T. A. Moore, A. L. Moore, *Acc. Chem. Res.* **2009**, *42*, 1890–1898.

[26] A. Sartorel, M. Carraro, F. M. Toma, M. Prato, M. Bonchio, K. N. Ferreira, T. M. Iverson, K. Maghlaoui, J. Barber, S. Iwata, et al., *Energy Environ. Sci.* **2012**, *5*, 5592.

[27] F. E. Osterloh, *Chem. Soc. Rev.* **2013**, *42*, 2294–2320.

[28] K. J. Young, L. A. Martini, R. L. Milot, R. C. S. Iii, V. S. Batista, C. A. Schmuttenmaer, R. H. Crabtree, G. W. Brudvig, *Coord. Chem. Rev.* **2012**, *256*, 2503–2520.

[29] A. W. Adamson, J. N. Demas, *J. Am. Chem. Soc.* **1971**, *93*, 1800–1801.

[30] H. D. Gafney, A. W. Adamson, *J. Am. Chem. Soc.* **1972**, *94*,

8238–8239.

[31] C. K. Prier, D. A. Rankic, D. W. C. MacMillan, *Chem. Rev.* **2013**, *113*, 5322–5363.

[32] K. Kalyanasundaram, *Coord. Chem. Rev.* **1982**, *46*, 159–244.

[33] L. Flamigni, A. Barbieri, C. Sabatini, B. Ventura, F. Barigelletti, *Photochem. Photophysics Coord. Compd. II*, Springer Berlin Heidelberg, Berlin, Heidelberg, **2007**, pp. 143–203.

[34] V. Balzani, S. Campagna, *Photochemistry and Photophysics of Coordination Compounds II*, Springer Berlin Heidelberg, **2007**.

[35] M. K. Nazeeruddin, A. Kay, I. Rodicio, R. Humphry-Baker, E. Mueller, P. Liska, N. Vlachopoulos, M. Graetzel, *J. Am. Chem. Soc.* **1993**, *115*, 6382–6390.

[36] T. W. Hamann, J. W. Ondersma, *Energy Environ. Sci.* **2011**, *4*, 370–381.

[37] C. Klein, M. K. Nazeeruddin, P. Liska, D. Di Censo, N. Hirata, E. Palomares, J. R. Durrant, M. Graetzel, *Inorg. Chem.* **2005**, *44*, 178–180.

[38] M. Tuikka, P. Hirva, K. Rissanen, J. Korppi-Tommola, M. Haukka, *Chem. Commun.* **2011**, *47*, 4499.

[39] C. Y. Chen, M. Wang, J. Y. Li, N. Pootrakulchote, L. Alibabaei, C. H. Ngoc-Le, J. D. Decoppet, J. H. Tsai, C. Grätzel, C. G. Wu, et al., *ACS Nano* **2009**, *3*, 3103–3109.

[40] F. Gao, Y. Wang, D. Shi, J. Zhang, M. Wang, X. Jing, R. Humphry-Baker, P. Wang, S. M. Zakeeruddin, M. Grätzel, *J. Am. Chem. Soc.* **2008**, *130*, 10720–10728.

[41] D. Kuang, C. Klein, S. Ito, J. E. Moser, R. Humphry-Baker, N. Evans, F. Duriaux, C. Grätzel, S. M. Zakeeruddin, M. Grätzel, *Adv. Mater.* **2007**, *19*, 1133–1137.

[42] P. Wang, C. Klein, R. Humphry-Baker, S. M. Zakeeruddin, M. Graetzel, *J. Am. Chem. Soc.* **2005**, *127*, 808–809.

[43] K.-J. Jiang, N. Masaki, J. Xia, S. Noda, S. Yanagida, *Chem. Commun.* **2006**, *0*, 2460.

[44] M. R. Wasielewski, *Chem. Rev.* **1992**, *92*, 435–461.

[45] G. F. Moore, J. D. Blakemore, R. L. Milot, J. F. Hull, H. Song, L. Cai, C. A. Schmuttenmaer, R. H. Crabtree, G. W. Brudvig, *Energy Environ. Sci.* **2011**, *4*, 2389.

[46] G. F. Moore, S. J. Konezny, H. E. Song, R. L. Milot, J. D. Blakemore, M. L. Lee, V. S. Batista, C. A. Schmuttenmaer, R. H. Crabtree, G. W. Brudvig, *J. Phys. Chem. C* **2012**, *116*, 4892–4902.

[47] S. Mathew, A. Yella, P. Gao, R. Humphry-Baker, B. F. E. Curchod, N. Ashari-Astani, I. Tavernelli, U. Rothlisberger, M. K. Nazeeruddin, M. Grätzel, *Nat. Chem.* **2014**, *6*, 242–247.

[48] G. D. Sharma, S. Prakash Singh, P. Nagarjuna, J. A. Mikroyannidis, R. J. Ball, R. Kurchania, *J. Renew. Sustain. Energy* **2013**, *5*, 43107.

[49] Y.-C. Chang, C.-L. Wang, T.-Y. Pan, S.-H. Hong, C.-M. Lan, H.-H. Kuo, C.-F. Lo, H.-Y. Hsu, C.-Y. Lin, E. W.-G. Diau, *Chem. Commun.* **2011**, *47*, 8910.

[50] A. Mishra, M. K. R. Fischer, P. Bäuerle, *Angew. Chem.* **2009**, *48*, 2474–2499.

[51] X. Li, L. E. Sinks, B. Rybtchinski, M. R. Wasielewski, *J. Am. Chem. Soc.* **2004**, *126*, 10810–10811.

[52] Á. J. Jiménez, R. M. K. Calderón, M. S. Rodríguez-Morgade, D. M. Guldi, T. Torres, *Chem. Sci.* **2013**, *4*, 1064–1074.

[53] Á. J. Jiménez, F. Spänig, M. S.R. Morgade, K. Ohkubo, S. Fukuzumi,D. M. Guldi, T. Torres, Photochemistry and Photophysics of Coordination Compounds II, **2007**, pp 143-203.

[54] A. Prodi, C. Chiorboli, F. Scandola, E. Iengo, E. Alessio, R. Dobrawa, F. Würthner, *J. Am. Chem. Soc.* **2005**, *127*, 1454–62.

[55] R. K. Dubey, M. Niemi, K. Kaunisto, K. Stranius, A. Efimov, N. V. Tkachenko, H. Lemmetyinen, *Inorg. Chem.* **2013**, 52 (17), 9761–9773.

[56] L. Feng, M. Rudolf, S. Wolfrum, A. Troeger, Z. Slanina, T. Akasaka, S. Nagase, N. Martín, T. Ameri, C. J. Brabec, et al., *J. Am. Chem. Soc.* **2012**, *134*, 12190–12197.

[57] S. Chen, P. Slattum, C. Wang, L. Zang, *Chem. Rev.* **2015**, *115*, 11967–11998.

[58] V. Kunz, V. Stepanenko, F. Würthner, *Chem. Commun.* **2015**, *51*, 290–293.

[59] S. Fukuzumi, K. Ohkubo, T. Suenobu, *Acc. Chem. Res.* **2014**, *47*, 1455–1464.

[60] M. R. Wasielewski, *Acc. Chem. Res.* **2009**, *42*, 1910–1921.

[61] T. J. Meyer, *Acc. Chem. Res.* **1989**, *22*, 163–170.

[62] L. Duan, F. Bozoglian, S. Mandal, B. Stewart, T. Privalov, A. Llobet, L. Sun, *Nat. Chem.* **2012**, *4*, 418–423.

[63] R. Matheu, M. Z. Ertem, J. Benet-Buchholz, E. Coronado, V. S. Batista, X. Sala, A. Llobet, *J. Am. Chem. Soc.* **2015**, *137*, 10786–10795.

[64] C. J. Richmond, R. Matheu, A. Poater, L. Falivene, J. Benet-Buchholz, X. Sala, L. Cavallo, A. Llobet, *Chem. - A Eur. J.* **2014**, *20*, 17282–17286.

[65] M. Natali, F. Puntoriero, C. Chiorboli, G. La Ganga, A. Sartorel, M. Bonchio, S. Campagna, F. Scandola, *J. Phys. Chem. C* **2015**, *119*, 2371–2379.

[66] M. Orlandi, R. Argazzi, A. Sartorel, M. Carraro, G. Scorrano, M. Bonchio, F. Scandola, *Chem. Commun.* **2010**, *46*, 3152.

[67] F. Puntoriero, G. La Ganga, A. Sartorel, M. Carraro, G. Scorrano, M. Bonchio, S. Campagna, *Chem. Commun.* **2010**, *46*, 4725.

[68] M. Burian, Z. Syrgiannis, G. La Ganga, F. Puntoriero, M. Natali, F. Scandola, S. Campagna, M. Prato, M. Bonchio, H. Amenitsch, *Inorganica Chim. Acta* **2017**, *454*, 171–175.

[69] A. S. Weingarten, R. V. Kazantsev, L. C. Palmer, M. McClendon, A. R. Koltonow, A. P. S. Samuel, D. J. Kiebala, M. R. Wasielewski, S. I. Stupp, *Nat. Chem.* **2014**, *6*, 964–970.

[70] M. T. Vagnini, A. L. Smeigh, J. D. Blakemore, S. W. Eaton, N. D. Schley, F. D'Souza, R. H. Crabtree, G. W. Brudvig, D. T. Co, M. R. Wasielewski, *PNAS* **2012**, *109*, 15651–6.

[71] J. T. Kirner, J. J. Stracke, B. A. Gregg, R. G. Finke, *ACS Appl. Mater. Interfaces* **2014**, *6*, 13367–13377.

[72] R. Al-Oweini, A. Sartorel, B. S. Bassil, M. Natali, S. Berardi, F. Scandola, U. Kortz, M. Bonchio, *Angew. Chem.* **2014**, *53*, 11182–11185.

[73] S. Piccinin, A. Sartorel, G. Aquilanti, A. Goldoni, M. Bonchio, S. Fabris, *PNAS.* **2013**, *110*, 4917–4922.

[74] H. Lv, Y. V. Geletii, C. Zhao, J. W. Vickers, G. Zhu, Z. Luo, J. Song, T. Lian, D. G. Musaev, C. L. Hill, *Chem. Soc. Rev.* **2012**, *41*, 7572.

[75] A. Sartorel, M. Bonchio, S. Campagna, F. Scandola, N. S. Lewis, D. G. Nocera, R. Eisenberg, H. B. Gray, C. Herrero, B. Lassalle-Kaisea, et al., *Chem. Soc. Rev.* **2013**, *42*, 2262–2280.

[76] A. Sartorel, P. Miró, E. Salvadori, S. Romain, M. Carraro, G. Scorrano, M. Di Valentin, A. Llobet, C. Bo, M. Bonchio, *J. Am. Chem. Soc.* **2009**, *131*, 16051–16053.

[77] M. D. Kärkäs, O. Verho, E. V. Johnston, B. Åkermark, *Chem. Rev.* **2014**, *114*, 11863–12001.

[78] Y. Guan, Y. Zakrevskyy, J. Stumpe, M. Antonietti, C. F. J. Faul, *Chem. Commun.* **2003**, *0*, 894–895.

[79] Y. Guan, S. H. Yu, M. Antonietti, C. Böttcher, C. F. J. Faul, *Chem. - Eur. J.* **2005**, *11*, 1305–1311.

[80] T. L. Doane, C. H. Chuang, R. J. Hill, C. Burda, *Acc. Chem. Res.* **2012**, *45*, 317–326.

[81] M. Supur, S. Fukuzumi, *J. Phys. Chem. C* **2012**, *116*, 23274–23282.

[82] A. R. Parent, R. H. Crabtree, G. W. Brudvig, *Chem. Soc. Rev.* **2013**, *42*, 2247–2252.

[83] Y. Liu, S.-X. Guo, A. M. Bond, J. Zhang, Y. V. Geletii, C. L. Hill, *Inorg. Chem.* **2013**, *52*, 11986–11996.

[84] N. Tasios, C. Grigoriadis, M. R. Hansen, H. Wonneberger, C. Li, H. W. Spiess, K. Mullen, G. Floudas, *J. Am. Chem. Soc.* **2010**, *132*, 7478–7487.

[85] M. Quintana, A. M. López, S. Rapino, F. M. Toma, M. Iurlo,

M. Carraro, A. Sartorel, C. MacCato, X. Ke, C. Bittencourt, et al., *ACS Nano* **2013**, *7*, 811–817.

[86] J. R. Swierk, T. E. Mallouk, *Chem. Soc. Rev.* **2013**, *42*, 2357–2387.

[87] J. Fielden, J. M. Sumliner, N. Han, Y. V. Geletii, X. Xiang, D. G. Musaev, T. Lian, C. L. Hill, *Chem. Sci.* **2015**, *6*, 5531–5543.

[88] J. C. Hill, K. S. Choi, *J. Phys. Chem. C* **2012**, *116*, 7612–7620.

[89] F. Ronconi, Z. Syrgiannis, A. Bonasera, M. Prato, R. Argazzi, S. Caramori, V. Cristino, C. A. Bignozzi, **2015**.

5. A look into carbon dots synthesis

Whereas much is known about the fascinating optical properties of carbon dots, little is known about how these materials form from the precursors. The task is not easy to accomplish. It has to be considered the difficulty in monitoring carbon dots reaction path, leading to unclear formation mechanism, and the high number of variables of the different methods. However, we believe that understanding the mechanism of how these materials grow and form would be pivotal in order to master carbon dots chemistry.

After introducing the contributions in this field, discussing the mechanisms proposed up to date, we present our investigation of a previously reported hydrothermal MW-assisted synthesis of carbon nanodots using arginine and ethylenediamine as precursors. We systematically vary the synthesis time reaction times in order to study the structural and optical changes during the formation process, analysing both reaction mixture and carbon dots after proper purification. Combining NMR, FT-IR, AFM, DLS, UV-Vis techniques and third generation synchrotron sources such as SAXS and WAXS, we were able to propose a formation mechanism and get new insights on the structural properties of carbon nanodots demonstrating the core/shell nature and master these properties synthesizing novel dots with controlled layer thickness.

The work presented in this chapter has been done in a collaborative work with Max Burian (Technische Universität Graz) who contributed with SAXS experiments and data evaluation, and with Dr. Francesca Arcudi (Università degli Studi di Trieste) e Dr. Luka Đorđević

(Università degli Studi di Trieste) that contributed with the experimental design and results.

5. A look into carbon dots synthesis

5.1 Introduction

5.1.1 Carbon dots formation: an empty folder

Since 2004, the development of carbon dots syntheses has been pursued intensively due to the technological applications and the scientific interest.[1] Indeed, these new members of the carbon nanomaterial family have drawn the attention of the scientific community due to their unique photoluminescence that found applications in optoelectronic devices, biological labelling, biomedicine and more recently photocatalysis.[2–8] A number of synthetic methods is available, all giving carbon-based dots different in size, shape, composition and optical properties.[2,9–12] In principle, it is possible to adjust these properties in the desired manner by controlling one of the different parameters (such as temperature, reaction time, precursors and so on) which essentially requires the understanding of the formation process. However, while many efforts have been directed towards the synthesis of new carbon dots and application in various fields, there is not a model that is able to predict the formation of the particles along time comprehensively. During carbon dots synthesis many reactions are taking place simultaneously, making it impossible to monitor and control all of them. A different approach is required, where the focus is on a rational control of particular final properties, whether it is the photoluminescence or the size. Researchers have made few attempts in these directions regarding both CQDs and CNDs. These works are remarkable but still not sufficient to gain a full comprehension of the CDs growth from molecular precursors. The main issues researchers have to deal with are the difficulty in

monitoring their complicated reaction path, leading to unclear formation mechanism, and the high number of variables of the different methods.

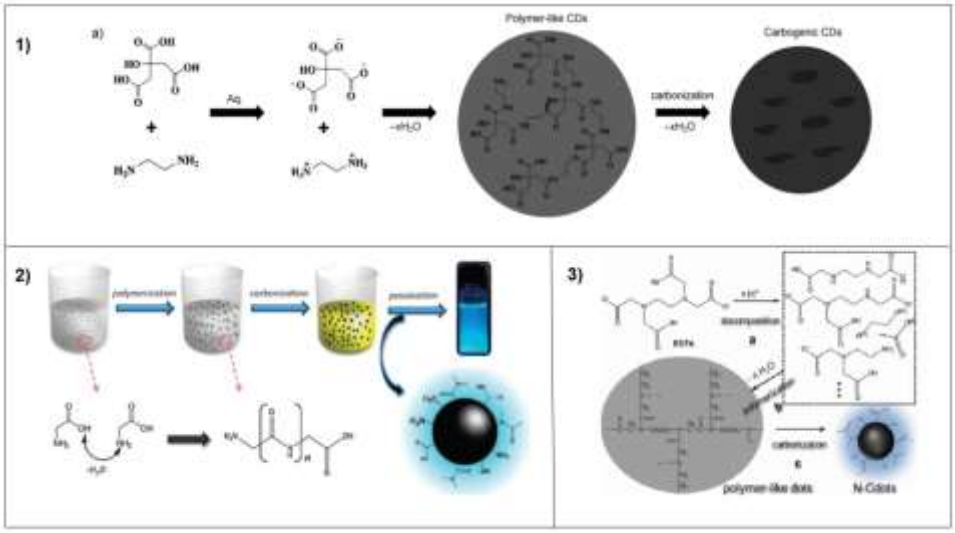

Figure 5.1 1) A synthetic route using citric acid and ethylenediamine: from ionization to condensation, polymerization, and carbonization. [13] **2)** Growth model for C-dots from glycine through dehydration, polymerization, carbonization, and passivation.[15] **3)** Decomposition-condensation polymerization-carbonization mechanism for the formation of C-dots. (a) Decomposition of EDTA; (b) Polymerization-growth procedure; and (c) Carbonization-aging for the formation of C-dots. [17]

Wang *et al.* suggested that carbon quantum dots were synthesized through “polymerization” and “carbonization” steps since the conditions were similar to the hydrothermal treatment of glucose (Figure 5.1.1).[13] The authors reported the red coloration during the reaction, which they attributed to the formation of oligosaccharides and aromatic compounds. Zhu *et al.* synthesized CNDs by hydrothermal treatment of citric acid and ethylendiamine, suggesting that the reaction was conducted by first condensing between the two precursors, whereupon they formed polymer like dots which were then converted in carbogenic ones.[14] Hsu *et al.* proposed a potential

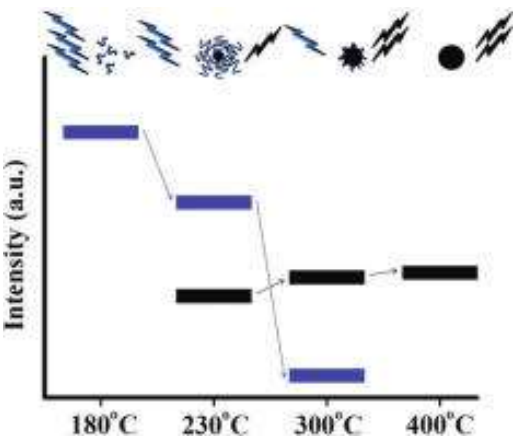

Figure 5.2 Schematic representation of the emission characteristics of three photoactive species produced from the thermal treatment of mixture of citric acid and ethylendiamine. During pyrolysis, the organic fluorophores (blue groups) are consumed for the build-up of the carbogenic core (black sphere) so that the PL component that corresponds to the carbogenic core (black bars) increases at the expenses of the component that arises from the organic fluorophores (blue bars). [16]

formation mechanism of carbon dots from glycine including dehydration, polymerization, carbonization, and passivation (Figure 5.1.2).[15] A breakthrough in this field is the work of Giannelis who, combining TEM, TGA, FT-IR and PL analyses, proposed a potential formation mechanism of CNDs from pyrolysis of citric acid and ethanolamine at different temperatures (Figure 5.2).[16] At first, carbon dots with high QY and strong PL due to amide-containing fluorophores are formed. As the pyrolysis proceeds, a carbogenic core is formed at the expense of the molecular fluorophores until obtaining CDs with PL arising only from the core. In a similar way, interesting formation mechanism of nitrogen-doped-carbon dots by hydrothermal treatment of ethylenediaminetetraacetic acid (EDTA) has been proposed by Zhang *et al.* who suggested the carbon quantum dots formed through three stages: decomposition, polymerization and carbonization. EDTA decomposed to remove one or more CH_3COOH groups (Figure 5.1.3).[17] Crosslinked polymerization then occurred via intermolecular amide linkage between the –NH and –COOH groups for the formation of the polymer-like CDs. A

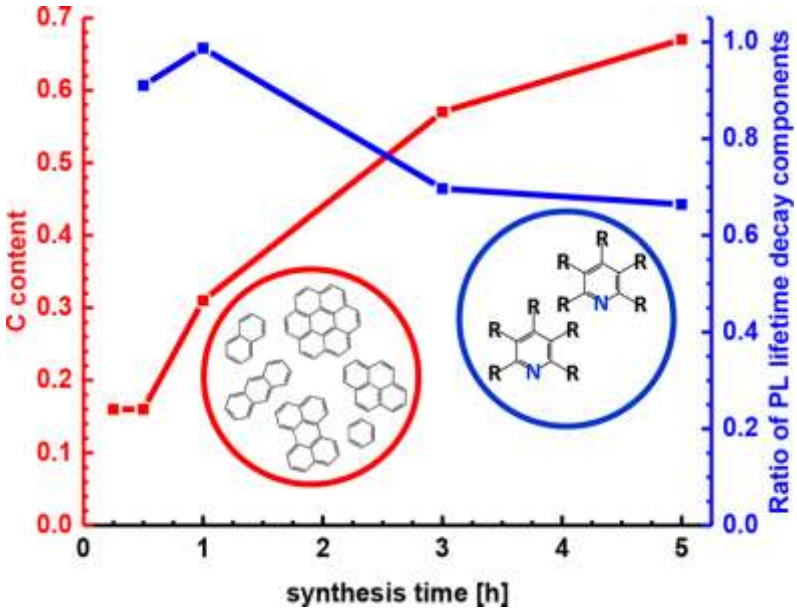

Figure 5.3 Carbon content in the CDs (left) and ratio between long and short decay components of the fluorescence lifetime (right) over the course of the synthesis of the CDs from citric acid and ethylendiamine. These parameters could represent the relative content of small molecular fluorophores similar to citrazinic acid (shown in a blue circle) and aromatic domains (represented in a red circle). [21]

carbonization aging process occurred to form small dots, which coupled with each other to form the final CQDs. Employing the same techniques, TEM, TGA, FT-IR and PL, the aforementioned authors Yu proposed, for carbon quantum dots made out of citric acid and monoethanolamine, the following mechanism: at first a large amount of monoethanolamine reacts with citric acid through intermolecular dehydration, which leads to the formation of large-sized polymer nanoparticles.[18] Then the polymer nanoparticles shrink due to continuous intramolecular dehydration and at this stage it is possible to observe C=C and C=N bonds forming and production of aromatic clusters inside the polymers. When this concentration of aromatic clusters reaches the critical supersaturation point in some local areas, a burst in carbon dots nucleation takes place. These nuclei

grow up driven by the enhanced aromatization degree of the polymers, increasing in number and size at the expense of the sacrificial polymers which finally disappear, with only CQDs remaining in the reaction mixture. Currently, the initial formation of a polymer chains with following partial carbonization to give CDs is the prevailing hypothesis. Indeed, in some cases researchers have been able to detect and isolate the molecules forming in the very first moments of the reaction and correlate them with the emission of the dots.[19,20] The very last contribution in support of this theory has been brought by Urban *et al*. (Figure 5.3).[21] He studied the evolution and the chemical nature of the fluorophores during the formation process of CQDs synthesized hydrothermally from citric acid and ethylenediamine. For the first time, instead of temperature or reagents nature, the variable taken in account was synthesis time. CQDs were formed within 30 minutes, maintaining the same size for the rest of the heating, and underwent a substantial change of their internal structure with formation of the aromatic domains. Indeed the authors were able to discriminate the contributions of small molecular fluorophores and aromatic domains to the overall fluorescence with time-correlated single photon counting. Consequently, some authors have suggested about the polymeric nature of carbon dots and even, how they could be formed just by aggregation of various polycyclic aromatic carbons.[22,23] Although we introduced both CQDs and CNDs, materials that we stated in Chapter 1 have different properties, from the list of works reported it appears that both classes undergo similar transformation at the initial stages. Whereas an amorphous core made of aromatic domains is the final state for CNDs, for CQDs this seems to be an

intermediate step, antecedent to aromatization and graphitization towards an ordered crystal lattice. Therefore, focusing on carbon nanodots formation, as we do in this chapter, would be pivotal to understand the first stages of all carbon dots growth. However, some of the techniques employed for CQDs, such as TEM and FL lifetime are not useful for amorphous particles such as nanodots. To gather enough information to solve the puzzle behind CDs formation we direct our attention to different analyses. In particular, third generation synchrotron sources now offer means to monitor particle by small and wide-angle X-Ray diffraction (SAXS, WAXS), as well as X-ray spectroscopy to obtain information on the evolution of the particle size distribution and optical properties as a function of time[24–26] and have been already applied in the field of inorganic quantum dots illustrating successfully the stages and the mechanism of their growth.[24–26] Consequently, these techniques, coupled with the information collected by NMR, FT-IR, AFM, UV-Vis spectroscopy will be a step-forward in the comprehension of the mechanism behind carbon dots formation.

5.1.2 Aim of the project

Carbon dots have been under the spotlight of research for the last decade. Their water-solubility, photostability, low toxicity, inexpensive nature and easy synthetic procedure, combined with their unique photoluminescence, have made these materials the perfect candidates for a number of applications that space from bioimaging to photocatalysis. [2–8]

Unlike many other carbon nanomaterials, carbon dots can be synthesized on large scale in different methods, which result in

modification of the optical and structural dimensions. Every time a parameter is changed, a new reagent is tried, a different work-up procedure is used, we obtain different CDs. Therefore, the ways carbon dots can be synthesized, and consequently their characteristics, are infinite. If tuning easily dots properties seems a great advantage, it also presents a drawback. There are so many variables in the synthetic protocols that is difficult to predict the final properties. Indeed, the achievements in this field have been reached by serendipity rather than design.

We believe that, at this stage, carbon dots chemistry requires a rational control in order to bridge the gap with inorganic quantum dots performances and become a real option for everyday applications. To do this, in this chapter, we present a systematic investigation of carbon dots formation following the hydrothermal synthesis from arginine and ethylenediamine at different reaction time. We propose a new mechanism and we show how the optical properties do not depend on the chemical rearrangements happening in the core. Moreover, we demonstrate the core/shell structure of carbon dots and master these properties synthesizing novel dots with controlled layer thickness.

5.2 Results and discussion

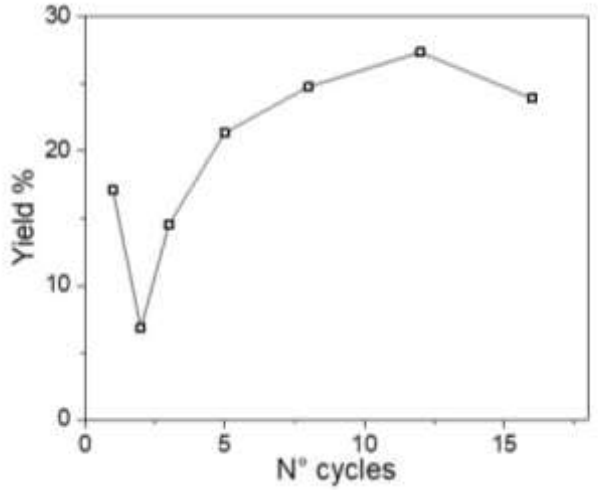

Figure 5.4 Yield, based on weight, of CNDs 1-16

As starting point, we employed arginine and ethylenediamine as precursors, which produce nitrogen-doped carbon nanodots under our previously reported hydrothermal MW-assisted protocol.[27] The procedure consists of different cycles of heating at 200 W with max. T 250°C (15 s) followed by 5 s of cooling. To gain information on the formation mechanism the reaction has been stopped at different times: after 1, 2, 3, 5, 8, 12 and 16 cycles. The reaction mixture was analyzed before and after work-up procedure (filtration and dialysis). From now on, we will refer at these compounds with the acronyms RM for reaction mixtures and as CNDs for carbon nanodots after proper work-up. The numeric suffix is related to the number of cycles before the reaction was ceased. We analyzed both structural and chemical/optical properties by SAXS, WAXS, DLS, Uv-Vis, Fluorescence, FT-IR and XPS.

In almost all samples, with the exception of CNDs 1, we detected the typical photoluminescence of nanodots. After 1 cycle we obtain a lot of material however the absence of emission reveals this mixture does not contain dots. Then, the yield (based on the weight) of the final product increases with time, raising quickly from 6% (CNDs 2) to 21% (CNDs 5) (Figure X). At this point, the amount of final product changes slightly to 27% (CNDs 12) and decreases to 24% when the heating is extended to 16 cycles.

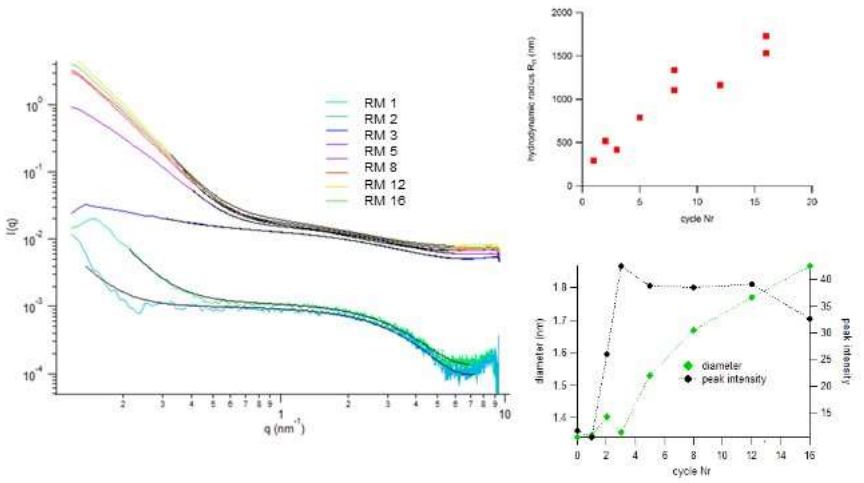

Figure 5.5 a) Scattering patterns of the reaction mixtures RM 1-16. **b)** Hydrodynamic radius resulted by SAXS patterns of RMs **c)** Particles diameter resulted by SAXS patterns of RMs

As we stated in section 5.1.3, small angle x-ray scattering (SAXS) gives detailed structural information of liquid samples on the sub-nanometer scale. SAXS patterns were recorded of the crude products RM. An overview of the scattering patterns is shown in Figure 5.5. First, and most dominantly, a clear increase in the overall scattering intensity is seen between RM 1 and RM 2, identifying the onset increased reactant concentration, most likely caused by

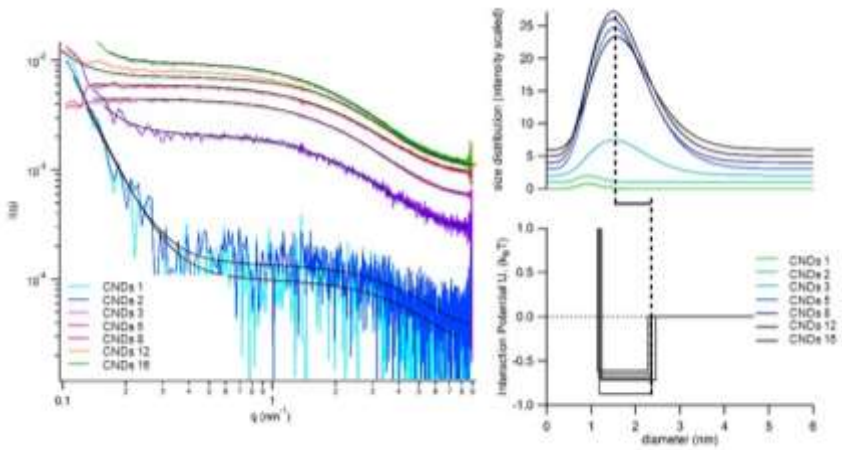

Figure 5.6 a) Scattering patterns of the CNDs 1-16. **b)** Size distribution showing hard-sphere distances and hard-contact diameter.

solvation of the initially solid arginine. In the consecutive cycles a strong increase in the low-q regime ($q < 1$ nm^{-1}) is visible. This is a strong index of large-scale aggregates formation as confirmed by dynamic light scattering (DLS) measurements where > 100 nm aggregates are observed from the very first cycles. In order to derive more detailed structural information from the scattering patterns, a parametric model was constructed, which includes two contributions: i) a Porod contribution, describing the aggregates formation and ii) a Schulz-distributed spherical formfactor contribution, describing single carbon nanodots. The quantitative results are found in Figure 5.5c. In agreement with the previous observation, carbon nanodots appear to form between cycles RM 1-3, whereas in the consecutive cycles the volume fraction of carbon nanodots remains constant. Hence, after the 3rd cycle, all reactants are consumed such that the following cycles induce a rearrangement and secondary aggregation processes. In order to distinguish the comparatively speaking weak carbon nanodots scattering contribution from the strong aggregate

contribution, SAXS patterns were recorded after filtration and dialysis, namely samples CNDs 1-16. The recorded scattering patterns can be found in Figure 5.6. Obviously, the aggregate scattering is not anymore witnessed in the scattering patterns. The absence of the previously dominant aggregate scattering now allow for a more detailed model, which now includes a sticky-hard-sphere structure factor, describing the interaction between single CNDs. First, a strong increase in the overall scattering intensity is found between CNDs 2-5, indicating the onset of carbon nanodots formation (see Figure 5.6b) at the second cycle. Interestingly, the size of carbon nanodots that form even at this early stage remain constant over the subsequent cycles, as no growth is witnessed (mean diameter of 1.66 nm). In agreement, the hard-contact diameter between the carbon nanodots, determined from the structure factor contribution, remains constant over the reaction cycles, whereas a hard-sphere distance of 2.33 nm is found. This further implies that there exists a difference between the observed carbon nanodots size and the hard-contact diameter of 0.67 nm. This can be explained by the following hypothesis: the carbon nanodots size relates to an electron dense core whereas the interaction diameter is enlarged by surface surfactants that – the equivalent to a core-shell structure. Notably, the average size of 2.47 nm reported in our previous work and determined by statistical analysis about one hundred nanoparticles at the AFM is in good agreement with the values observed at SAXS.[27]

At this point we demonstrated how the core/shell structure of carbon nanodots remains unaltered once is formed. However, there is a number of chemical reactions that may affect the optoelectronic

properties of the dots. In particular, due to their unique PL, we expect absorption and emission spectra to be a fruitful source of information for our investigation. Despite the different reaction times, RM and CNDs show similar absorption spectra (Figure 5.9-5.10). In both cases it is possible to notice a gradual increase of the band at 290 nm, absent in CNDs 1-3, which is ascribed to the π-π* transition of the conjugated C=C units from the carbon core.

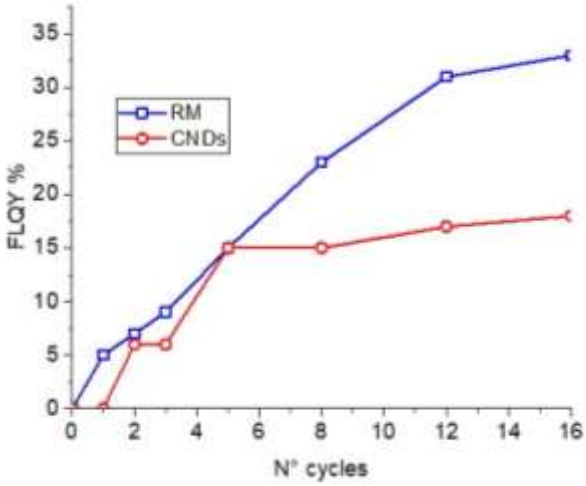

Figure 5.7 Quantum yield trend of CNDS and RMs

On contrary, emission spectra of RM show different features along the cycles. It is possible to observe the typical PL of carbon dots starting from the very first cycle. However, these particles grow rapidly in size in the first 3 cycles affecting the emission wavelengths. Indeed, maximum excitation wavelength shifts from 330 nm RM 1 to 300 nm RM 5 and it remains constant among the following cycle. Whereas the emission of RM 5 resembles closely the one of the final purified dots, in the other cases we find additional features in the spectra. Between RM 1 and RM 3 we noticed excitation-independent

emission at 500 nm, this contribution is the greatest after 2 cycles. After RM 5 the fluorescence at excitation wavelengths 320nm and 340 nm becomes more prominent. These features are ascribed to the smallest and most fluorescent fraction of carbon dots that we have separated, through size-exclusion chromatography, and characterized in a recent work.[27] This contribution is not present after the work-up procedure; therefore this fraction is washed out during the dialysis which is estimated to remove compounds with MW lower than 1000. Indeed, emission spectra of CNDs 5-16 look identical and the differences observed between the crudes are ascribed either to small fragments either to particles bigger than 100 nm.

In both series the QY increases gradually to 0.15 after 5 cycles of heating. However, in the crude the QY keep rising, reaching a value of 0.33 for RM 16, while in the final dots CNDs 5-16 the quantum yield retains a value around 0.15. These results are in agreement with what we observe at the emission spectra, indeed we ascribed the new features in RM 8-16 to small carbon dots which have higher emission with QY of 0.46.[27] To exclude any contribution from larger particles removed during filtration, we recovered them from the filter, sonicated it in small amount of milliQ water and measured absorption and emission of the solution. Whereas the absorption spectra show similarities with the ones of CNDs, we did not notice any emission from these materials. Consequently, the differences between the emission of RMs and CNDs are related to molecules, polymers and dots too small to be retained during the dialysis process. Despite working on very different carbon dots, Giannelis analyzed big carbon nanodots of 20 nm diameter while Urban reported CQDs of 1 nm

diameter, they both showed similar QY trend during, a trend very different from the one we observed.[16,21] Both authors reported an initial high PL intensity with emission independent on the excitation wavelength. These features were attributed to organic fluorophores that are gradually consumed for the build up of the carbogenic core that will lead to the typical PL of carbon dots. Our experiments showed completely different results. In fact, the representative fluorescence is observed even after 30 s, QY increases gradually during the synthesis, and organic fluorophores seem to be formed only at the end of the reaction. Therefore, the formation pathway Gianellis and Urban proposed, that is i) formation of organic fluorophores, ii) formation of aromatic domains iii) carbonization processes with disappearance of initial fluorophores, could not apply to our synthesis.

We know that the chemical and structural modifications happening in the very first cycles are the ones responsible for the fluorescence. Heating the reaction longer than 5 cycles won't give higher yield or QY however these doesn't mean that other changes are not involved. The analyses of both series by FT-IR and XPS could provide useful information on the functional groups that are formed during the reaction and if these moieties have influence on the optical features. As shown in Figure X, after first cycle ethylenediamine peaks at 1590 cm-1 and 1460 cm-1 are not observed, therefore all the precursor has already reacted. On the contrary, arginine is still present as indicated by the stretching of C=O at 1670 cm-1 and 1620 cm-1. As the reaction proceed, after 5 cycles a new peak appears at 1760 cm-1 (C=O of ketone/anhydride) and the amide stretching moves to 1690 cm-1. The last new features

emerge at the 8th cycle (RM 8 and CDs 8): C=C stretching is visible at 1650 cm-1 and C-O is detected at 1320 cm-1 and 1277 cm-1. In the following cycles no further modification will be noticed.

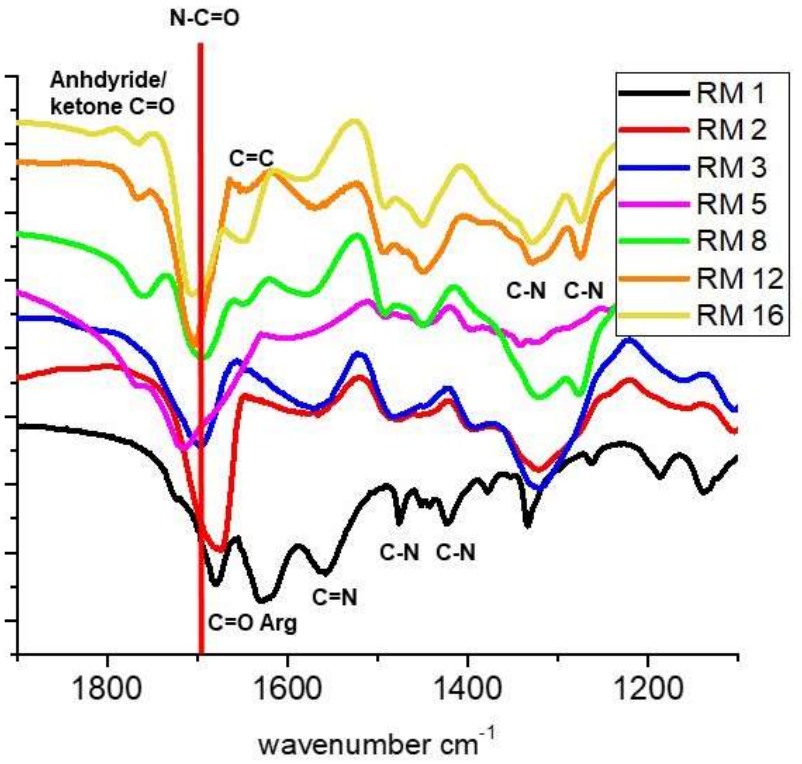

Figure 5.7 FT-IR spectra of RM 1-16.

FT-IR confirms that C=C bonds are formed after 8 cycles while Uv-Vis spectra tell us that these bonds keep forming during time reaching the maximum for CNDs 16/RM 16. However, the fluorescence profile is constant after 5 cycles of heating, proving these functional groups have no influence on these optical properties. In the SAXS experiments, we confirm dots are made of a dense core and a soft shell where the emissive domains are

situated. Therefore, this chemical reactions involve only the core of the dots.

So far, we listed our analyses on structure, photoluminescence and chemical composition of carbon dots, therefore it is time to combine all this information and propose a mechanism for the formation of such nanoparticles. Since the precursors are consumed after the very first cycle, as proved by FT-IR and SAXS, during the synthesis we can distinguish three different groups of material: i) big aggregates > 100 nm, ii) carbon nanodots iii) small molecules/polymeric aggregates. Carbon dots and big aggregates follow a different formation pathway, indeed while they both form in the first cycles, aggregates keep forming during time while CNDs stop after cycle 5. If CNDs came from fragmentation of the bigger particles, their quantity should increase along the cycles. On the contrary, the yield between CNDs 5 and CNDs 12 is similar, with even a small drop for CNDs 16. Small molecules/polymeric aggregates start forming at cycle 5 and increase in number in the following cycles. These particles are very emitting, raising the QY of the crude mixture and have a MW smaller than 1000 MW. In this case, we cannot attribute safely their origin. They could come either from bigger aggregates fragmentation (since their quantity is proportional of the big nanoparticles one) or from degradation of CNDs (since the final yield slightly drop in the last cycles).

Regarding the formation of carbon nanodots, we propose a mechanism consisting of 4 different steps: i) aggregation of organic molecules CNDs 1–3, ii) shell formation CNDs 2–5, iii) core

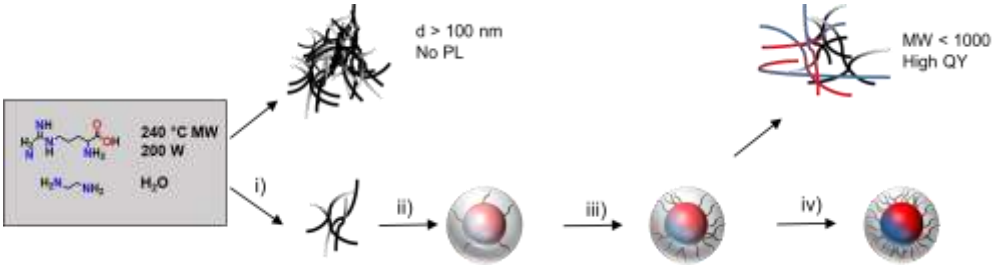

Figure 5.8 Formation of carbon nanodots from arginine and ethylenediamine as precursors. i) aggregation of organic molecules CNDs 1–3, ii) shell formation CNDs 2–5, iii) core formation CNDs 3-5 iv) formation of aromatic groups in the core CNDs 8-16. By-products are big aggregates > 100 nm and small molecules/polymeric aggregates.

formation CNDs 3-5 iv) formation of aromatic groups in the core CNDs 8-16. After the first cycle, the precursors have been consumed forming bigger organic molecules, very little emission is observed by particles not big enough to remain in the dialysis tube. In the next cycle first CNDs are observed, however QY is low and emission different from the final product: shell starts forming. In cycle 3 the few dots formed have already the final core/shell structure and overall size as the same emission profile, however the QY is still low. After 5 cycles the optical properties have been defined and the reaction yield is close to the maximum. In the following cycles we observe a refinement in QY and emission without any substantial modification. On the other side, chemical modifications keep interesting carbon dots. As proved by FT-IR and UV-Vis we noticed C=C formation, however, since these reactions do not affect the PL we ascribed them to processes involving the amorphous core.

To validate the core-shell hypothesis, so to provide further evidence that the carbon nanodots in fact consist of an electron dense core covered by a surface shell, the carbon nanot synthesis was repeated using different amines with increasing backbone length. Figure 5.8

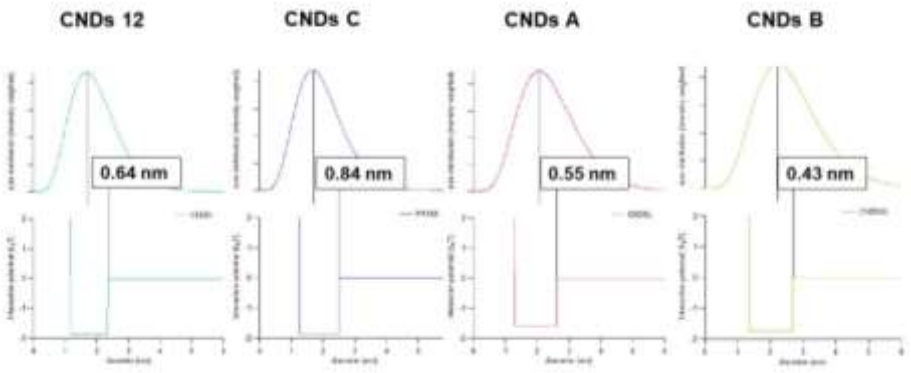

Figure 5.9 Core-shell structure of CNDs 12, CNDs C, CNDS A and CNDs B.

shows an overview of the results of the SAXS analysis.. With the same procedure employed previously, 200 W, T max 250 °C 12 cycles of 15 heating with 5 s of cooling intervals, we synthesized three new dots, namely CNDs A. CNDs B and CND C. For CNDs A and CNDs B we used 2,2′-(Ethylenedioxy)bis(ethylamine) and 1,11-Diamino-3,6,9-trioxaundecane respectively, instead of ethylendiamine. For the last dots CNDs C we made react CNDs 12 with Meldrum's acid in order have a controlled increase in shell thickness. One more time, information on size and structure were provided by SAXS analyses where in each case, a core-shell structure was witnessed. CNDs B resulted to be the biggest with a diameter of 2.67 nm, followed by CND A with similar dimensions (2.62 nm). As expected CND C (2.50 nm), are slightly bigger than CNDs 12 (2.33 nm). While general dimensions matched the expectations, thickness of the layers was less predictable. CNDs C have a shell of 0.84, 0.20 nm thicker than CNDs 12. These dimensions are in agreement with the length of the functional groups added by reaction of terminal primary amines with CNDs C showed the largest shell along the series. Whereas we have demonstrated

that arginine contributes the most to the aromatic core, larger amines have great impact on the core dimensions. Indeed the external layer of CNDs A (0.55 nm) and CNDs B (0.43 nm) is considerable smaller, therefore thicker shells require more reactive diamines, not longer ones. Indeed, the Kaiser Test showed that CNDs A (880 μmol g^{-1}) and CNDs B (700 μmol g^{-1}) own less free amines than CNDs 12 (1350 μmol g^{-1}).

5.2.1 Conclusions

Summarizing our findings, we investigate the synthesis of carbon nanodots by hydrothermal MW-assisted protocol from arginine and ethylendiamine playing with the variable of reaction time. We believe the formation of CNDs consists of 4 different steps: i) condensation of organic molecules CNDs 1–3, ii) shell formation CNDs 2–5, iii) core formation CNDs 3-5 iv) formation of aromatic groups in the core CND 8-16. In addition, we detected three different groups in the reaction mixture, which, besides CNDs, are big no emitting aggregates > 100 nm, and high emitting small molecules/polymeric aggregates. Moreover, we provided new evidences of how carbon nanodots in fact consist of an electron dense core covered by a surface shell. Finally, to bring new proofs of this core-shell strcture, we synthesize three novel CNDs A-C with different layer thickness.

5.3 Experimental Section

5.3.1 Instruments and materials

Chemicals

L-Arginine (Fluorochem, > 98%), Ethylendiamine (Sigma-Aldrich > 99.5%). Kaiser test kit was purchased from Sigma-Aldrich. Dialysis tubes with molecular weight cutoff 0.5-1KDa were bought from Spectrum Labs. Ultrapure fresh water obtained from a Millipore water purification system (>18Milli-Q, Millipore) was used in all experiments.

Apparatus and characterization

The microwave synthesis was performed on a CEM Discover-SP.
Uv-Vis spectra were recorded on a PerkinElmer Lambda 35 UV-Vis spectrophotometer. Fluorescence UV-Vis spectra were recorded on a Varian Cary Eclipse Fluorescence Spectrophotometer. All the spectra were recorded at room temperature using 10 mm path-length cuvettes.
Fourier-Transform Infrared (FT-IR) spectra have been recorded on a Varian 660 FT-IR with KBr pellets. Atomic force microscopy (AFM) images were obtained with a Nasoscope IIIa, VEECO Instruments. As a general procedure to perform AFM analyses, tapping mode with a HQ:NSC19/ALBS probe (80kHz; 0.6 N/m) (MikroMasch) from drop cast of samples in an aqueous solution (concentration of few mg/mL) on a mica substrate was performed. The obtained AFM images were analyzed in Gwydion 2.46.
X-ray photoemission spectroscopy (XPS) spectra of the samples were measured on a SPECS Sage HR 100 spectrometer using a non-monochromatised Mg-Kα radiation of 1253.6 eV and 250 W, in

an ultra-high vacuum chamber at pressure below 8 x 10^{-7} mbar. For each analysis, an aqueous solution (c.a. 3 mg/mL) of material were deposited on a gold thin film. The calibration was done using the 3d5/2 line of Ag. Survey and high resolution spectra were collected with pass energy of 30 and 15 eV and 0.5 and 0.15 eV/step, respectively. CasaXPS 2.3.17 PR1.1 and Avantage (Thermo Fisher Scientific) software were used for data processing and fitting. Curve fittings of the C1s and N1s spectra were realized using a Gaussian-Lorentzian peak shape after performing a Shirley background correction, to finally obtain the relative percentage of each type of bond inside the analyzed sample.

The quantum yield measurements were performed with quinine sulphate in 0.10 M H_2SO_4 (literature quantum yield 0.54 at 360 nm) as the standard[28]. The absorption factors f_x and f_{st} of the standard and the sample were calculated from the measured absorbance values (A) at the excitation wavelength using equation (1) The index *x* denotes the sample, and the index *st* denotes the standard.

$$f = 1 - 10^{-A\lambda_{exc}}$$

The fluorescence quantum yields were calculated according to equation below.

I is the measured integrated fluorescence emission intensity, *f* is the absorption factor, η is the refractive index of the solvent and Φ is the quantum yield. The index *x* denotes the sample, and the index *st* denotes the standard.

$$\Phi_x = \Phi_{st} \cdot \frac{I_x}{I_{st}} \cdot \frac{f_{st}}{f_x} \cdot \frac{\eta_x^2}{\eta_{st}^2}$$

5.3.2. Synthesis of CNDs

RM 1-16 were obtained via microwave irradiation of an aqueous solution of L-Arginine and Ethylendiamine (EDA) (0.5 mmol). Typically (87.0 mg), EDA (33.0 mL), Milli-Q water (100.0 µl) and 0.25 mmol of the appropriate quinones were heated at 240°C, 26 bar and 200 W for a variable amount of time going from 15 s (RM 1) and 240 s (RM16). The powder material was obtained without any further purification by freeze-drying.

CNDs 1-16 were obtained via microwave irradiation of an aqueous solution of L-Arginine and Ethylendiamine (EDA) (0.5 mmol). Typically (87.0 mg), EDA (33.0 mL), Milli-Q water (100.0 µl) and 0.25 mmol of the appropriate quinones were heated at 240°C, 26 bar and 200 W for a variable amount of time going from 15 s (CNDs 1) and 240 s (CNDs 16).

In the process of microwave heating, the solution changed color from transparent to brown as a result of carbon nanodots formation. The reaction mixture was filtered (0.1 µm microporous membrane), washed with Milli-Q water, and dialyzed against Milli-Q water for 48 h. The powder material was obtained by freeze-drying.

5.3.3 Supporting Figures

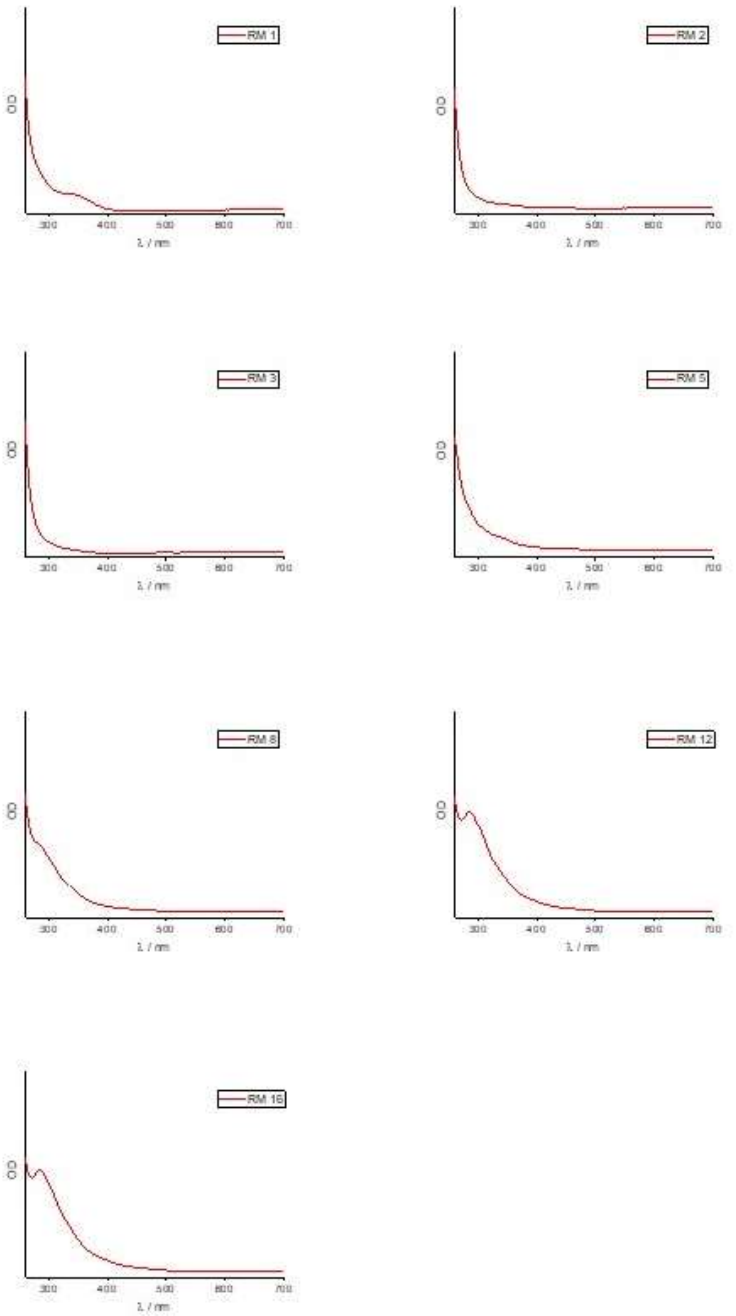

Figure 5.10 UV-Vis absorption spectra of RM 1-16

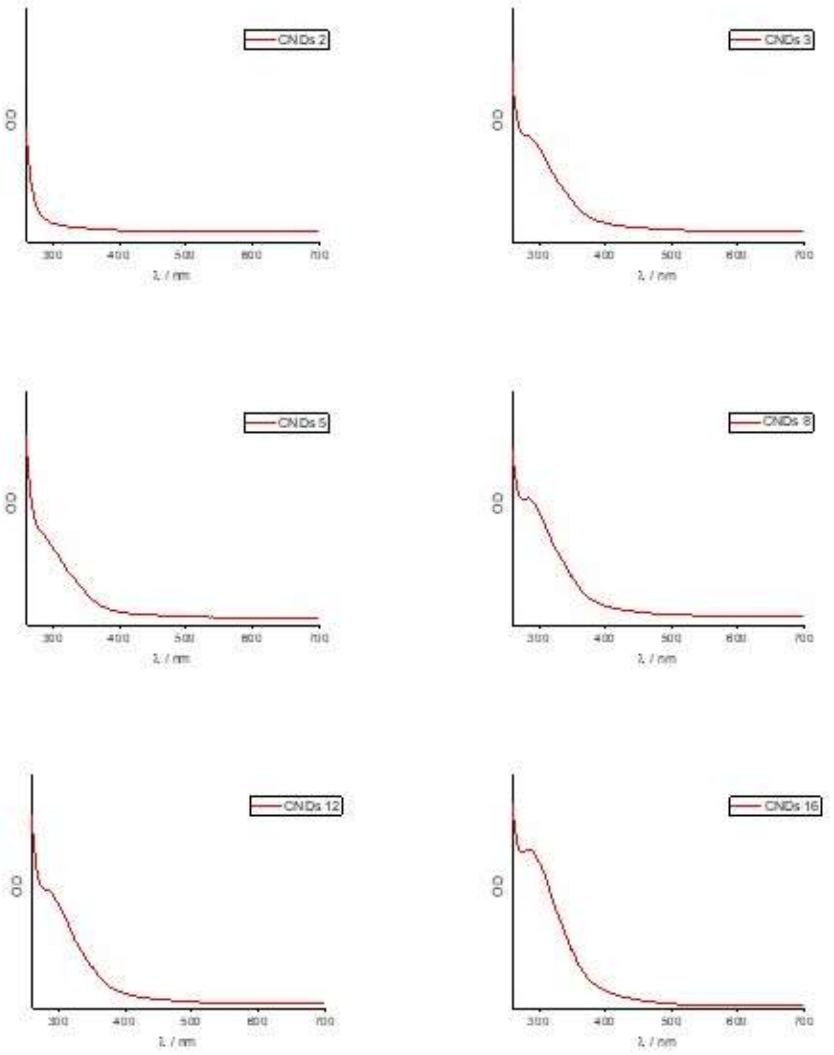

Figure 5.11 UV-Vis absorption spectra of CNDs 2-16

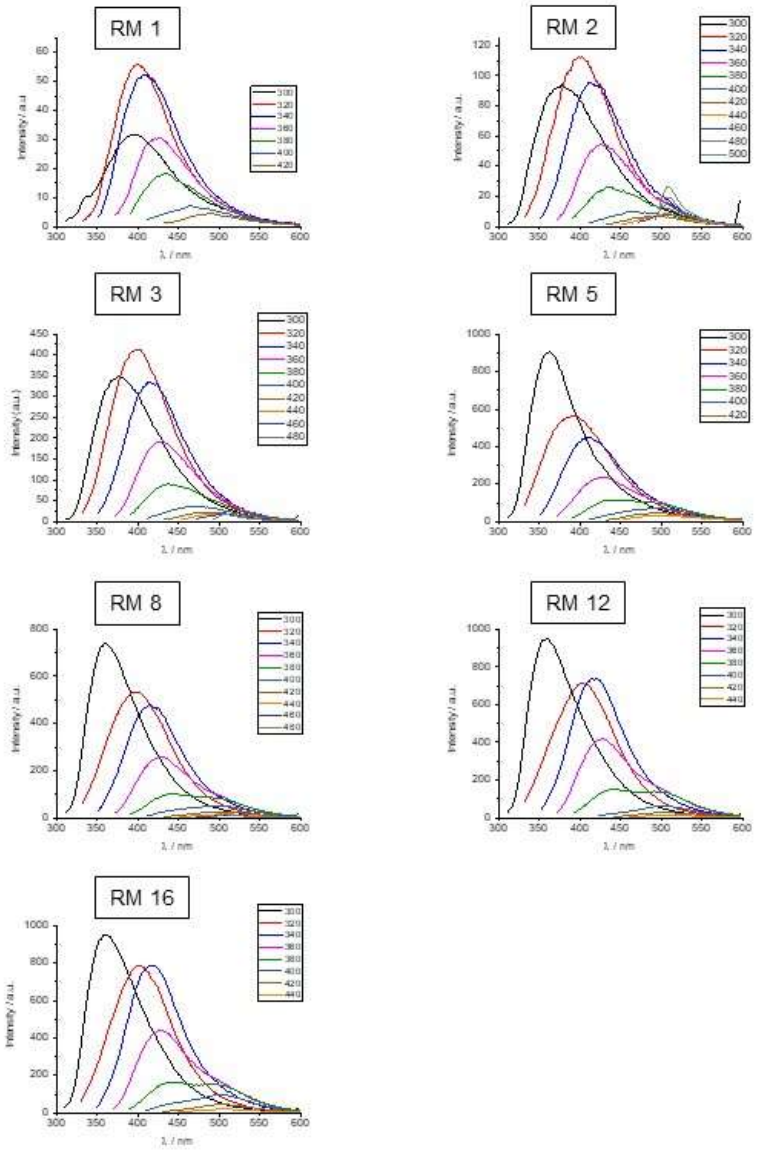

Figure 5.12 Fluorescence spectra of RM 1-16

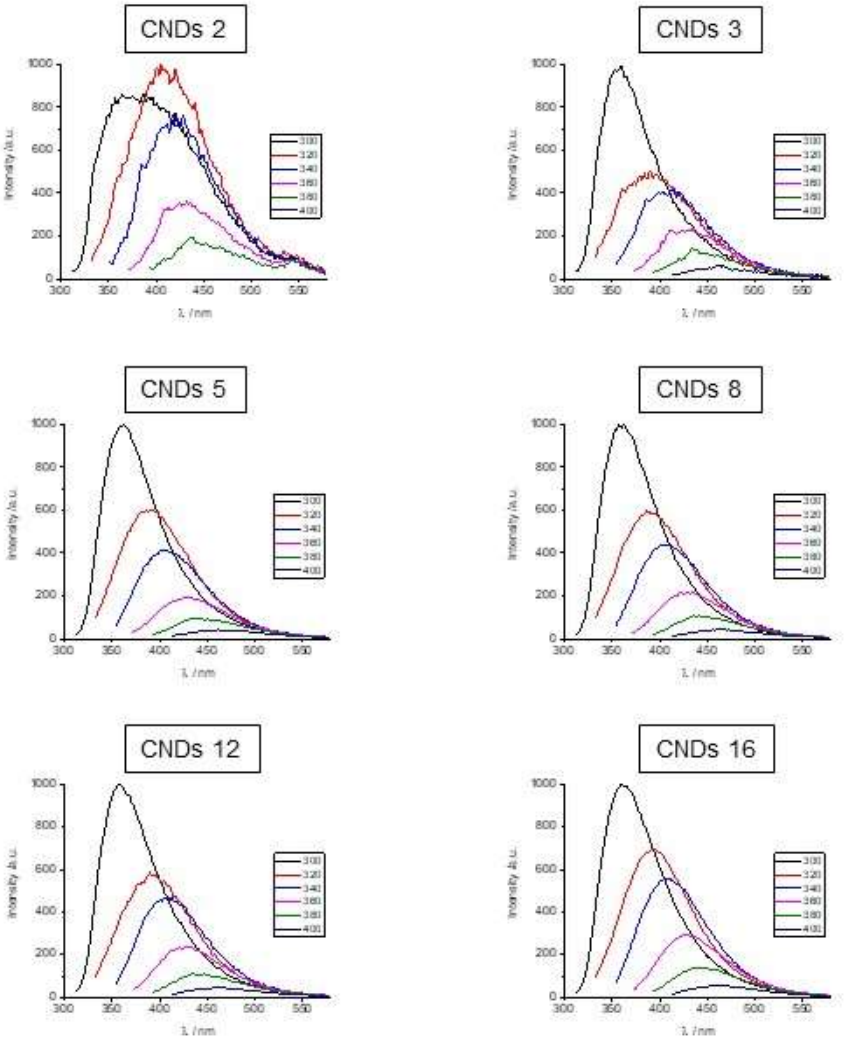

Figure 5.13 Fluorescence spectra of CNDs 2-16

5.4 References

[1] L. Cao, X. Wang, M. J. Meziani, F. Lu, H. Wang, P. G. Luo, Y. Lin, B. A. Harruff, L. M. Veca, D. Murray, *J. Am. Chem. Soc.* **2007**, *129*, 11318–11319.

[2] F. Yuan, S. Li, Z. Fan, X. Meng, L. Fan, S. Yang, *Nano Today* **2016**, *11*, 565–586.

[3] S. Y. Lim, W. Shen, Z. Gao, L. Cao, X. Wang, M. J. Meziani, F. S. Lu, H. F. Wang, P. G. Luo, Y. Lin, *Chem. Soc. Rev.* **2015**, *44*, 362–381.

[4] G. E. LeCroy, S. T. Yang, F. Yang, Y. Liu, K. A. S. Fernando, C. E. Bunker, Y. Hu, P. G. Luo, Y. P. Sun, *Coord. Chem. Rev.* **2016**, *320–321*, 66–81.

[5] R. Wang, K.-Q. Lu, Z.-R. Tang, Y.-J. Xu, *J. Mater. Chem. A* **2017**, *5*, 3717–3734.

[6] G. A. M. M. Hutton, B. Reuillard, B. C. M. M. Martindale, C. A. Caputo, C. W. J. J. Lockwood, J. N. Butt, E. Reisner, *J. Am. Chem. Soc.* **2016**, *138*, 16722–16730.

[7] J. B. Essner, G. A. Baker, *Environ. Sci. Nano* **2017**, *4*, 1216–1263.

[8] X. Li, M. Rui, J. Song, Z. Shen, H. Zeng, *Adv. Funct. Mater.* **2015**, *25*, 4929–4947.

[9] P. Mirtchev, E. J. Henderson, N. Soheilnia, C. M. Yip, G. A. Ozin, X. Sun, Z. Ding, M. Gratzel, R. S. Ruoff, M. Chen, *J. Mater. Chem.* **2012**, *22*, 1265–1269.

[10] S. Chandra, S. H. Pathan, S. Mitra, B. H. Modha, A. Goswami, P. Pramanik, *RSC Adv.* **2012**, *2*, 3602.

[11] R. Tian, S. Zhong, J. Wu, Y. Geng, B. Zhou, Q. Wang, W. Jiang, *J. Mater. Chem. C* **2017**, *9174*, 9174–9180.

[12] Q.-Q. Shi, Y.-H. Li, Y. Xu, Y. Wang, X.-B. Yin, X.-W. He, Y.-K. Zhang, *RSC Adv.* **2014**, *4*, 1563–1566.

[13] X. Jia, J. Li, E. Wang, *Nanoscale* **2012**, *4*, 5572.

[14] S. Zhu, Q. Meng, L. Wang, J. Zhang, Y. Song, H. Jin, K. Zhang, H. Sun, H. Wang, B. Yang, *Angew. Chem.* **2013**, *52*, 3953–3957.

[15] P.-C. Hsu, H.-T. Chang, *Chem. Commun.* **2012**, *48*, 3984.

[16] M. J. Krysmann, A. Kelarakis, P. Dallas, E. P. Giannelis, *J. Am. Chem. Soc.* **2012**, *134*, 747–750.

[17] Q.-Q. Shi, Y.-H. Li, Y. Xu, Y. Wang, X.-B. Yin, X.-W. He, Y.-K. Zhang, *RSC Adv.* **2014**, *4*, 1563–1566.

[18] Y. Hu, J. Yang, J. Tian, J.-S. Yu, *J. Mater. Chem. B* **2015**, *3*, 5608–5614.

[19] A. Das, V. Gude, D. Roy, T. Chatterjee, C. K. De, P. K. Mandal, *J. Phys. Chem. C* **2017**, *121*, 9634–9641.

[20] A. Sharma, T. Gadly, S. Neogy, S. K. Ghosh, M. Kumbhakar, *J. Phys. Chem. Lett.* **2017**, *8*, 1044–1052.

[21] F. Ehrat, S. Bhattacharyya, J. Schneider, A. Löf, R. Wyrwich, A. L. Rogach, J. K. Stolarczyk, A. S. Urban, J. Feldmann,

Nano Lett. **2017**, *17*, 7710–7716.

[22] M. Fu, F. Ehrat, Y. Wang, K. Z. Milowska, C. Reckmeier, A. L. Rogach, J. K. Stolarczyk, A. S. Urban, J. Feldmann, *Nano Lett.* **2015**, *15*, 6030–6035.

[23] S. Tao, S. Zhu, T. Feng, C. Xia, Y. Song, B. Yang, *Mater. Today Chem.* **2017**, *6*, 13–25.

[24] F. Hubert, F. Testard, A. Thill, Q. Kong, O. Tache, O. Spalla, *Cryst. Growth Des.* **2012**, *12*, 1548–1555.

[25] B. Abécassis, F. Testard, Q. Kong, B. Francois, O. Spalla, *Langmuir* **2010**, *26*, 13847–13854.

[26] B. Abécassis, F. Testard, O. Spalla, P. Barboux, *Nano Lett.* **2007**, *7*, 1723–1727.

[27] F. Arcudi, L. Dordevic, M. Prato, *Angew. Chem.* **2016**, *55*, 2107–2112.

[28] C. Würth, M. Grabolle, J. Pauli, M. Spieles, U. Resch-Genger, *Nat. Protoc.* **2013**, *8*, 1535–1550.

6. Mastering the electrochemical properties of CDs

Carbon dots (CDs) are photoluminescent nanoparticles that currently hold a great promise in biological, optoelectronic and photocatalytic applications. However, the main drawback that impedes the advancement of this field is a lack of rational control of their photophysical and electrochemical properties. In this chapter, we show how carbon nanodots (CNDs) redox potentials can be customized by employing quinones, common electron acceptors, as dopants in a microwave-assisted bottom-up synthesis. Hence, we prepared a library of CNDs with different electrochemical properties. We envisage that this approach will strengthen the use of these materials for *ad-hoc* applications, mainly in photocatalysis.

The work presented in this chapter has been done in a collaborative work with Dr. Francesca Arcudi (Università degli Studi di Trieste) e Dr. Luka Đorđević (Università degli Studi di Trieste) that contributed with the experimental design and results.

6. Mastering the electrochemical properties of CDs

6.1. Introduction

6.1.1 The design of photoactive hybrids

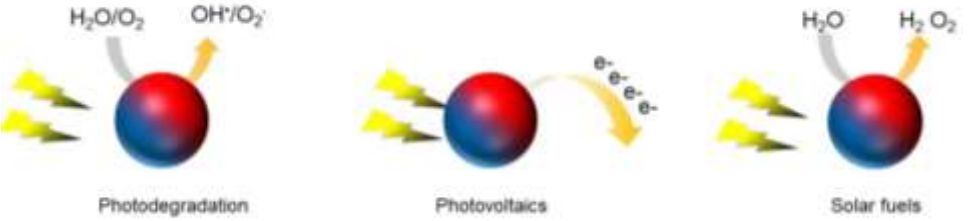

Figure 6.1 Photocatalytic applications of carbon dots.

Carbon dots own fascinating optical and electronical properties, thus, it is not surprising they have been introduced into the fields of photocatalysis, photovoltaics, and, more recently, fuel production. Moreover, the development of efficient photocatalysts is an important issue in environmental remediation after contamination with organic pollutants from the textile and food industries. The degradation of such pollutants should result in waste elimination yielding, idyllically, CO_2 and H_2O as by-products.

A first milestone for these applications was marked by reporting the photoinduced electron transfer of water-soluble CDs.[1] Indeed, their photoluminescence (upon 425 nm excitation) was quenched by 2,4-dinitrotoluene (-0.9 V vs. NHE)[2] and N,N-diethylaniline (0.88 V vs. NHE)[3] confirming their double nature as both electron acceptors and electron donors. Consequently, it was reported that CDs, in composite photocatalysts, could efficiently trap photogenerated electrons from

semiconductors, leading to enhanced separation efficiency of photoinduced electrons and holes.[4]

First nanoparticles-dots based catalysts (CDs/TiO_2 and CDs/SiO_2) were designed to exploit the full spectrum of sunlight, taking advantage of the upconversion luminescence (UPCL) of dots.[5] Upon illumination of CDs/TiO_2 or CDs/SiO_2, the CDs absorb visible light which is then reemitted at shorter wavelength (325 to 425 nm) via UPCL, exciting TiO_2 or SiO_2, leading to electron/hole (e^-/h^+) pairs.[6] Subsequently, electron/hole pairs react with the adsorbed oxidants/reducers (such as O_2/OH^-) to give reactive oxygen species (ROS) (e.g. $O_2^-/OH\cdot$), which can finally lead to the degradation of dyes like methyl blue.

Employing the same mechanism, many CDs-metal based photocatalysts, such as CDs/ZnO, CDs/Fe_2O_3 and CDs/Ag/Ag_3PO_4have been reported, all showing good photocatalytic activity.[7–9] The hybrids show increased photodegradation performances compared to the pristine inorganic materials. The rapid escalation of attention towards carbon dots led to the design of novel systems like CDs/g-C_3N_4,[10,11] CDs/Bismute oxide hybrid nanosheets[4] and CDs/In_2S_3.[12] The higher activity of the hybrids, compared to pristine semiconductors/nanoparticles, is an improvement added by the presence of CDs. The latter act as an electron sink to trap electrons emitted from semiconductor, excited by visible light, thus reducing electron/hole recombination in the composite. Moreover, due to UCPL properties, CDs could absorb longer wavelength and then emit shorter wavelength light, which could, in turn, excite the

semiconductor to form electron/hole pairs. Finally, π-π interactions, between the outer shell of the nanoparticles and the pollutants, foster the enrichment of the latter on the surface of the composite. Besides, it was confirmed that the electron transfer properties of CDs could enhance the stability of semiconductor photocatalysts in addition to their activity.[13] The consequent investigation on the mechanism by electron spin resonance ESR confirmed that positive holes and O^{2-} were the responsible for pollutants degradation.[12]

Much effort has been made on this topic with a big amount of works describing very different systems, all working better than pristine inorganic materials. However, an in deep comparison between the catalysts, in the identical conditions, is still missing while it appears instrumental to define a ranking of these dyes. This an indispensable step if we want these photocatalysts to be reliable for industry in water treatments, where nanoscale TiO_2 is still the first choice.[14] We believe new works should focus on improving the catalytic performances more than assembling original nanohybrids. Moreover, investigating new pollutants looks a fool's errand since the active ROS species have low selectivity and are equally effective against the most of the aromatic molecules.

6.1.2 Carbon dots in photovoltaics

Photodegradation is just the first field where CDs found application as photocatalysts, but in recent years, energy production has become subject of studies for carbon dots technologies, since the race to the development of an economically viable energy sources is getting every day more relevant. CDs are good candidates for photovoltaic

applications when building up dye-sensitized solar cells (DSSC). This kind of solar cells are usually composed of a mesoporous wide-band-gap semiconductor (TiO_2, WO_3, SnO_2) sensitized with a light-absorbing dye, a redox electrolyte and a counter electrode.[15] Carbon dots could play the photosensor role perfectly: they have excellent photostability, good solubility in many solvents, tunable surface chemistry and broad absorptions.[16–19] In addition, they easily transport charge in solar cells.[20–24] The first one to be designed in this way was a CDs-sensitized nanocrystalline TiO_2 solar cell that, under AM 1.5 illumination, showed Power Conversion Efficiency (PCE) of 0.13%.[17] It was envisaged that refinements in the surface chemistry, corrosion stability, charge transport and charge injection properties of CDs could lead to improved performances, however new systems didn't show any enhancement with efficiency ranging from 0.06% to 0.13 %,[17,25,26] far below 7-12% of ruthenium based sensitizers DSSC [27–29] or 6-10 % of inorganic quantum dots solar cells.[30–36] These relatively modest performances were attributed to low coverage of the photoelectrodes, non-optimized electrolytes, and incomplete understanding of the electronic structure of CDs.[37] A small step forward, to 0.24%, was achieved by the sensitization with CDs made from citric acid, urea and formic acid in a one-step hydrothermal synthesis, in mesoscopic solar cells.[38] The improvement was related to optimization of the CDs coverage on the electrode. Better efficiency, up to 0.53%, was reached by a series of biomass derived dots, just using an aqueous iodide electrolyte rather than an acetonitrile-based one, which was linked to a quenching of the fluorescence on the CDs.[39] However, the highest efficiency (0.79%), up to now, has been

reached by nitrogen doped carbon dots, obtained from pyrolysis of citric acid and ammonia.[40] The authors suggested that the heteroatom doping may be beneficial, however they didn't provide any comparison with other solar cells based on dots without nitrogen.

New works on DSSCs have to deal with many issues because the PCE needs further improvements in order to become a viable alternative to the current solar-cell devices. Light harvesting of dots should be increased in the visible and near-IR regions to take advantage of the whole solar spectrum. Furthermore, charge transfer processes and reducing recombination should be improved. In addition, the fabrication of devices require optimization such as alternative electrolytes,[41] counter electrodes[42] and light scattering layers.[43]

6.1.3 Carbon dots and solar fuels

Besides electricity from solar cells, the global energy crisis calls for urgent actions like the sustainable production of solar fuels, renewed daily from water and carbon dioxide under just visible light. Put differently, we want clean fuel (oxygen and hydrogen) generated by clean energy source (sun), ideally, in a cheap way. The development of such system is not trivial. The whole process requires a perfect matching between the oxidation/reaction sites and the adsorption of photons trough light harvesting. Therefore, a common goal in this field is the development of a stable visible-light-responsive photocatalyst capable of a high overall water splitting activity, focusing on improved catalytic conditions and novel materials. Because of their light harvesting and electron transfer ability carbon dots are promising

candidates for this role, however their applications have been unexplored for a long time.

The photo reduction of carbon dioxide to formic acid with polyethylene glycol-passivated carbon nanodots, modified with deposits of Au or Pt, was the first example where CDs were selected as the primary photosensitizer[19,44]. At a later time, Reisner *et al.* reported the key case of CDs as photocatalysts in homogenous solution with a carboxylate-terminated CDs working as a photosensitizer for hydrogen evolution, once coupled with a nickel molecular catalyst (NiP).[45–47] In the photocatalytic scheme, CDs absorb UV and visible light and directly transfer photoexcitated electrons to electron acceptors and catalysts inside the solution. Through parameter optimization, best performances of 398 μmol H_2 (g CDs)$^{-1}$ h^{-1}, optimized for NiP, were reached under full solar spectrum light irradiation at one sun intensity. Successively, the graphitization of the core in such carbon dots boosted the performances of one order of magnitude 7950 μmol H_2 (g CDs)$^{-1}$ h^{-1}. The increased activity was related to better hole scavenging by electron donor and thereby significantly extension of the lifetime of the photogenerated electrons, as observed by transient absorption.[48] Another important achievement reached by Reisner *et al.* has been the coupling of the aforementioned dots with two semibiological photosynthetic systems, in particular with hydrogenase (H2ase) for reduction of protons to H_2 using ethylendiaminetetraacetic acid (EDTA) as sacrificial electron donor.[49] Electrostatic interactions between enzymes (owning negatively charged residues at the electron entry sites) and photosensitizers was achieved by chemical modification of CDs, *i.e.* capping them with tertiary amines.

6. Mastering the electrochemical properties of CDs

Even if, in the most recent work, carbon dots overtook Ru-sensitizer performances, their application in catalysis has still some limitations. Carbon dots have a broad absorption below 400 nm with a maximum at 300 nm while sunlight, the final energy source target, irradiates intensively above 450 nm leading nature to build up red-absorbing chromophores. Furthermore, electrons recombination is still a key limiting factor and one-electron reactions occurring between the photosensitizer and the catalyst can result in the formation of potentially destructive radical species for such a full organic matrix like these materials. To avoid these issues, two different approaches can be taken into consideration: a) the design of new hybrids with other known photosenziters like porphyrins, perylene bimides or Ru based chromophores [25,50,51] b) a different reaction route in order to avoid the four electron/four protons process. A metal-free carbon nanodots–carbon nitride (C_3N_4) nanocomposite was synthesized by the latter approach and, up to date, is the most successful application of CDs in energy and environment and one of the most fascinating steps towards water splitting in everyday life.[52] Combining the properties of the two materials, it was possible to obtain a high-performance composite photocatalyst via stepwise $2e^-/2e^-$ processes:

(i) $2H_2O \rightarrow H_2O_2 + H_2$;

(ii) $2H_2O_2 \rightarrow 2H_2O + O_2$

where C_3N_4 was the photocatalyst and CDs the chemical catalyst. The quantum effiency was about 16% for λ = 420 nm and 6.3% for λ = 580 nm. The 2.0% Solar-to-Hydrogen efficiency (STH) obtained was at least one order of magnitude larger than that previously reported for any stable water-splitting photocatalyst.[53] It is close to 5% STH, which

allowed achievement of the U.S. Department of Energy price target for H_2 generation. Furthermore, CDs/C_3N_4 maintained a high rate of water splitting (for $\lambda > 420$ nm) with an impressive stability in 200 runs of recycling use over 200 days. Although the reported photocatlytic effiency is surprising, it is still not satisfactory. Optimization would concern the interface between the CDs and the photocatalyst. CDs/C_3N_4 was the first example reporting the two electrons/two electrons water oxidation to which followed a series of carbon dots co-doped with nitrogen, sulphur and transition metals. While the performances of these compounds are lower than the dots/nitrides hybrid, it is remarkable that the same catalytic mechanism could be applied for a big variety of carbon dots, leaving room for further improvements and optimization towards the production of cheap commercial H_2 from photocatalysis.[54]

In this section, we listed few roles of CDs as photosensitizers, spectra converters, sole photocatalysts and electron mediators. This field remained unexplored for many years and only in the past six years there have been significant achievements. However, there are still many issues to be solved and improvements to reach. It is needed to look at the influence the defects on CDs surface have on their optical and electronic properties. Techniques are still not capable of defining and manipulating the surface of dots, thus more effort has to be put into defining the well-detailed structures of these materials. Furthermore a proper purification protocol is instrumental and the connection between precursors and final materials deserves further investigation. So far, most of the works were focused in proposing new syntheses starting from very different reagents and leading to a huge

variety of dots with disparate size and PL. However, it is still difficult to predict these final properties lacking in controllable tuning. To improve catalytic performances we need to understand what substrates do for any specific applications instead of simple serendipity.

While it is now slightly predictable how to play with the quantum yield through heteroatom doping or surface modification, less is known about tuning redox properties of dots. A library of CDs with different HOMO-LUMO energy levels would be pivotal to design a catalytic system with appropriate matching of energy levels. This goal could be accomplished by doping with redox-active molecules, or subsequent surface modification.

6.1.4 Aim of the project

The goal of this chapter is to synthesize novel carbon nanodots with different redox properties. The creation of a library of CNDs that differ in electrochemical properties will give us new insights about redox tuning of these nanoparticles, electrochemical properties that will be exploited for specific catalytic reactions according to the potentials required by any particular process.

In order to obtain novel CNDs with tuned redox potentials we modified our previously reported hydrothermal MW-assisted protocol and, besides Arg and EDA, we introduced in the reaction mixture different commercially available quinones leading to the formation of six new CNDs. The choice has fallen upon quinones, since it is well known they are easily reduced to hydroquinones, being good oxidizing derivatives of aromatic compounds. The reduction potentials of all doped CNDs were less negative than non-doped CNDs (-2.52 vs SCE) ranging from - 1.52 to - 2.05 V vs SCE. On contrary, the oxidation potential were less predicatble, in the range 0.98 – 1.48 V vs SCE (non-doped CNDs 1.18 V vs SCE). Finally, we probed if the CNDs with tunable electrochemical properties could undergo electron transfer, which is pivotal to find applications in catalysis. Therefore, we examined the reducing power by studying the photoreduction of methyl viologen in aqueous ethylene diamine tetracetic acid. All the CNDs tested reported good activity, overtaking the performances of previously reported CQDs used for proton photoreduction, a cataltytic process that could be the next applications for this group of CNDs.

6.2. Results and discussion

We selected six commercially available compounds as starting dopants: benzoquinones (CNDs **2-4**), naphthoquinones (CNDs **5**) and anthraquinones (CNDs **6-7**). In all cases, after the thermal treatment for 180 s at 200 W with max T. 250°C, the color of the reaction mixture turns to dark brown, as a result of the formation of CNDs. Afterwards, the reaction mixture is filtered, dialyzed and freeze-dried in order to obtain the final carbon nanodots as solids, whose optical, electrochemical, morphological and structural properties are studied in depth. CNDs **2**-**4** are prepared in 40% yield (based on weight), while reactions with naphthoquinone (18%) and anthraquinones (10%) give lower yields, which we ascribe to the lower reactivity and solubility of the starting quinones in the aqueous reaction mixture.

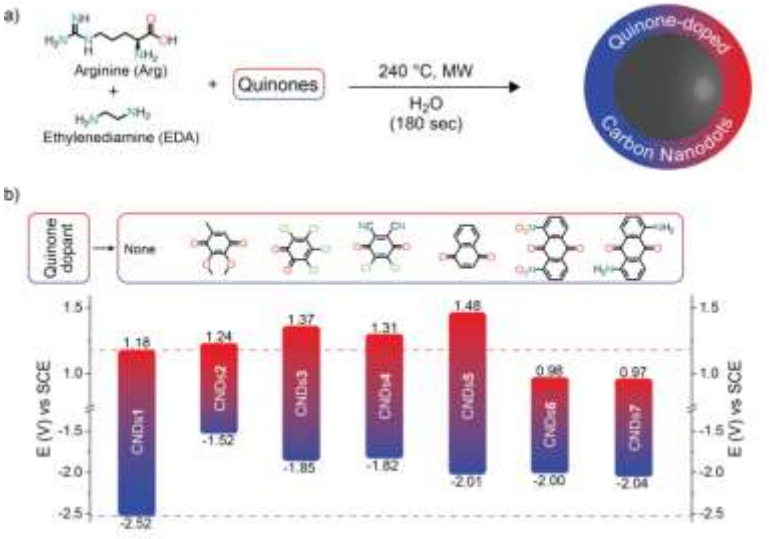

Figure 6. 2. a) Reaction scheme for the bottom-up quinone-doped synthesis of CNDs; b) redox potentials of the CNDs (structures of the corresponding starting quinones used as dopants).

6. Mastering the electrochemical properties of CDs

First of all, we investigate the electrochemical properties of the novel nanodots (Figures 6.1, 6.2 and Table 6.1) through cyclic voltammetry in high gradient dimethylformamide (DMF), in order to access a wide window of potentials and avoid large errors of low conductivity solvents (like dichloromethane or tetrahydrofuran).[55] CNDs **1**, prepared without quinones are, in principle, good candidates. for applications such as catalysis.[56,57] Cyclic voltammetry exhibits E = - 2.52 V at the cathode and E = + 1.18 V at the anode vs SCE, so both the reduced and oxidized species are found to be good oxidant/reductant that could be coupled with a wide range of appropriate catalysts.[50] As shown by the values in Table 6.1, polycyclic quinones such as CNDs **3** (+ 1.37 V), CNDs **4** (+ 1.31 V) and CNDs **5** (+ 1.48 V) show the highest potentials (Figure 5.1 and Figures 5.5-5.10). These CNDs reveal higher values than tris-(2,2'-bipyridine)ruthenium^{2+} ($Ru(bpy)_3^{2+}$) (+ 1.29 V vs SCE), which is the standard photocatalyst for water oxidation reaction, thus leading to new opportunities in this field.[56,58] Lower potentials are obtained by doping with 2,3-dimethoxy-5-methyl-*p*-benzoquinone (CNDs **3**) (+ 1.24 V) or anthraquinones (CNDs **6-7**) (+ 0.98 V,+ 0.97), showing an oxidation value similar to CNDs **1** (1.18 V) but with notable differences in the HOMO-LUMO energy levels (Figure 6.5-6.10). As expected, the reduction potentials of all CNDs have less negative values than CNDs **1** ranging from - 1.52 (CNDs **2**) to - 2.05 V vs SCE (CNDs **5**).

Tables 6.1 Potential of synthesized CNDs1**-7**

	E_{ox} (V)[a]	E_{red} (V)[a]	HOMO (eV)[b]	LUMO (eV)[b]	HOMO-LUMO gap (eV)[b]	Optical gap (eV)[c]
CNDs **1**	1.18	-2.52	-5.5	-2.5	3.0	3.4
CNDs **2**	1.24	-1.52	-5.1	-3.5	1.6	2.6
CNDs **3**	1.37	-1.85	-5.6	-3.0	2.6	2.6
CND s**4**	1.31	-1.82	-5.5	-3.0	2.5	2.7
CNDs **5**	1.48	-2.01	-5.4	-2.8	2.6	2.5
CNDs **6**	0.98	-2.00	-5.2	-2.8	2.4	2.3
CNDs **7**	0.97	-2.04	-5.2	-2.7	2.5	2.8

[a] Values (±10 mV) in DMF 100 mV/s vs SCE. Processes are quoted as irreversible.
[b] Values were calculated from the onset of the reduction/oxidation peak as described in the Experimental Section.[59,60]
[c] Values were calculated from the onset of the absorption band.[13,61]

Moreover, CNDs **2-4** display a second reduction peak independent of the quinone dopant, around - 2.3 V (Table 6.1). All the potentials are sufficiently negative to efficiently inject electrons into the conduction band of TiO_2 ($E_F \approx -0.5$ V).[62] Thus, from the electrochemical point of view, all the above-mentioned nanodots, are good candidates for operation in DSSC as dyes or for proton reduction (E_0 = -0.59 V vs SCE).[63]

We recently reported how the steep slope of the monoelectron oxidation peaks suggests that a high number of amino groups can be easily oxidized on the surface of the CNDs.[51] In particular, the CV of CNDs **1** display a close similarity with the CV of phenethyleamine and

benzylamine leading to the conclusion that these amino groups, on the dots surface, are capable of forming reductive or oxidative species

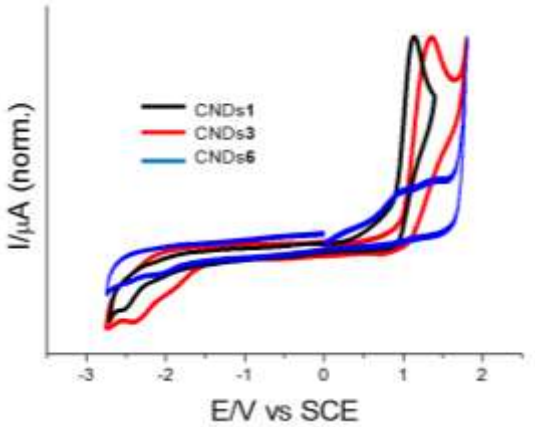

Figure 6.2. Cyclic voltammetry of CNDs **1** (black trace), CNDs**3** (red trace) and CNDs **6** (blue trace) in DMF. Supporting electrolyte: $TBAPF_6$ (0.1 M). GE electrode. Scan rate: 100 mV/s using a platinum wire as counter electrode. Values reported in Table 1.

during voltammetric scan. The CVs of CNDs **2-7** (Figure 6.2 and Figure 6.5-6.10) show similar features, the oxidation peaks are related to the same amino moieties of CNDs **1**, with minor differences associated to divergent chemical surroundings. Due to the high quantity of amines present on the surface of the dots these peaks cover the signal of other processes such as those from the quinones used for the doping.

In the CVs of CNDs **6** - CNDs **7** these features are less prominent, the amount of amines is lower and consequently it is possible to observe a first oxidation peak around 1.0 V vs SCE besides the usual one at 1.3-1.4 V. All the process are quoted as irreversible which, considering the polymeric nature of the surface, can be ascribed to conformational

reorganization and variations of the energy levels promoted by addition/removal of one electron.[64]

The amount of primary amines on CNDs surface was evaluated by Kaiser test to detect the presence of primary amines and bring a further proof to the conclusions reached by CV analysis.[65] Indeed, all colorimetric tests gave positive results, indicating the presence of free amino groups on the nanodots surface. A general trend is observed with CNDs doped with polycyclic quinones (CNDs **5** = 296 µmol g^{-1}, CNDs **6** = 258 µmol g^{-1}, CNDs **7** = 235 µmol g^{-1}) bearing less amines on the surface compared to CNDs **2-4** (CNDs **2** = 500 µmol g^{-1}, CNDs **3** = 1050 µmol g^{-1}, CNDs **4** = 900 µmol g^{-1}). In any case, all the CNDs prepared with quinones, show less amino groups when compared with the reference (CNDs **1**), suggesting that the reaction between amines and quinones has occurred during the synthesis. These primary amines could be exploited, in the future, for post-functionalization binding covalently catalysts and photosensitizers since, the covalent hybrids could yield better perfomances.[51,66–68]

The structure and composition of CNDs were determined by FT-IR spectroscopy and X-ray photoelectron spectroscopy (XPS). All FT-IR spectra (Figure 6.3 and Figure 6.11-6.14) show features around 1660 cm^{-1} (C=O), 1380 cm^{-1}, 1320 cm^{-1} (C-O), 1110 cm^{-1} 1175 cm^{-1} (O-C-O), typical of oxygenated functional groups on the surface. In most cases (CNDs **2, 4, 5, 6**) we observed a weak peak at 1765 cm^{-1}, ascribed to carboxylic acids. Similarly, the presence of C=N and C-N moieties is detected by the peaks at 1440cm^{-1}, 1490 cm^{-1} and 1550 cm^{-1}, while C-H stretching is well observed at 2900 cm^{-1}. Notably

CNDs **2-4**, showed IR-spectra similar to the CNDs **1**, whereas naphthoquinone- and anthraquinones-based nanodots (CNDs **6-8**) exhibited more intense C=N and C-N peaks. Moreover, all spectra showed a broad peak at around 3200 cm^{-1} which identifies N-H/O-H bonds. To further confirm the functional groups on the CNDs surface, XPS measurements were performed. From the full-scan XPS spectra of CNDs**2-7** (Figures 6.15-6.21)**,** the peaks related to C1s, N1s, O1s, at c.a. 286.4 eV, 400.6 eV, 532.4 eV, respectively, can be identified. The atomic percentages range from 64.0 to 67.5 for C1s, 19.4 to 25.8 for N1s and 9.2 to 15.3 in the case of O1s (Table 6.2), indicating that doping with quinones significantly alters the composition of nanodots. The C and N configurations of the CNDs **2-7** were determined by a detailed peak fitting analysis (Figure 6.15-6.21). The C1s and N1s of all the CNDs show the same multiple surface components, according to the nanodots without quinones,[50] but with different contents. The C1 spectra of CNDs **2-7** was deconvoluted in five peaks corresponding to sp^2(C=C) at c.a. 284.6 eV, sp^3(C-C, C-H) at c.a. 285.7 eV, C-O/C-N/C-Br at c.a. 286.7 eV, C=O/C=N at c.a. 288.6 eV, as well as O-C=O at c.a. 289.7 eV. The N1s spectra was deconvoluted in four peaks centered at c.a. 398.4, 399.6, 400.7, 401.9 eV corresponding to C=N, NH_2, C-N-C and N-C_3, respectively, with amines contents in good agreement with Kaiser test[50]. Interestingly, moieties like NO_2 (CNDs **6**), and Cl (CNDs **3-4**), were not detected, suggesting they are substituted during the nanodots synthesis. The morphology of the novel nanodots was investigated by atomic force spectroscopy (AFM) (Figures 6.3 and 6.15-6.21), confirming the round shape and dimensions comparable to CNDs **1**. CNDs **2** are the smallest ones

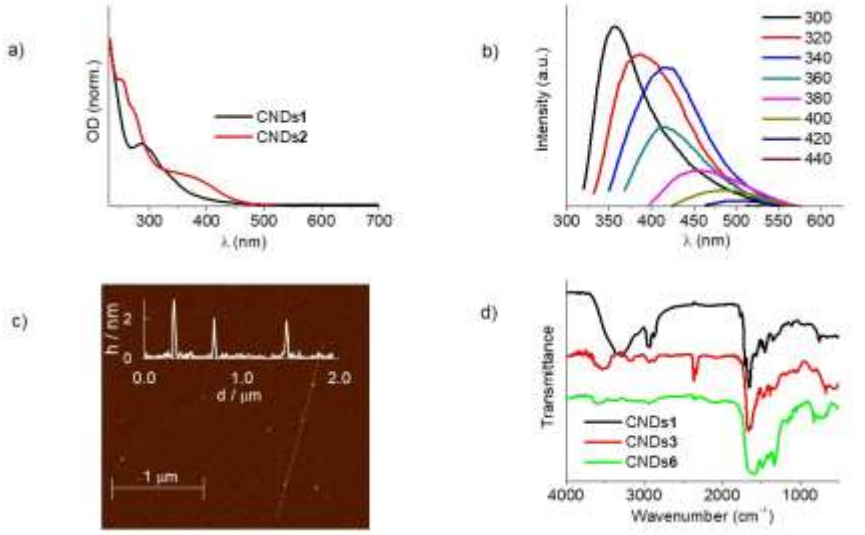

Figure 6.3. a) UV-Vis absorption spectra of CND s**1** and CNDs **2** in water; b) FL spectra of CNDs **2** in water (298 K) at different excitation wavelengths; c) Tapping mode AFM images of CNDs**3** (2.5 x 2.5 μm) on mica substrate; d) FT-IR spectra of CNDs **1** - CNDs **3** - CNDs **6.**

around 1.5 nm, while chlorinated quinones and naphtaquinone yield slightly bigger nanoparticles around 2 nm in diameter, but still smaller than CNDs **1** (around 2.5 nm). Different sizes were reached by CNDs **4-5** with dimensions around 3-4 nm.

Optical properties are the most interesting feature of nanodots and depend on core nature and chemical composition of the surface.[69,70] We expected the quinones to affect differently this behavior showing variations in the absorption and emission spectra, although not considerable. To the naked eye, the aqueous solutions of CNDs **2-5** are yellow at daylight, while CNDs **6-7** appeared light red (Figure 6.4). Solutions were stable for weeks at room temperature with no changes in the spectral features.

UV-Vis spectra differ slightly from CNDs **1** with a general broader absorbance above 380 nm. All CNDs show an absorption band

between 280 nm and 305 nm (Figure 6.27-6.32) with CNDs **2** presenting the shortest wavelength (Figure 6.3) and CNDs **6** the longest wavelength, which are attributed to various π-π* (C=C) and n-π* (C=O) transitions.[6] Furthermore, these CNDs exhibit more complex spectra than the reported dots CNDs **1**: CNDs **2** (Figure 6.3) showed two other peaks at 255 nm and 380 nm and CNDs **5** one at 480 nm.

The mechanism governing the luminescence of carbon dots is still under investigation.[71,72] The emission is attributed to core and surface state related emission, in particular when excitation wavelength dependence is observed, leading to multi-fluorescence colors under different excitation wavelengths. Therefore, their typical emission spectrum may arise not only from particles of different size but also from a distribution of emissive domains on each dot originating from electronic conjugate structures and emissive domains.[19,73,74]

Whereas the absorption spectra presented differences between the synthesized nanodots, it is the emission spectroscopy that shows the greatest differences after quinones doping. All CNDs show the typical wavelength-dependent emission (Figures 6.3 and 6.32-6.37). Most of the reported CNDs show emission peaks at 350 nm (at 300 nm excitation) and only CNDs **3** exhibit the greatest intensity emission at 380 nm upon excitation at 320 nm. On shifting the excitation to longer wavelengths, CNDs **2-7** show contrasting behavior: while CNDs **2-3** and CNDs **6** have similar spectra with emission maximum at 530 nm (when excited at 440 nm), CNDs **4** present emission at longer wavelength and CNDs **5-7** do not show any emission when excited above 400 nm. QYs go from as low as 0.05 for CNDs **2**, to a 0.21 for

nanodots doped with anthraquinones CNDs **6-7** which is a higher value than the one of CNDs **1** (0.17).[50] Taken in concert, our data suggest different surface group distributions on the prepared CNDs, which is agreement with the structural investigation.

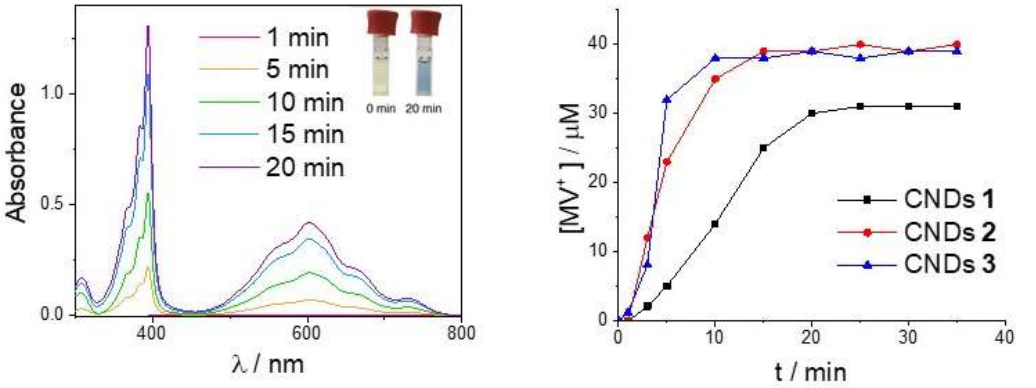

Figure 6.4 a) Time-resolved UV-Vis spectra of CNDs **1** (0.5 mg mL^{-1}) with methyl viologen dichloride (MV^{2+}, 40 µM) in aqueous EDTA (0.1 M, pH 6) recorded under full solar spectrum irradiation at 1 sun intensity. The spectra are background corrected for CNDs **1** and MV^{2+}absorption. Inset: cuvette before/after irradiation. a) Plots of $MV^{+\bullet}$ formation. Concentration estimated using absorbance at 605 nm, ε= 13700 M^{-1} cm^{-1};[78]

Finally, we probed if the CNDs with tunable electrochemical properties could undergo electron transfer, which is pivotal to find applications in catalysis. Therefore, we examined the reducing power by studying the photoreduction of methyl viologen (MV^{2+}: $E°'$ = - 0.69 V vs SCE)[75] and its ability to quench photoluminescence (Figure 6.39).[45] Solutions of CNDs **1**-**3**, in aqueous ethylene diamine tetracetic acid (EDTA, 0.1 M, pH 6), were irradiated in the presence of MV^{2+} (40 µM), under Ar. These conditions followed the ones previously used for carbon-based dots that perform hydrogen evolution, in order to have a direct comparison of the catalytic activity.[48] Kinetics of MV^{2+} photoreduction

was monitored for 30 min, with concentrations normalized for absorption (CNDs **1** 0.5 mg mL^{-1}, CNDs **2** 0.06 mg mL^{-1}, CNDs **3** 0.17 mg mL^{-1}). As showed in Figure 4a, CNDs doped with quinones are considerably more efficient with faster initial rate (CNDs **2** = 9.2 x 10^{-8} M s^{-1}, CNDs **3** = 2.0 x 10^{-7} M s^{-1}) than CNDs **1** (3.0 x 10^{-8} M s^{-1}) and quantitative conversion. Moreover, CNDs **2**-**3** are more efficient than the reported graphitized CDs, whose maximum initial rate is 8.7 x 10^{-7} M s^{-1}.[48] The trend between the doped CNDs series does not mirror the reduction potential, but seems rather to be affected by the higher absorption of CNDs **2** and **3** in the visible region (Figure 6.39). Since the reduction potential of protons at pH 6 is 0.6 vs. SCE, lower than the one of MV^{2+}, implementation of doped CNDs in proton reduction appear to be the obvious next application.

6.2.1 Conclusions

We have prepared and characterized a redox library of carbon nanodots. CNDs with tunable oxidation/reduction potentials were prepared by adding to the reaction mixture (of arginine and ethylene diamine) commercially available quinones, employing a fast bottom-up MW-assisted hydrothermal treatment and a facile purification procedure. Benzoquinone-, naphthoquinone- and anthraquinone-based carbon nanodots exhibited interesting electrochemistry with oxidation potentials between 1.48 V and 0.98 V vs SCE and reducing one in the range - 1.52 V and - 2.05 V vs SCE. Moreover, we report the electron transfer ability of these dots by photoreduction of methyl viologen. Notably, the catalytic activities performed by these materials

were higher compared to other carbon dots used for the photoreduction of protons. Therefore, these nanodots could be the perfect candidates for the design of more efficient hydrogen evolving catalytic systems.

6. Mastering the electrochemical properties of CDs

.3 Experimental section

6.3.1 Instruments and materials

Chemicals

L-Arginine (Fluorochem, > 98%), Ethylendiamine (Sigma-Aldrich > 99.5%), Tetrahydroxyquinone (Sigma-Aldrich, > 99.5%), 2,3-Dimethoxy-5-methylquinone (Sigma-Aldrich, 99%), Chloranil (Sigma-Aldrich, > 99%), 2,3-Dichloro-5,6-dicyano-1,4-benzoquinone (Fluorochem, > 96%), 1,4-Naphthoquinone (Sigma-Aldrich, > 97%), 1,5-Diaminoanthraquinone (Sigma-Aldrich, > 97%), 1,8-Dinitroanthraquinone (Sigma-Aldrich, > 97%), $TBAPF_6$ (Sigma-Aldrich, 98%), DMF (Sigma-Aldrich, anhydrous, 99.8%). Kaiser test kit was purchased from Sigma-Aldrich. Dialysis tubes with molecular weight cutoff 0.5-1KDa were bought from Spectrum Labs. Ultrapure fresh water obtained from a Millipore water purification system (>18Milli-Q, Millipore) was used in all experiments.

Apparatus and characterization

The microwave synthesis was performed on a CEM Discover-SP.
Uv-Vis spectra were recorded on a PerkinElmer Lambda 35 UV-Vis spectrophotometer. Fluorescence UV-Vis spectra were recorded on a Varian Cary Eclipse Fluorescence Spectrophotometer. All the spectra were recorded at room temperature using 10 mm path-length cuvettes. Fourier-Transform Infrared (FT-IR) spectra have been recorded on a Varian 660 FT-IR with KBr pellets. Atomic force microscopy (AFM) images were obtained with a Nasoscope IIIa, VEECO Instruments. As a general procedure to perform AFM analyses, tapping mode with a

HQ:NSC19/ALBS probe (80kHz; 0.6 N/m) (MikroMasch) from drop cast of samples in an aqueous solution (concentration of few mg/mL) on a mica substrate was performed. The obtained AFM images were analyzed in Gwydion 2.46. The electrochemical characterization was carried out in N,N,Dimethylformamide (DMF)/0.1 M tetra-butylammonium hexafluorophosphate ($TBAPF_6$). Oxygen was removed by purging the DMF solution with high-purity Nitrogen. A typical three-electrode cell was employed, which was composed of glassy carbon working electrode, a platinum wire as counter, and a silver wire as quasi-reference (QRE) electrode. A simple cell CHI220 from CH. Instruments was used. The potential reference electrode was calibrated before the measurements Ferrocene/Ferrocenium (Fc/Fc+) redox couple as the internal standard. The formal potential of Fc/Fc+ is 0.464V for DMF against the KCl saturated calomel electrode (SCE). The GC electrode were polished twice with 0.05 and 0.1 colloidal silica polishing suspension and ultrasonically rinsed with deionized water for 15 minutes. The electrodes were electrochemically activated in the background solution by means of several voltammetry cycles at 100mV/s between the anodic and cathodic solvent/electrolyte discharges. The cyclic voltammetry (CV) measurements were carried out at a scan rate of 0.1 V/s. The HOMO and LUMO energy levels of the different dots was calculated from the onset oxidation potential (Eox(onset)) and the onset reduction potential (ERed(onset)).[59,76]

$$E_{HOMO} = -(4.65\ \text{eV} + E_{[onset,ox\ vs.\ Fc^+/Fc]})$$
$$E_{LUMO} = -(4.65\ \text{eV} + E_{[onset,red\ vs.\ Fc^+/Fc]})$$

6. Mastering the electrochemical properties of CDs

X-ray photoemission spectroscopy (XPS) spectra of the samples were measured on a SPECS Sage HR 100 spectrometer using a non-monochromatised Mg-Kα radiation of 1253.6 eV and 250 W, in an ultra-high vacuum chamber at pressure below 8 x 10^{-7} mbar. For each analysis, an aqueous solution (c.a. 3 mg/mL) of material were deposited on a gold thin film. The calibration was done using the 3d5/2 line of Ag. Survey and high resolution spectra were collected with pass energy of 30 and 15 eV and 0.5 and 0.15 eV/step, respectively. CasaXPS 2.3.17 PR1.1 and Avantage (Thermo Fisher Scientific) software were used for data processing and fitting. Curve fittings of the C1s and N1s spectra were realized using a Gaussian-Lorentzian peak shape after performing a Shirley background correction, to finally obtain the relative percentage of each type of bond inside the analyzed sample.

The quantum yield measurements were performed with quinine sulphate in 0.10 M H_2SO_4 (literature quantum yield 0.54 at 360 nm) as the standard[77]. The absorption factors f_x and f_{st} of the standard and the sample were calculated from the measured absorbance values (A) at the excitation wavelength using equation (1) The index *x* denotes the sample, and the index *st* denotes the standard.

$$f = 1 - 10^{-A\lambda_{exc}}$$

The fluorescence quantum yields were calculated according to equation below, where

I is the measured integrated fluorescence emission intensity, *f* is the absorption factor, η is the refractive index of the solvent and Φ is the quantum yield. The index *x* denotes the sample, and the index *st* denotes the standard.

$$\Phi_x = \Phi_{st} \cdot \frac{I_x}{I_{st}} \cdot \frac{f_{st}}{f_x} \cdot \frac{\eta_x^2}{\eta_{st}^2}$$

Photo-induced single electron transfer ability was investigated through the photoreduction of the redox indicator methyl viologen. Reduction of MV^{2+} to $MV^{+\bullet}$ is a kinetically fast reversible single electron transfer process with a concurrent color change from colorless to blue, which can be monitored by UV-Spectroscopy. Solutions of CNDs **1-3** with concentrations normalized for their absorption (CNDs**1** 0.5 mg mL^{-1}, CNDs **2** 0.06 mg mL^{-1}, CNDs **3** 0.17 mg mL^{-1}) in aqueous ethylenediaminetetraacetic acid (EDTA, 0.1 M, pH6) were irradiated (AM1.5G, 1 sun) in the presence of 40 μM MV^{2+}. The formation of MV+• was estimated by the absorption at 605 nm, where ε is 13700 M^{-1}.[78]

6.3.2. Synthesis of CNDs

CNDs **2-7** were obtained via microwave irradiation of an aqueous solution of L-Arginine and Ethylendiamine (EDA) (0.5 mmol). Typically (87.0 mg), EDA (33.0 mL), Milli-Q water (100.0 μl) and 0.25 mmol of the appropriate quinones were heated at 240°C, 26 bar and 200 W for 180 seconds as we previously reported.[50]

6. Mastering the electrochemical properties of CDs

In the process of microwave heating, the solution changed color from transparent to brown as a result of carbon nanodots formation. The reaction mixture was filtered (0.1 μm microporous membrane), washed with Milli-Q water, and dialyzed against Milli-Q water for 48 h. The powder material was obtained by freeze-drying.

6.3.3 Supporting figures

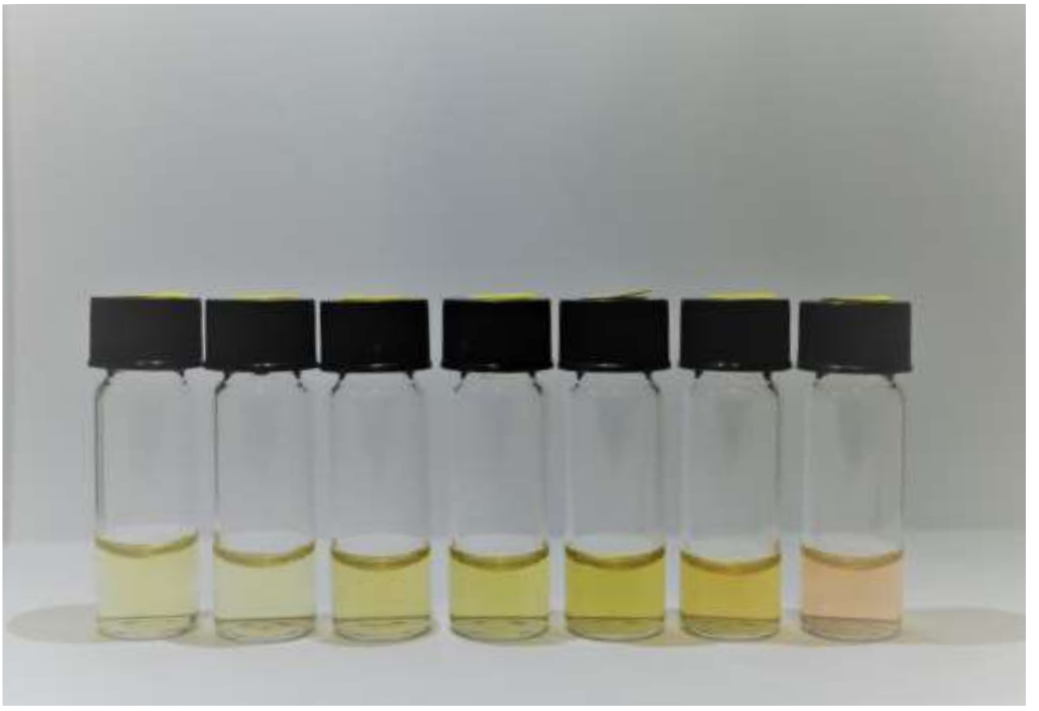

Figure 6.4. Photograph of the CNDs **1-7** aqueous solutions (left to right) after dialysis.

6. Mastering the electrochemical properties of CDs

Cyclic voltammetry

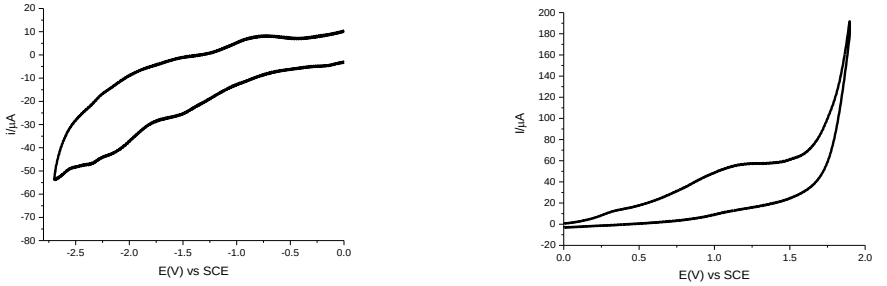

Figure 6.5. Cyclic voltammetry of CNDs **2** in DMF. Supporting electrolyte: $TBAPF_6$ (0.1 M). GE electrode. Scan rate: 100 mV/s using a platinum wire as counter electrode. Values reported in Table 1.

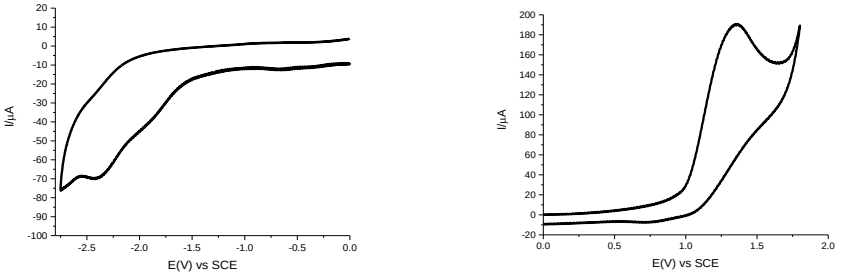

Fgure 6.6. Cyclic voltammetry of CNDs **3** in DMF. Supporting electrolyte: $TBAPF_6$ (0.1 M). GE electrode. Scan rate: 100 mV/s using a platinum wire as counter electrode. Values reported in Table 1.

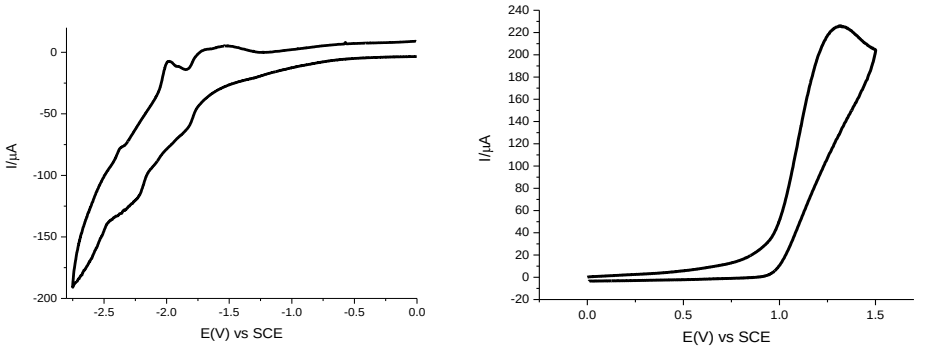

Figure 6.7. Cyclic voltammetry of CNDs **4** in DMF. Supporting electrolyte: $TBAPF_6$ (0.1 M). GE electrode. Scan rate: 100 mV/s using a platinum wire as counter electrode. Values reported in Table 1

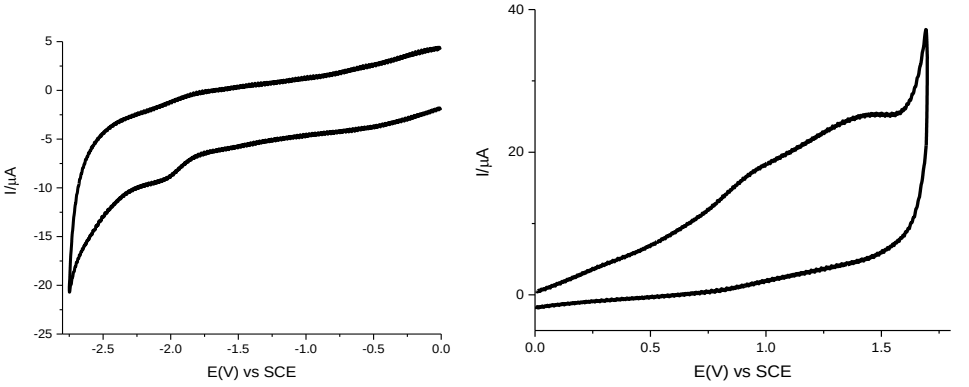

Figure 6.8. Cyclic voltammetry of CNDs **5** in DMF. Supporting electrolyte: $TBAPF_6$ (0.1 M). GE electrode. Scan rate: 100 mV/s using a platinum wire as counter electrode. Values reported in Table 1

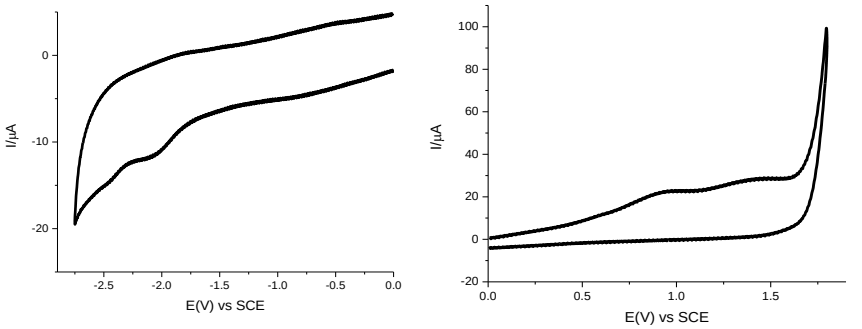

Figure 6.9. Cyclic voltammetry of CNDs **6** in DMF. Supporting electrolyte: $TBAPF_6$ (0.1 M). GE electrode. Scan rate: 100 mV/s using a platinum wire as counter electrode. Values reported in Table 1

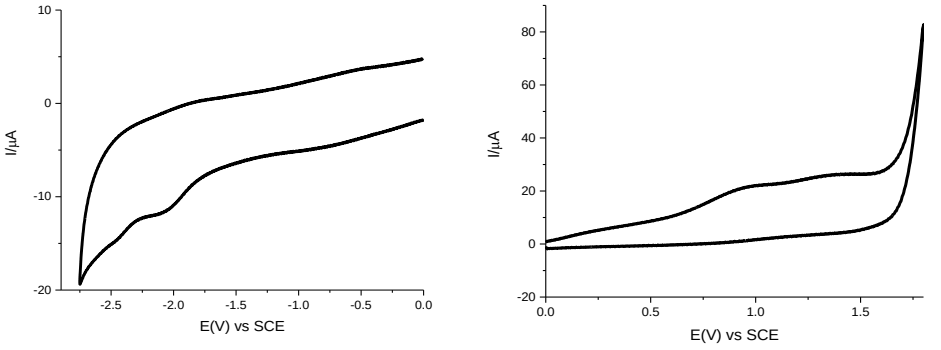

Figure 6.10. Cyclic voltammetry of CNDs **7** in DMF. Supporting electrolyte: $TBAPF_6$ (0.1 M). GE electrode. Scan rate: 100 mV/s using a platinum wire as counter electrode. Values reported in Table 1

FT-IR spectra

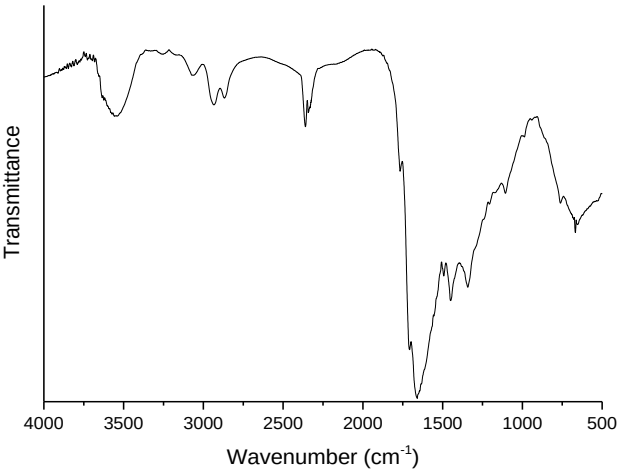

Figure 6.11. FT-IR spectrum of CNDs **2**

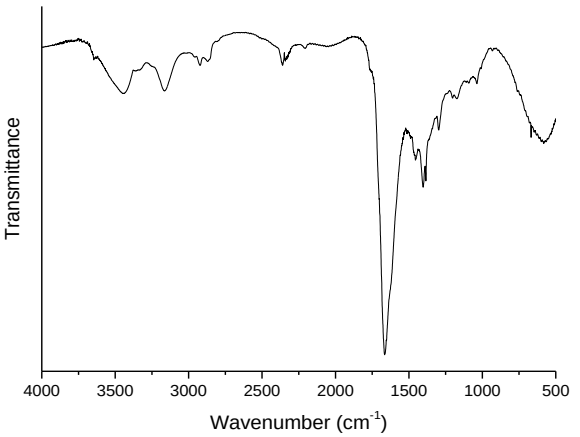

Figure 6.12. FT-IR spectrum of CNDs **4**

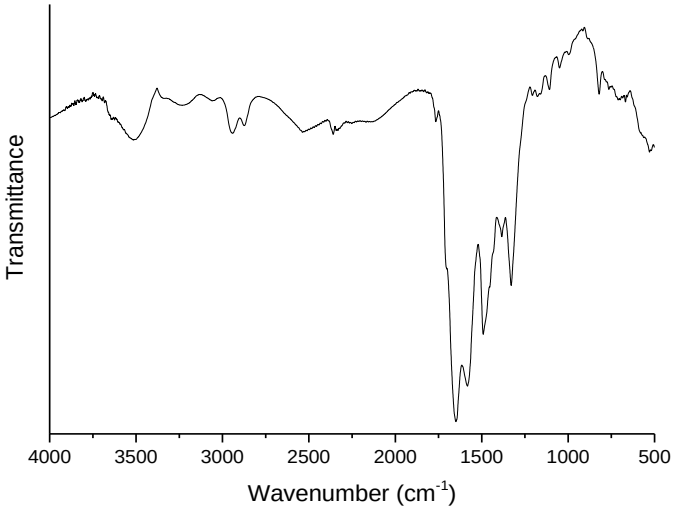

Figure 6.13. FT-IR spectrum of CNDs **5**

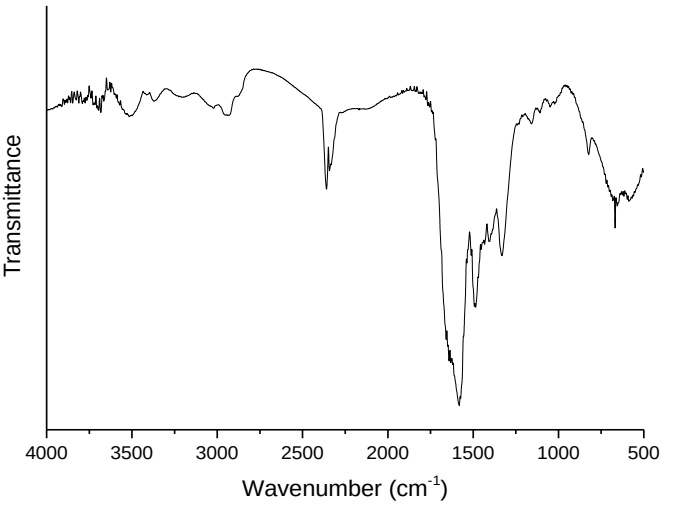

Figure 6.14. FT-IR spectrum of CNDs **6**

XPS measurements

Table 6.2, Percentages of C, N, and O atoms in CNDs **2-7** as determined by XPS measurements.

	CNDs2	**CNDs3**	**CNDs4**	**CNDs5**	**CNDs6**	**CNDs7**
C%	**65.0**	**66.8**	**67.5**	**64.0**	**66.1**	**66.7**
C=C	9.6	6.9	5.6	3.6	7.4	2.6
C-C	42.3	35.9	42.4	30.2	25.2	21.7
C-O C-N	30.3	42.3	31.5	35.5	42.0	57.7
C=O C=N	14.7	9.3	14.6	14.9	10.7	9.5
O-C=O	3.0	5.5	5.9	15.8	14.3	8.5
N%	**25.8**	**20.2**	**20.5**	**20.7**	**19.4**	**22.1**
C=N	10.5	7.8	7.9	6.1	3.3	4.6
NH_2	13.5	17.0	14.2	29.3	26.2	20.3
C-N-C	69.3	68.7	73.9	55.5	61.9	66.6
N-C3	6.6	6.4	3.9	9.1	8.6	9.4
O%	**9.2**	**13.0**	**12.1**	**15.3**	**14.5**	**11.2**

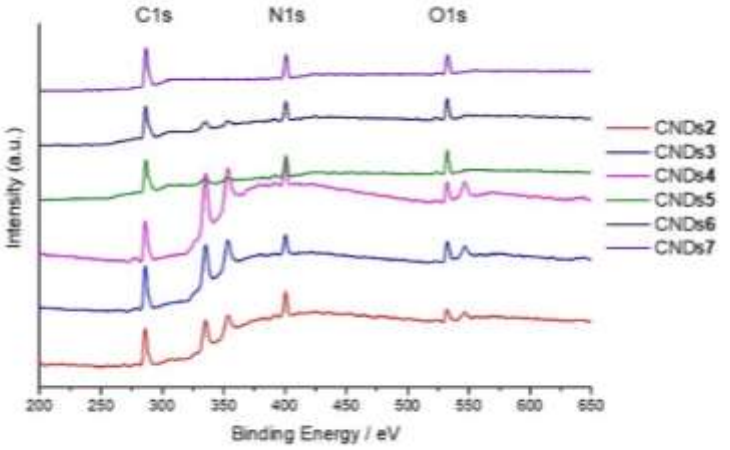

Figure 6.15. XPS survey of CNDs **2-7.**

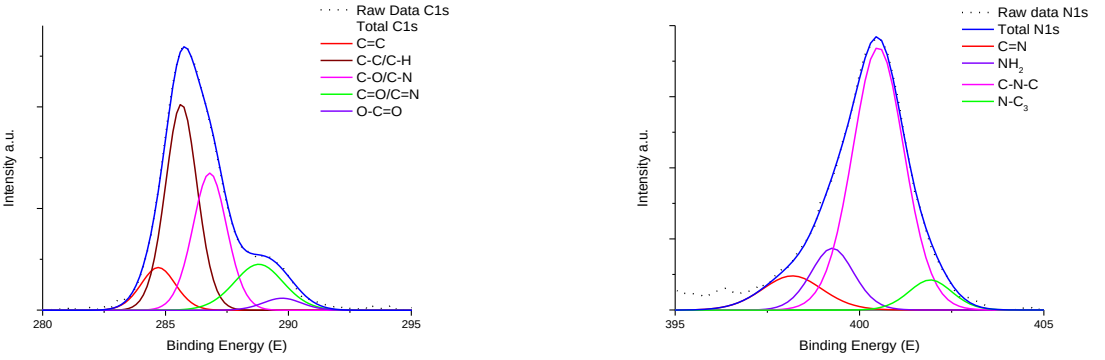

Figure 6.16. Deconvoluted C1s and N1s spectra of CNDs **4**

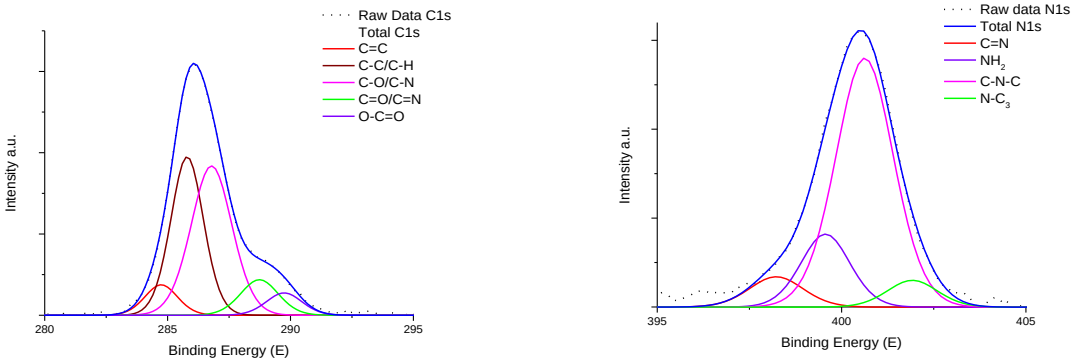

Figure 6.17. Deconvoluted C1s and N1s spectra of CNDs **5**

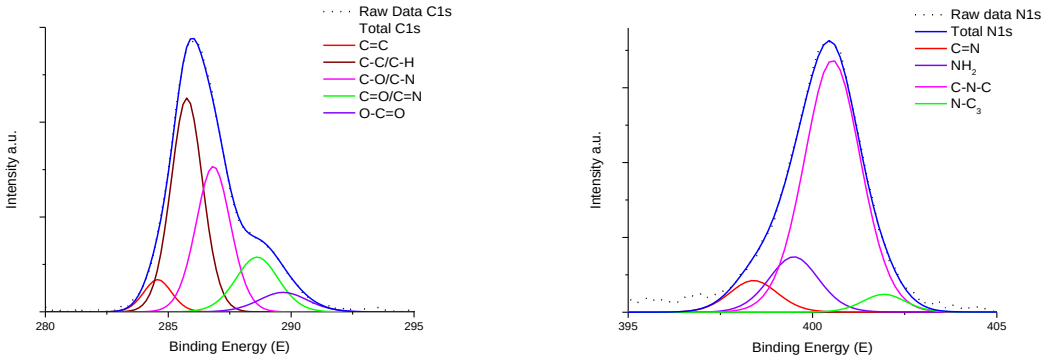

Figure 6.18. Deconvoluted C1s and N1s spectra of CNDs **6**

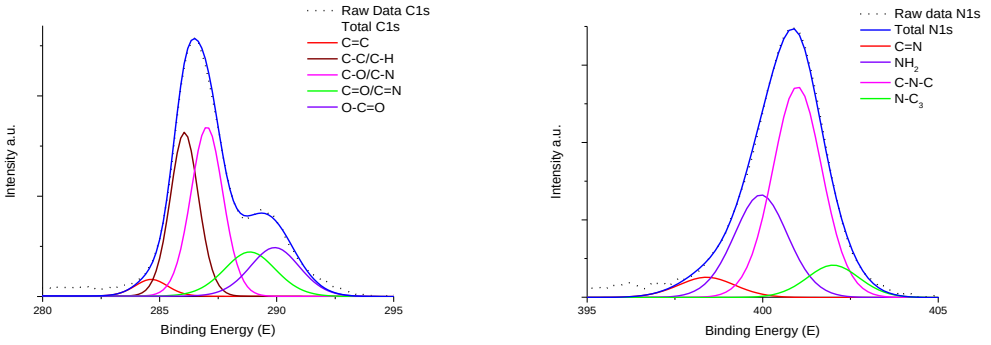

Figure 6.19. Deconvoluted C1s and N1s spectra of CNDs **7**

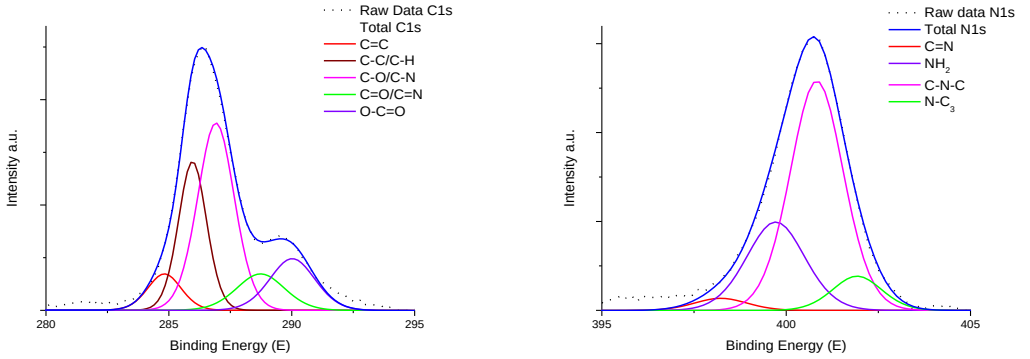

Figure 6.20. Deconvoluted C1s and N1s spectra of CNDs **8**

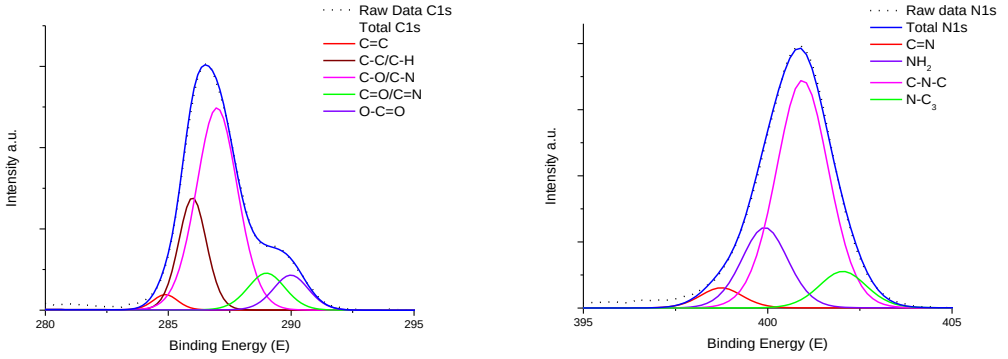

Figure 6.21. Deconvoluted C1s and N1s spectra of CNDs **9**

Atomic Force Microscopy (AFM) images

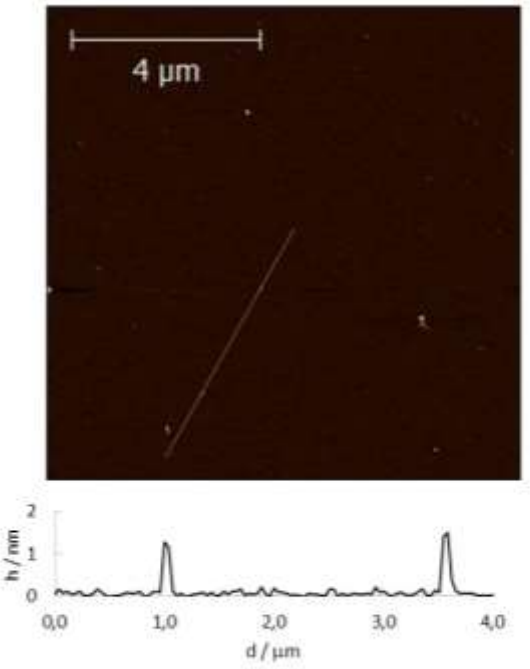

Figure 6.22. Tapping mode AFM image and height profile of CNDs **2**

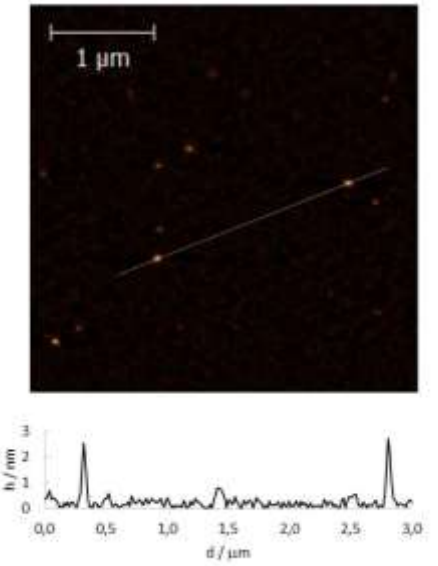

Figure 6.23. Tapping mode AFM image and height profile of CNDs **4**

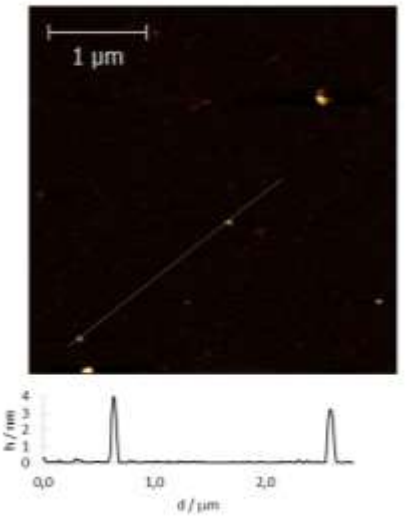

Figure 6.24. Tapping mode AFM image and height profile of CNDs **5**

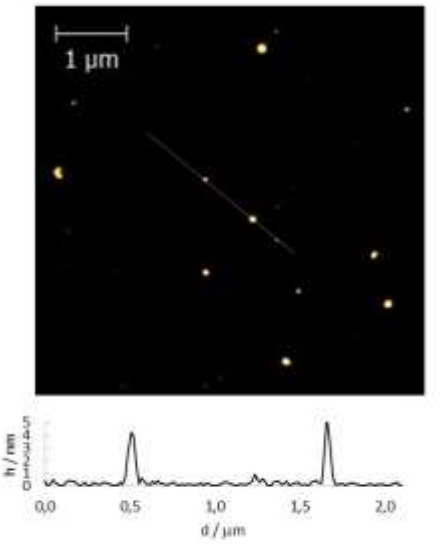

Figure 6.25. Tapping mode AFM image and height profile of CNDs **6**

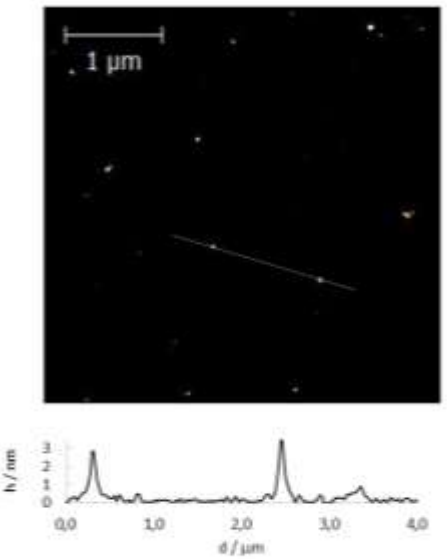

Figure 6.26. Tapping mode AFM image and height profile of CNDs **7**

6. Mastering the electrochemical properties of CDs

Absorption spectra

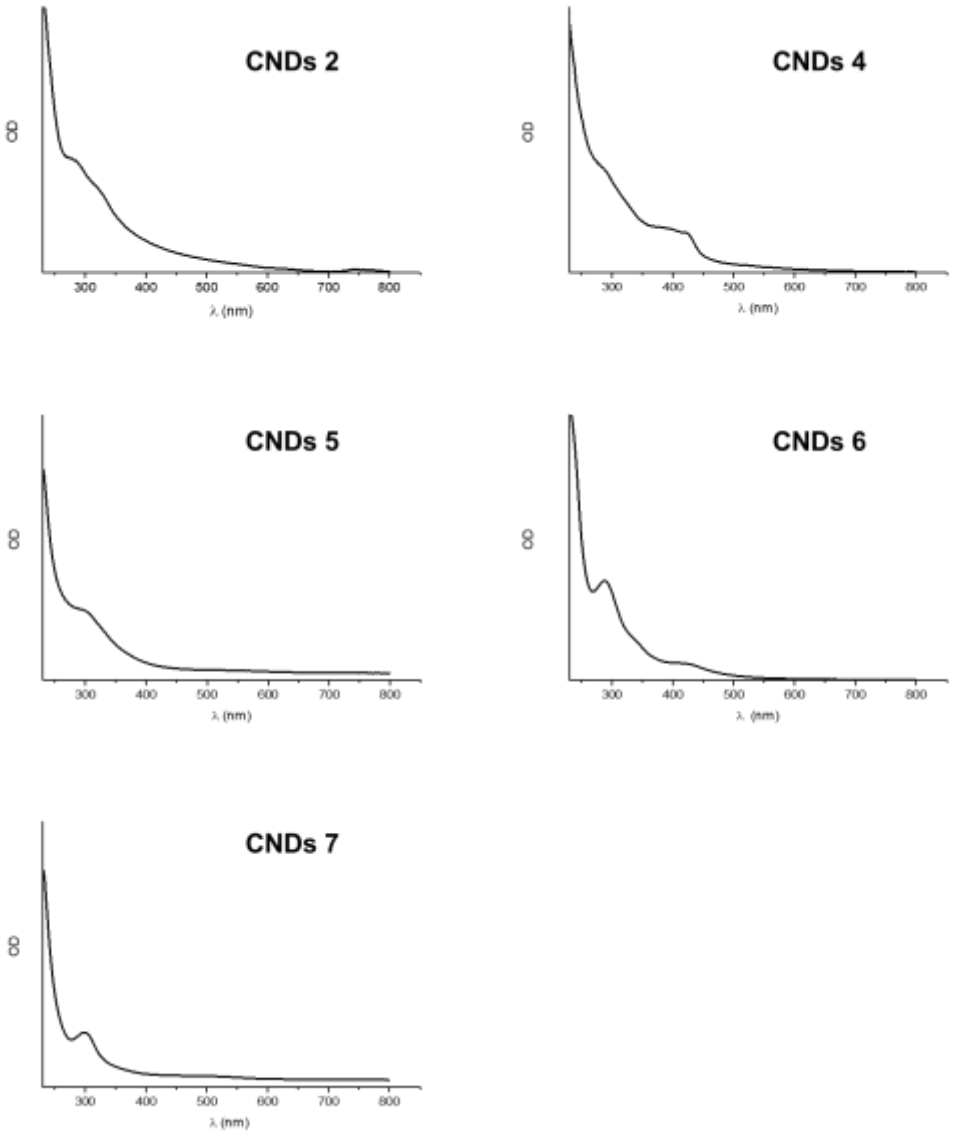

Figure 6.27 Uv-Vis spectra of CNDs **2, 4-7.**

6. Mastering the electrochemical properties of CDs

Emission Spectra

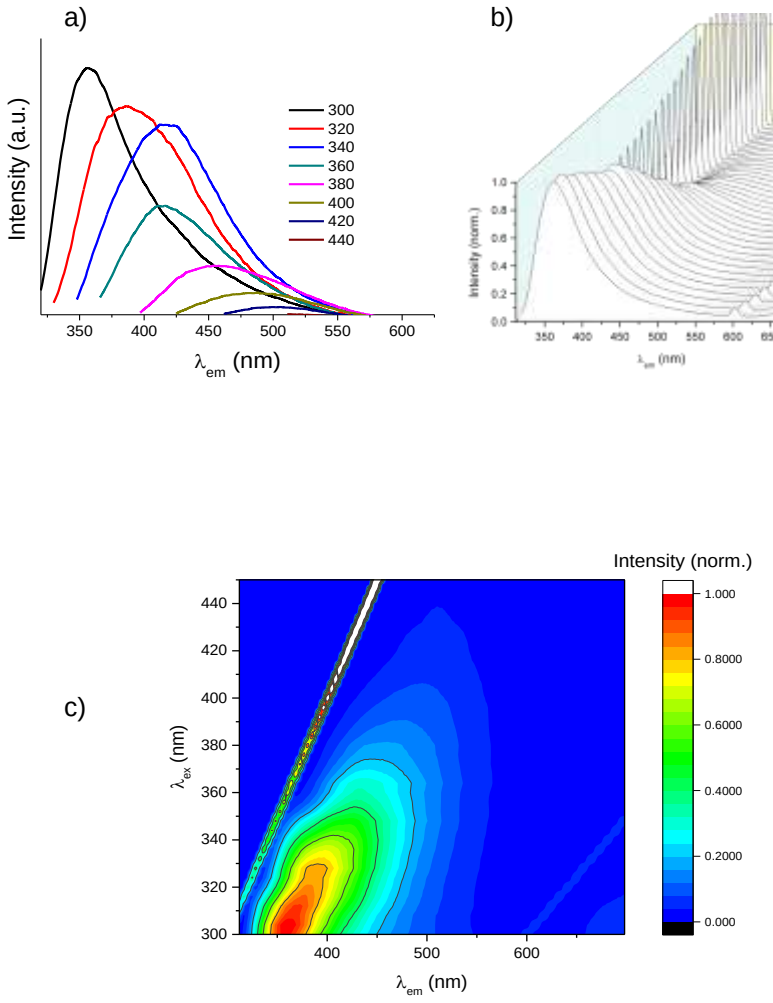

Figure 6.28. a) FL spectra of CNDs **2** in water at different excitation wavelengths (300-440 nm). b) 3D Fluorescence emission spectra of WCNDs by exciting at different wavelengths (300-450 nm). c) Fluorescence matrix scan experiment showing the fluorescence mapping by exciting at different wavelengths.

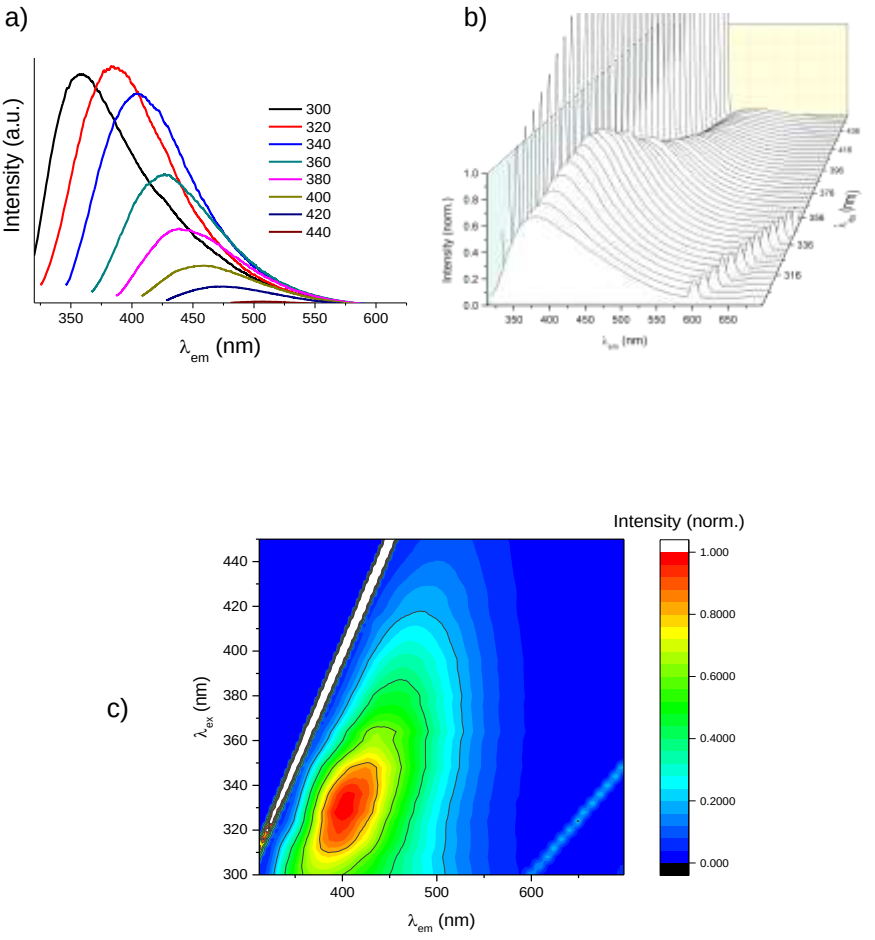

Figure 6.29. a) FL spectra of CNDs **3** in water at different excitation wavelengths (300-440 nm). b) 3D Fluorescence emission spectra of WCNDs by exciting at different wavelengths (300-450 nm). c) Fluorescence matrix scan experiment showing the fluorescence mapping by exciting at different wavelengths.

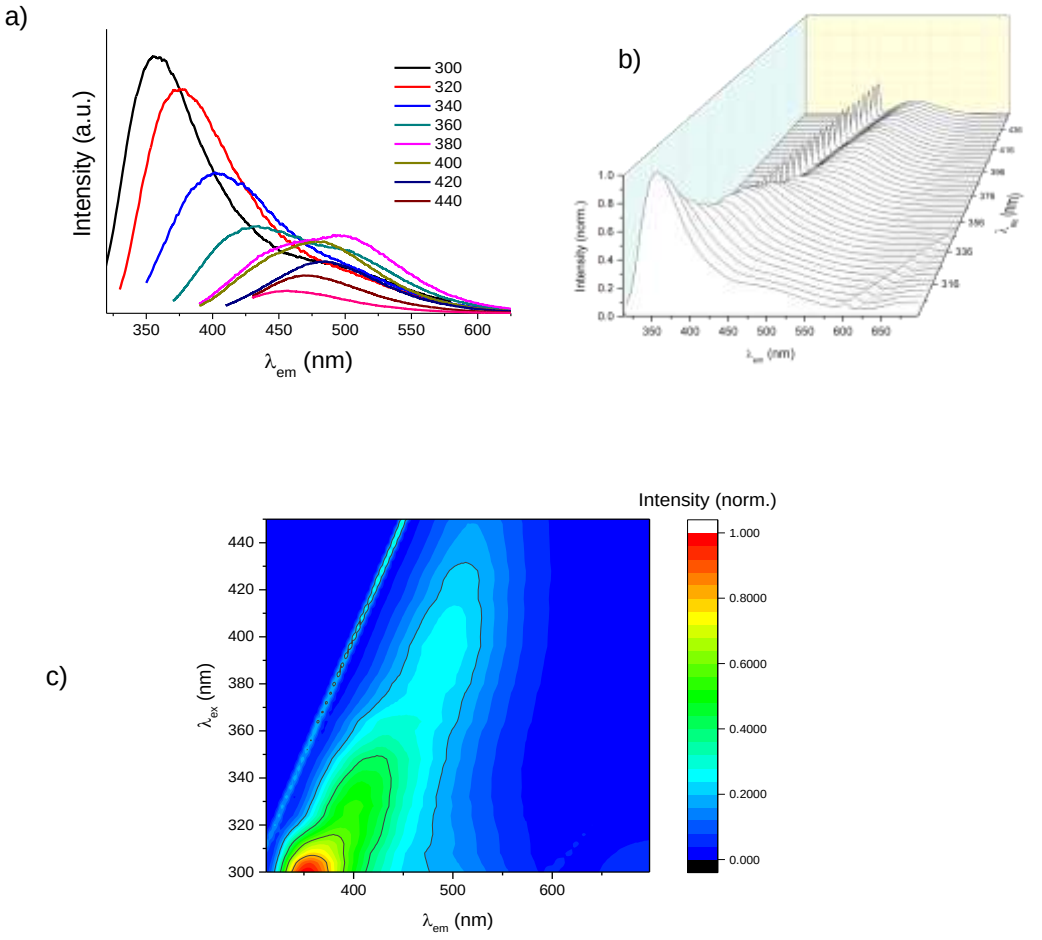

Figure 6.30. a) FL spectra of CNDs **4** in water at different excitation wavelengths (300-440 nm). b) 3D Fluorescence emission spectra of WCNDs by exciting at different wavelengths (300-450 nm). c) Fluorescence matrix scan experiment showing the fluorescence mapping by exciting at different wavelengths.

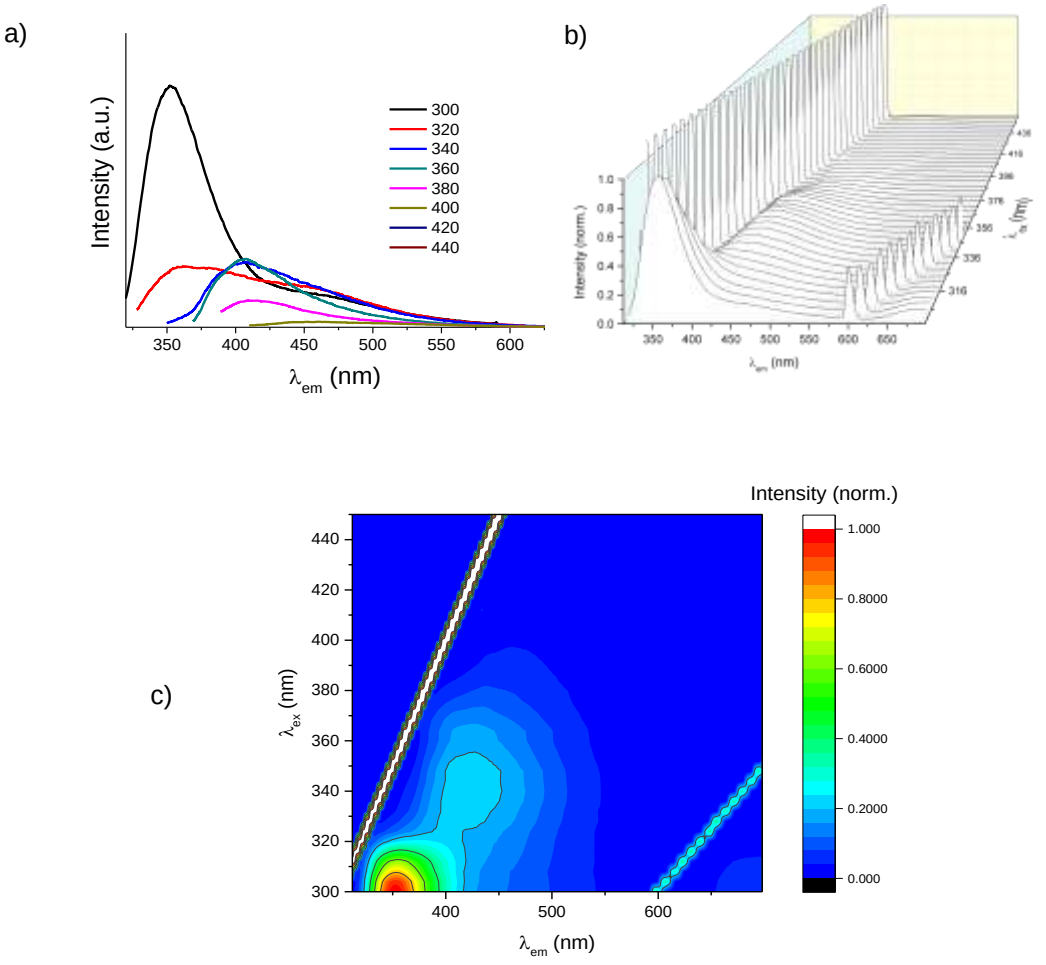

Figure 6.31. a) FL spectra of CNDs **5** in water at different excitation wavelengths (300-440 nm). b) 3D Fluorescence emission spectra of WCNDs by exciting at different wavelengths (300-450 nm). c) Fluorescence matrix scan experiment showing the fluorescence mapping by exciting at different wavelengths.

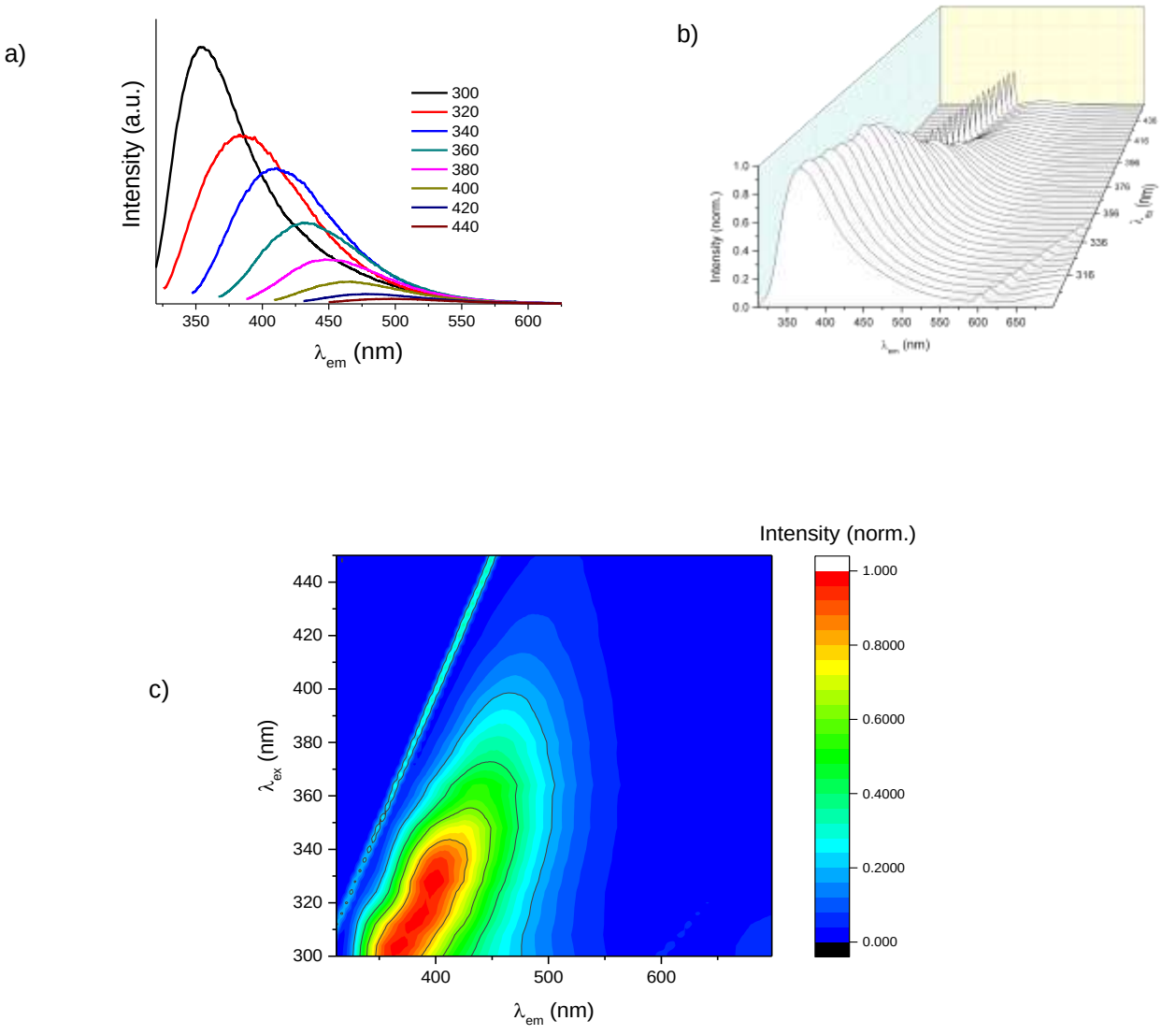

Figure 6.32. a) FL spectra of CNDs **6** in water at different excitation wavelengths (300-440 nm). b) 3D Fluorescence emission spectra of WCNDs by exciting at different wavelengths (300-450 nm). c) Fluorescence matrix scan experiment showing the fluorescence mapping by exciting at different wavelengths.

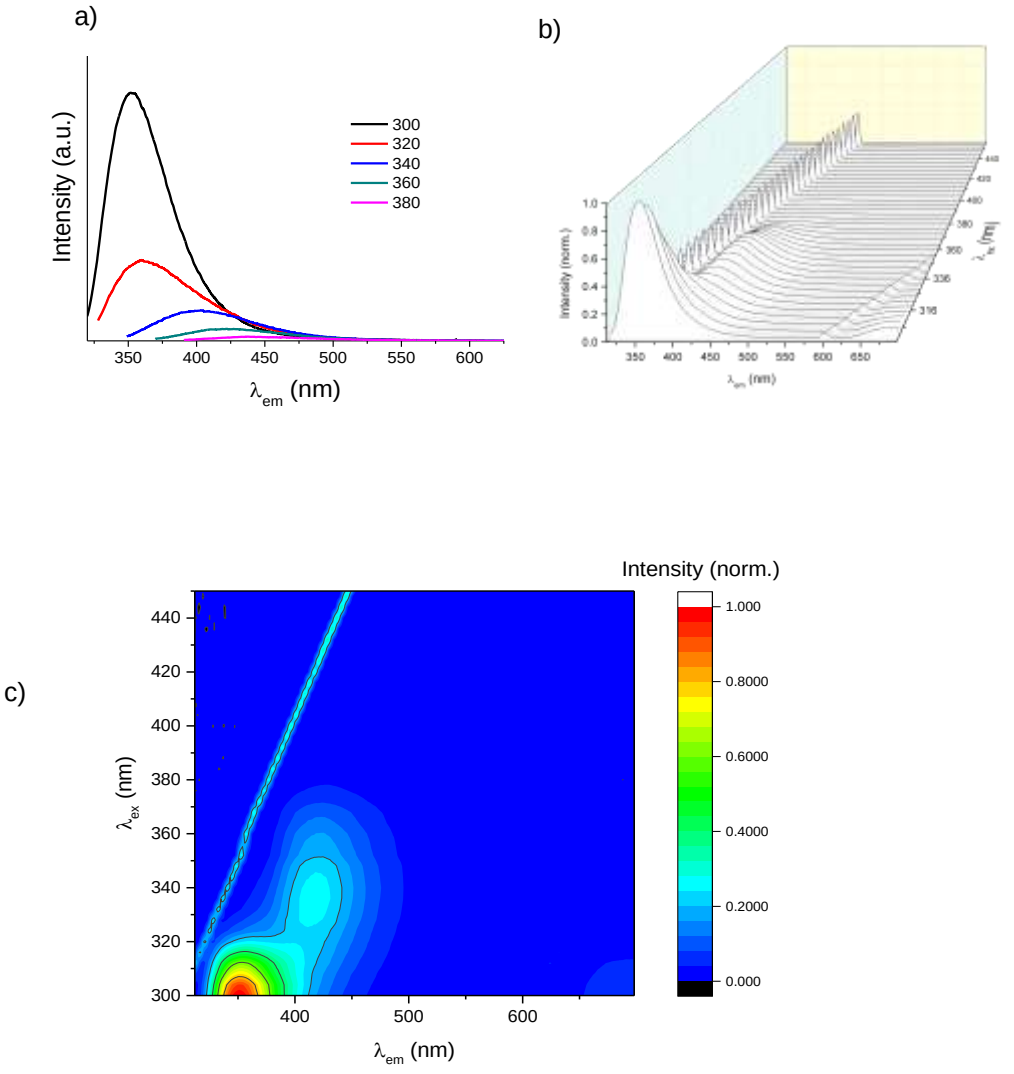

Figure 6.33. a) FL spectra of CNDs **7** in water at different excitation wavelengths (300-440 nm). b) 3D Fluorescence emission spectra of WCNDs by exciting at different wavelengths (300-450 nm). c) Fluorescence matrix scan experiment showing the fluorescence mapping by exciting at different wavelengths.

6. Mastering the electrochemical properties of CDs

Electron transfer

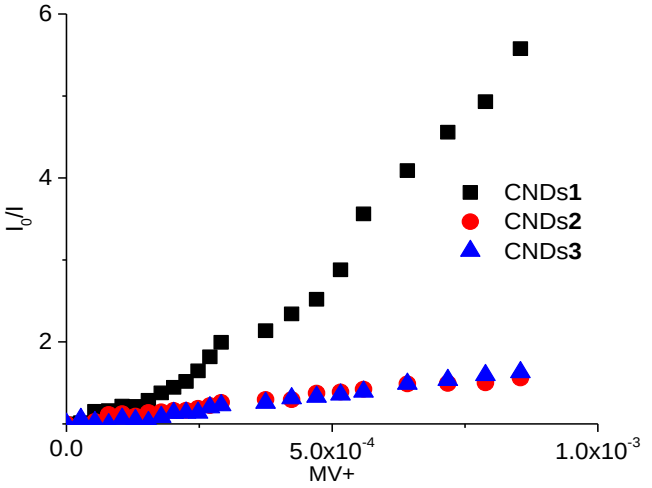

Figure 6.34. Quenching of CNDs **1-3** emission by MV^{2+} addition.

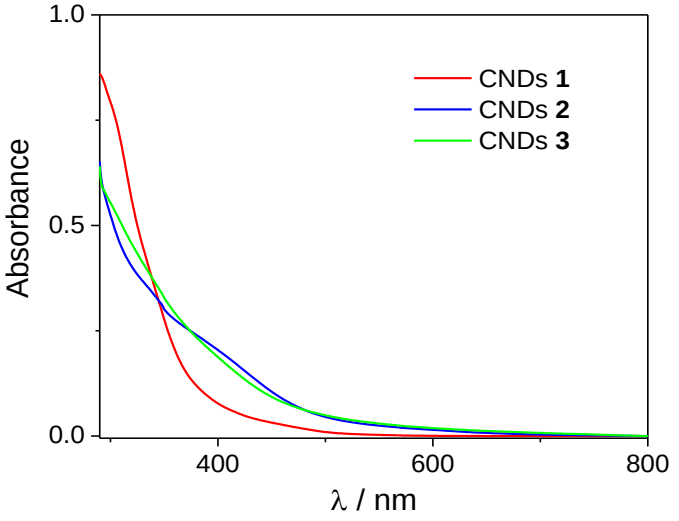

Figure 6.35. Uv-spectra of CNDs **1** (0.5 mg mL^{-1}), CNDs **2** (0.06 mg mL^{-1}) and CNDs **3** (0.17 mg mL^{-1}) in EDTA 0.1 M, pH 6.0.

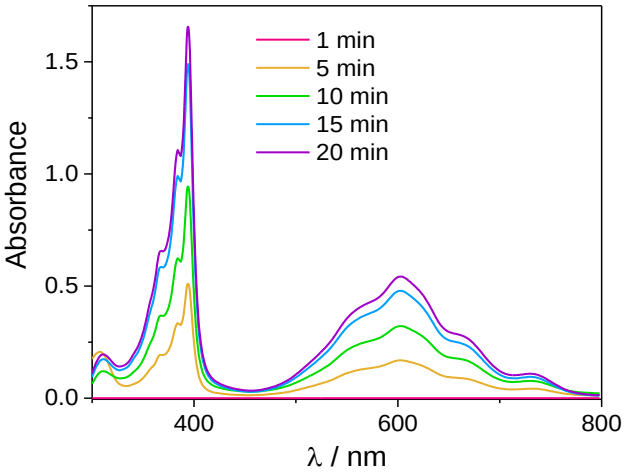

Figure 6.36. UV-vis spectra of CNDs **2** (0.06 mg mL^{-1}) with methyl viologen dichloride (MV^{2+}, 40 µM) in aqueous EDTA (0.1 M, pH 6) under full solar spectrum irradiation. The spectra are background corrected for CNDs **2** absorption.

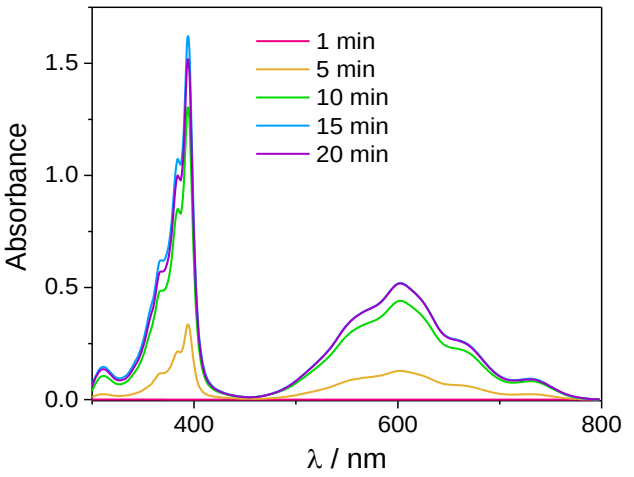

Figure 6.37. UV-vis spectra of CNDs **3** (0.17 mg mL^{-1}) with methyl viologen dichloride (MV^{2+}, 40 µM) in aqueous EDTA (0.1 M, pH 6) under full solar spectrum irradiation. The spectra are background corrected for CNDs **3** absorption

6.4 References

[1] X. Wang, L. L. Cao, F. S. Lu, M. J. Meziani, H. Li, G. Qi, B. Zhou, B. A. Harruff, F. Kermarrec, Y.-P. Sun, *Chem. Commun.* **2009**, *271*, 3774.

[2] H. Sohn, R. M. Calhoun, M. J. Sailor, W. C. Trogler, *Angew Chem.* **2001**, *40*, 2104–2105.

[3] Y. P. Sun, C. E. Bunker, B. Ma, *J. Am. Chem. Soc.* **1994**, *116*, 9692–9699.

[4] J. Xia, J. Di, H. Li, H. Xu, H. Li, S. Guo, *Appl. Catal. B Environ.* **2016**, *181*, 260–269.

[5] H. Li, X. He, Z. Kang, H. Huang, Y. Liu, J. Liu, S. Lian, C. H. A. Tsang, X. Yang, S. T. Lee, *Angew. Chem.* **2010**, *49*, 4430–4434.

[6] H. Li, Z. Kang, Y. Liu, S.-T. Lee, X. Y. Xu, R. Ray, Y. L. Gu, H. J. Ploehn, L. Gearheart, K. Raker, *J. Mater. Chem.* **2012**, *22*, 24230.

[7] H. Zhang, H. Ming, S. Lian, H. Huang, H. Li, L. Zhang, Y. Liu, Z. Kang, S.-T. Lee, *Dalt. Trans.* **2011**, *40*, 10822.

[8] H. Yu, H. Zhang, H. Huang, Y. Liu, H. Li, H. Ming, Z. Kang, *New J. Chem.* **2012**, *36*, 1031.

[9] H. Zhang, H. Huang, H. Ming, H. Li, L. Zhang, Y. Liu, Z. Kang, *J. Mater. Chem.* **2012**, *22*, 10501.

[10] R. Yang, X. Lu, X. Huang, Z. Chen, X. Zhang, M. Xu, Q. Song,

L. Zhu, *Appl. Catal. B Environ.* **2015**, *170–171*, 225–232.

[11] Y. Guo, P. Yao, D. Zhu, C. Gu, W. Knoll, Q. Li, Z. G. Zou, X. P. Sun, Z. H. Kang, X. Yang, et al., *J. Mater. Chem. A* **2015**, *3*, 13189–13192.

[12] C. Huang, Y. Hong, X. Yan, L. Xiao, K. Huang, W. Gu, K. Liu, W. Shi, *RSC Adv.* **2016**, *6*, 40137–40146.

[13] S. Y. Lim, W. Shen, Z. Gao, L. Cao, X. Wang, M. J. Meziani, F. S. Lu, H. F. Wang, P. G. Luo, Y. Lin, *Chem. Soc. Rev.* **2015**, *44*, 362–381.

[14] M. N. Chong, B. Jin, C. W. K. Chow, C. Saint, *Water Res.* **2010**, *44*, 2997–3027.

[15] M. Grätzel, *J. Photochem. Photobiol. C Photochem. Rev.* **2003**, *4*, 145–153.

[16] Y. Li, Y. Hu, Y. Zhao, G. Shi, L. Deng, Y. Hou, L. Qu, *Adv. Mater.* **2011**, *23*, 776–780.

[17] P. Mirtchev, E. J. Henderson, N. Soheilnia, C. M. Yip, G. A. Ozin, X. Sun, Z. Ding, M. Gratzel, R. S. Ruoff, M. Chen, et al., *J. Mater. Chem.* **2012**, *22*, 1265–1269.

[18] V. Gupta, N. Chaudhary, R. Srivastava, G. D. Sharma, R. Bhardwaj, S. Chand, *J. Am. Chem. Soc.* **2011**, *133*, 9960–9963.

[19] L. Cao, S. Sahu, P. Anilkumar, C. E. Bunker, J. Xu, K. A. S. Fernando, P. Wang, E. A. Guliants, K. N. Tackett, Y.-P. Sun, *J. Am. Chem. Soc.* **2011**, *133*, 4754–4757.

[20] F. Lodermeyer, R. En, D. Costa, R. E. Casillas, F. T. U. Kohler, P. Wasserscheid, M. Prato, D. M. Guldi, *Environ. Sci.* **2015**, 8, 241.

[21] R. D. Costa, S. Feihl, A. Kahnt, S. Gambhir, D. L. Officer, G. G. Wallace, M. I. Lucio, M. A. Herrero, E. Vázquez, Z. Syrgiannis, *Adv. Mater.* **2013**, *25*, 6513–6518.

[22] R. Casillas, F. Lodermeyer, R. D. Costa, M. Prato, D. M. Guldi, *Adv. Energy Mater.* **2014**, *4*, 1301577.

[23] Y. Li, Y. Zhao, H. Cheng, Y. Hu, G. Shi, L. Dai, L. Qu, Q. Yi, G. Zou, H. Zhang, et al., *J. Am. Chem. Soc.* **2012**, *134*, 15–18.

[24] F. Wang, D. Kozawa, Y. Miyauchi, K. Hiraoka, S. Mouri, Y. Ohno, K. Matsuda, *Nat. Commun.* **2015**, *6*, 6305.

[25] V. Strauss, J. T. Margraf, K. Dirian, Z. Syrgiannis, M. Prato, C. Wessendorf, A. Hirsch, T. Clark, D. M. Guldi, *Angew. Chem.* **2015**, *54*, 8292–8297.

[26] J. Briscoe, A. Marinovic, M. Sevilla, S. Dunn, M. Titirici, *Angew. Chem.* **2015**, *54*, 4463–4468.

[27] B. O'Regan, M. Grätzel, *Nature* **1991**, *353*, 737–740.

[28] M. K. Nazeeruddin, A. Kay, I. Rodicio, R. Humphry-Baker, E. Mueller, P. Liska, N. Vlachopoulos, M. Graetzel, *J. Am. Chem. Soc.* **1993**, *115*, 6382–6390.

[29] M. Sánchez Carballo, M. Urbani, A. K. Chandiran, D. González-Rodríguez, P. Vázquez, M. Grätzel, M. K. Nazeeruddin, T.

Torres, *Dalt. Trans.* **2014**, *43*, 15085–15091.

[30] Z. Pan, I. Mora-Seró, Q. Shen, H. Zhang, Y. Li, K. Zhao, J. Wang, X. Zhong, J. Bisquert, *J. Am. Chem. Soc.* **2014**, *136*, 9203–9210.

[31] C.-H. M. Chuang, P. R. Brown, V. Bulović, M. G. Bawendi, *Nat. Mater.* **2014**, *13*, 796–801.

[32] B. Bai, D. Kou, W. Zhou, Z. Zhou, S. Wu, *Green Chem.* **2015**, *17*, 4377–4382.

[33] Z. Ning, Y. Ren, S. Hoogland, O. Voznyy, L. Levina, P. Stadler, X. Lan, D. Zhitomirsky, E. H. Sargent, *Adv. Mater.* **2012**, *24*, 6295–6299.

[34] W. Ma, S. L. Swisher, T. Ewers, J. Engel, V. E. Ferry, H. A. Atwater, A. P. Alivisatos, *ACS Nano* **2011**, *5*, 8140–8147.

[35] X. Zhang, E. M. J. Johansson, J. Zhang, N. Vlachopoulos, E. M. Johansson, M. G. Ramsey, R. H. Friend, N. C. Greenham, U. Scherf, K. Meerholz, et al., *J. Mater. Chem. A* **2017**, *5*, 303–310.

[36] Y. Cao, A. Stavrinadis, T. Lasanta, D. So, G. Konstantatos, *Nat. Energy* **2016**, *1*, 16035.

[37] J. B. Essner, G. A. Baker, *Environ. Sci. Nano* **2017**, *4*, 1216–1263.

[38] J. T. Margraf, F. Lodermeyer, V. Strauss, P. Haines, J. Walter, W. Peukert, R. D. Costa, T. Clark, D. M. Guldi, B. Yang, et al., *Nanoscale Horiz.* **2016**, *1*, 220–226.

[39] A. Marinovic, L. S. Kiat, S. Dunn, M. M. Titirici, J. Briscoe, *ChemSusChem* **2017**, *10*, 1004–1013.

[40] H. Zhang, Y. Wang, P. Liu, Y. Li, H. G. Yang, T. An, P.-K. Wong, D. Wang, Z. Tang, H. Zhao, *Nano Energy* **2015**, *13*, 124–130.

[41] Y. Q. Zhang, D. K. Ma, Y. G. Zhang, W. Chen, S. M. Huang, *Nano Energy* **2013**, *2*, 545–552.

[42] J. Briscoe, S. Dunn, *Adv. Mater.* **2016**, *28*, 3802–3813.

[43] Q. Tang, W. Zhu, B. He, P. Yang, *ACS Nano* **2017**, *11*, 1540–1547.

[44] S. Sahu, Y. Liu, P. Wang, C. E. Bunker, K. A. S. Fernando, W. K. Lewis, E. A. Guliants, F. Yang, J. Wang, Y.-P. Sun, *Langmuir* **2014**, *30*, 8631–8636.

[45] B. C. M. Martindale, G. A. M. Hutton, C. A. Caputo, E. Reisner, *J. Am. Chem. Soc.* **2015**, *137*, 6018–6025.

[46] B. C. M. Martindale, E. Joliat, C. Bachmann, R. Alberto, E. Reisner, *Angew. Chem.* **2016**, *55*, 9402–9406.

[47] M. A. Gross, A. Reynal, J. R. Durrant, E. Reisner, *J. Am. Chem. Soc.* **2014**, *136*, 356–366.

[48] B. C. M. Martindale, G. A. M. Hutton, C. A. Caputo, S. Prantl, R. Godin, J. R. Durrant, E. Reisner, *Angew. Chem.* **2017**, *56*, 6459–6463.

[49] G. A. M. M. Hutton, B. Reuillard, B. C. M. M. Martindale, C. A.

Caputo, C. W. J. J. Lockwood, J. N. Butt, E. Reisner, *J. Am. Chem. Soc.* **2016**, *138*, 16722–16730.

[50] F. Arcudi, L. Dordevic, M. Prato, *Angew. Chem.* **2016**, *55*, 2107–2112.

[51] S. Carrara, F. Arcudi, M. Prato, L. De Cola, *Angew. Chem.* **2017**, *56*, 4757–4761.

[52] J. Liu, Y. Liu, N. Liu, Y. Han, X. Zhang, H. Huang, Y. Lifshitz, S.-T. Lee, J. Zhong, Z. Kang, *Science* **2015**, *347*.

[53] J. B. L. Liao, Q. Zhang, Z. Su, Z. Zhao, Y. Wang, Y. Li, X. Lu, D. Wei, F. R. Hernandez, *Nat. Nanotechonology* **2014**, *9*, 69–73.

[54] X. Wu, C. Zhu, L. Wang, S. Guo, Y. Zhang, H. Li, H. Huang, Y. Liu, J. Tang, Z. Kang, *ACS Catal.* **2017**, *7*, 1637–1645.

[55] C. G. Zoski, *Handbook of electrochemistry*, **2007**, 892.

[56] C. K. Prier, D. A. Rankic, D. W. C. MacMillan, *Chem. Rev.* **2013**, *113*, 5322–5363.

[57] M. D. Kärkäs, O. Verho, E. V. Johnston, B. Åkermark, *Chem. Rev.* **2014**, *114*, 11863–12001.

[58] K. Kalyanasundaram, *Coord. Chem. Rev.* **1982**, *46*, 159–244.

[59] C. Ye, M. Li, J. Luo, L. Chen, Z. Tang, J. Pei, L. Jiang, Y. Song, D. Zhu, *J. Mater. Chem.* **2012**, *22*, 4299.

[60] J. Hou, M.-H. Park, S. Zhang, Y. Yao, L.-M. Chen, J.-H. Li, Y. Yang, *Macromolecules* **2008**, *41*, 6012–6018.

[61] J.-L. Bredas, *Mater. Horiz.* **2014**, *1*, 17–19.

[62] L. Lasser, E. Ronca, M. Pastore, F. De Angelis, J. Cornil, R. Lazzaroni, D. Beljonne, *J. Phys. Chem. C* **2015**, *119*, 9899–9909.

[63] A. Kudo, Y. Miseki, A. Fujishima, T. N. Rao, D. A. Tryk, A. Fujishima, X. Zhang, D. A. Tryk, A. Fujishima, K. Honda, et al., *Chem. Soc. Rev.* **2009**, *38*, 253–278.

[64] T. Johansson, W. Mammo, M. Svensson, M. R. Andersson, O. Inganäs, *J. Mater. Chem.* **2003**, *13*, 1316–1323.

[65] E. Kaiser, R. L. Colescott, C. D. Bossinger, P. I. Cook, *Anal. Biochem.* **1970**, *34*, 595–598.

[66] A. Sartorel, M. Carraro, F. M. Toma, M. Prato, M. Bonchio, K. N. Ferreira, T. M. Iverson, K. Maghlaoui, J. Barber, S. Iwata, et al., *Energy Environ. Sci.* **2012**, *5*, 5592.

[67] J. D. Blakemore, R. H. Crabtree, G. W. Brudvig, *Chem. Rev.* **2015**, *115*, 12974–13005.

[68] F. Arcudi, V. Strauss, L. Đorđević, A. Cadranel, D. M. Guldi, M. Prato, *Angew. Chem.* **2017**, *56*, 12097–12101.

[69] V. Strauss, J. T. Margraf, C. Dolle, B. Butz, T. J. Nacken, J. Walter, W. Bauer, W. Peukert, E. Spiecker, T. Clark, et al., *J. Am. Chem. Soc.* **2014**, *136*, 17308–17316.

[70] L. Wang, S. J. Zhu, H. Y. Wang, S. N. Qu, Y. L. Zhang, J. H. Zhang, Q. D. Chen, H. L. Xu, W. Han, B. Yang, et al., *ACS Nano*

2014, *8*, 2541–2547.

[71] S. Zhu, Y. Song, X. Zhao, J. Shao, J. Zhang, B. Yang, *Nano Res.* **2015**, *8*, 355–381.

[72] F. Ehrat, S. Bhattacharyya, J. Schneider, A. Löf, R. Wyrwich, A. L. Rogach, J. K. Stolarczyk, A. S. Urban, J. Feldmann, *Nano Lett.* **2017**, *17*, 7710–7716.

[73] Y.P. Sun, B. Zhou, Y. Lin, W. Wang, K. A. S. Fernando, P. Pathak, M. M. Meziani, B. A. Harruff, X. Wang, H. Wang, *J. Am. Chem. Soc* **2006**, *128*, 7756–7757.

[74] X. Wang, L. Cao, S. T. Yang, F. Lu, M. J. Meziani, L. Tian, K. W. Sun, M. A. Bloodgood, Y. P. Sun, *Angew. Chem.* **2010**, *49*, 5310–5314.

[75] C. L. Bird, A. T. Kuhn, *Chem. Soc. Rev.* **1981**, *10*, 49.

[76] C. M. Cardona, W. Li, A. E. Kaifer, D. Stockdale, G. C. Bazan, *Adv. Mater.* **2011**, *23*, 2367–2371.

[77] C. Würth, M. Grabolle, J. Pauli, M. Spieles, U. Resch-Genger, *Nat. Protoc.* **2013**, *8*, 1535–1550.

[78] C. L. Bird, A. T. Kuhn, *Chem. Soc. Rev.* **1981**, *10*, 49.

7. Acknowledgments

Al mio relatore di tesi, il Prof. Maurizio Prato, per avermi dato la possibilità di svolgere questo dottorato nel suo gruppo di ricerca. Grazie per avermi concesso autonomia e libertà di scelta in molti ambiti della mia ricerca permettendomi di sbagliare (molto) ma anche di imparare (tanto). Grazie per la comprensione nei momenti di difficoltà, le motivazioni e l'entusiasmo con cui ha accolto le mie idee, aiutandomi a chiarire un po' i miei ragionamenti.

A Zois, per l'accoglienza iniziale, i primi mini-group meeting, le lunghe discussioni, il tanto entusiasmo, le pazienti correzioni e le "crazy ideas" delle sette di sera. Per avermi introdotto al mondo coloratissimo delle PBI e agli strani ritmi del sincrotrone.

A Francesca, che a metà del mio dottorato mi ha proposto di lavorare con lei in una chimica a me completamente nuova e di cui ero molto scettico (mi sbagliavo). Mi ha insegnato tutto quello che so sui carbon nandodots e fatto vedere come si lavora in modo scrupoloso. Grazie per la pazienza, le risate, i consigli, i suggerimenti con cui ha cercato di cambiare la mia indole confusionaria e approssimativa (e la mia disabilità in campo grafico).

A Luka, per avermi dato un po' di basi di chimica organica di sintesi, tanti consigli e molte correzioni. Penso che sia un modello di riferimento per la capacità e l'entusiasmo che un ricercatore dovrebbe avere. Grazie per essere sempre stato schietto con me, perché solo così posso migliorare come chimico e persona.

A Max, che mi ha pazientemente insegnato i trucchi e i segreti del sincrotrone, per le tante nottate passate insieme alla "austrian beamline" e le crisi di sonno superate ridendo.

A Erica, per la sua disponibilità e gentilezza durante il periodo trascorso a Padova, e con cui ho condiviso i momenti di difficoltà quando gli esperimenti di fotocatalisi non davano buoni risultati.

Alla Prof. Marcella Bonchio, mia relatrice di tesi specialistica, per avermi continuato a spronare anche dopo il conseguimento della tesi e per avermi sempre accolto a braccia aperte nel suo laboratorio ogni qual volta dovessi affrontare interessanti esperimenti di catalisi.

Tutti gli altri componenti del gruppo: Michele, Eleonora, Susanna, Myriam, Dani, Ana, Marina, Eva, Cristina, Nuria, Alejandro, Angela, Jenni, Manuel per tutte le battute, i pranzi (soprattutto le pizze), i post-laboratorio e altri momenti passati insieme.

I miei genitori che sempre mi hanno seguito in questo percorso, pur lasciandomi tutta la libertà che potevo desiderare, la cui presenza è stata sempre essenziale e motivo di sicurezza.

A mia nonna Anna, che nonostante abbia già avuto a che fare con un chimico padovano un po' di tempo fa, si è sempre mostrata interessata alle mie ricerche e al mio percorso di studi, credendo in me e motivandomi (e anche viziandomi).

E a tutti gli altri, che non nomino perché non posso essere troppo serio, a quelli che sono a Schio, a chi ha corso con me a Trieste, ai parenti, ai compagni dei Summano Cobras, alla redazione di Spirito Trail, a chi ha fatto con me uno dei mille sport provati in questi anni, a sci-hub, al Carso, a Carlotta, alla mensa, ai cinghiali.

E poi a Me, perché si.